DEVELOPMENT OF HIGH-SPEED MICROMACHINING CENTER AND ITS PERFORMANCE EVALUATION IN MICRO AND DIAMOND TURNING

BY

ARNAB DAS
Admission No. 18DR0039

THESIS

SUBMITTED TO

INDIAN INSTITUTE OF TECHNOLOGY
(INDIAN SCHOOL OF MINES), DHANBAD

For the award of the degree of

DOCTOR OF PHILOSOPHY

December 1, 2023

Form No: PH13

INDIAN INSTITUTE OF TECHNOLOGY (INDIAN SCHOOL OF MINES) DHANBAD

CERTIFICATE FROM THE SUPERVISOR(S)

(To be submitted at the time of Thesis Submission)

This is to certify that the thesis entitled "**Development of high-speed micromachining center and its performance evaluation in micro and diamond turning**" being submitted to the Indian Institute of Technology (Indian School of Mines), Dhanbad by Mr. **Arnab Das**, Admission No. **18DR0039**, for the award of Doctor of Philosophy (Ph.D.) Degree is a bonafide work carried out by him, in the Department of **Mechanical Engineering**, IIT (ISM), Dhanbad, under my supervision and guidance. The thesis has fulfilled all the requirements as per the regulations of this Institute and, in my/our opinion, has reached the standard needed for submission. The results embodied in this thesis have not been submitted to any other university or institute for the award of any degree or diploma.

Vivek Bajpai

Signature of Supervisor

Name: Prof. Vivek Bajpai

Date: 01/12/2023

Form No: PH12

INDIAN INSTITUTE OF TECHNOLOGY (INDIAN SCHOOL OF MINES) DHANBAD

CERTIFICATE REGARDING ENGLISH CHECKING

(To be submitted at the time of Thesis Submission)

This is to certify that the thesis entitled "**Development of high-speed micromachining center and its performance evaluation in micro and diamond turning**" being submitted to the Indian Institute of Technology (Indian School of Mines), Dhanbad by Mr. **Arnab Das**, Admission No. **18DR0039**, for the award of Doctor of Philosophy (Ph.D.) Degree has been thoroughly checked for quality of English and logical sequencing of topics.

It is hereby certified that the standard of English is good and that grammar and typos have been thoroughly checked.

It is now worthy for evaluation by the panel of examiners.

Signature of Supervisor (s)

Name: Prof. Vivek Bajpai

Date: 01/12/2023

Signature of Scholar

Name: Arnab Das

Date: 01/12/2023

Form No: PH11

INDIAN INSTITUTE OF TECHNOLOGY (INDIAN SCHOOL OF MINES) DHANBAD

CERTIFICATE FOR CLASSIFIED DATA

(To be submitted at the time of Thesis Submission)

This is to certify that the thesis entitled "**Development of high-speed micromachining center and its performance evaluation in micro and diamond turning**" being submitted to the Indian Institute of Technology (Indian School of Mines), Dhanbad by Mr. **Arnab Das** for award of Doctor of Philosophy (Ph.D) Degree in **Mechanical Engineering** does not contains any classified information. This work is original and yet not been submitted to any institution or university for the award of any degree.

Signature of Supervisor

Signature of Scholar

Form No: PH10

INDIAN INSTITUTE OF TECHNOLOGY (INDIAN SCHOOL OF MINES) DHANBAD

COPYRIGHT AND CONSENT FORM

(To be submitted at the time of Thesis Submission)

To ensure uniformity of treatment among all contributors, other forms may not be substituted for this form, nor may any wording of the form be changed. This form is intended for original material submitted to the IIT (ISM), Dhanbad and must accompany any such material in order to be published by the ISM. Please read the form carefully and keep a copy for your files.

TITLE OF THESIS: "Development of high-speed micromachining center and its performance evaluation in micro and diamond turning"

AUTHOR'S NAME & ADDRESS: Arnab Das & 8, Kumar Para Lane, Kadamtala, Howrah – 711101, West Bengal

COPYRIGHT TRANSFER

1. The undersigned hereby assigns to Indian Institute of Technology (Indian School of Mines), Dhanbad all rights under copyright that may exist in and to: (a) the above Work, including any revised or expanded derivative works submitted to the ISM by the undersigned based on the work; and (b) any associated written or multimedia components or other enhancements accompanying the work.

CONSENT AND RELEASE

2. In the event the undersigned makes a presentation based upon the work at a conference hosted or sponsored in whole or in part by the IIT (ISM) Dhanbad, the undersigned, in consideration for his/her participation in the conference, hereby grants the ISM the unlimited, worldwide, irrevocable permission to use, distribute, publish, license, exhibit, record, digitize, broadcast, reproduce and archive; in any format or medium, whether now known or hereafter developed: (a) his/her presentation and comments at the conference; (b) any written materials or multimedia files used in connection with his/her presentation; and (c) any recorded interviews of him/her (collectively, the "Presentation"). The permission granted includes the transcription and reproduction of the Presentation for inclusion in products sold or distributed

by IIT(ISM) Dhanbad and live or recorded broadcast of the Presentation during or after the conference.

3. In connection with the permission granted in Section 2, the undersigned hereby grants IIT (ISM) Dhanbad the unlimited, worldwide, irrevocable right to use his/her name, picture, likeness, voice and biographical information as part of the advertisement, distribution and sale of products incorporating the Work or Presentation, and releases IIT (ISM) Dhanbad from any claim based on right of privacy or publicity.
4. The undersigned hereby warrants that the Work and Presentation (collectively, the "Materials") are original and that he/she is the author of the Materials. To the extent the Materials incorporate text passages, figures, data or other material from the works of others, the undersigned has obtained any necessary permissions. Where necessary, the undersigned has obtained all third party permissions and consents to grant the license above and has provided copies of such permissions and consents to IIT (ISM) Dhanbad.

GENERAL TERMS

* The undersigned represents that he/she has the power and authority to make and execute this assignment.
* The undersigned agrees to indemnify and hold harmless the IIT (ISM) Dhanbad from any damage or expense that may arise in the event of a breach of any of the warranties set forth above.
* In the event the above work is not accepted and published by the IIT (ISM) Dhanbad or is withdrawn by the author(s) before acceptance by the IIT(ISM) Dhanbad, the foregoing copyright transfer shall become null and void and all materials embodying the Work submitted to the IIT(ISM) Dhanbad will be destroyed.
* For jointly authored Works, all joint authors should sign, or one of the authors should sign as authorized agent for the others.

Signature of the Author

Acknowledgments

I am very grateful to GOD ALMIGHTY without whose grace and blessings this study would not have been possible.

I extend my immeasurable appreciation and gratitude for the help and support I received from all the people who somehow contributed to making this study possible.

Foremost, I would like to express my sincere gratitude to my supervisor **Prof. Vivek Bajpai**, Associate professor, Department of Mechanical Engineering, IIT (ISM) Dhanbad, for his valuable guidance, encouragement, immense support, and freedom throughout my Ph.D. journey. It is a great honour to execute my research work under his supervision. His constant energy and immense enthusiasm for research always motivated me. Further, I would be thankful to him for providing excellent research facilities and resources throughout my work and for his willingness to spare time for clarifying my doubts and research discussion.

I wish to express my sincere thanks to **Prof. Amit Rai Dixit**, Chairperson of the Doctoral Scrutiny Committee (DSC), Department of Mechanical Engineering, IIT (ISM), Dhanbad for his intimate inspiration and suggestions. I also wish to express my sincere thanks to **Prof. Sachin Kumar Singh**, DSC Member, Associate Professor, Department of Mechanical Engineering, **Prof. Madan Lal Chandravanshi**, DSC Member, Assistant Professor, Department of Mechanical Engineering, **Prof. Abhishek Kumar Singh**, DSC Member, Associate Professor, Department of Mathematics & Computing, and **Prof. A.C.S. Rao**, Assistant Professor, Department of Computer Science and Engineering, IIT (ISM) Dhanbad for their constant inspiration and thought-provoking suggestions. I also thank **Prof. Rajiv Shekhar**, Director, IIT (ISM) Dhanbad for providing all the necessary infrastructure and facilities for the research work during the period of study.

I would like to express my gratitude to **Prof. N. K. Singh**, Associate Professor, Department of Mechanical Engineering, IIT (ISM) Dhanbad for his valuable suggestions which inspired me a lot throughout this journey. Further, I would like to thank **Prof. Deepak Kumar Mandal**, Associate Professor, Department of Mechanical Engineering, IIT (ISM) Dhanbad for providing his research instruments to conduct experimental work.

I also thank all faculties and staff members in the Department of Mechanical Engineering, Central Workshop and Central Research Facility, IIT (ISM) Dhanbad who associated with me directly and indirectly during this study to support my Ph.D. work.

I individually thank all of my lab mates **Dr. Mohan Kumar, Dr. Rachit Ranjan, Dr. Shashank Shukla, Dr. Deepak Kumar, Ankit Jain, Ravi Shankar Rai, Rajesh Sahoo, Abisoor Rishi, Abhipsa Kar, Prince Anand**, and **Sumit Kumar** for their continuous help, support, and sharing their knowledge on various aspects during my research period. Further, I would like to thank **Chitransh Singh** for associating with me to perform several experimental and analytical works.

The dissertation would have been impossible without the support of my family. I express my deepest gratitude to my family- mother **Smt. Rina Das**, father **Sri Jyotirmay Das**, elder sister **Smt. Priyanka Das**, brother in law **Sri Sandipan Patra** for their love and support throughout my life. Special thanks to my dearest friends **Shriya Chakraborty** and **Sandeep Kumar Paral** for their continuous motivation and support. Without their love, support, respect, and care, it is not possible to complete this journey.

Funding Support:

This research work has been financially supported by the Department of Science and Technology (DST), India under project number DST(SERB)/533/2017- 18/Mechanical Engineering (File No. ECR/2016/001956). An instrument from the FIST grant has been used in the thesis: project sanction number: SR/FST/ET- II/2018/222(C) date: 14 March 2019 for the Mechanical Engineering Department.

Place: IIT ISM Dhanbad
Date: December 1, 2023

Arnab Das
(18DR0039)

Abstract

The fabrication of high-accuracy miniaturized components is an expeditious trend in modern manufacturing which promoted the requirement of several micro-machining technologies. Fabrication of miniaturized cylindrical components with high dimensional accuracy and smooth surface finish at all surfaces is very difficult due to very small surface area. Micro turning technology can be utilized to machine the cylindrical surface of the component, whereas diamond turning can be applicable for the flat surfaces of the component. However, low component stiffness resulted in significant deformation and dimensional inaccuracy of the component. This phenomenon restrains the application of micro turning. Moreover, low material removal rate in micro turning restricted its industrial application. Additionally, significant surface roughness, tool wear, and cutting force have been generated in mechanical micro turning process especially for ductile materials. High speed machining could be incorporated to improve the productivity and reduce the cutting force. However, the machining performance is affected by machine tool vibration during high speed micromachining where high speed spindle is the major source of vibration. Therefore, dynamic stability is a major criteria for a high speed micromachining center to perform mechanical micro turning with high accuracy and precision. Additionally, rapid heat generation at the tool-work interface further degraded the tribological performance. On the other way, nano finishing on the flat surface can be generated by diamond turning. However, the development of diamond turning machine tool is very expensive. Additionally, the conventional diamond turning machine tool comprises of air bearing spindle which possessed low stiffness and dynamic imbalance. In addition, it is very difficult to maintain the superior dynamic performance in diamond turning machine tool. All these phenomenon affect the surface generation. Hence, maintaining the surface quality and tribological performance is a major challenge in both these technologies.

In this study, a dynamically stable high speed micromachining center has been developed. The focus was to develop a closed type machine structure with minimized vibration to accommodate a high speed spindle and linear stages in a rigid manner. The developed

machine structure has provided high stiffness and damping capability to the machine tool without utilizing vibration absorbers. The amplitudes of vibration have been approached towards nanometer level during machining throughout the working range of the spindle. After development of the machine tool, some preliminary high speed micro turning experiments have been performed on lead free brass using cooled air as coolant. However, the achieved surface roughness was in the level of 2 μm. After that, high speed micro turning has been performed on miniaturized lead free brass incorporating minimum quantity lubrication (MQL). All the process parameters have been varied during the experiment and the machining performances have been evaluated. Smoother surface finish (S_a = 281 nm) has been achieved on the lead free brass component at higher cutting speed with favorable chip breaking. However, the flank wear has been increased at elevated cutting speed. The tribological performance of lead free brass in high-speed micro turning has been further improved incorporating hybrid cryogenic cooling. In this process, a simultaneous flow of liquid nitrogen and vegetable oil-based MQL has been supplied to the machining interface. The strategy has shown superior performance to improve the surface quality, chip breakability, and reduce burr formation on machined surface as compared to cutting oil based MQL and cryogenic cooling. S_a of 165 nm has been achieved using this technology. Moreover, the cutting tool has shown steady state performance in this technique.

Furthermore, a cost-effective diamond turning technology has been proposed in this study for producing mirror finish on difficult-to-machine lead free brass. Ceramic bearing spindle has been incorporated in this study. Face turning operations have been performed in an economically developed machine tool at high cutting speed. Mirror surface finish has been achieved with S_a ranging from 7 nm to 51 nm. The axial spindle drift was small. Therefore, large periodic fluctuation of surface profile and the "Lobes-star" error have been reduced on the machined surface. Additionally, the amplitudes of machine tool vibration have been appeared in the nanometer level. Negligible tool wear has been observed as well. This technology can be a comprehensive means of the present expensive diamond turning machine tools for producing superfinished surfaces. All these technologies proposed in this study can be incorporated for industrial applications to enhance the machining performance with high productivity even for highly ductile and poorly machinable lead free brass alloys. Additionally, all these technologies are economically and environmentally sustainable.

List of Symbols

V_c	Cutting speed (m/min)
f	Feed rate ($\mu m/rev$)
a_p	Depth of cut (μm)
R_t	Theoretical surface roughness
R_a	Average linear surface roughness
R_q	Linear root mean square surface roughness
R_z	Linear maximum peak to valley height
R_p	Surface peak height in linear mode
S_a	Average areal surface roughness
S_q	Areal root mean square surface roughness
S_z	Areal maximum peak to valley height
R_{PS}	Roughness due to plastic side flow
R_{edge}	Roughness of the tool cutting edge
E	Young's modulus of work material (Pa)
σ_y	Flow stress of work material (Pa)
α	Tool rake angle
α_e	Effective rake angle
β_s	Friction angle
ϕ	Principal cutting edge angle
h	Uncut chip thickness (μm)
h_{min}	Minimum uncut chip thickness (μm)
r_e	Tool cutting edge radius (μm)
r_n	Tool nose radius (μm)

F_c	Cutting force (N)
F_t	Thrust force (N)
B_{hp}	Burr height (μm)
V_B	Flank wear width (μm)
b	Flank wear length (μm)
h_e	Elastic recovery of the machined surface (μm)
H	Hardness of workpiece material (Pa)
ε_p	Plastic strain of work material
N	Spindle rotational speed (rpm)
ζ	Angular damping ratio of spindle
A	Amplitude of axial vibration due to spindle drift
MRR	Material removal rate
MQL	Minimum quantity lubrication
CMQL	Cryogenic assisted minimum quantity lubrication
EDM	Electro-discharge machining
ECDM	Electro-chemical discharge machining
SCD	Single crystal diamond
PCD	Polycrystalline diamond
SPDT	Single point diamond turning
UPM	Ultraprecision machining
UPDT	Ultraprecision diamond turning
PMMA	Polymethyl methacrylate
BUE	Built-up edge
FEM	Finite element modelling
FRF	Frequency response function
ANOVA	Analysis of variance
FESEM	Field emission scanning electron microscope
EDS	Energy dispersive spectroscopy
LN2	Cryogenic cooling technique
LN2 + MQL	Hybrid cryogenic cooling technique
FFT	Fast Fourier transform

Contents

List of Figures

List of Tables

1 Introduction

This chapter incorporates a brief introduction about micro turning, and ultra-precision diamond turning processes. The basic principles, applications, and challenging issues especially related to the surface quality and machining performance are discussed. In addition, the requirement of high speed micromachining center and novelty of the present research, its industrial importance, and the organization of the thesis are included in this chapter.

1.1 Background

The fabrication of high-accuracy miniaturized components is an expeditious trend in modern manufacturing having several applications in aerospace, automobile, electronics, and biomedical industries. High dimensional accuracy and smooth surface finish are the major characteristics of those miniaturized components. The growing demand for high-accuracy miniaturized components has promoted the requirement of several micro-machining technologies [15, 16, 17, 2]. Mechanical micromachining is one of the adaptable micromachining technologies used in modern manufacturing. However, the stiffness of the component plays a significant role in mechanical micromachining as it involves direct interaction of the cutting tool and workpiece. The miniaturized components possess very low stiffness due to small scaling issues. This resulted in significant dimensional inaccuracy under the action of cutting force during the micromachining operation. Even the sharp edges of the

cutting tool were subjected to rapid deformation and tool wear enduring the chip load. In addition, producing smooth surfaces over those miniaturized components is a challenging task considering several issues generated during mechanical micromachining. Especially, for ductile materials, a tendency of rapid plastic deformation of the surface is developed during micromachining which causes material pile-up and plastic side flow of the machined surface [6]. Therefore, a significant amount of surface roughness is developed on the machined surface. Furthermore, the ploughing effect of the cutting tool over the machined surface is significant for mechanical micromachining which causes substantial degradation of the machined surface [18]. Moreover, the tribological performance in machining is degraded. Fabrication of miniaturized cylindrical components with smooth surface at all the faces is very difficult due to very small surface area. This is very less convenient to dissipate the cutting heat and resist the deformation of the surface. Micro turning operation can be utilized to machine the cylindrical surface of the component. While diamond turning can be applicable for the flat surfaces of the miniaturized cylindrical component.

1.2 Micro turning process

Micro turning is commonly considered as high-precision mechanical micromachining technology where miniaturized cylindrical components are turned to fabricate high-accuracy products. Several industrial components such as micro-shaft for micro motors, micro-pin for electronic product, micro-jack for printed circuit board assembly, micro-needle for bio-medical application, etc. are fabricated by micro turning process [19]. There is no fundamental difference in the working principle of micro turning process with the conventional turning process except the scaling issue. The tool parameters in terms of cutting edge radius, nose radius are in the micron range. Therefore, the uncut chip area becomes smaller (within the level of 1000 μm^2). Additionally, the uncut chip thickness and depth of cut are comparable or smaller than the tool cutting edge radius and depth of cut. Therefore, the phenomena of rubbing and ploughing of the cutting tool are significant on the machined surface in micro turning. As a result, the machined surface in micro turning is highly vulnerable for damage and deformation. Three-dimensional structures can be generated by this process in micro scale [20]. Fig. 1.1 shows the micro turning operation to fabricate a micro shaft. However, significant deformation due to low component stiffness results in substantial dimensional inaccuracy [1]. This in turn restricts the application of micro turning. Moreover, previous literature reported the mechanical micro turning operations at very low cutting speed resulting in a very low material removal rate [20, 21]. Therefore, owing to low productivity mechanical micro turning has been less applicable for industrial purposes. Additionally, significant surface roughness, tool wear, and cutting

force have been generated in mechanical micro turning process [22, 23]. As a result, the application of mechanical micro turning is very less in commercial and research purposes. Fig. 1.2 clearly shows the number of researches on micro turning are significantly lower as compared to other mechanical micromachining processes such as micro-milling and micro-drilling. Meanwhile, researchers have focused on nonconventional micro turning technology. However, desired surface quality and material removal rate was not observed [24, 25]. Researchers already focused on lithographic technique rather than micro turning process to fabricate microneedles [26]. High speed machining could be a comprehensive means to improve the productivity and reduce the cutting force. However, rapid heat generation at the tool-work interface induced significant deformation of the machined surface as well as the development of rapid tool wear. Additionally, poor dynamic performance of the machine tool in terms of vibration affected the machined surface significantly in case of high speed micromachining [27].

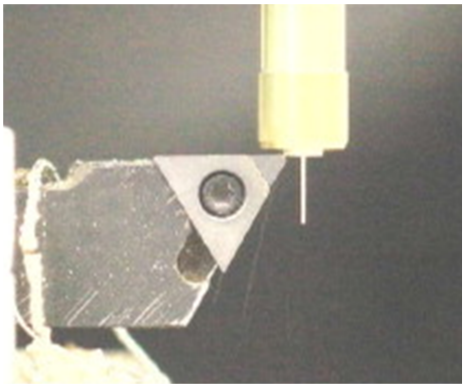

Figure 1.1: Micro turning operation to fabricate micro shaft [1]

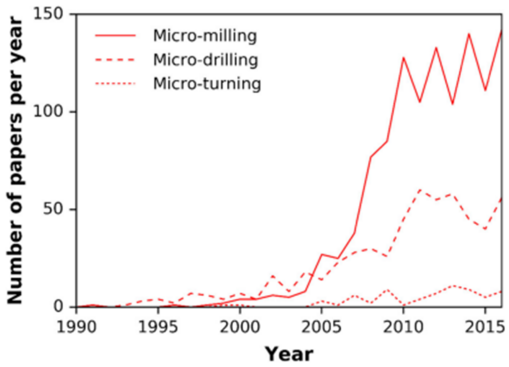

Figure 1.2: Comparison between the number of papers published on several mechanical micromachining processes [2]

1.3 Ultra-precision diamond turning process

To achieve nano finishing on the miniaturized components, ultra-precision diamond turning is a comprehensive means. It can produce super finished surfaces without application of expensive post-processing techniques like polishing [28]. This technology utilizes a single point diamond turning insert having ultra-sharp cutting edges as the cutting tool during machining. The cutting edge radius of the diamond insert ranges below 100 nm [29]. Additionally, high hardness, stiffness, and wear resistance of diamond result in superior performance of the diamond insert. Diamond turning has been widely used for machining of non-ferrous metals such as aluminium and copper based alloys [30, 31]. Ultraprecision diamond turning has been extensively applied to fabricate optical components such as different optical lenses, scanners, computer memory disks, optical molds, infrared imaging optics etc [32]. In addition, miniaturized metallic mirror can be useful for spacecraft industries where weight of the component plays a significant role. For example, Chabot et al. [33] applied diamond turning technology to fabricate image slicers of aluminium for astronomical applications. Fig. 1.3 (a) shows the diamond turning on the freeform surface of aluminium 6061 to fabricate microlens array. A magnified view of machining zone showing the diamond tool and workpiece is presented in Fig. 1.3 (b). Fig. 1.3 (c) presents the optical profilometry of the freefrom surface with 4×4 hexagonal microlens array. However, the development of ultra-precision machine tool is very expensive as it required very costly high-precision air bearing spindle. Although a little amount of imbalance induced severe axial vibration of the spindle which caused fluctuation of the axial depth of cut. Consequently, the tool profile over the machined surface fluctuates leading to lobes-star error on the machined surface [9]. It induced variation of surface roughness along the machined surface. However, complete elimination of the dynamic imbalance is not possible in the air bearing spindle due to low dynamic stiffness and damping capability. Higher compressibility of air is responsible for the problem [34]. In addition, the machine tool dynamics significantly influence surface generation in diamond turning. A marginal tool vibration may cause substantial surface degradation due to small scaling issue [35]. This phenomenon is completely influenced by machine tool dynamics.

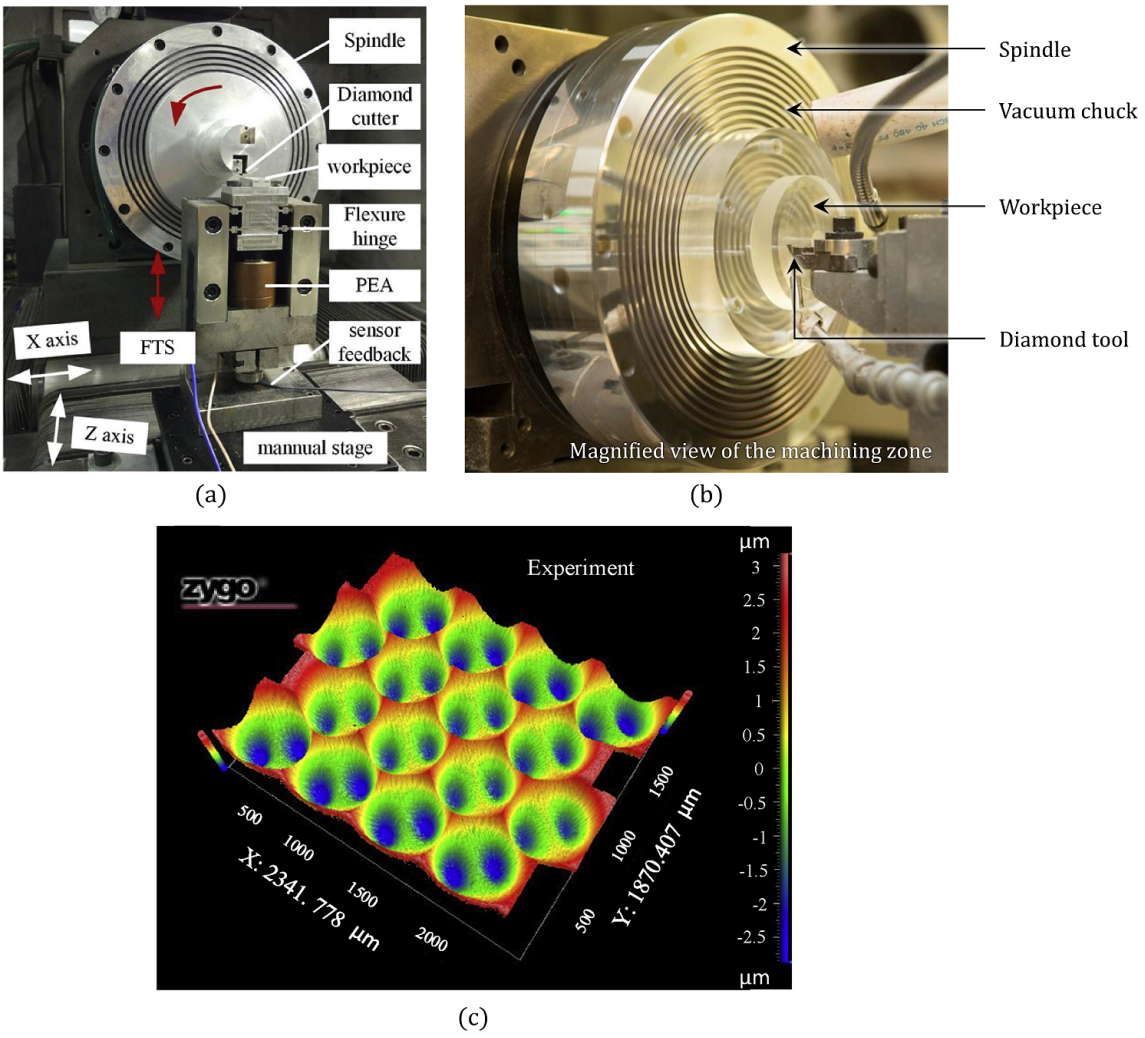

Figure 1.3: (a) Diamond turning of aluminium alloy to fabricate microlens array; (b) Magnified view of the machining zone in diamond turning; (c) 3D profilometry of the machined surface of 4×4 hexagonal microlens array [3]

1.4 Requirement of high speed micromachining center

The trend of miniaturization in the production world requires some significant changes in the manufacturing technologies. The size of the workpiece as well as the cutting tools are decreasing in recent days in accordance with the miniaturization. Therefore, the uncut chip area are very small during machining of those small components using small cutting tools. In this case, high speed micromachining is required to increase the material removal rate. High speed micromachining center is required to perform the micromachining operation. It comprises of a high speed spindle which can rotate at high rotational speed based on the requirement (10000 to 450000 rpm [36]). Besides, it is required to evacuate the chips from the machining zone during micromachining to resist chip accumulation. The micro

tools have shown lesser resilience against the chip loading due to its fragile nature [37]. Therefore, these tools are more susceptible for breakage under chip loading. High speed micromachining is a comprehensive means to remove the chips from the machining zone. High rotational speed of the workpiece or cutting tool easily evacuates the chips from the tool and workpiece surface, and restricts the accumulation. Therefore, the breakage or deformation of the miniaturized workpiece and cutting tools can be restricted under the chip loading. In addition, this phenomenon reduced the time of the cutting heat to flow from the chips to the tool or workpiece and resists the damage. Moreover, the uncut chip thickness in high speed machining is much smaller as compared to the conventional machining. This phenomenon further reduced the cutting force and the consumption of the specific cutting energy. Therefore, a smooth interaction can be established between the cutting tool and the workpiece which developed better dynamic stability during the micromachining operation. As a result, the product accuracy can be improved in high speed micromachining compared to conventional micromachining. All of these advantages are promoting the requirement of high speed micromachining center. Even in diamond turning operation, high speed micromachining can be incorporated to establish better dynamic stability and improve the product accuracy.

Meanwhile, machine tool vibration is a major issue involved in high-speed micromachining. High speed spindles are the major source of vibration due to high speed rotation. This phenomenon further leads to deterioration of surface finish, precision and accuracy in micro features. Additionally, chatter is developed which is responsible for rapid tool wear and tool breakage. All of the previous studies regarding the development of high speed micromachine tool reported remarkable machine tool vibration [38, 39]. Therefore, vibration is the major problem which limited the application of high-speed micromachining for industrial purposes. It has limited the number of researchers working on the development of high-speed micro machine tool. Hence, proper design is immensely required for a high speed micromachining center to minimize the machine tool vibration.

1.5 Research novelty and originality

The research work presented in this report is significantly novel as the utilization of high speed micro turning is not explored so far in previous researches. Previous experiments on micro turning were performed at low to moderate cutting speed (Less than 1 to 57 m/min), while the present study reveals the micro turning operation at high cutting speed i.e., 100 m/min to 240 m/min with good accuracy, surface finish, and tool wear performance. A dynamically stable high speed micromachining center has been developed indigenously for the research work. In addition, this study reveals some favorable machining conditions for a

poorly machinable material lead free brass having highly industrial and R&D significance. This incorporates the novelty of the present study as well. Moreover, a cost-effective ultra-precision diamond turning technology has been proposed using ceramic bearing spindle to fabricate nano finished surfaces. This technology was successfully able to generate nano finishing in an economical manner which included novelty in this research.

1.6 Industrial importance

This present research is important to the machining industry especially for the fabrication of miniaturized components in terms of the following points:

- It discloses the development of a dynamically stable high speed micromachining center. This machine tool is capable to machine complex shapes in an efficient manner.
- The present study discloses high speed micro turning operation which can be utilized to improve the productivity of miniaturized cylindrical components.
- This study shows efficient machining performance of poorly machinable lead free brass with optimum process parameters and cooling techniques like hybrid cryogenic cooling.
- The present study reveals a cost-effective ultra-precision diamond turning operation by ceramic bearing spindle. Promising results has been achieved in terms of nano finishing on machined surface and dynamic stability of machine tool. This technology can be incorporated in optical and space industries to fabricate super finished components in an economical manner.

1.7 Organization of the thesis

The thesis comprises of seven chapters. The brief description of each chapters are given below:

- **Chapter 1** deals with the brief introduction about micro turning and diamond turning processes; the research novelty and the industrial importance of the present research work.
- **Chapter 2** presents the literature survey of the previous researches describing the state of the art of micro turning and diamond turning. In addition, the enormous efforts of the researchers to enhance the machining performance in micro and diamond

turning are included in this chapter. Research gaps obtained in previous studies are reported. The scope and motivation of the present study are included. The problem is defined with the aim and objectives of the present study in this chapter.

- **Chapter 3** focuses on development of a dynamically stable high speed micromachining center. The vibration analysis of the machine tool, and some preliminary experiments of micro turning are incorporated in this chapter.

- **Chapter 4** describes the experimental study of high-speed micro turning operation on lead free brass using minimum quantity lubrication. The analysis of machined surface topography, burr formation on the machined surface, chip morphology, and tool wear behavior are reported. Additionally, the evaluation of optimum process parameters using statistical tools is incorporated in this chapter.

- **Chapter 5** reveals the application of hybrid cryogenic cooling technique to enhance the machinability of lead free brass in high speed micro turning operation. The process performance are reported in terms of surface topography, microhardness, burr formation on the machined surface, chip morphology, and tool wear under minimum quantity lubrication, cryogenic cooling, and hybrid cryogenic cooling technique. In addition, the economical and environmental sustainability of the process are described in this chapter.

- **Chapter 6** presents the feasibility study of an cost-effective ultra-precision diamond turning operation using ceramic bearing spindle. The comparison of surface parameters achieved in this investigation with previous literatures is studied. Additionally, the economical behavior of the presented machine tool is reported.

- **Chapter 7** presents the key concluding remarks determined in each study and the scope of future work.

2

Literature Review

The investigation of the machining performance for ductile materials have been carried out since the last century. However, very few of the recent studies on this topic have been focused on micro turning and diamond turning technology. Moreover, high speed micromachining has been adopted over conventional micromachining for better productivity and machining outcomes. Several technologies such as process parameter optimization, tool geometry optimization, cooling and lubricating techniques, hybrid and nontraditional methods, and tool texturing have been accomplished to improve the machining performance in macro and micro scale. In addition, several studies have been focused on diamond turning to improve the surface quality and additional surface characteristics. This chapter deals with the state of the art and the challenging aspects of micro turning and diamond turning technology. The literature survey is categorized in two parts. First part contains the review on micro turning and the superiority of high speed turning. The historical development of high speed micromachining center has been discussed in this portion as well. The second part reported the prior art on diamond turning of ductile materials emphasizing the surface quality and tribological performance enhancement. Eventually, this chapter incorporates a brief discussion on the research gaps identified from the literature survey, the scope of work, and the objectives of the present research work.

2.1 Micro turning

2.1.1 Effects of different parameters on machining performance in micro turning

Effects of process parameters

The machining performance is highly influenced by three process parameters i.e. cutting speed, feed rate, and depth of cut during micro-turning operation. The micro turning technology has been introduced in the earlier 2000s by Lu and Yoneyama [40]. To maintain the dimensional accuracy and resist the workpiece deformation were the major challenging issues in that time. The experiments have been performed at very low cutting speed. Piotrowska et al. [41] developed a two-dimensional mathematical model considering variable feed rate which successfully predicted the tool tip positions as well as cutting and feed forces for small depth of cut during micro-turning process. However, multidimensional model of turning dynamics was still not reported which can accurately predict the surface profile, cutting forces and the actual depth of cut which can be slightly differed from the applied depth of cut due to elastic deflection of the cutting tool. Durairaj and Gowri [42] determined better surface quality and tool wear properties at a combination of low cutting velocity, feed and cutting depth during micro-turning of Inconel 600. However, the experiments have been performed at low cutting speed. In addition, the flank wear width was significantly high in some cases. Meanwhile, high cutting speed as well as feed rate was responsible for increasing the cutting temperature which further resulted in machined surface defects [43]. Jagadesh and Samuel [44] determined that cutting force has been increased with cutting speed at lower depth of cut, while it has shown opposite trend at higher depth of cut. In general, the ploughing effect was significant at lower depth of cut which further increased due to lower uncut chip thickness at higher cutting speed. Consequently, the cutting force has been increased. Meanwhile, the cutting force has been increased at higher feed rate. The surface roughness was ranged in 0.2 to 0.6 μm. However, the machining was performed at low to moderate cutting speed (19 to 57 m/min). In addition, the chips were discontinuous during micro turning of titanium alloy at lower feed rate and transformed to continuous chips at higher feed rate [45]. The localized strain in the shear band caused shear instability of titanium alloy leading to saw tooth chip formation. The chip serration for titanium alloy was emphasized at high feed rate due to higher temperature generation [46]. An increasing trend of cutting force has been observed by Oliveira et el. [47] with feed rate and depth of cut. However, the depth of cut was significantly higher to be considered as micro turning. Singh et al. [21] determined low cutting force at lower feed rate during micro turning of brass alloy at low cutting speed. However, opposite trend

of cutting force has been reported with feed rate at higher cutting speed. Nevertheless, the cutting speeds were substantially low causing degradation in productivity. Significant tool wear has been reported by Selvakumar et al. [48] during micro turning of titanium alloy even in low cutting speed. In addition, the tool wear has been reduced at higher spindle rotational speed. At higher feed rate (25 $\mu m/rev$), significant crater wear and built-up edge formation has been observed during micro turning of titanium alloy which in turn enhanced the machined surface roughness [46].

Effects of tool geometry

The undeformed chip thickness was almost comparable to the cutting edge radius. Therefore, micro-turning has been considered as a negative rake angle process as defined in Fig. 2.1 (a). The effective negative rake angle can be determined from Fig. 2.1 (a). In this figure, $AB = AC = r_e$ and $AD = (r_e - h)$; where, h is the undeformed chip thickness and r_e is the cutting edge radius. Meanwhile, $\angle ABD = |\alpha_e|$. Therefore, the effective negative rake angle is defined as Equation 2.1 [4].

$$\alpha_e = -sin^{-1}\left(1 - \frac{h}{r_e}\right) \tag{2.1}$$

From Fig. 2.1 (b), it can be seen that the specific cutting energy gradually increased with decreasing the ratio ($\frac{h}{r_e}$). Additionally, smoother surface was obtained in this range. However, a critical point was situated and further reduction of the ratio led to rapid increase in specific cutting energy. The effective rake angle at the critical point was the critical negative rake angle. Further reduction of the ratio led the cutting tool ploughing over the workpiece surface with no chip formation. This was also responsible for rapid increase in surface roughness. The selection of suitable cutting edge radius and chamfer angle was necessary in order to obtain favorable chips, low cutting forces and improved tool life [49]. Increasing the chamfer angle led to increase the tool life, while increased the cutting force as well. The tool geometry has significant effect over cutting temperature as well. Increasing the cutting edge radius led to increase in cutting temperature [43]. In addition, sharp edge cutting tool was subjected to affirmed lesser chip-tool contact length and secondary shear zone thickness. Therefore, cutting temperature and cutting force have been reduced for sharp edge cutting tool compared to others two. Ozel et al. [50] proposed variable edge micro tools (variable honing and waterfall honing) over uniform edge cutting tool to reduce the cutting temperature, plastic strain, and tool wear. The variable micro geometry restrained the heat accumulation and stress concentration at the cutting edge. Moreover, favorable surface finish was obtained with variable micro geometry of cutting inserts during high-speed turning of ferrous alloy AISI 4340 (Cutting speed = 300 m/min)

[51]. Kaymakci et al. [52] developed a consolidated model of cutting force for turning, boring, drilling and milling operation based on the geometry of the cutting inserts and material properties. The friction factor based on tool geometry played a significant role to determine the cutting force in this model.

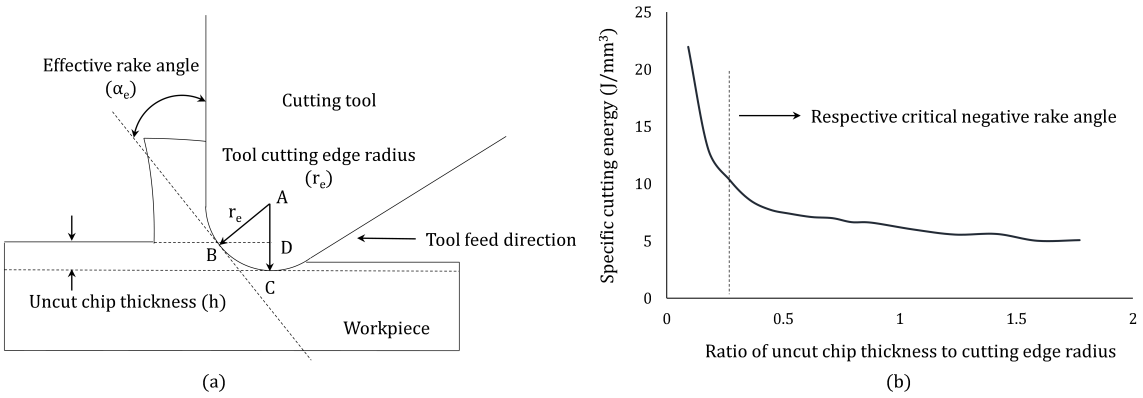

Figure 2.1: (a) Effective rake angle during micro turning process, (b) Variation of specific cutting energy with ($\frac{h}{r_e}$) ratio [4]

The consumption of cutting power was also dependent upon tool geometry. Higher tool nose radius, nose angle and cutting edge radius led to increase the volume involvement of the turning insert into the work material and reduced the power consumption [5]. Therefore, C type cutting inserts (80^o diamond shape) consumed less cutting power and resulted in low cutting force followed by T type (60^o triangular shape) and D type (55^o diamond shape) turning inserts. Fig. 2.2 represents the schematic view of different types of turning inserts. Meanwhile, the cutting force was enhanced at higher feed rate [5]. Liu et al. [53] investigated optimum tool rake angle in order to perform micro-turning of SiC particle reinforced aluminium matrix composites through brittle-ductile transition. A suitable negative rake angle was responsible of favorable plastic deformation of the work material and chip formation which further improved the surface quality. However, larger negative rake angle led to higher cutting force, tool wear and machined surface roughness as a consequence of significant ploughing. They determined -30^o as the optimum rake angle to improve surface quality and minimize tool wear. Wu et al. [54] revealed that higher cutting edge radius was responsible as well to enhance the cutting force during micro turning along with the feed rate. Additionally, material grain size significantly influenced the shearing and ploughing action; therefore, the cutting force has been increased when machining smaller grain sized material.

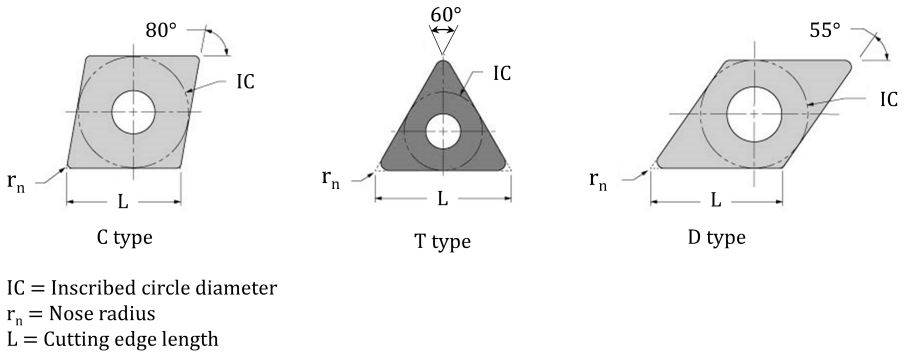

Figure 2.2: Schematic view of different types of turning inserts [5]

Effects of physical phenomenon

The surface roughness in a machining process can be theoretically approximated as, ($R_t = \frac{f^2}{8r_n}$), where f denotes feed rate and r_n is the nose radius [55]. However, the surface integrity during machining not only depends on the process parameters and geometry of the cutting tool, but also depends on various physical parameters. Liu et al. [6] determined the influence of plastic flow of workpiece material due to the indentation of the cutting tool over machine surface as shown in Fig. 2.3. This is a common phenomenon in ductile material where yielding is more significant than fracture. They developed a theoretical model of surface roughness considering the roughness of the cutting edge (R_{edge}) and this model favourably anticipated the machined surface roughness as Equation 2.2 to Equation 2.4 [6].

$$R_{total} = R_t + R_{PS} + R_{edge} \tag{2.2}$$

$$R_{PS} = k_1 lnx + k_2 \tag{2.3}$$

$$x = \frac{E cot\theta}{\sigma_y e} \tag{2.4}$$

R_{PS} is the roughness of the workpiece surface caused by plastic side flow; and k_1 and k_2 are two constants need to be calibrated through turning operation. Rheological factor x can be determined from Equation. 2.4 where E denotes young's modulus and σ_y is the average flow stress of the work material. θ is the semi-apical angle of the indenter (cutting tool) and e is an additional variable considering the strength variation between the work material. In addition. strain hardening of the work surface played a significant role on surface generation in micro turning. The strain hardening phenomenon was increased for lower shear transformation zone volume. This phenomenon possessed a dense atomic packing at the subsurface and restrained the atomic mobility. Further, higher cutting speed

and depth of cut enhanced the strain hardening of the machined surface in micro turning of bulk metallic glass [56]. He et al. [14] enlisted all the parameters having remarkable influence on turned surface roughness which incorporated minimum uncut chip thickness, material spring back, and plastic side flow. The parameters influencing the machined surface roughness and their influences are enlisted in Table 2.1

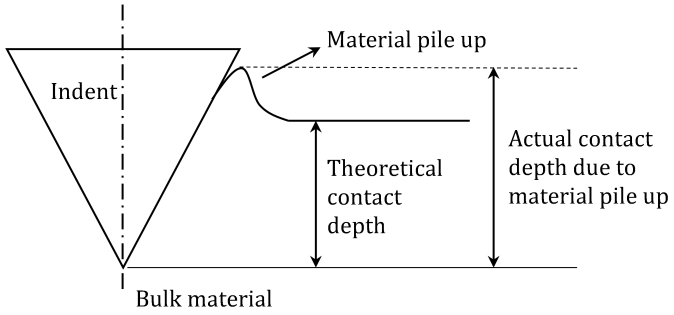

Figure 2.3: Plastic side flow due to indentation of the cutting insert into workpiece [6]

Table 2.1: List of influencing parameters over surface roughness [14]

Sl No.	Main object	Parameter classification	Specific parameters	Influence type (On increasing)
1.	Machine tool	Process parameters	Cutting speed	Decrease (Sometimes increase)
			Feed rate	Increase
			Depth of cut	Increase
		Dynamic properties	Vibration amplitudes	Increase
2.	Cutting tool	Materials properties	Tool material	Indirect
		Tool geometry	Rake angle	Increase for negative rake angle
			Cutting edge radius	Increase
			Nose radius	Decrease
			Edge waviness	Increase
3.	Workpiece material	Mechanical properties	Hardness	Increase
			Young's modulus	Increase
		Materials properties	Grain size and orientation	Indirect
4.	Machining environment	Process factors	Coolant	Decrease
		Other factors	Temperature	Increase

2.1.2 High speed machining over conventional micromachining

Cutting speed is a prominent factor influencing the machining dynamics and tribological performance in mechanical micromachining. In general, the micro components possessed very low stiffness and strength due to its low volume. Additionally, the micro cutting tool exhibits sharp cutting edge (In the level of 5 μm) that is much weaker and prone to breakage [57]. These are the major impediments for the application of conventional mechanical micromachining operation. Moreover, the material removal rate is significantly low in conventional micro turning process due to very low cutting speed. Therefore, high speed micro turning can be adopted to improve the material removal rate. Additionally, the chip load is inversely proportional with the cutting speed. Therefore, high cutting speed is able to reduce the chip load on the cutting edge of the micro tool. Subsequently, the cutting force is reduced in mechanical micromachining [58, 59]. This can be a solution to resist the breakage of sharp cutting edges of micro tool and the deformation of the micro components.

Furthermore, higher cutting speed produced remarkable surface finish in mechanical micromachining process [60]. Even at higher feed rate, the surface quality was not degraded significantly during machining at higher cutting speed. This is attributed to smaller uncut chip thickness at higher cutting speed [61]. High cutting speed during mechanical micromachining caused higher amount of heat diffused to the workpiece. Therefore, the ductility of the workpiece material has enhanced. This phenomenon led to higher plastic strain rate of the workpiece material and elongation along the force exerted by the cutting tool. Therefore, the area offered to resist the deformation was increased which in turn reduced the burr formation in mechanical micromachining [62]. Resultantly, the surface quality was enhanced. High speed machining precipitated favorable outcomes in case of macro turning as well. The surface quality was enhanced at higher cutting speed during machining of Hastelloy C22 [63]. Altin [64] determined that principle cutting force as well as machined surface roughness can be reduced with increasing the cutting speed during finished turning of Hastelloy X. However, cutting temperature was increased at higher cutting velocity which led to enhancement in tool wear and machined surface defects in some cases [43]. Zheng et al. [65] observed that the higher cutting temperature in high speed turning precipitated significant tool wear. Additionally, the surface roughness has been increased as well at higher cutting velocities in this case. Tan et al. [66] further reported that tool wear has been increased at higher cutting speed and depth of cut. Meanwhile, machine tool vibration was a major problem in high speed micromachining which significantly deteriorated the performance in machining. In this case, high speed spindle was the major source of vibration [67].

2.1.3 Historical development of high speed micromachining center

Several approaches have been reported for development of the ultra-precision machine tools since early 1980s [68]. The development of mechanical micromachining technologies has been initiated at the end of the twentieth century. However, the focus has been shifted to high speed micromachine tool in the last two decades. For example, Vogler et al. [69] developed a high speed machine tool for meso-scale machining. The spindle of the machine tool can run upto 150000 rpm and able to generate smooth surfaces. However, this machine tool was not able to hold micro cutting tools and hence, cannot be considered as a micronachining center. Another mesoscale machine tool was developed by Lee et al. [70] which comprises a high speed spindle. The spindle was able rotate upto 145000 rpm. However, significant vibration has been taken place during machining which caused degradation of surface finish. Meanwhile, Luo et al. [71] developed a bench-top UPM machine tool which was capable to machine miniaturized components with high accuracy. The accuracy of the spindle and stages including the damping quality of the machine struc-

ture has significant influence on the machining accuracy in that machine tool. A semi high speed micro-milling machine tool has been developed by Bang et al. [72] for the fabrication of micro components at low cost. This machine tool comprised of a spindle having maximum rotational speed of 30000 rpm. Li et al. [73] developed a high speed machine tool for mesoscale milling. However, the desired level of dimensional accuracy and surface was not achieved. Huo et al. [38] combined ultra-precision machining with high speed micromchining and developed a 5 axis high speed micro-milling machine tool "UltraMill". It comprised of air bearing slideways and air bearing spindle which can rotate upto 200000 rpm. They concluded that closed type machine structure showed higher stiffness and damping capability as compared to open type machine structure. However, tool vibration was still there in the machine tool affecting machining accuracy. Jahanmir [36] developed ultra-high speed micromachining center by increasing the spindle rotational speed upto 450000 rpm to achieve better productivity and machining efficiency. However, poor surface quality has been observed over aluminium alloy at higher rotational speed due to excess tool wear and built-up edge formation. Additionally, Mittal et al. [39] developed a high speed micromachining center comprising a high speed spindle mounting in a rigid type granite structure. However, significant chatter has been determined during machining at higher rotational speed. Although the number of researches involved in the development of high speed micromachining center are significantly less, most of the developed high speed micromachining centers are still in the research stage. Very few of them have fulfilled the requirement to be used for industrial purposes. Therefore, only a few number of industrial manufacturers are there in the world such as Kern Microtechnik, Mikrotools, Datron etc. those have successfully develop the high speed micromachining centers for industrial application.

High-speed micro machine tools require high speed spindles to maintain the machining speed and efficiency. But at high spindle speeds, acute vibration takes place in the machine tools [67]. This jeopardizes the dimensional accuracy; precision and surface finish of micro size products. Apart from this, chatter may occur due to vibration and it can lead to tool wear and breakage of the cutting tool [27]. Chatter may also affect the spindle and the machine tool [74]. Therefore, vibration isolation is necessary to maintain the accuracy and surface finish of the machined surface and also to maintain the tool life. The stiffness of the machine structure plays a very crucial role for machining efficiency and vibration isolation of a machine tool [75]. Hence, the high-speed micro-machine structure must have good static, dynamic stiffness and damping performance for quality machining performance [15].

Park et al. [76] proposed a design methodology of a meso-scale machine tool based on analytical and finite element modeling. They focused on optimization of the structure in

order to achieve higher stiffness. It was found that the vibration increases and the stiffness reduces with the increase in height of the column. The stiffness of the machine structure has been considered as a crucial factor influencing the product quality in terms of dimensional precision and surface finish [75]. Liang et al [77] designed an ultra-precision diamond fly-cutting machine tool. For improvement in accuracy of the ultra-precision machine, the authors focused on minimizing the size of machine components to reduce the cantilever action and thus, decrement in deformation due to vibration. They also suggested closed type structure for better rigidity. Therefore, the most considerable factor during development of a high-speed precision machine tool is minimization of machine tool vibration which creates a major area for research.

2.1.4 Techniques to improve machining performance in macro and micro turning

Application of cooling techniques

Machining of titanium based alloys can be performed at a low cutting speed range (30 m/min to 60 m/min) considering its poor machinability owing to low thermal conductivity. During high-speed machining of titanium alloys (60-120 m/min or above) expeditious tool wear has been taken place which significantly affected the surface topology of the workpiece and tool life [78]. This was due to highly localized cutting zone temperature and intense chemical affinity of titanium alloys to the tool material. Application of cryogenic cooling has reduced the tool wear during turning of Ti6Al4V at moderate cutting speed (70 m/min). However, during high-speed turning (above 100 m/min), the cryogenic liquid was unable to reach the chip-tool interface and the effect has been diminished [78]. Ezugwu et al. [7] achieved good quality surface finish over Ti6Al4V during high-speed turning (175 m/min – 200 m/min) with PCD tools with conventional and high-pressure coolant supplies. However, comparatively rough surface was achieved during turning at higher cutting speed (200 m/min) using high pressure coolant. Meanwhile, softening of machined surface has been occurred using high pressure coolant supply which substantially improved the life of the PCD inserts. Fig. 2.4 represents the effect of high pressure coolant over surface roughness at different cutting speed. Steady state surface finish has been observed with prolonged tool life applying high pressure coolant at 11 MPa as compared to conventional coolant supply. However, a large fluctuation of surface roughness has been observed by further increasing the coolant pressure to 20.3 MPa. Meanwhile, the tool failure was significant at conventional coolant supply owing to high cutting speed. Therefore, the machining was no longer existed at conventional coolant supply. Chetan et al. [79] compared the machining performance of Nimonic 90 and Ti6Al4V at dry and

MQL condition. They determined higher strength and higher chip-tool contact length of Nimonic 90 as compared to Ti6Al4V originated rapid tool wear which consequently increased the cutting force. During high-speed turning of Ti6Al4V at dry condition, nose wear progression was more prominent at low feed rate and intense abrasive wear has taken place at higher feed rate. Nevertheless, application of MQL significantly reduced the tool wear during turning of both Nimonic 90 and Ti6Al4V [79].

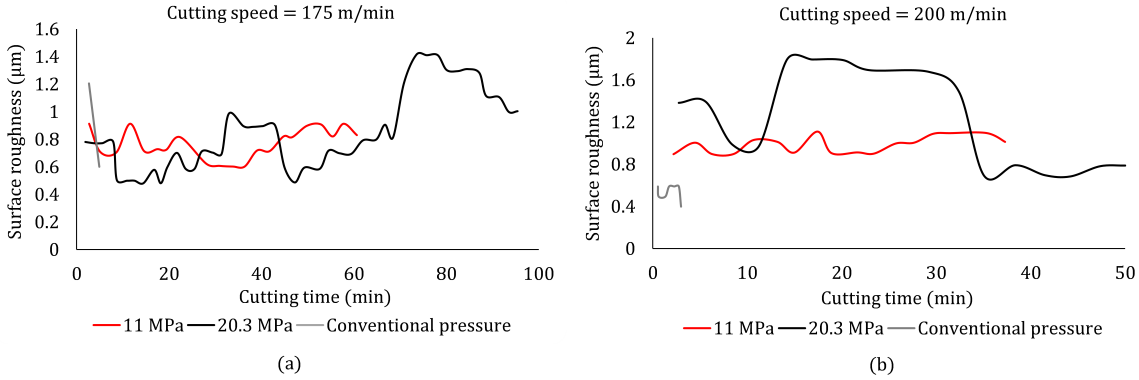

Figure 2.4: Effect of coolant supply at different pressure over surface roughness at different cutting speed [7]

Cryogenically treated carbide inserts significantly reduced the tool wear at low cutting speed during turning of difficult-to-machine nimonic 90 alloy [80] as it improved the strength and wear resistance of the cutting tool. However, coating of the inserts played a significant role in addition with cryogenic treatment to prevent the flank wear during high-speed turning (80 m/min). Parthiban et al. [81] investigated that cryogenic treatment followed by oil quenching of carbide tools resulted in excellent surface finish; and reduction in tool wear and cutting force during high-speed turning operation. Additionally, the best surface finish and optimum cutting force were reported at high cutting speed, high feed rate and low depth of cut. The surface roughness has been improved by approximately 72% with deep cryogenically treated (-145^o C) cemented carbide tools during turning of Hastelloy C22 [63]. In addition, it improved the wear resistant properties of the cutting tool and restrained the built-up edge formation during machining. Minimum quantity lubrication (MQL) is another emerging technology which has significantly improved the tool life and surface quality during high speed machining of difficult-to-machine materials. The surface quality has been improved substantially with predominant reduction in tool wear, cutting force, and cutting temperature even at high cutting speed using MQL [82]. This technology was able to reduce the cutting force in micro turning operation as well [47]. A moderate cutting speed (60 m/min) and low feed rate (0.075 mm/rev) have precipitated better surface finish on Inconel 625 alloy. Nevertheless, introduction of hBN nanoparticles into the MQL remarkably reduced the surface roughness and tool wear during turning at

high cutting speed.

Hybridization and Nontraditional machining methods

Tool based mechanical micromachining exhibits rapid tool wear. This problem has promoted the development of hybridization of mechanical micromachining process. Ultrasonic vibration assisted turning method is a hybridization process which utilizes high frequency and low amplitude vibration in order to resist continuous contact between workpiece and cutting tool. Thus, it prevents tool wear [83]. Liu et al. [84] utilized radial ultrasonic vibration-assisted turning in order to generate micro dimples over workpiece surface. They investigated that the width of the micro dimples can be enlarged with increasing the nose radius of the tool and a moderate amount of clearance angle. However, tool vibration and deflection must be highly precise to maintain the dimensional accuracy of the dimples. Hot machining that involved heating of the workpiece surface below recrystallization temperature before machining, is another well-established method for machining hard-to-machine materials. Sofuoglu et al. [83] developed a combined method of ultrasonic vibration assisted turning with hot machining and achieved better surface finish over Hastelloy X. This method was capable to maintain a stable depth of cut throughout the machining process owing to ultrasonic vibration and thermal softening. However, increase in cutting temperature resulted in reduction of tool life. Additionally, the average surface roughness was in the level of 1.5 μm and sometimes higher than 2.5 μm especially at low cutting speed. Therefore, a localized cooling was necessary during hot ultrasonic assisted turning. Cryogenic cooling could be a better solution of that issue.

Asad et al. [1] developed a hybridization of micro EDM with micro turning in which the electrode of micro EDM has been fabricated using micro turning process. However, turning of micro shafts was very difficult because of very low stiffness. Therefore, rapid deflection has been taken place during the micro turning operation. Specially designed PCD tools with sharp cutting edge were able to turn those micro shafts which was an expensive process. Srivastava et al. [85] performed turning operation over aluminium based hybrid metal matrix composite using Wire-EDM. However, desirable surface finish was not found due to decomposition of the re-solidified layer. Nevertheless, the machined surface was free from any scratch marks. Abrasive water jet turning produced much better surface finish as compared to Wire-EDM [85]. However, promising results were still unachievable. Song et al. [86] utilized a strip electrode for turning operation with EDM process which improved the MRR by significant amount as compared to Wire-EDM due to higher machining area. Additionally, the surface roughness was much lower compared to Wire-EDM; however, higher peak current induced significant surface roughness due to higher discharge energy.

The nontraditional techniques such as electro-chemical turning has provided well surface topography after machining. The surface roughness can be minimized in electro chemical turning by increasing the rotational speed of the workpiece and applied voltage [87]. However, decreasing the feed rate of the cathode (tool) has resulted in deterioration of the surface finish. Wire based electrochemical turning process was capable to produce micro products efficiently [88]. Meanwhile, increase in wire feed rate and rotational speed induced geometrical error of the turned products and higher surface roughness. In addition, clogging was a severe problem during micro-machining with electrochemical turning due to small nozzle diameter [89]. Electrochemical micro turning with flat jet technique was developed by Kunieda et al. [90]. This technique was capable to produce micro features over cylindrical jobs with high machining speed and good dimensional accuracy. The small jet thickness assisted in maintaining the dimensional accuracy without clogging effect. Tool wear was also minimized in this technique. Meanwhile, Kibria et al. [24] performed laser assisted micro turning as a non-contact type technique. However, it was very difficult to maintain constant depth of cut throughout the machining process. Additionally, this process induced substantial increase in surface roughness during the machining process. Das et al. [25] have gone for electrochemical micro turning on titanium alloy. However, the material removal rate was very low. In addition, maintaining the dimensional accuracy throughout the process was very difficult which in turn increased the surface roughness.

Application of micro textured tools

Recent trend is to generate micro textures over the turning inserts in order to reduce the contact length of chip and cutting tool. Subsequently, the frictional force and cutting force were minimized. Arulkirubakaran et al. [91] determined that tools having perpendicular textures with the principle cutting edge have shown better performance in terms of low frictional force, cutting force, cutting zone temperature as well as tool wear even at high cutting speed. Micro texturing over the flank face of turning insert assisted in reducing the tool flank wear and improved surface roughness [92]. The cutting temperature during machining with micro textured tools was much lesser as the micro grooves over flank surfaces acted as fins to take away the additional heat generated in machining process. Micro holes over rake and flank surface affirmed continuous penetration and retention of the lubricating fluid while application of MQL during machining of hard titanium alloys [93]. In this case, the micro holes accumulated some amount of lubricant due to capillary effect and performed as a reservoir during the machining operation. Consequently, the cutting vibration, tool wear, cutting zone temperature, cutting force have been reduced remarkably with improved surface quality. However, cutting temperature, tool wear have been increased significantly at higher cutting velocity. Alagan et al. [94] performed facing operation of

Alloy 718 with textured carbide inserts and achieved better superior resistance properties and tool life as compared to non-textured tool. However, the experiments were performed at moderate cutting speed (60 m/min) because the favorable effects of tool texturing were diminished at higher cutting speed due to enormous growth of tool wear. The micro textured cutting tool worked predominantly for micro turning as well to reduce the tool-chip contact length and store the lubricant during machining [95]. Therefore, a significant reduction in cutting forces, machining temperature, surface roughness, and tool wear was reported during micro turning with textured tool under MQL condition.

2.2 Diamond turning

2.2.1 Mechanism of surface generation in diamond turning

Ultraprecision diamond turning is a complex material removal process where the surface finish is considered as the principal output parameter. During machining, the cutting tool indents into the workpiece surface and moves along the feed direction. The feed motion of the cutting tool left some feed marks on the machined surface with certain frequency, resulting in surface waviness. In general, the cutting tool moves over the workpiece surface along the feed direction during turning operation leaving periodic feed marks over the surface. The feed marks are constant periodic fluctuations with larger wavelengths. Therefore, it has been considered as surface waviness. The frequency of the surface waviness decreased at higher feed rate. The successive movement of the tool profile on the machined surface periodically forms the surface roughness profile. The profile contains clear tool mark and periodic sharp peaks of the feed components [96]. High cutting speed resulted in removal of the tool marks and the peaks on the machined surface [96, 97]. Sometimes interference of the cutting tool occurred into the workpiece surface which indicate the indentation of the cutting tool into the uncut area of the workpiece in a single pass which is to be cut in the next pass. This phenomenon resulted in some irregular tool profile along the feed direction leading to irregular feed marks and sharp peak formation enhancing the surface roughness [96]. The uncut chip area is compressed and extruded by sharp cutting edge of diamond tool generating the machined surface. However, the elastic recovery of the work material due to plastic deformation and material flow prompted elevated peak height on the machined surface inducing additional surface roughness [96, 97]. Moreover, if any hard particle soluble or mixed in the material, it may be cut or pulled out from the material by the diamond tool during machining. During cut-through process, clean cutting of the particles has been taken place generating smoother surface. However, cracks or pits have been observed on the machined surface during pulling out process generating surface

roughness [97].

In ultraprecision micro/nano cutting, tool nose arc projects directly onto the machined surface along the tool path. Therefore, the arc geometry is extremely relevant to the machined surface topography [98]. This projection moves along the infeed direction following the tool path with each rotation and generates total machined surface. Besides, brittle fractures have been observed for brittle materials causing crack generation on the bulk material that led to curved fracture edges on the craters. This phenomenon was enhanced at higher depth of cut and induced some machined surface roughness [99]. Wang et al. [100] investigated that the surface generation was substantially influenced by the fracture mechanism of SiC particles appeared in Al matrix composite. The relative position of those hard particles with the cutting tool and its fracture behaviors such as top side fracture, residual fragmentation, complete debonding induced severe surface defects during micro cutting. For example, cavities were found due to the complete debonding of the particles. The fluctuation of thrust force during diamond turning induced some tool vibration. Subsequently, the distance between the tool and workpiece periodically fluctuated and the periodic profile has been projected on the machined surface producing micro-waved surface profile [101].

Diamond turning of bulk metallic glasses generated high cutting temperature for long duration. Resultantly, significant oxidation occurred on the machined surface. This phenomenon precipitated micro/nano structures on the outer circle region of the finished surface [102]. Additionally, some surface roughness was induced. In ideal case, the tool profile projected repeatedly with the interval of tool feeding along radial direction of diamond turned surface and generated the surface profile as shown in Fig. 2.5 (a). The simulated surface topography generated in ideal condition is depicted in Fig. 2.5 (b) [8]. Eventually, Huang and Yan [103] revealed two types of surface defects induced by diamond turning on ZnSe crystal. Firstly, micro fracture was observed along the cleavage planes perpendicular to the cutting direction caused by ploughing effect. Additionally, submicron pits were found on the grains whose cleavage plane was perpendicular to the cutting plane. This phenomenon was prompted by tearing action during elastic recovery of the work material. Both these fractured cleavage planes crossed each other producing step-like structure on the machined surface.

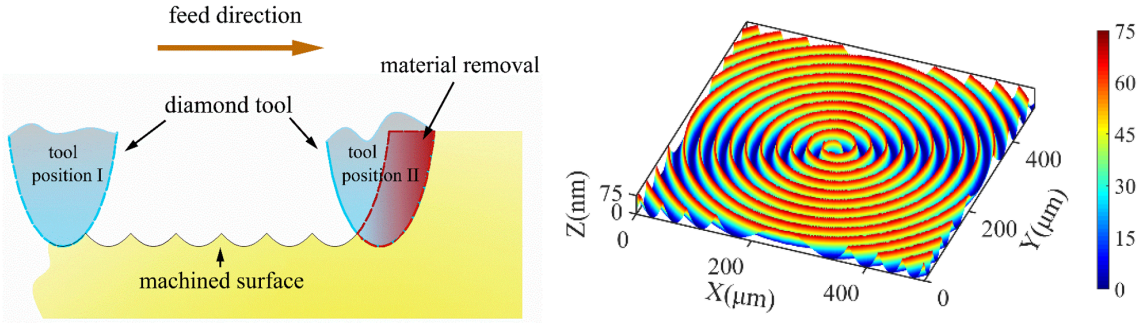

Figure 2.5: (a) Ideal cross-sectional profile generated in ultraprecision diamond turning; (b) Simulated 3D surface topography under ideal condition [8]

2.2.2 Machinability of different materials in diamond turning

Metals and alloys

Different non-ferrous materials such as aluminium, copper, electroless nickel and their alloys have shown favorable machinability in ultra-precision diamond turning. For example, To et al. [104] determined better machinability of single crystal aluminium in terms of chip formation, cutting force, and surface finish during amorphous nature of work material. Polycrystalline materials such as oxygen-free copper have shown deprived performance producing predominant burrs and surface integrity [105]. The variation in mechanical properties in multiple grains was accounted for this phenomenon. Similarly, presence of hard micro particles in polycrystalline Al 6061 T6 was responsible for crack generation and surface degradation during diamond turning [106]. Although this phenomenon could be prevented by introducing ultrasonic vibration-assisted machining. Diamond turned aluminium alloy RSA 905 having ultra-fine microstructure after rapid solidification was compatible for producing optical grade surfaces [107]. However, rapid tool wear and thermo-chemical erosion of the cutting edge were major issues at moderate to high feed rate.

Apart from crystal structure and grain size, surface roughness of these non-ferrous alloys also depends on various machining factors. Wang et al. [108] determined high-frequency tool-tip vibration as the most dominant parameter rather than crystal structure influencing surface generation. Meanwhile, tribological performance in terms of frictional properties of aluminium alloys were significantly dominated by tool geometry and wiper cutting edge have shown superior performance for this phenomenon [109]. Additionally, Guo et al. [110] determined a proportional relationship of cutting force with depth of cut and feed rate; while the surface roughness and form error were found to be lesser at higher depth of cut for V-groove cutting over RSA-905 aluminium alloy. A minimum surface roughness (R_a) of 15 nm was generated at a combination of 5 μm depth of cut, 100

mm/min feed rate, and 1000 rpm spindle rotational speed. The reflectance of machined surface is not always influenced by surface roughness. Although, both were found to be increased with reduction in feed rate [111]. Nevertheless, the reflectance was reduced at very low feed rate due to ploughing action causing unstable chip formation.

Nickel is not a diamond turnable material due to presence of two unpaired d electrons leading to acute tool wear; whereas electroless nickel deposition has shown good machinability in diamond turning producing less tool wear and surface roughness [112]. Although, dislocation of carbon atoms from the diamond tool causes rapid tool wear during diamond turning of electroless nickel. Addition of phosphorous was a solution to this problem [113]. Nickel silver is another diamond turnable material having huge applications in the optical industry. The hardness of these alloys played a major role in terms of reducing the plastic deformation and burr formation [114].

In contrary, ferrous materials, titanium and nickel-based alloys have shown poor machinability in diamond turning subjected to rapid tool wear and degradation of the surface finish. In general, ferrous materials have large chemical affinity towards the diamond tool. Diffusion of carbon atoms into the ferrous alloys and formation of carbide particles under high pressure and temperature have been observed during the machining process [115, 116]. Additionally, graphitization and oxidation intensified in the diamond tool wear at higher cutting temperatures. Rapid chemical tool wear occurs in the diamond tool deteriorating the surface finish. To restrict this phenomenon, the reduction of machining temperature has been focused by the researchers using cryogenic cooling [32]. Another tool wear minimization approach has been developed by restricting the tool-work contact. Ultra-intermittent diamond cutting was incorporated for this purpose [115]. Furthermore, minimum quantity lubrication (MQL) [117] and cryogenic assisted minimum quantity lubrication [11] have been utilized for ferrous alloys to improve the machinability by certain extent.

Low thermal conductivity of titanium alloy has made the material difficult-to-machine due to rapid heat accumulation at the cutting zone resulting in intense tool wear. Further low elastic modulus of these alloys led to rapid elastic recovery during machining inducing surface roughness. The machinability of Ti6Al4V in diamond turning was improved by microstructure alteration [118]. Further, advanced cooling method like CMQL [119] and heat dissipation technique like thermoelectric cooler [120] were utilized for titanium alloy to improve the machining performance. However, limited numbers of researches have been reported on diamond turning of these alloys.

Brittle materials

Ultraprecision diamond turning is widely used to machine brittle materials. Silicon is one of them having superior optical applications. However, silicon has been subjected to rapid brittle fracture during machining degrading the surface quality and machinability. Therefore, researchers have focused on ductile regime diamond turning of silicon [121]. In this case, the material removal was governed by the plastic flow rather than brittle fracture. The ductile mode machining was largely dependent on the uncut chip thickness that to be below the critical value. Machining parameters, tool geometry, and material crystallography were prominent for this phenomenon [122]. In general, low feed rate and low depth of cut with larger negative rake angle promoted the plastic flow of the machined surface and improved the surface finish of silicon during ductile mode diamond turning. Besides, monocrystalline silicon was subjected to phase transformation to amorphous during diamond turning and lost the bond strength. Therefore, the silicon atoms were removed from the bulk material and distinguished as hard particles in the chip formation zone [123]. These 'dynamic hard particles' were dispersed at the lower segment of chip formation zone and resulted in groove like flank wear due to abrasion. Diamond tool was subjected to SiC formation and sp3-sp2 hybridization resulting in severe chemical tool wear during machining of silicon [124]. Additionally, the temperature gradient across rake and flank face governed severe flank wear which can be moderately reduced by suitable coating [125]. High cutting speed and feed rate with larger negative rake angle consumed high specific cutting energy resulting in high cutting temperature promoting intense tool wear due to oxidation and graphitization [126]. Previous research suggested surface defect machining method (SDM) for silicon machining to reduce the diamond tool wear as this method leads to favorable chip segmentation and reduction in shear angle and specific cutting energy [126].

The surface roughness of KDP crystal has been increased monotonically with increase in feed rate [127]. In addition, 2 nm surface roughness (R_a) was achieved at a combination of 1 $\mu m/rev$ feed rate, 1200 rpm spindle speed, 3 μm depth of cut, and 15^o tool inclination angle. Silicon carbide (SiC) is one of the most frequently used ceramic materials in optical and mold making industries. Nano finishing was achieved on SiC by diamond turning in ductile mode. As the depth of cut reduced at low cutting speed during nanomachining of monocrystalline SiC in SPDT, the machining mode converts from brittle to ductile which reduced the cutting force [128]. However, larger negative rake angle caused unfavorable shearing on SiC surface and increased the cutting force by marginal amount. Reaction bonded silicon carbide was a specially fabricated hard ceramic material required very hard cutting tool for machining. Although nano finishing (R_a = 23 nm) was achieved on this material during diamond turning with large negative rake angle (-40^o) and large feed rate

(72 $\mu m/rev$) [129]. However, tool wear was a serious problem while diamond turning of these hard ceramic materials. Similarly, high cutting speed induced significant brittle fracture on the surface of tungsten carbide and developed rapid tool wear [130].

Zong et al. [131] proposed an oblique diamond turning model of ZnS crystal to predict the critical uncut chip thickness for brittle to ductile transition which considerably reduce the shear stress distribution in the cutting zone. Subsequently, the surface defect formation due to brittle fracture was restrained improving quality of the machined surface. Additionally, sharp edges of diamond tool substantially reduced the surface roughness of MgAl2O4 spinel ceramic by enabling the effect of ductile regime machining [132]. Significant surface roughness was observed on Fluorophlogopite ceramic in diamond turning which further increased at higher feed rate and depth of cut due to predominant brittle fracture [133]. Brittle to ductile transition is a prevailing phenomenon during diamond turning of brittle materials which significantly enhance the surface quality. However, diminishing diamond tool wear is still a challenging issue.

Polymeric materials

Very few researches have been focused on diamond turning of polymeric materials. In general, the polymeric materials have viscous property. Consequently, the shear stress increased at high strain rate, while reduced at higher temperature. For significant viscous deformation, tearing occurred on the machined surface [134]. Meanwhile, submicron surface roughness (R_a) was achieved on thermoplastic polymers which was even below 100 nm in some cases. As compared to thermosetting polymers (LCLE, HCLE), thermoplastic polymers (LDPE, HDPE) acquired smoother surface due to higher glass transition temperature and better molecular mobility which further improved at higher cutting speed during diamond cutting [134]. However, significant friction induced some electric charge on the machined surface during diamond turning which in turn causes electrical discharge in between tool and workpiece [135]. Therefore, severe tool wear was developed even at low cutting speed. Specially selected monocrystalline diamond for cutting tool and their crystal orientation improved the mechanical stability and reduced tool wear [136]. Meanwhile, strong electrostatic field in the machining zone enhanced chip adhestion to the diamond tool and raised the surface integrity of optical polymer [137].

The surface roughness of optical polymer was increased at higher cutting speed and feed rate. An average surface roughness (R_a) of 11 nm was generated on PMMA polymer at lower tool overhang and higher tool nose radius with moderate spindle speed (1000 rpm), moderate feed rate (5 $\mu m/min$), and higher depth of cut (15 μm) [138]. In addition, Liman et al. [139] generated 1.7 nm surface roughness (R_a) on the same material at higher spindle speed (4000 rpm), higher feed rate (12 mm/min), and moderate depth of cut (25 μm).

Spindle speed was the most prominent process parameter affecting surface roughness. Soft polymeric materials such as hydrophilic acrylic were easily machinable in diamond turning to achieve mirror surface finish. However, hydrophobic polymers were poorly machinable at room temperature considering its flexibility and smearing phenomenon on the machined surface [140].

Composite materials

Limited numbers of researches have been reported on diamond turning of composite materials. SiC reinforced Al metal matrix composite was the most common composite material machined by diamond turning. The relative position of the SiC particles with the cutting tool during machining governed the variation of stress pattern and magnitudes resulting in variation of cutting force [141]. Although the cutting force was varied from 0.1 to 0.8 N. It was possible to generate 30 nm surface roughness by diamond turning on SiC particle reinforced Al matrix composite at a spindle speed of 7500 rpm, feed rate of 26 mm/min, and depth of cut of 1.9 μm [142]. The surface roughness was increased at higher feed rate and depth of cut, especially at lower spindle speed. Additionally, ultrasonic vibration-assisted diamond turning has been applied to improve the surface finish on the composite [143]. Moreover, Combination of low cutting speed and low depth of cut improved the surface quality of metal matrix composites (MMC). High localized cutting temperature induced tool wear in single crystal diamond (SCD) insert which was governed by chipping and cleavage fracture at the cutting edge [12]. Whereas built-up-edge was found in polycrystalline diamond tool (PCD). Both these tools were susceptible to significant tool wear during machining of MMCs; although slightly higher tool wear was reported in PCD tools. Meanwhile, both the tools were able to generate surfaces having R_a of less than 50 nm. Higher feed rate and depth of cut induced predominant cutting force during diamond turning of polytetrafluoroethylene (PTFE) composite with PCD tool [144]. Besides, low feed rate and higher nose radius precipitated better surface finish. Nevertheless, the surface generated was quite rough (R_a = 2 to 6 μm) which indicated poor machinability of PTFE composite. To avoid the brittle fracture on work surface, Wang et al. [145] applied ductile regime machining on SiC/Al composite in diamond turning. It was possible to generate 50 nm surface roughness (R_a) on the material which increased at lower cutting speed and higher feed rate. However, defects like holes, pits, tearing, grooves, voids have been found on diamond turned surface irrespective of ductile mode machining.

2.2.3 Effect of different parameters on surface topography in diamond turning of ductile metals and alloys

The features of diamond turned components are superior dimensional accuracy with nanometric surface finish and submicron form accuracy. However, the surface generation is dependent on several variables and minor variation can affect the surface finish significantly depending on the scaling issue. Therefore, a lot of researches have been reported to determine the optimum values of those influencing variables. These factors are summarized as machine tool dynamics, spindle dynamics, process parameters, tool geometry, machining environment, materials swelling. The influencing factors and their major components are depicted in Fig. 2.6.

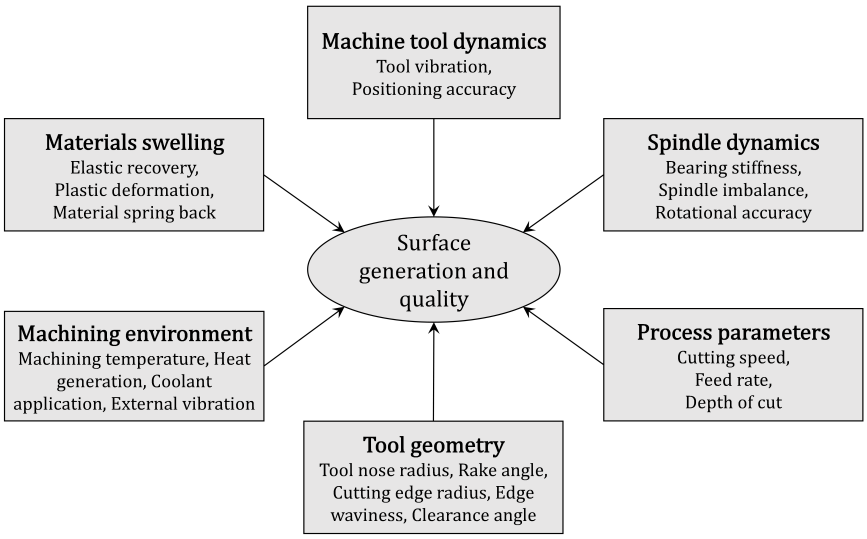

Figure 2.6: Major factors and their components influencing surface roughness in ultraprecision diamond turning

Machine tool dynamics

The performance of the machine tool in terms of stiffness and thermal stability of the machine structure, spindle accuracy, drive stiffness has remarkable impact on the form accuracy and roughness of the machined surface in UPDT. The determine the performance of the machine tool. Restraining thermal deformation, vibration isolation, restricting the heat transfer and thermal radiation, controlling the atmospheric temperature were main focus to improve the machining accuracy in diamond turning. Therefore, compact capsule type structure was developed with lightweight and rigid machine bed in early 90s [146]. Further, Shriyotha et al. [147] preferred aerostatic guideways for its frictionless performance with linear motor drive for its enhanced positional control. In addition, rigid thermally

stable ceramic structure was preferred for the machined tool which was capable to machine free-form surfaces with 1 nm motion accuracy. Ulmer Jr. et al. [148] emphasized on vibration isolation to improve the overall performance of ultraprecision machine tool and applied vibration absorbing coupler and spindle balancing for this purpose. Yao et al. [149] developed an alignment method focusing on compensating the angular errors, parallelism, and linearity to eliminate the positioning error and improve form accuracy of a swing arm UPDT machine.

Some researches have been focused on positioning error monitoring technology. For example, Zou et al. [150] established a variance-based sensitivity analysis method for error source analysis considering multi-body system theory. This method was capable to identify geometrical errors and 50% improvement in form accuracy of the machined surface was possible after required modification in design and processing. Dahabi et al. [151] developed a mathematical model to predict cylindrical part profiling error which was prompted from the variation in machine tool rigidity. The geometrical errors in machine tool affected the performance of the optical aspheric components mainly due to displacement error along Z direction resulted in Z coordinate distortion of the cutting tool [152]. Buhmann et al. [153] presented a novel positioning method using an optical probe with two horizontal and one rotational axis integrated in a diamond turning machine. The offset between the probe and the spindle axis was determined to minimize the measurement deviation and confirm the straightness of the axis.

Undesirable dynamic performance of machine tool develops tool vibration which is a predominant mean to affect the surface topography in UPDT. Steady and simple harmonic tool-work vibration along infeed direction caused phase shifts which further generated wavy surface profile over machined surface in single point diamond turning [154]. In diamond turning marginal amount of tool-work vibration deteriorated the optical surface quality in terms of microscopic variation in height of the spiral groove generated by tool feed along the tool path [155]. Apart from these, some studies focused on the relative vibration along cutting direction. Wang et al. [156] established a novel surface roughness model for SPDT based on high-frequency tool tip vibration along the cutting direction where impact of the cutting tool with chips and workpiece was considered as the major source of tool-tip vibration. Elastic recovery of work material underneath the flank face of cutting tool; and consequently, process damping and non-harmonic periodic excitation of the tool tip were responsible of surface roughness as well. High-frequency tool tip vibration augmented the strain rate in tool vibration which further responsible for adiabatic shear bands formation in UPDT [157]. This shear band formation has contributed to instability of cutting forces, cutting heat; and therefore, deteriorated the surface finish. Spiral marks over the machined surface have been observed due to high frequency tool tip vi-

bration generated along the cutting force direction [108]. Zhang and To [35] considered the variation of stiffness and damping capacity of the diamond tip, tool tip and tool shank for the multimode tool vibration which caused non-uniform zebra striped pattern over the diamond turned surface. The typical distance between the striped patterns varied from 30 to 50 μm which could be reduced by enhancing the tool stiffness. Additionally, chatter was developed when the resonance occurred between the machining frequency and natural frequency of the machine tool; and consequently, surface finish has been deteriorated [158]. Meanwhile, Yip et al. [159] introduced an eddy current damping effect that significantly reduced the tool-tip vibration in UPDT. However, the application of eddy current damping effect was limited to the electrically conductive materials. Based on the prior researches, some challenges have been arisen such as, difficulties in monitoring of relative displace between tool and workpiece due to tool vibration; difficulties in controlling and minimization of the tool-tip vibration.

Spindle dynamics

Spindle dynamics played a significant role in surface generation. In general, high precision air bearing spindle is used in diamond turning operation. Nevertheless, spindle imbalance was a common phenomenon in air bearing spindle which caused drift motion of the spindle axis. Overhung masses in the spindle resulted in gyroscopic motion and axial and conical movement of the spindle [160]. Huang et al. [161] investigated that fluctuation in depth of cut was developed due to eccentric mass induced spindle unbalancing and drift of the axis. This phenomenon further increased with cutting speed. The measurement of the spindle drift exhibited a complex process. The fluctuation of the depth of cut formed a star like feature at the center of the machined surface which was called "Lobes-star" error [9]. This was responsible for straight concentric spokes over the free form surface irrespective of tool geometry and work material. Additionally, the spindle imbalance induced drift motion resulted in taper groove formation at the center of the workpiece due to conical whirl of the spindle axis. Fig. 2.7 (a) shows the "Lobes-star" error and center groove formed due to spindle unbalance. Dynamic balancing of the spindle system was a solution to minimize those error from the machined surface as shown in Fig. 2.7 (b). However, complete elimination of those error was not possible.

Undesirable dynamic performance of air bearing spindle caused spindle vibration which significantly deteriorated the surface profile in UPDT [162, 35]. Axial vibration was prominent for surface roughness of the free form surface at the center, whereas twin tilted vibration has shown its dominance outside the center. Both these vibrations resulted in generation of concave, periodic concentric, spiral, radial and two-fold patterns over the free form machined surface. Furthermore, imbalance in air bearing spindle induced force vibration

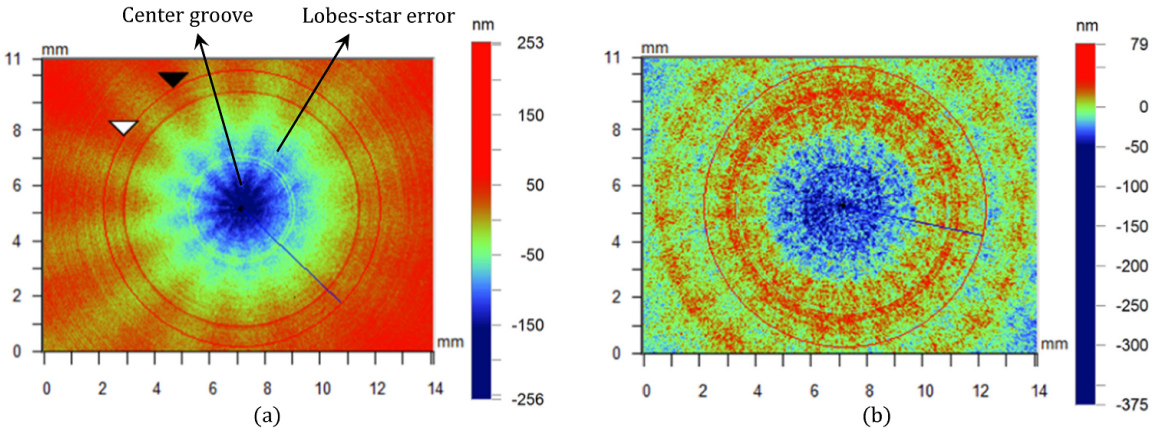

Figure 2.7: Machined surface generated by (a) unbalanced, and (b) balanced air bearing spindle [9]

resulted in straight radial pattern or quasi-elliptical (due to spindle whirling under forced vibration) convex or concave shape at the machined surface and deteriorated surface finish [163, 164]. He and Zong [165] stated the center of workpiece surface as the most affected zone due to multi-frequency vibration which further jeopardized specular reflectivity in that zone. However, spindle balancing and optimization of process parameters might be an effective solution to that problem.

The spindle vibration in an ultraprecision machine tool can be reduced by utilizing higher bearing stiffness and low overhanging [34]. In general, higher compressibility of air led to low stiffness and damping performance of the air bearing causing significant difficulties in dynamic balancing [34]. Considering this problem, Fedorynenko et al. [166] utilized hydrostatic bearing spindle for ultra-precision machining which exhibited higher stiffness as compared to aerostatic bearing spindle. Moreover, hydrostatic bearing spindle exhibited higher dynamic stiffness and damping capability which significantly improved the dynamic characteristic as compared to aerostatic spindle [34]. In summary, spindle vibration can be minimized upto certain extent by reducing overhung unbalanced masses, reducing natural frequency, providing extra damping material or providing balancing masses. However, investigating the sources of spindle vibration and its isolation are still a challenging issue which in turn deteriorates the surface quality in ultraprecision diamond turning.

Process parameters

Process parameters i.e. cutting velocity, feed rate and depth of cut are the most crucial factors influencing surface roughness in UPDT. In general, high spindle rotational velocity in combination with low feed rate has been appropriated for reduced surface roughness in UPDT. Some research revealed feed rate as the most dominant process parameter in-

fluencing machined surface roughness in UPDT [154]; besides, some research remarked depth of cut as insignificant for surface roughness [167]. Hocheng and Hsieh [168] investigated that surface roughness of Phosphor bronze lens mold was reduced at low feed rate and high cutting speed. The depth of cut was not significant in that case. However, feed rate was the only key machining parameter according to Tauhiduzzaman and Veldhuis [169] for SPDT of strain hardened aluminium where the best quality surface (0.02 nm) has been achieved at lowest feed rate (0.2 $\mu m/rev$). Similar tendency has been observed for pure copper where average surface roughness of 2.53 nm achieved at 0.5 $\mu m/rev$ feed rate [170]. Additionally, Li et al. [111] determined an optimum range of feed rate from 3 mm/min to 7 mm/min for reducing the surface roughness with improved stabilized reflectance of Al6061 mirrors. Besides, lower feed rate precipitates lower surface roughness as determined by Yu et al. [171]. Although, the material removal rate was very low at low feed rate. A combination of low feed rate and high cutting speed reduced the surface roughness on aluminium alloy RSA 905 as it facilitated better chip fragmentation which in turn prevented the obstruction in lubricant flow at the chip-tool interface [30]. Opposite trend has been observed for Copper based alloy with cutting speed and feed rate in UPDT as high cutting speed and low feed rate resulted in concentrated tool trajectories on the machined surface prompting excess material removal [8]. Therefore, the surface roughness and form accuracy was degraded. In some cases, a strain gradient in the work material ahead of the cutting tool caused strengthening and rapid plastic side flow especially at low feed rate [170]. This phenomenon induced higher surface roughness at low feed rate. Fig. 2.8 shows the reduction of surface roughness at lower feed rate and depth of cut as lower heat generation and plastic deformation on the machined surface [10]. While feed rate was more dominant for surface generation rather than depth of cut.

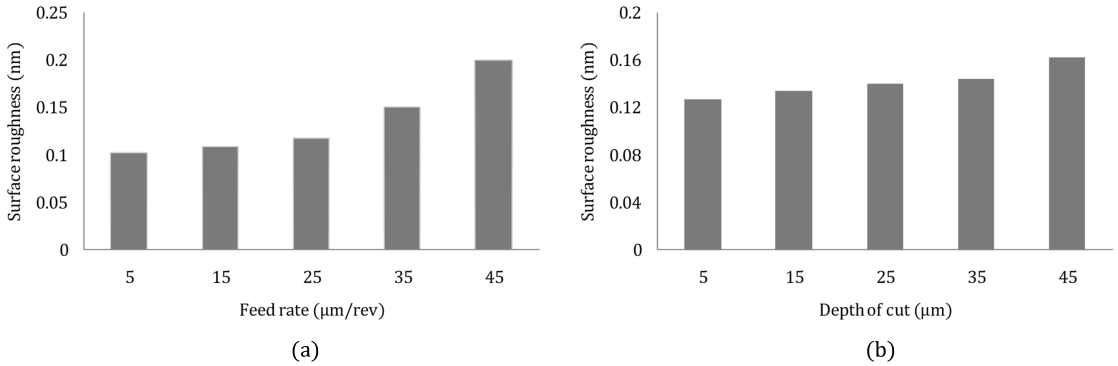

Figure 2.8: Surface roughness variation on Al6061 in diamond turning at different (a) feed rate, and (b) depth of cut [10]

Additionally, increasing cutting speed induced higher surface roughness on titanium alloy (Ti6Al4V) in ultraprecision diamond turning where a minimum of 76.71 nm surface

roughness has been achieved in low-speed cryogenic MQL condition [119]. At high cutting speed, the uncut chip thickness was significantly low which facilitated rapid ploughing and plastic side flow of work material. Although several researches was performed in this area, the effect of high-speed machining was still unexplored. In addition, very few researches have been focused on process parameter optimization for surface generation on ferrous materials and hard superalloys in UPDT.

Tool geometry

In machining process, the machined surface roughness depends on sharpness of the machined tool to a great extent. The typical shapes of single point diamond tools are triangular and diamond. The geometrical parameters of the diamond cutting tool include cutting edge, nose radius, cutting arc, rake angle, offset angle, cylindrical edge, cutting height, diamond depth, and nose waviness. Single point diamond tools are characterized by nanometric cutting edge radius (less than 50 nm), high reliability, and superior stiffness with wear resistance. These all comprehensively induced ultraprecision micro cutting with superior cutting accuracy. The most fundamental geometrical parameter affecting the surface roughness is tool nose radius and the theoretical surface roughness is inversely proportional to it. Most of the researches have presented the decreasing trend of surface roughness with rising nose radius [10, 8]. However, dissimilar trend was explained by Yu et al. [171] that very big nose radius was unable to access the micro structured surface.

Tool rake angle is a dominant geometrical factor surface formation on brittle materials. However, no significant influence of tool rake angle was reported on surface generation for ductile materials. Although larger negative rake angle produced irregular and coarse shear bands as a consequence of larger frictional force [172]. This phenomenon might increase the surface roughness in diamond turning. Therefore, 0^o rake angle was mostly preferred.

The tool edge radius defines the sharpness of the single point diamond tool. Sharper tools led to reduction in the minimum uncut chip thickness and improved the surface finish in UPDT [158]. Tool cutting edge radius was considered as a predominant factor in the surface roughness prediction model established by Zong et al. [170] accounting the size effect. Minimum surface roughness was found when the maximum uncut chip thickness was equal to the cutting edge radius. To achieve better surface roughness, a combination of lower cutting edge radius, low feed rate and higher cutting speed was preferable. The fluctuation of surface height as well as the surface step height in grain boundary decreased with reducing the cutting edge radius [173]. This was attributed to significant ploughing of the cutting tool over the work surface when the cutting edge radius became higher. He et al. [174] proposed the tool edge waviness was directly replicated on the machining surface resulting in surface roughness. Moreover, small clearance angle led to higher proximity

area between the workpiece and tool flank face, resulting in higher friction and chemical tool wear. The tool work interference subsequently increased with the reduction of the tool clearance angle enhancing the normal cutting force [175]. The overall effects of diamond tool geometry on machined surface roughness are summarized in Fig. 2.9.

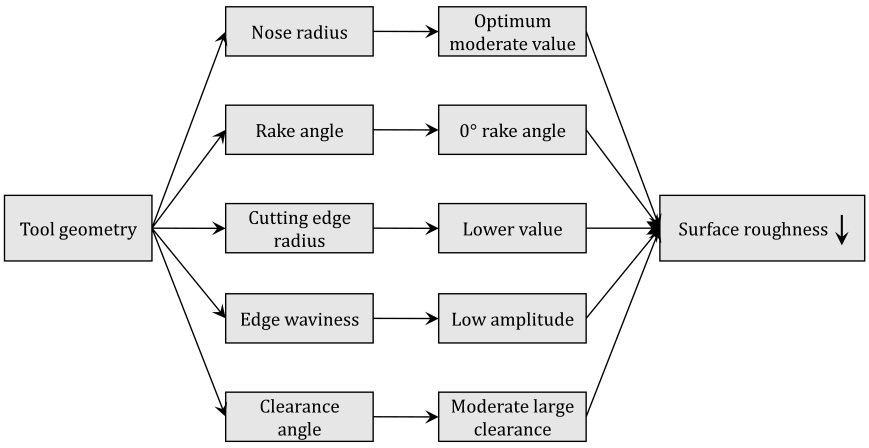

Figure 2.9: Different tool geometrical parameters with their optimum conditions to improve the surface roughness in diamond turning

Machining environments

The environmental conditions during machining such as machining temperature, coolant supply, heat generation, environmental noise and vibration directly influence the machining operation in ultraprecision diamond turning. Variation in those parameters deteriorates the surface generation of the finished components. Heat generated during machining resulted in thermal deformation of the cutting tool and workpiece; subsequently, rapid machining error has been observed. The rotation of the spindle caused temperature difference from ambient and induced thermal deformation of the spindle causing machining error, especially at higher rotational speed [176]. The thermal expansion generated in machining caused material swelling which induced surface roughness on the machined surface [177].

Superalloys such as Ti6Al4V possess low thermal conductivity, accumulating high cutting heat at the chip-tool interface which deteriorates the surface quality in ultraprecision machining. To compensate this drawback in diamond turning, Yip and To [120] developed a heat dissipation technique applying a fixture containing thermoelectric cooler which minimized the cutting force and surface roughness on titanium alloy and generated 16 nm surface roughness (R_a). Similarly, Huang et al. [119] applied cryogenic minimum quantity lubrication (CMQL) for diamond turning of Ti6Al4V and achieved a minimum surface roughness (R_a) of 76.71 nm. In this phenomenon, cryogenic was able to reduce the cutting temperature; while MQL reduced the chip-tool friction, plastic deformation of the ma-

chined surface, and adherence of work material to the diamond tool, and BUE formation. Therefore, these two combinedly provided a favorable cooling and lubricating action in machining. Similar observations have been found by Zou et al. [11] for steel alloy as compared to flood cooling, cryogenic gas cooling, and minimum quantity lubrication. Fig. 2.10 shows the reduction in surface roughness and tool wear using CMQL technology for diamond turning of steel alloy. Moreover, superimposing magnetic field in SPDT reduced the grain size and the grain pile up over the machined surface [178]. This technique enhanced the micro-hardness and ductility of titanium alloy as well. Surface treatment such as nitridation and plasma-assisted machining were able to generate better finishing on ferrous alloy due to lesser diamond tool wear [179]. Furthermore, ultrasonic vibration diamond turning produced better surface finish on Ti6Al4V and improved its machinability [180]. Similar trend was followed by carbon steel S235, where specific cutting energy decreased at higher vibration frequency [181].

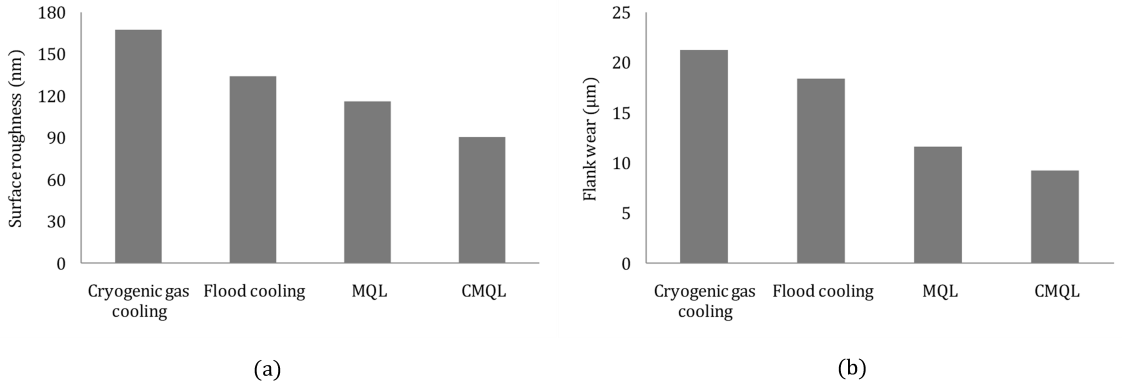

Figure 2.10: Variation of (a) surface roughness, and (b) tool wear in UPDT of 3Cr2NiMo steel under different cooling conditions [11]

Materials swelling

Materials swelling directly influence the machined surface roughness in UPDT which is a common phenomenon for ductile materials. Material swelling even caused tool tip vibration and uneven machined surface [159]. The amount of materials swelling is governed by the plastic deformation and elastic recovery of the work material after the interaction of the cutting tool. Previous researches revealed that distortion of the tool profiles has been taken place by materials swelling and influenced the surface roughness profile [182]. The amount of plastic deformation induced different surface roughness profiles on the single crystal material under same cutting conditions. However, the prediction of the plastic deformation in diamond turning was not a common practice at this time. The effect of materials swelling and elastic recovery has been overcome by incorporating low depth of

cut and front clearance for ductile materials [183]. From a recent study, it was investigated that the material swelling and spring back varied significantly with different microstructures for a variation of strength and ductility. Consequently, different surface profiles were generated on the machined surface [118]. Therefore, the alloys with coarse grain structure was subjected to higher surface roughness; while smoother surface profile was obtained on alloys with lamellar martensitic structure.

The swelling was strongly dependent on hardness and elastic modulus of work material, tool geometry and heat generation [184]. Diamond turning with sharper tool and small depth of cut involved small cutting area which increased the specific cutting energy and enhanced the materials swelling. Additionally, increasing workpiece temperature reduced the spring back, elastic recovery, and material swelling. Meanwhile, reducing feed rate enhanced the stress concentration at the frontward of cutting edge leading to increase in material swelling [170]. For polycrystalline materials, variation in elastic and plastic properties in individual grains caused difference in elastic recovery and variation in surface profile across the grains [31]. For titanium alloys, low thermal conductivity and low elastic modulus caused less heat dissipation and high elastic recovery respectively. Both these phenomenon led to intense material swelling resulting in dimensional inaccuracy of the machined components [185]. Intermittent diamond cutting reduced this tendency to a great extent.

2.2.4 Tool wear in diamond turning of ductile metals and alloys

Tool wear defines the extent of tool sharpness. The presiding tool wear mechanisms were micro-chipping of the cutting edge and built-up edge formation during diamond turning of aluminium [186]. Steel has shown low machinability with single crystal diamond tool for high cutting temperature attributed to chemical tool wear in terms of oxidation, graphitization, and diffusion of tool material into steel. Therefore, reduction in contact time between diamond tool and steel workpiece accomplished low tool wear [115]. Yingfei et al. [12] investigated that microchipping, cleavage fracture, and abrasive wear were predominant for SCD tool. Higher cutting force for diamond cutting of steel 1215 attributed to significant enhancement in cutting edge radius followed by severe tool wear compared to Al6061 [187]. Wu et al. [188] identified diamond tool wear by micro breakage of cutting edge (upto 24 km machining length) which further converted into cleavage fracture and uniform mechanical wear after long distance machining in UPDT of copper. Consequently, notable periodic surface micro-topography and elevated material pile up were developed deteriorating the optical performance of the copper components. Sharma et al. [189] investigated that diamond tool was more susceptible to tool wear during interaction of hard particles appeared in the surface of copper beryllium (CuBe) alloy. Diffusion of carbon atom and its

amorphization resulted in formation of blunt cutting edge in diamond tool.

Although favorable hardness, toughness, thermal conductivity, wear resistance have promoted diamond tool for ultraprecision machining, tool wear was an inevitable phenomenon which further influenced by several machining parameters. Wang et al. [190] proposed that high negative rake angle increased the gap between tool flank surface and finished surface reducing machining temperature, and diamond tool wear. Furthermore, plasma nitriding treatment of steel alloy (die steel) reduced the availability of unpaired d-electron in the steel alloy by combining with nitrogen and restrained the chemical affinity towards diamond tool [191]. Thus, the catastrophic failure of diamond tool was restricted by some extent, although it improved microchipping of the cutting edge. The predominant mechanisms of flank wear in diamond tool are shown in Fig. 2.11 (a). Meanwhile, diamond tool wear increases radius of cutting edge resulting in enhancement of cutting force and cutting vibration. Consequently, chip formation and surface generation were jeopardized as shown in Fig. 2.11 (b) [13]. In order to control the tool wear, some preventive methodologies such as proper lubrication, optimization of process parameters, hybridization process are required.

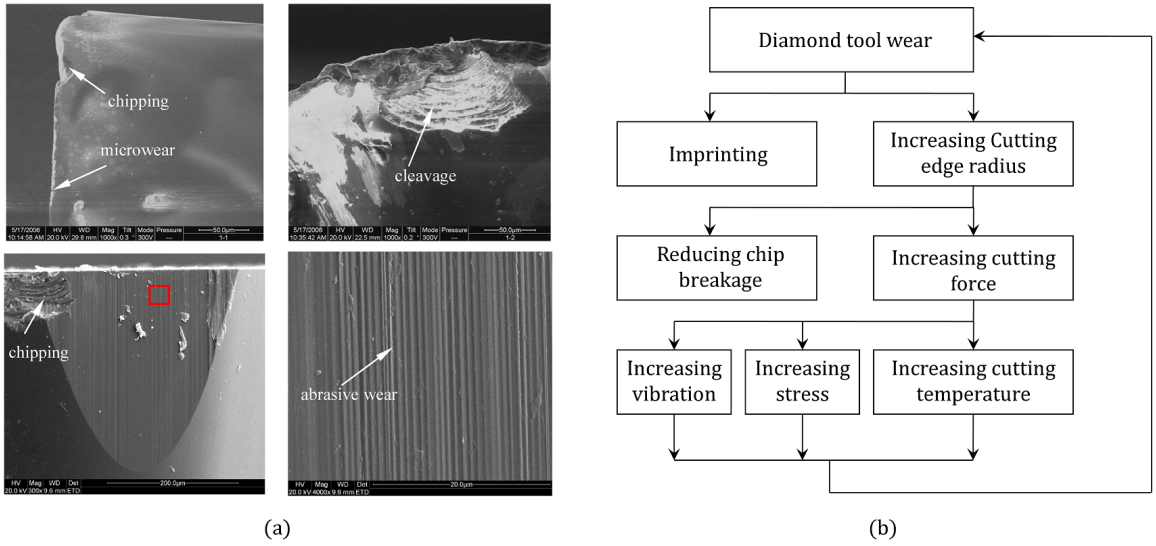

Figure 2.11: (a) General mechanisms of flank wear in diamond tool [12]; (b) A schematic framework presenting the effect of tool wear in diamond turning [13]

2.2.5 Chip formation in diamond turning of ductile metals and alloys

Chip formation morphology are the key physical parameters that define the material removal mechanism and the machinability of the work material. The microstructure of the polycrystalline alloys contains coarse or fine lamellar structure. Due to smaller depth of cut in ultraprecision machining, the lamellar structure became aligned with the cutting track

and broken into small particles. These particles scattered over the machined surface and induced some external stress [192]. Additionally, this phenomenon changed the crystal orientation. The chip formation was largely influenced by the crystallographic orientation and factors. The crystallographic orientation in an anisotropic material influenced the shear angle and resultantly the shear deformation during machining was dominated by this phenomenon which prompted the chip formation [193]. Higher depth of cut and tool-work friction resulted in elevated lamellar thickness of the chips formed indicating inhomogeneous and non-uniform strain distribution in diamond turning of brass alloy [194].

In ductile mode machining, ploughing was dominant due to elastic recovery on flank face consuming high specific cutting energy. Subsequently, a nonlinear variation in uncut chip thickness was observed [195]. The Merchant's model was failed to explain the behavior of chip formation in the presence of fine or coarse shear bands especially with negative rake angle cutting tool, due to involvement of larger volume in elastic deformation [172]. Meanwhile, serrated chip formation with regularly spaced shear bands was observed during micro-cutting of brass alloys by diamond tools having 0^o rake angle. In general, high yield strength materials are prone to regular space shear band formation, while larger cutting temperature reduced the yield strength of brass alloy and exhibited serrated chips with narrow shear bands in diamond turning [172]. Moreover, high frequency tool tip vibration was prominent for cyclic tool-work displacement with rapid stress field variation and strain rate in the primary shear zone. This phenomenon accelerated the formation of adiabatic shear bands resulting in serrated chips [157]. A cyclic transient shear angle variation was observed for ductile materials due to material anisotropy which caused cyclic cutting force variation and lamellar chip formation [196]. Ti6Al4V exhibited lamellar martensitic microstructure that possessed inferior ductility and lesser plastic side flow. This phenomenon resulted in large shear angle in diamond turning facilitating lamellar chip formation with smaller thickness [118].

2.3 Research gaps

From the detailed literature survey, following research gaps have been determined:

1. The material removal rate of micro turning need to be improved by combining high speed machining with micro turning technology.

2. Vibration is a common issue generated in high speed mechanical micromachining where high speed spindle is the major source of vibration. This phenomenon directly influences the dimensional accuracy and surface finish during machining. Therefore, development of a vibration free dynamically stable high speed micro machining

setup is a challenging aspect.

3. Rapid heat generation during high speed micro turning technology need to be minimized by incorporating proper cooling and lubricating technique. The penetration of coolant or lubricant at the chip-tool interface need to be improved during high speed micro turning.

4. The machining performance in high speed micro turning in terms of machined surface quality, tool wear behavior, and chip breaking performance are required to be enhanced. Especially for highly ductile materials, the plastic deformation of the machined surface is very difficult to restrain in high speed micromachining.

5. It is very difficult to develop a dynamically stable ultraprecision diamond turning machine tool in an economical way as all the ultraprecision drive systems and spindle involved high development cost.

6. The air bearing spindle possessed lower dynamic stiffness; and hence, it is a challenging issue to control the drift motion of spindle axis and its effect on machined surface. The stiffness used for diamond turning is required to be improved.

7. Controlling the diamond tool wear is a challenging issue especially during machining of ferrous alloy and hard superalloys. More researches need to explored on diamond turning of these materials.

2.4 Scope of work and problem definition

In recent years, the demand of miniaturized cylindrical components with smooth surfaces have been enhanced enormously. However, low productivity has limited the application of micro turning to machine miniaturized cylindrical components. Additionally, the machining performance has been degraded rapidly during micro turning of miniaturized components. Therefore, surface generation, tool wear behavior, and chip breakability are need to be improved during micro turning process. High speed micromachining can be adopted to enhance the productivity; however, machine tool vibration affected the accuracy and surface quality of those products. Therefore, the dynamic stability needs to be improved for high speed micromachine tool to restrict the machine tool vibration. Additionally, it may help to maintain the dimensional accuracy of the machined components as well as machining performances. Similar characteristic is required for an ultra-precision machine tool as well which involved exorbitant cost to develop a dynamically stable diamond turning machine tool. This is responsible for the elevated price of the miniaturized optical

components. Additionally, the error developed on the machined surfaces due to spindle imbalance is required to be minimized. Using spindle of high dynamic stiffness could be a comprehensive means of that problem. Therefore, there is a scope of improvement in the process dynamics related to micro and diamond turning to enhance the machining performance which has remarkable importance for industrial and research purposes. The primary focus of the research work should be the development of a dynamically stable high speed micromachining center to perform micro turning and diamond turning operations.

The chip breakability is a significant parameter influencing the machining performance especially for ductile materials. For a highly ductile material, shear strength is very high causing unfavorable and long chip formation [197]. The long chips accumulate at the tool tip and cause enhanced friction at the tool-work interface. Consequently, rapid tool wear and surface degradation are observed. In addition, rapid plastic deformation of the machined surface of ductile materials developed significant surface roughness [198]. However, due to scaling issues, small amount of surface degradation substantially deteriorated the dimensional accuracy and quality of the miniaturized product. Moreover, micro cutting tools have sharp cutting edge with lower strength [199]. Therefore, the failure of the cutting edge is quite rapid in micro cutting. Hence, tribological improvement is immensely necessary during micro cutting operation of miniaturized components.

The machining performance in macro scale has been improved upto certain extent utilizing high speed machining in terms of cutting force and surface finish [64]. However, rapid heat generation during high speed cutting significantly influenced the tool wear behavior [200]. Therefore, proper cooling technology can be incorporated for better tribological performance during utilization of high speed machining in micro scale. Minimum quantity lubrication could be a comprehensive means which is environmentally sustainable as well reducing consumption of hazardous coolant [201]. In addition, cryogenic cooling has been utilized as an effective cooling strategy. This reduced the ductility of workpiece material resulting in better chip breakability as well. Figure 2.12 depicts the identified problems in the research field and their probable solutions.

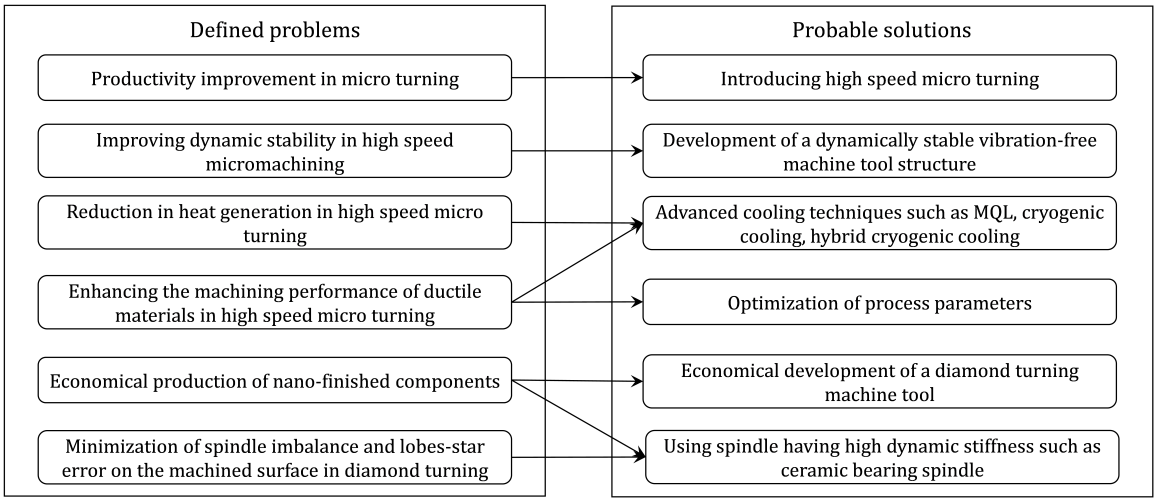

Figure 2.12: Problem definition with the probable solutions

2.5 Aim and objective of the research

Based on the defined problem, the aim of the present work is to **"develop a high-speed micromachining center and its performance evaluation in micro and diamond turning".** The performance in micromachining is focused on surface generation, tool wear behavior, chip breaking performance especially for ductile materials. The objectives of the research are follows:

1. Introducing high speed micro turning to improve the material removal rate of miniaturized components without sacrificing the machining performance.

2. Development of a dynamically stable high speed micromachine tool to minimize the machine tool vibration during high speed micromachining.

3. Investigation of proper process parameters and machining environments to improve the surface quality and tribological behavior in high speed micro turning especially for ductile materials.

4. Development of a cost-effective ultra-precision diamond turning machine tool having enhanced spindle stiffness to achieve nano finished surfaces in economical manner.

3

Development of a dynamically stable high speed micromachining center and preliminary experiments

This chapter reveals the development of a dynamically stable high speed micromachining center. It is focused on the design and development of a closed type machine structure for vibration minimization of a high-speed micro-machining center. The objective of the machine structure is to accommodate a high speed spindle and linear stages in a rigid manner. The developed machine structure has provided high stiffness and the damping capability to the machine tool without utilizing vibration absorbers. The models of the machine structures have been generated and assembled in AutoCAD 3D. The performance of the integrated micro-machine tools in terms of static stiffness, dynamic rigidity, and resonant conditions was determined by finite element analysis. The best model has been selected and proposed for manufacturing. Eventually, after manufacturing and assembly, micro-milling experiments have been performed and it was observed that the amplitude of vibration was approaching towards nanometer level throughout the working range of the high-speed spindle. The machine tool was capable to fabricate miniaturized components with smooth surface finish. After the development of the micro-machining center, some preliminary high speed micro turning experiments have been performed on lead free brass

using cooled air as coolant. The achieved surface roughness was in the level of 2 μm.

3.1 Introduction

Micro-machining technologies have versatile applications in several industries like electro-optics, automotive, biotechnology, aerospace, information technology etc to fabricate high accuracy miniaturized components. The growing demand of micro-machining technology has facilitated the requirement of high-performance and efficient ultra-precision machines tools [15]. Highly precise complex 3D shapes with mirror finish on different materials can be fabricated in these ultra-precision machine tools in an expeditious and cost-effective way [202, 203]. Micro-machining is adaptable for generating miniaturized components with complex geometric features and mirror finish on difficult-to-machine materials [204, 205], even on silicon. The major limitation of micro-machining is low tool stiffness and low MRR. High speed micro-machining has been adopted to improve MRR and reduce the chip load. The mechanism of chip formation and the grade of surface finish have made high-speed micro-machining a distinctive one from other traditional material removal processes [206]. The static and dynamic performances of the high-speed micro-machine tools have directly influenced the machining performances. However, determination of the dynamic performances of these high-speed machine tools is a challenging issue by creating real prototype [207]. Finite element analysis has been adopted as a comprehensive mean for this issue [38]. High speed micromachine tools are very much assailable to vibration where high speed spindle has been considered as the major source of vibration. Therefore, minimization of the structural vibration is the most considerable factor during development of a high-speed micro machine tool.

For structural vibration minimization, Yang et al. [208] developed a vibration isolator mechanism based on quasi zero stiffness which significantly reduced the vibration transmissibility. Therefore, it has worked as an effective mean of low frequency vibration. Additionally, Zhang et al. [209] applied an active vibration control method using nonlinear vibration absorber which resulted in lower resonant amplitude of vibration. Semm et al. [210] incorporated substructure coupling approach considering local and global damping to improve the accuracy of FEM simulation in order to determine damping performance of a machine tool. Zhang et al. [211] proposed a discrete time-delay chatter control method with closed loop chatter stability model for milling process. It stabilized the machining parameters and reduced the amplitude of chatter vibration by 78.6%. Orra and Chaudhury [212] presented an electro-magneto-rheological damping system with a closed loop feedback control system to suppress the machine tool vibration during turning process. The damper has been attached under the tool holder and generated counter force to suppress

tool vibration when excited by current signal. Representing the contacts in machine tool is a challenging issue which is required for accurate prediction of machine tool behavior. For ease of computational issues, the contact forces have been directly mapped onto the FE model of machine tool topological optimization problem [213]. Mohammadi and Ahmadi [214] proposed a single degree of freedom model with nonlinear restoring force to determine the vibration response of a KUKA machining robot at tool center point. However, it cannot accurately predict the system dynamics.

The design of the machine structure is significant for vibration isolation of the precision micro-machine tool. The machine structure contributes to the machine tool dynamics. Therefore, a highly rigid machine structure might be able to reduce the machine tool vibration for a micro machining center. The goal of the research was to reduce the vibration of the machine structure so that number of resonances with the working frequency of the machine tool can be reduced. The perfect design of the machine structure possessed very low amplitude of vibration under the resonance condition within the working range.

3.2 The design and analysis of the micro-machining center

3.2.1 Preparation of the model

The design approach is a trial and error approach that incorporated 3D modelling of the structure components, their assemblies and finally evaluation of their performances by FEM analyses. Based on the results of the analyses, the change of materials, structural configuration and the dimensional optimization have been performed to improve the performances in terms of static, dynamic stiffness and damping capability. Eventually, the best model has been selected as the vibration free structure and proposed for manufacturing. Most of the previous researches have focused on external vibration absorbers in mechanical structures to improve the damping capability [215, 216]. However, this research is focused on the internal damping capability of the structure to reduce the machine tool vibration without utilizing any external vibration absorber. The design of the machine structure for the high speed micro-machining center has been made closed type because of the fact that open type structure are more assailable to vibration [38].

3.2.1.1 Structural configuration

The parts of the high-speed micro-machining center were divided into two categories. The machine structure is the stationary part and the other parts such as spindle, linear stages are moving parts. According to the bearing stiffness, accuracy, damping capacity and

thermal performance, a spindle of model AG62-60-0.24-P-DS, manufactured by Fischer spindle was selected for high speed operation. The specifications of the spindle have been described in Table 3.1. The spindle holding fixture was made of mild steel. Further, the linear stages of model LMS-200-200 (Holmarc made) were selected based on their resolution, accuracy and repeatability. The specifications of the linear stages have been represented in Table 3.2. The linear stages consist of high precision lead screw having pitch of 1 mm; and a stepper motor having torque of 10 kg-cm, 56 mm frame size and micro step mode. After the selection of the moving parts, the machine structure was designed for providing the accommodation of these parts and vibration isolation of the overall machine tool. The whole design approach incorporated a number of 3D models among which the best one has been selected for manufacturing based on static and dynamic stability. This description only involved the best model which has been considered as vibration free.

Table 3.1: Technical specifications of the high-speed spindle

Parameter	Value	Parameter	Value
Spindle speed	10000 - 60000 RPM	Lubrication system	Grease
Motor type	Asynchronous	Mass	3.3 kg
Torque	0.24 N.m	Tool change	Pneumatic
Motor power	1.5 kW	Spindle runout	2 μm
Cooling system	Liquid	Bearing type	Steel ball bearing

Table 3.2: Technical specifications of the motorized linear stages

Stages	Travel range (mm)	Resolution (nm)	Accuracy (μm)	Repeatability (μm)	Maximum travel speed (mm/min)	Minimum travel speed (mm/min)	Load carrying capacity (kg)
X stage	150	312	2.5	2.5	240	0.01	50
Y stage	150	312	2.5	2.5	240	0.01	20
Z stage	150	312	2.5	2.5	240	0.01	50

Machine bed accommodates the overall machine tool. So the stiffness and the load carrying capacity of the machine bed must be high enough. For the machine structure, the length of the machine bed is 660 mm and the width is 556 mm. The maximum height of the machine bed is 100 mm. Two slots of 50 mm depth were given at both sides of the bed. The frame columns were attached into the slots of the bed from bottom as well as from transverse side so that the transverse movement of the frame column due to vibration

could be restricted. The X-Y linear stages were fixed at the center of the machine bed from the transverse side. The total distance required in X or Y direction for the travel of the X-Y linear stages is 350 mm (200 mm stage width + 150 mm travel). Therefore, the distance provided between two slots is 356 mm so that the X-Y linear stages can travel without getting obstructed between the frame columns. A through hole of 40 mm diameter was provided at the machine bed so that the wires connected to the control systems of the spindle and linear stages can be passed through that hole.

The design of the frame column was generated as per the vibration point of view and the manufacturability of the material. The thickness of the frame column is 100 mm and its height is 275 mm. The heights of the frame columns were optimized in the experimental range in order to minimize the natural vibration. The thickness was adjusted to provide sufficient stiffness. The frame columns are carrying the load of the upper block. The upper block is a trapezoidal shaped block designed for the closed type machine structure. It carries the vertical linear stage along with spindle holding fixture and spindle. The thickness of the upper block is 100 mm and the maximum height is 207.5 mm. The height of the upper block has been adjusted to minimize the natural vibration of the overall machine structure. After generating each part of the machine structure they were integrated. Fig. 3.1 represents the CAD models of all components of the vibration free high-speed micro-machining center. Fig. 3.2 (a) represents the unassembled vibration free machine structure which has been integrated with spindle and linear stages as shown in Fig. 3.2 (b). All the components have been numbered separately in the exploded view in Fig. 3.1 and represented with the same number in the assembled view in Fig. 3.2.

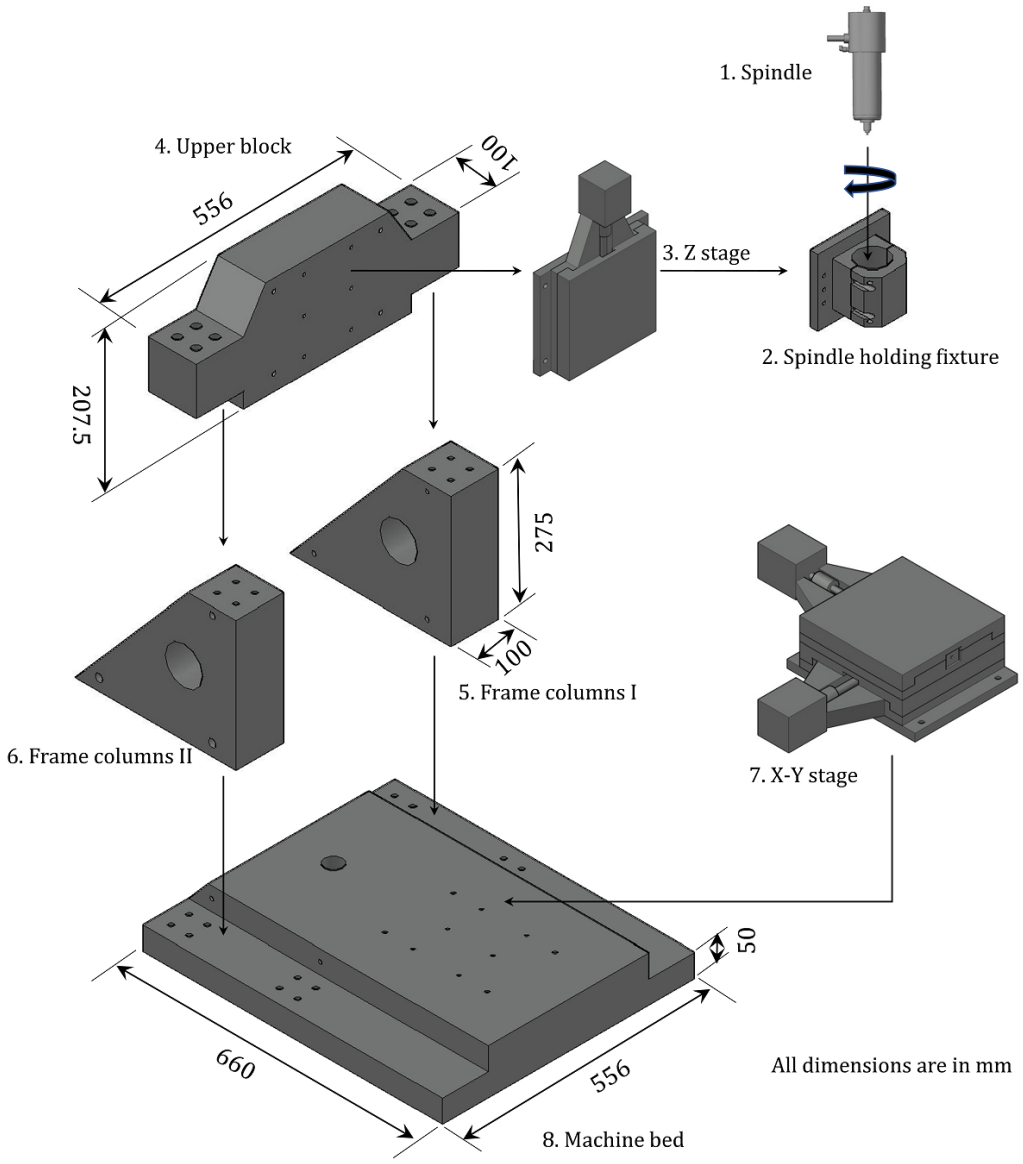

Figure 3.1: The components of the vibration free high-speed micro-machining center prepared in AutoCAD

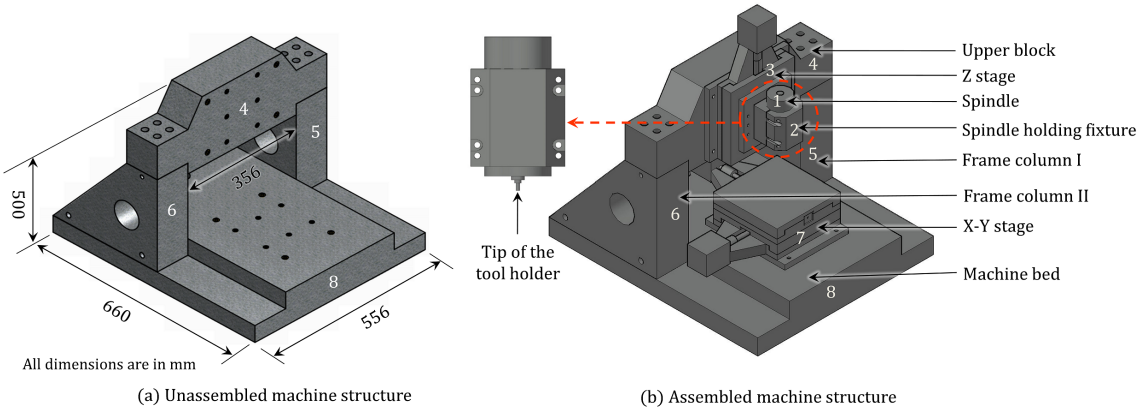

(a) Unassembled machine structure (b) Assembled machine structure

Figure 3.2: CAD model of the vibration free machine structure

3.2.1.2 Materials selection

The succeeding design criterion involved selection of the material for the machine structure. A material having higher damping capacity, good specific stiffness, and small thermal expansion co-efficient with low specific heat capacity may be considered as good structural material. Additionally, the manufacturability of materials has been considered during design. Therefore, the material selection is the predominant factor in machine tool design. Generally, metallic structures possesses low damping performance due to lower damping capacity [217]. Cast iron has been used for conventional machine structure for higher damping characteristics and load carrying capacity [218]. However, elevated processing cost and poor environmental properties have limited cast iron for precision machine tool structure [219]. Natural granite has shown better performance than cast iron in terms of rigidity, damping quality, thermal stability and dynamic load carrying capacity [220, 221]. Besides, good form stability and flatness have made natural granite superior for high-speed ultra-precision machine tool structure. Based on all these characteristics, both cast iron and natural granite were selected for the machine structure i.e., machine bed (component 8), frame columns (Component 5 and 6), and the upper block (component 4) as shown in Fig. 3.2. The performances were evaluated for a single unassembled model of machine frame as shown in Fig. 3.2 (a), using both the materials in ANSYS modal analysis. Fig. 3.3 (a) shows the comparison of natural frequencies of the structure using both cast iron and natural granite. The minimum natural frequency of the structure was 1118.8 Hz when the material was cast iron. However, the minimum natural frequency was 1528.9 Hz using natural granite as the material of the machine structure. A 36% improvement in natural frequency has been observed for a single model, when the material was changed from cast iron to natural granite. Therefore, the structure made of natural granite should create less number of resonances with the working spindle as compared to the structure made of cast

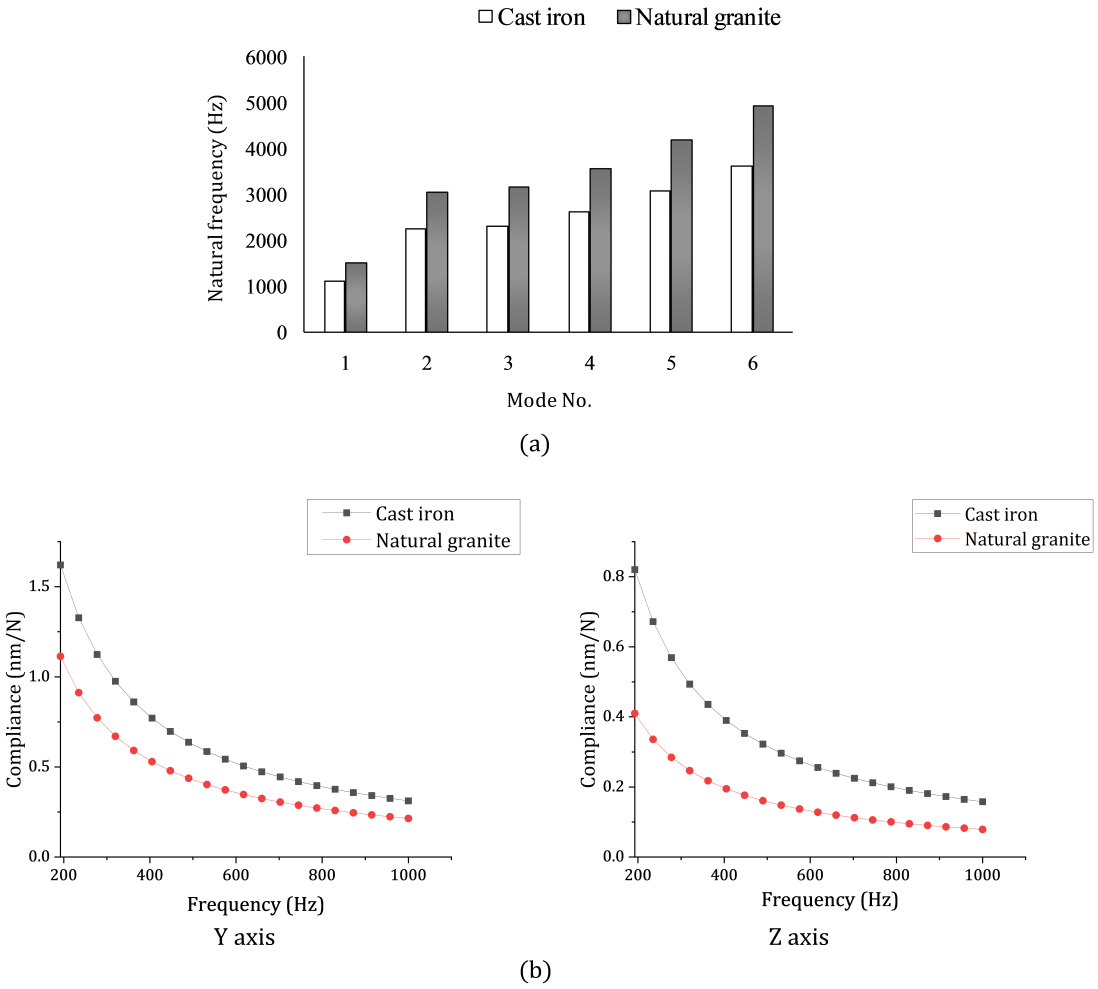

Figure 3.3: Comparative results of the proposed machine frame using cast iron and natural granite (a) Comparison of natural frequencies determined in modal analysis, (b) Comparison of dynamic compliance calculated from harmonic response analysis

iron. Additionally, harmonic response analysis on the structure using both the materials has shown better dynamic performances for natural granite. A set of constant forces has been applied on the front face of the structure and its dynamic response has been determined for both the materials in terms of dynamic compliance. As shown in Fig. 3.3 (b), dynamic compliance in both Y and Z direction is lesser for natural granite compared to cast iron and hence the structure has been subjected to lower deformation when made of natural granite. Hence, natural granite is capable for higher vibration damping as compared to cast iron. For better performance, natural granite was selected as the material of the invented machine structure. The materials involved in the FE analysis and their mechanical properties have been depicted in Table 3.3.

Table 3.3: Mechanical properties of the materials involved in FEA

SL. No.	Materials	Density (kg/m^3)	Young's modulus (GPa)	Poisson's ratio	Damping characteristics (Log decrements)
1.	Natural granite	2900	90	0.25	0.015
2.	Cast iron	7200	120	0.26	0.0045
3.	Mild steel	7850	210	0.3	0.0023
4.	Stainless steel	8000	193	0.3	0.0023
5.	Aluminium alloy (B51S)	2800	80	0.033	0.0003

3.2.1.3 Modelling of the linear stages

The stiffness of the linear stages directly influences the dynamic behavior of the micro-machine tool. LMS-200-200 linear stages comprises of lead screw based drive mechanism. The linear stages have been driven by stepper motor of 10 kg-cm torque. For stick-slip free positioning, linear guide ways with V grooved guides and crossed rollers have been incorporated. To establish a practical model of the linear stages in FE model, the CAD model of the linear stages have been prepared as shown in Fig. 3.4 (a). The carriages and the base have been mentioned in the figure. The rolling interface between the cross roller and V grooves directly influences the structural dynamics. However, it is difficult to represent the rolling interface in FE model. Therefore, the rolling interfaces have been represented as spring element in the linear stages. One dimensional spring system has been assumed for the linear stages. To determine the stiffness of the spring elements, static structural analysis of the linear stage was performed in ANSYS. The maximum allowable load has been applied on the carriage. From static structural analysis, the stiffness of the spring elements have been estimated. The stiffness of the spring elements has been incorporated in the FE model of the micro-machining center. The outcome of static structural analysis has been depicted in Fig. 3.4 (b). In general, the contacts in the elements of the linear stages are sliding metal to metal contact. Therefore, damping properties of the interfaces of linear stages has been considered for metal to metal damping. Constant damping ratio ($\xi = 0.04$) has been considered for each interface in the linear stages due to metal to metal contact.

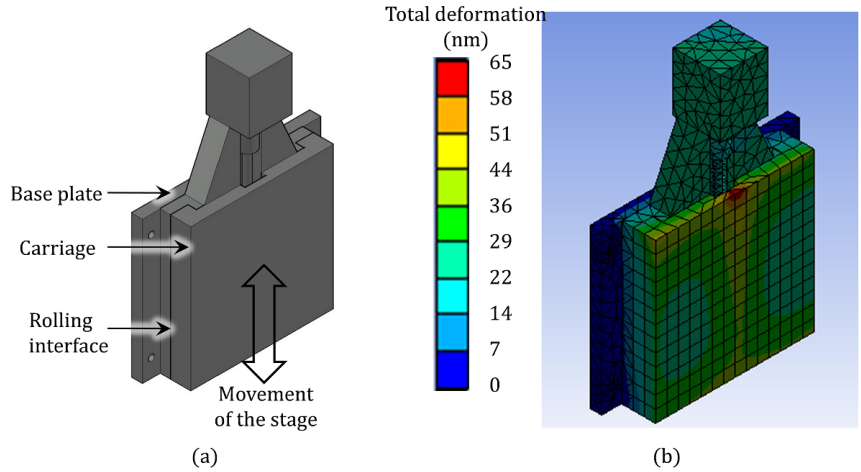

Figure 3.4: (a) CAD model of the linear stage, (b) Deformation of the stage in static structural analysis

3.2.2 Finite element modelling

3.2.2.1 Static structural analysis

Static structural analysis has calculated the influence of static loading on the machine structure neglecting the effects of vibration. The basic governing equation involved in static structural analysis includes the Hooke's law which states that $[F] = [K][x]$, where $[F]$, $[K]$,and $[x]$ represents the force matrix, stiffness matrix, and displacement matrix respectively. Hence, the deformation in terms of displacement is calculated for an externally applied force using the law. Static structural analysis of the assembled CAD model of the machine structure has been performed in ANSYS considering the materials of each part and applying constant static load of 5 N (point load) in each X, Y and Z direction at the tip of the tool holder of the spindle. The bottom of the machine bed was kept fixed. The rotor of the spindle was given a rotational speed of 60000 rpm which is equivalent to the maximum rotational speed of the spindle. The static performance of the machine tool has been determined in terms of the static stiffness of the tip of tool holder. The stiffness in each direction has been depicted in Fig. 3.5. Negligible deformation and stress have been observed in the overall machine structure in static structural analysis. The maximum von Mises stress was 27.5 MPa found in the structure. The bearing parameters like axial and radial bearing stiffness, damping coefficients have been selected based on the original bearing parameters of the spindle. The maximum deformation and stress have been found at the tip of tool holder in the spindle. The magnitude of the maximum deformation was 0.47 μm. It can be seen that the proposed machine structure has provided superior rigidity as compared to previously reported models for micro-machining center [38].

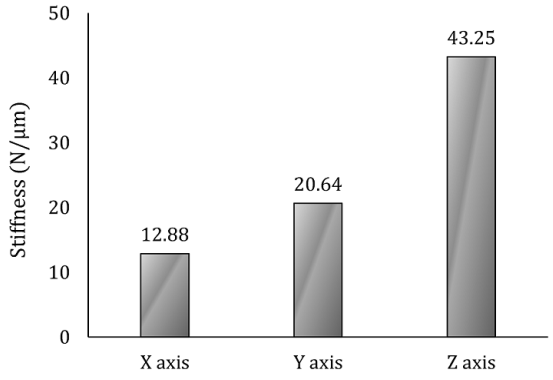

Figure 3.5: The static stiffness of the proposed model calculated from static structural analysis

3.2.2.2 Modal analysis

After static structural analysis, the natural frequencies of the assembled machine tool models have been determined by modal analysis in ANSYS workbench. This analysis uses Block Lanczos mode extraction method to determine the natural frequencies. The structural configurations which created less number of resonances within the working frequency of the spindle were selected. The purpose of the modal analysis was to find out the corresponding rotational speeds for resonance. Maximum rotational speed of 60000 rpm has been applied at the spindle collet. The spindle frequency can be depicted from the equation f=N/60, where N and f represents the rotational speed and corresponding working frequency of the spindle respectively. Therefore, the maximum working frequency of the spindle was 1000 Hz. The natural frequency of 1st mode of the assembled model was 663.76 Hz determined in modal analysis. It was found that only four natural frequencies are there below or adjacent to 1000 Hz as shown in Fig. 3.6. However, in the first three natural frequencies, deformations were found only in the stepper motors of linear stages according to the mode shapes. In the fourth mode, deformation has been observed at the structure and the spindle head. Therefore, the structure may create resonance within the working frequency of the spindle at the fourth mode frequency. The stepper motor was the only deformable zone in the machine tool for the first three mode shapes because it has no mechanical support from both sides and therefore, this is completely at cantilever stage. The first four mode shapes have been represented in Fig. 3.7.

The material selection, structural configuration, and dimensional change played a major part to determine the mode shapes, natural frequencies, and deformations in different mode shapes under resonance. A small increase in height of the upper block resulted in deformation in the spindle head as shown in the mode shapes, represented in Fig. 3.8. All of the issues have been taken into consideration during the design of the machine structure.

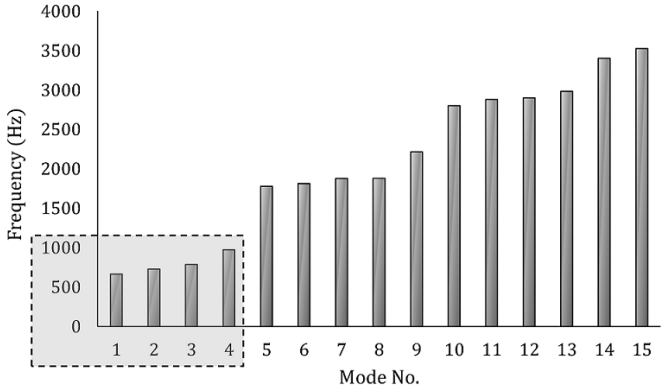

Figure 3.6: Plots of first 15 natural frequencies of the proposed assembled machine structure determined in ANSYS modal analysis

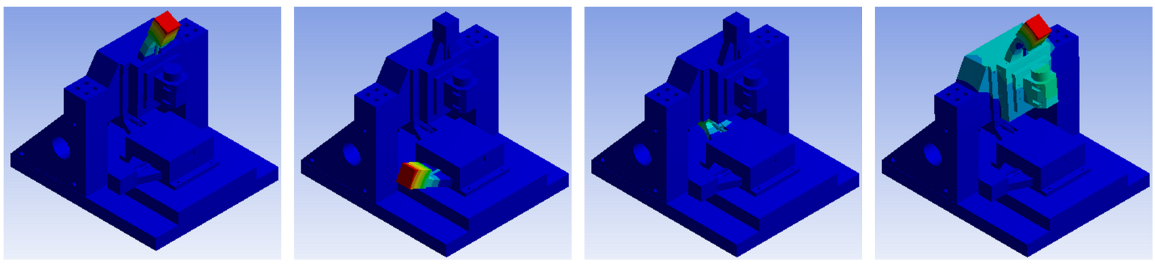

(a) 1st Mode shape (b) 2nd Mode shape (c) 3rd Mode shape (d) 4th Mode shape

Figure 3.7: First four mode shapes of the assembled machine structure, determined in ANSYS modal analysis

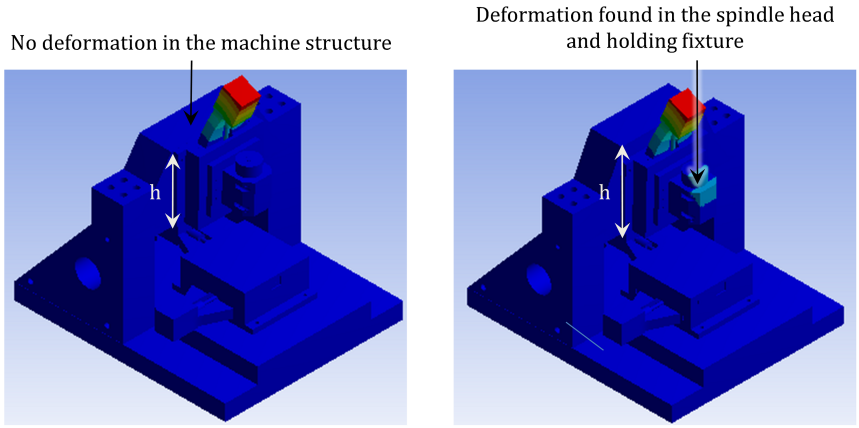

(a) h = 207.5 mm (b) h = 250 mm

Figure 3.8: First mode shapes of the assembled machine structure with different heights of the upper block

The proposed model has shown promising result considering the dimensions and spaces for movement of the stages. It was not much excited within the working frequency of the spindle in terms of creating resonances. However, the resonant frequencies have changed under the action of forced vibration occurring due to the action of cutting force. Therefore, dynamic response of the machine tool need to be evaluated to determine the effect of machining operation on the machine structure.

3.2.2.3 Harmonic response analysis

Harmonic response analysis was performed on the assembled models of the machine tools to check the amplitude of vibration under forced vibration. In this analysis, the machine structure has been excited by a series of harmonic cutting forces F, acting between the micro tool and the workpiece. The harmonic force F can be expressed as, $[F = F_0 sin(\omega t)]$; where ω is the given frequency of the cutting operation [38]. The tip of the tool holder has been given an average cutting force F_0. The range of frequency was given according to the working cutting frequency i.e. 166 Hz to 1000 Hz. Constant 5 N force has been applied in each X, Y and Z directions. The cutting force has been specified based on some previous literature on mechanical micro-machining [222, 223]. However, the cutting force can vary for different cutting conditions and work materials. As a result, the deformation found in the simulation can be deviated from the deformation found in experiments. The damping ratio of each material has been calculated from their log decrement values and incorporated in the FEM analysis. Additionally, for the interfaces of linear stages, constant damping ratios for metallic contact have been considered in the analysis. The model which showed lowest amplitude of vibration under the action of cutting force has been finalized as the best structure within the experimental range. Further, that machine structure was proposed for manufacturing. The amplitude of vibration for the proposed machine structure was approaching towards nanometer level. The maximum amplitude was 0.516 micron along Y axis and the peak was found at 235 Hz. However, maximum amplitude along Z axis was 0.197 micron and corresponding frequency was 235 Hz. Fig. 3.9 represents the dynamic compliance of the tip of tool holder of the assembled machine tool calculated from harmonic response simulation. It shows that the vibration was prominent at the frequency of 235 Hz along both the direction. However, the structure has shown good dynamic stability as the amplitude was at nanometer level. Therefore, the structure was well designed for vibration isolation considering high static stiffness, less number of resonances under free and forced vibration, nanometric amplitude under cutting condition without obstructing the motion of the linear stages. The deformation was measured along these two directions because the maximum deformation was found in Y and Z directions in the mode shapes found in modal analysis and the deformation along X direction was

negligible. The designed structure has created less number of resonances with the working frequency of the spindle under dynamic condition as well. Additionally, the structure is highly rigid. Therefore, the periodic fluctuation of cutting force during micromachining can be easily absorbed by the machine structure. This phenomenon does not let the tool deflection during the micro cutting and thus reduced tool work vibration and chatter. Therefore, the structure has provided good rigidity and damping performance to the overall high speed micro-machining center. It absorbed a huge extent of noise generated by vibration during the machining operation. Hence, the structural damping contributed considerably to reduce the vibration of high-speed micro-machining center.

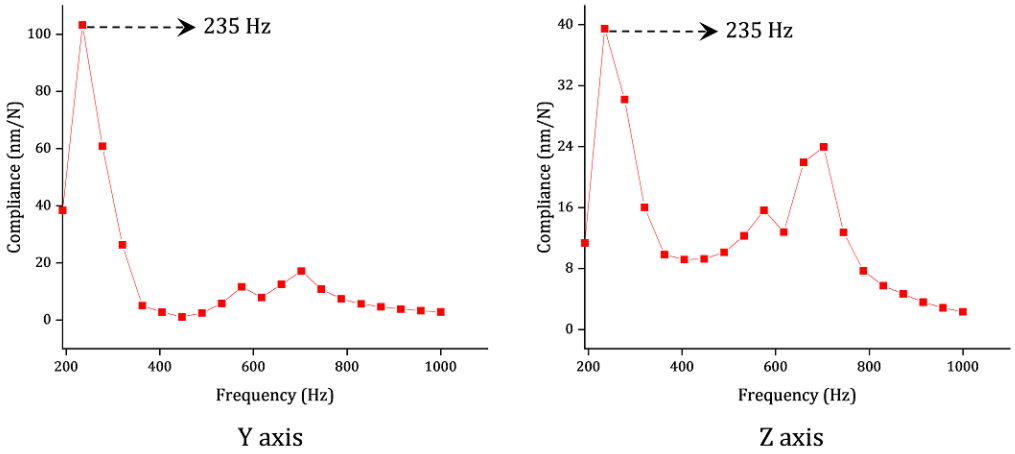

Figure 3.9: Plots of dynamic compliance of the assembled machine tool model determined from harmonic response analysis in ANSYS

After evaluating the performance in ANSYS, the model was proposed for manufacturing. The maximum floor area required for the machine structure was 660 mm × 556 mm. The maximum height of the structure was 500 mm. The weight of the complete structure was 200 kg. The attachments with fasteners take a major part for structural damping as slightly loose fastening may results in enormous vibration in the machine structure. It was taken into consideration during manufacturing.

3.3 Experimental performance of the micro-machining center

3.3.1 Experimental setup

After manufacturing, the machine structure has been assembled with the spindle and linear stages. Fig. 3.10 represents the assembled high-speed micro-machining center (Model

V60). All the components in the machine tool have been numbered as shown in the exploded view of CAD model in Fig. 3.1. Experimental frequency response analysis has been performed in the assembled machine tool during machining to check the amplitude of vibration. Micro-milling operations have been performed under dry condition with constant chip load (Chip load= $\frac{f}{NZ}$; where f is feed rate per min, N is rpm, and Z is the number of flutes). The rotational speed has been varied from 10000 to 60000 rpm as mentioned in Table 3.4. The feed rates have been varied accordingly to maintain constant chip load. The chipload was $1\mu m$ for each run with two flute milling cutter. Depth of cut was constant for each run. The vibration data have been collected by accelerometers using Bruel and Kjaer 4 channel dynamic signal analyzer. Two accelerometers were mounted along Y and Z axis to capture the vibration data. The positions of mounting the accelerometers have been shown in Fig. 3.10. The recorded signals were processed in MeScope Ves software and the amplitudes of vibration were determined. The experiment has been performed with a two flute milling cutter. Furthermore, the machining experiment has been repeated with a four flute milling cutter with same process parameters. The chipload in each run became $0.5\mu m$ as the number of flutes became double with same feed rates and cutting speeds as the previous experiment. These results were compared with the results of harmonic response analysis performed in ANSYS in order to determine the similarity. The experimental conditions have been illustrated in Table 3.4. Eventually, tapping test has been performed on the micro-machining center to check the chatter stability for the machine tool.

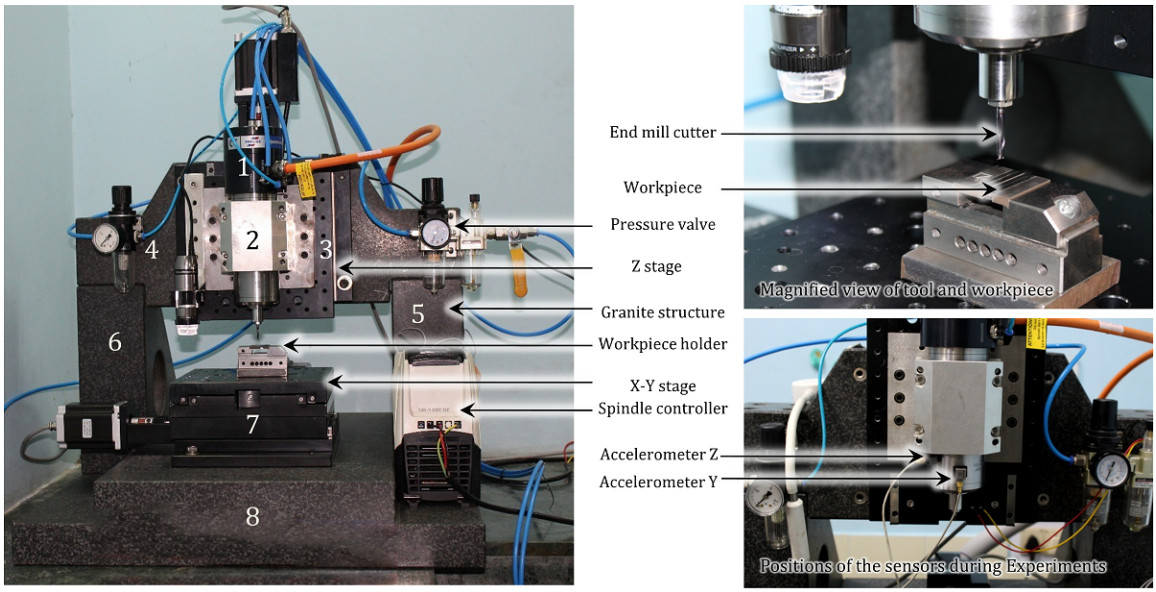

Figure 3.10: Assembled high-speed micro-machining center with the proposed machine structure made of natural granite

Table 3.4: Machining conditions during experimental frequency response analysis

Cutting tool	Two flute and four flute milling cutter; Cutter diameter 1 mm
Tool material	TiAlN coated tungsten carbide
Workpiece	Mild steel
Spindle rotational speed (rpm)	10000, 11000, 12000, 13000, 14000, 15000, 16000, 17000, 18000, 19000, 20000 , 22000, 24000, 26000, 28000, 30000, 33000, 36000, 39000, 42000, 45000, 48000, 51000, 54000, 57000, 60000
Feed rate (mm/min)	20, 22, 24, 26, 28, 30, 32, 34, 36, 38, 40, 44, 48, 52, 56, 60, 66, 72, 78, 84, 90, 96, 102, 108, 114, 120
Depth of cut	50 μm
Cutting conditions	Dry

3.3.2 Experimental frequency response analysis

The amplitude of vibration of the machine structure was approaching towards nanometer level during machining with two flute milling cutter. The FRF plots along Y and Z axes have been shown in Fig. 3.11 (a) and (b) respectively. These show that the maximum amplitude of the structure was 0.47 micron in Y direction while cutting mild steel. The corresponding frequency at which the maximum amplitude occurred was 250 Hz. The maximum amplitude of the structure in the Z direction was 0.112 micron while the machining operation and the corresponding frequency at resonance was 211 Hz. The plot was similar to that one found in the harmonic response analysis of the model in ANSYS. Slight variation was due to discontinuous plot in experimental frequency response analysis and due to the presence of higher order frequency as well. It was found that the resonance zone occurred in between 190 Hz and 270 Hz. However amplitude is more dominant at 250 Hz along Y axis and 211 Hz along Z axis. The rotational speeds have been varied with 1000 rpm interval between 10000 to 20000 rpm as the larger peaks have been observed within the interval. After 30000 rpm, the interval of rpm variation was taken 3000 rpm as the peaks became smaller in that region. Additionally, lesser number of peaks were seen after 30000 rpm. During machining at each rotational speed, the FRF plot gives the peaks at the resonant frequencies. The final FRF plot has been generated as the overlay trace of different FRF plots at different rotational speeds. Furthermore, the amplitudes of the peaks, found in the FRF generated after machining in each rotational speed have been plotted. Fig. 3.11 (c) and (d) represents the variations of amplitudes with rotational speed along Y and Z axis. It can be illustrated that the amplitude of vibration has been

reduced with increasing the rotational speed. Lower peaks have been generated at higher rotational speed. This phenomenon occurs because of two reasons. In general, the cutting force reduces with increasing the rotational speed. Therefore, the specific cutting energy has been reduced at higher rotational speed. This will lead to lower force transmission to the structure at higher rotational speed. Additionally, the structure has the ability to absorb the force transmitted at higher rotational speed. Consequently, the amplitudes have been reduced at higher spindle rpm.

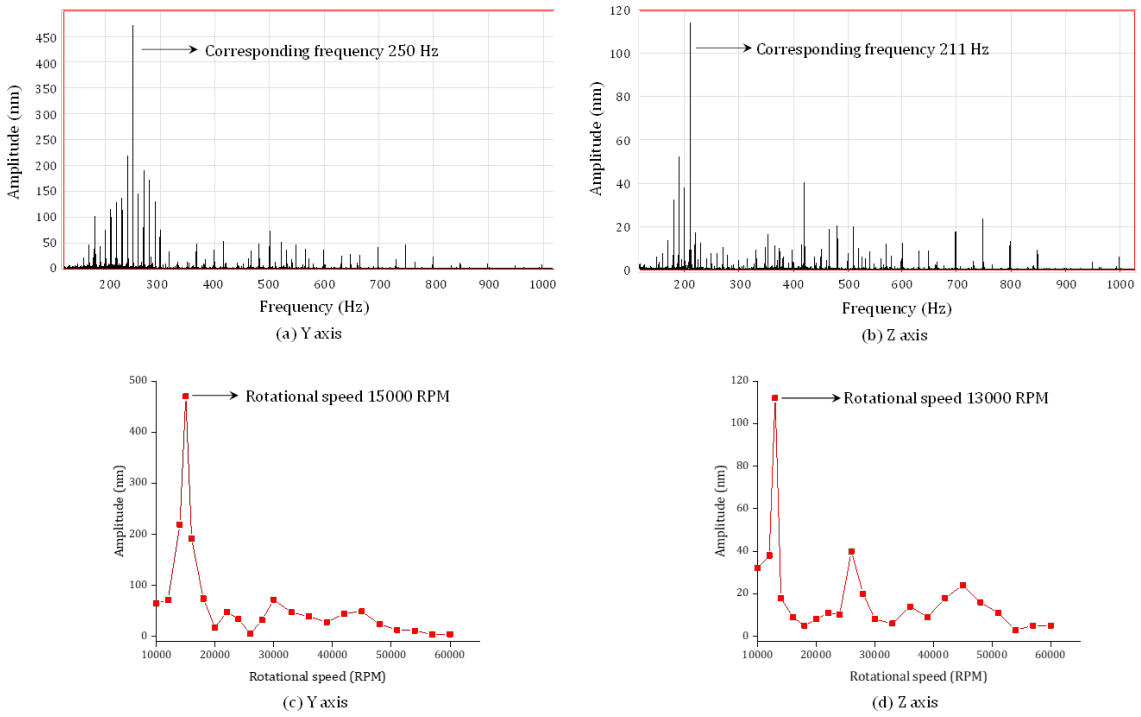

Figure 3.11: The variations of (a) Amplitude vs Frequency along Y axis, (b) Amplitude vs Frequency along Z axis, (c) Amplitude vs Rotational speed along Y axis, (d) Amplitude vs Rotational speed along Z axis achieved in experimental frequency response analysis of the developed high-speed micromachining center while machining with two flute milling cutter

The machining operation performed by four flute milling cutter precipitated that maximum amplitude along Y direction was 0.38 micron and corresponding resonant frequency was 250 Hz. However, the maximum amplitude along Z axis was 0.091 micron and corresponding resonant frequency was 211 Hz. The frequency response plots along Y and Z axes for this experiment have been depicted in Fig. 3.12 (a) and (b) respectively. This experiment has shown good similarity with the resonant frequencies achieved in previous experimental result as well as in the result of ANSYS. The plot was similar with the plot achieved in simulation. Probable occurrence of second order frequency (higher order) has led to a peak at 422 Hz along Z axis. Fig. 3.12 (c) and (d) depicted the variation

of amplitudes with rotational speed. The graphs have been plotted following the similar phenomenon as mentioned for Fig. 3.11 (c) and (d), taking the amplitudes of peaks in each rotational speed. The decreasing trend of amplitudes with rotational speed was observed in this case as well. The variation of amplitude was attributed to the variation of cutting force in both experiments. However, a constant average cutting force was considered in harmonic response analysis in ANSYS. The comparisons of maximum amplitudes and corresponding frequencies determined in both the experiments and the FEM analysis have shown in Fig. 3.13.

As shown in the plots of Fig. 3.11 and Fig. 3.12, the amplitudes of vibration have been reduced significantly when the machining has been performed with four flute milling cutter as compared to two flute milling cutter under similar machining conditions. The reduction of maximum amplitude was 20% along Y axis and 19% along Z axis. In some cases at higher frequencies, the amplitude of vibration slightly increased for four flute milling cutter as compared to two flute milling cutter. This was possible due to chatter in the cutting tool resulted from tool wear as a result of continuous machining. However, for most of the cases, decreasing trend of vibration amplitudes has been observed for four flute milling cutter compared to two flute milling cutter. As the number of flutes increased, the chip load on the tool has been reduced to half for the four flute milling cutter. This resulted in lower cutting force requirement in machining. Subsequently, the specific cutting energy has been reduced during machining. As a result, lesser amount of force was transmitted to the cutting tool. Consequently, the amplitudes of vibration have been reduced for four flute milling cutter.

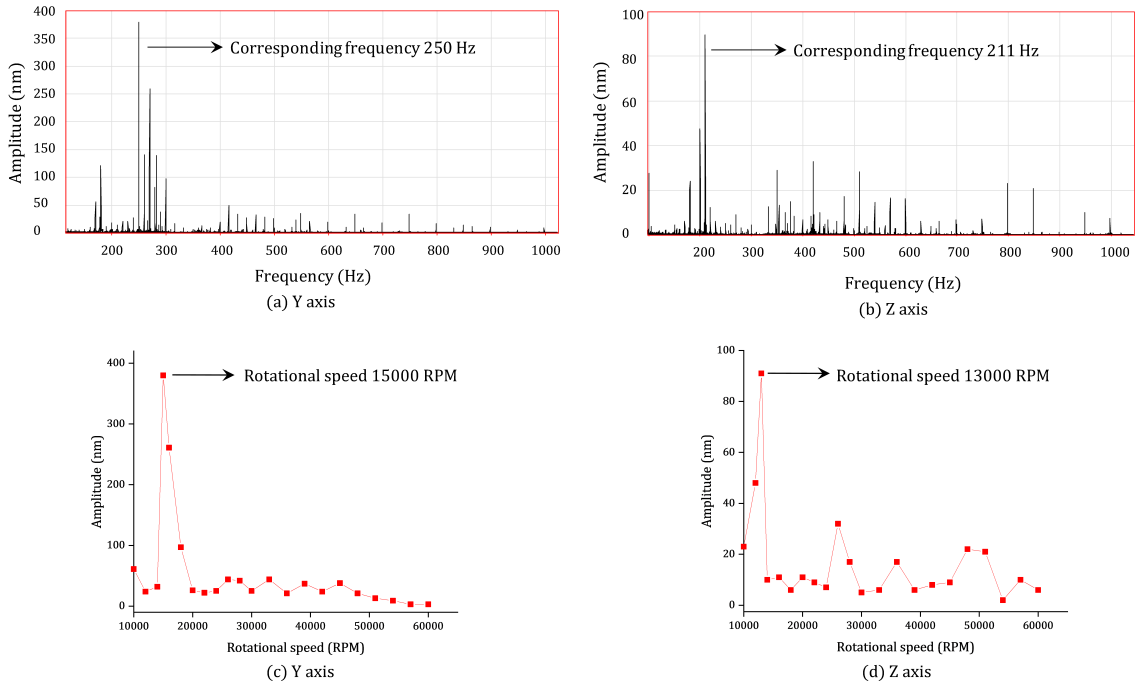

Figure 3.12: The variations of (a) Amplitude vs Frequency along Y axis, (b) Amplitude vs Frequency along Z axis, (c) Amplitude vs Rotational speed along Y axis, (d) Amplitude vs Rotational speed along Z axis achieved in experimental frequency response analysis of the developed high-speed micromachining center while machining with four flute milling cutter

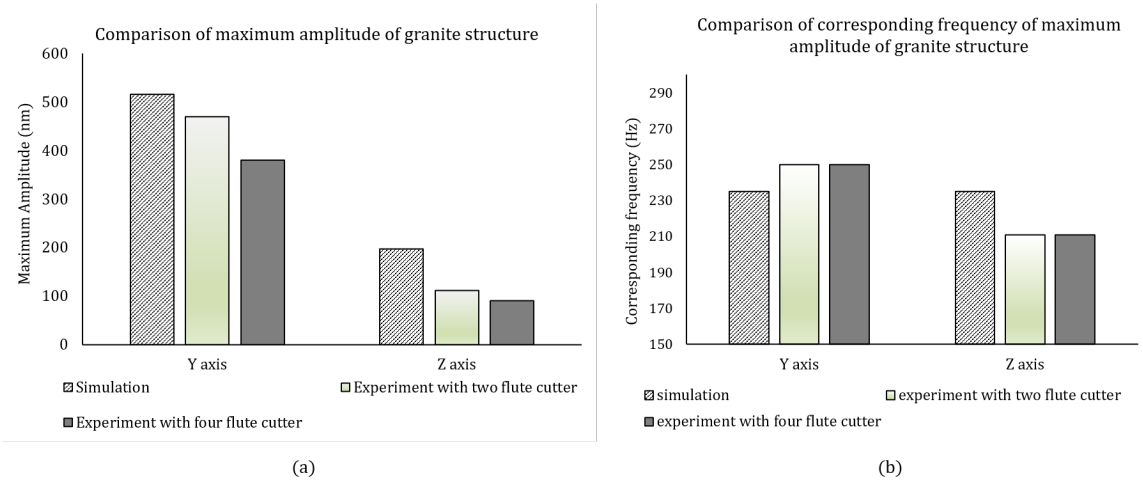

Figure 3.13: Comparison of (a) maximum amplitude; and (b) corresponding frequencies of the developed micromachining center, determined in ANSYS harmonic response analysis, experimental frequency response analysis with two flute cutter and experimental frequency response analysis with four flute cutter

3.3.3 Tapping test on the machine tool

The tapping test has been performed to measure Frequency Response Functions (FRF). In general, the accelerometers are mounted and impact is provided at the tip of the cutting tool for tapping test. However, in the micro-machining set up, the size of the cutting tool is very small. Therefore, it was not possible to mount the accelerometers at the tool tip. The accelerometers were mounted at the tip of the spindle collet along radial (Y) and axial (Z) direction. The spindle collet has been excited by impact hammer and the FRF data have been acquired. The range of frequency has been selected from 150 Hz to 400 Hz, as higher peaks found by simulation lie within this range. The FRF plots along Y axis and Z axis are represented in Fig. 3.14 (a) and (b). The spectra depicts a stable plot along both radial and axial direction. The peaks represented the resonant frequencies. Higher order peaks represented the harmonic components of the lower order peaks. Sometimes, the waveform was noisy which was due to variation of impulse on the spindle tip. The plots have shown good similarity in terms of resonant frequencies with the same achieved in ANSYS harmonic response analysis and machining test. The maximum peaks found in tapping test along radial and axial directions were at 229 Hz and 218 Hz respectively. However, both the peaks found in harmonic response analysis in ANSYS were at 235 Hz. The comparison of the resonant frequencies achieved in tapping test and ANSYS are illustrated in Fig. 3.14 (c).

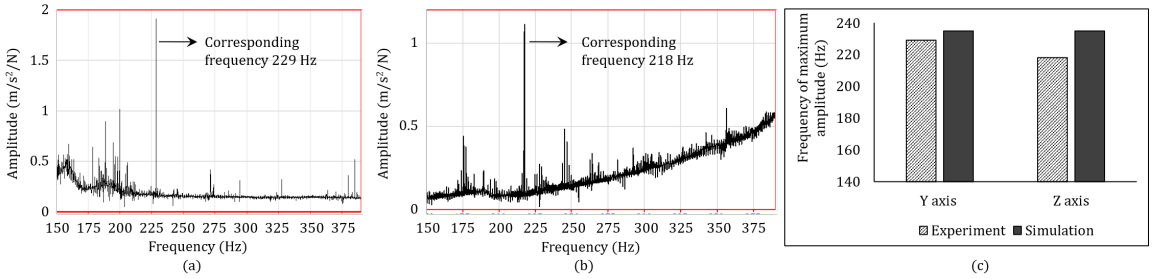

Figure 3.14: (a) FRF plots generated in tapping test along Y axis; (b) FRF plots generated in tapping test along Z axis; (c) Comparison of resonant frequencies corresponding to maximum peaks achieved in tapping test and ANSYS simulation

The amplitude found was almost negligible, therefore, it can be concluded that the structure is vibration free upto the maximum rotational speed of the working spindle. The amplitude has a tendency to be reduced with operating frequency. Therefore, the machine structure can be operated for ultra-high speed machining as well. The machining vibration has been reduced to great extent using the developed machine structure. An average surface finish of 100 nm has been achieved on difficult-to-cut materials by micro-milling operation in the machine tool. The machining was performed upto the maximum rotational speed of the spindle (60000 rpm) without breakage of the cutting tool. Hence, promising accuracy,

precision, surface finish of micro-machined components have been achieved in the micro-machining center. Fig. 3.15 (a) depicts the movement of the milling cutter on the workpiece surface during micro-milling operation. It can be seen that the tool movement was uniform along the infeed direction and any transverse movement due to vibration was not found. Fig. 3.15 (b) illustrates the surface roughness profile on Inconel 718 during micro-milling with 400 μm end mill cutter. The spindle rotational speed, feed rate and depth of cut was 20000 rpm, 160 mm/min and 30 μm respectively. The machining has been performed under dry condition and average surface roughness R_a of 98.51 nm has been achieved on the machined surface. The surface roughness has been measured in Contact type stylus profilometry (DektakXT, Bruker). Hence, super-finished surfaces can be achieved on micro features of difficult-to-machine materials in the developed micro-machining center.

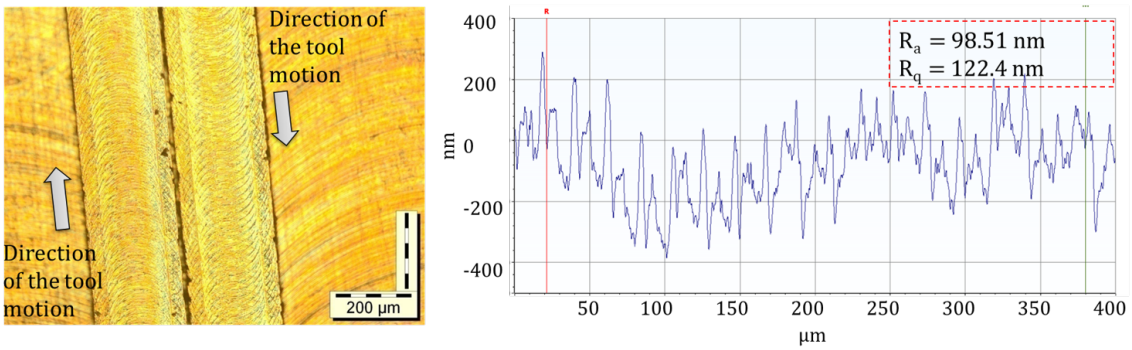

(a) (b)

Figure 3.15: (a) Tool feed marks on micro grooves of 200 µm width and 60 µm depth, generated on high strength super alloy Ti6Al4V by high-speed micro-milling, (b) Surface roughness profile on Inconel 718 during micro-milling with 400 μm end mill cutter

3.4 Preliminary experiments of micro turning

3.4.1 Experimental process

After successful development of the high speed micro-machining center, some preliminary micro turning experiments have been performed to check the feasibility of the process. The similar experimental setup which was shown in Fig. 3.10 has been applied for turning operation. The workpiece has been clamped in the collet of the spindle. A toolpost containing the tool holder and cutting tool was attached to the X-Y stage. The feed motion has been provided to the workpiece by means of the Z stage, while depth of cut has been provided by adjusting the X-Y stage. The turning operation has been performed along vertical direction. The workpiece was small round bar of lead free brass having 3 mm diameter and 50

mm length. The brass alloy consists of 58% copper, 39% zinc, and a little amount of impurity like oxide contents. Sandvik made TiAlN (PVD) coated cemented carbide inserts have been used for micro turning. The cutting tool has 0^o rake angle, 6^o side relief angle, 35^o end relief angle, and 30 μm nose radius. In addition, the principal and end cutting edge angle were 90^o and 9^o respectively. The details of tool geometry have been represented in Table 1. Cooled air has been injected to the machining interface at high pressure (0.8 bar) for cooling operation. The major objective was to investigate the surface behavior on the micro samples of lead free brass in high speed micro turning. Therefore, the experiments were performed at constant cutting speed of 100 m/min. Three different levels of feed rate (7.5, 10, 15 $\mu m/rev$) and depth of cut (30, 40, 50 μm) has been selected for the experiments. Taguchi L9 orthogonal array design has been utilized to prepare the design of experiment. The machining length was 3 mm for each sample. The surface roughness of the machined components have been measured by Mitutoyo make portable surface roughness tester (model "SJ-210"). It is comprised of a stylus probe having diameter 5 μm. Additionally, the surface topography of the machined samples have been captured and analyzed by optical microscope (Model BX51M, Olympus).

3.4.2 Analysis of the results

In general, the cutting edge of the tool leaves some feed marks on the workpiece surface due to feed motion resulting in surface roughness. However, the machined surface roughness strongly depends on machining parameters, extent of cutting heat generation, plasticity of the workpiece material. The design of experiment along with the surface roughness values have been depicted in Table 3.5. It has been observed that the surface roughness values have not much changed with length due to small machining length. From Table 3.5, it can be seen that best surface profile has been achieved at feed rate and depth of cut of 7.5 $\mu m/rev$ and 50 μm respectively. Average surface roughness (R_a) of 0.3 μm has been obtained in this combination. In contrary, combination of feed rate and depth of cut of 10 $\mu m/rev$ feed rate and 30 μm respectively precipitated maximum average surface roughness (R_a) of 4.53 μm. A wide range of surface roughness has been achieved in the full experiment.

The surface roughness data has been analyzed by Taguchi method to determine the individual effect of feed rate and depth of cut. Fig. 3.16 (a) represents their influences on surface roughness. It was observed that the average surface roughness has been increased initially and then decreased on increasing the feed rate. The experiment has been repeated twice and similar trend has been found in each case. The surface roughness has been increased drastically when the feed rate has been changed from 7.5 $\mu m/rev$ to 10 $\mu m/rev$. In general, the surface roughness monotonically increases with feed rate. However, in this study, the surface roughness has not followed the traditional trend. This was observed

Table 3.5: Design of experiment with measured surface roughness

Experiment No.	Feed rate ($\mu m/rev$)	Depth of cut (μm)	R_a (μm)	R_q (μm)	R_z (μm)
1.	7.5	30	1.69	2.12	8.52
2.	7.5	40	2.11	2.7	10.67
3.	7.5	50	0.3	0.37	1.72
4.	10	30	4.53	6	24.06
5.	10	40	3.75	5.04	25.9
6.	10	50	0.74	1.1	6.09
7.	15	30	2.53	3.24	12.09
8.	15	40	2.92	3.91	16.04
9.	15	50	1.55	2.05	9.1

mainly for two reasons. Firstly, the overhang length of the workpiece has led to some extent of tool-work relative vibration. This resulted in increment in surface roughness on the machined surface. Additionally, the cutting tool has followed a step tool path as shown in Fig. 3.16 (b). It governed smooth turning operation during machining from A to B. However, significant amount of chips accumulated on the principal cutting edge of the turning inserts during cutting from B to C and C to D as shown in the Fig. 3.16 (b). Rapid ductility of lead free brass has promoted the tendency of longer chip formation and accumulation (as shown in Fig. 3.18 (b)). The accumulated chips on the cutting edge has interacted with the work surface and created some scratch marks on the machined surface generated on BC and CD of the sample. Therefore, the surface roughness has been increased rapidly in the section BC and CD, as compared to the section AB. Fig. 3.17 depicts the microscopic images of surface topographies for experiment 1 and 3. The sections for experiment 1 and 3 can be considered as section CD and AB respectively. It can be seen that the surface topography was quite smooth for experiment 3 with straight tool marks on the machined surface. However, some cross scratch marks has been observed on the machined surface for experiment 1. It can be noticed that the amount of plastic deformation on the machined surface was higher for experiment 1 due to excessive rubbing of the chips accumulated on the cutting edge of the turning insert. This resulted in formation of peaks on the machined surface increasing the surface integrity. Eventually, high cutting speed during the micro turning operation expedited rapid plastic deformation on the machined surface. The surface roughness was seen to be decreased with increasing the depth of cut. This has been attributed to the similar phenomenon generated due to step tool path. Additionally, the

uncut chip thickness has been increased with increasing the depth of cut as well. This phenomenon reduced the tendency of rubbing and ploughing of the cutting edge on the work surface. As a result, the deformation of the surface has been reduced upto certain extent.

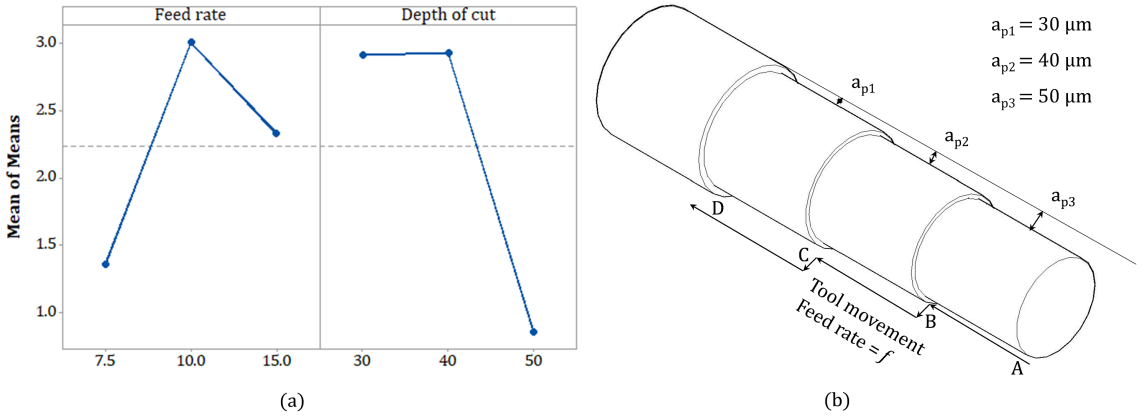

Figure 3.16: (a) Influence of feed rate and depth of cut on average surface roughness determined in the high speed micro turning experiment, (b) Step tool path followed during the experiment

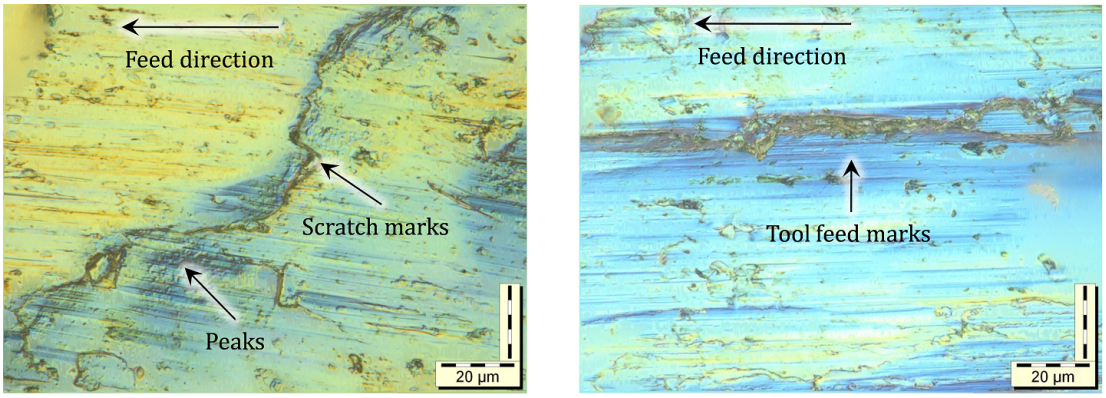

(a) f = 7.5 µm/rev, a_p = 30 µm (Experiment 1) (b) f = 7.5 µm/rev, a_p = 50 µm (Experiment 3)

Figure 3.17: Microscopic view of the machined surface determined in the experiment

Brass exhibits high thermal conductivity. However, the heat generation was quite rapid due to high cutting speed. Moreover, low surface area of the components has resulted in rapid heat accumulation at the chip-tool interface during high speed micro turning. Under dry condition, the samples have been subjected to burning and degradation of the work surface due to this phenomenon. Therefore, the application of coolant has been emphasized for high speed micro turning. The application of cooled air was adaptable for some extent. It restrained the burning and rapid plastic deformation of the work surface. However, promising result was still not achieved. Direct application of minimum quantity lubrication

or cryogenic fluid may reduce the amount of plastic deformation and the surface roughness as well. Additionally, a proper tool path is required to be followed during micro turning to reduce the chip accumulation on the cutting edge. This can be beneficial to improve the surface quality as well.

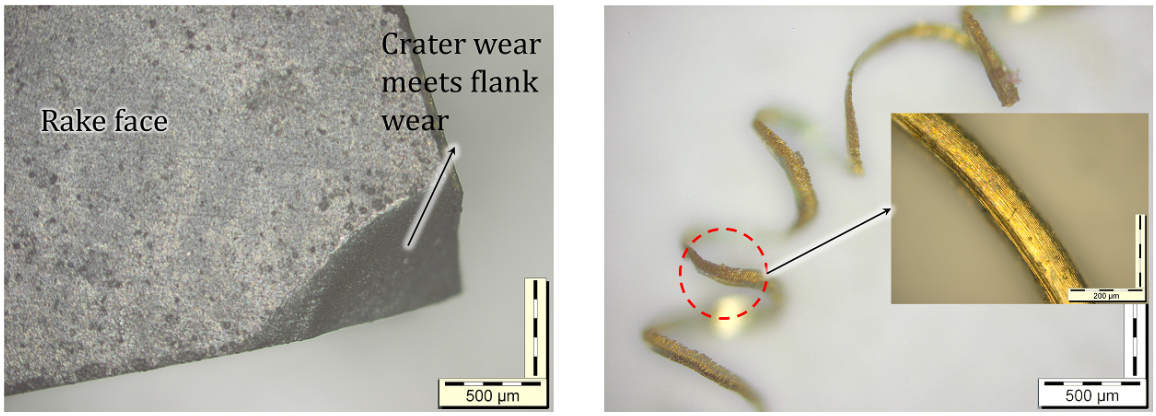

(a) (b)

Figure 3.18: (a) Microscopic image of the cutting tool used for high speed micro turning operation at a feed rate of 15 $\mu m/rev$; (b) Microscopic image of the chip generated at a feed rate of 7.5 $\mu m/rev$ and depth of cut of 50 $\mu m/rev$

Fig. 3.18 (a) represents the the microscopic image of the cutting tool which has been used at feed rate of 15 $\mu m/rev$. It clearly shows rapid amount of tool damage during the cutting operation. The crater wear formed over the rake surface near the tool tip has been propagated and met with the flank wear. It indicates rapid accumulation of the chips near the tool tip causing this type of damage. Further, the chip morphology presented in Fig. 3.18 (b) shows the evidence of longer chip formation which led to the chip accumulation at the tool tip.

3.5 Summary

In this chapter, the development of a dynamically stable high speed micro-machining center is described. For this purpose, a design approach of vibration free machine structure has been presented for the micro-machining center. This design methodology has incorporated the modelling and assembly of the machine structure including material selection. Subsequently, FEM analyses i.e. static structural analysis, modal analysis and harmonic response analysis have been performed to evaluate the static and dynamic performances of the assembled machine structure. Based on the results of FEM analyses, the best model has been selected as vibration free and proposed for manufacturing. The machine structure was made of natural granite which has shown superior dynamic performance as compared

to cast iron. Eventually, experimental frequency response analyses have been performed during mechanical micro-machining to check the similarity with FEM results. The experimental results have shown good similarities with the FEM results in terms of resonant frequencies, amplitude of vibration and natural frequencies. The amplitude of the machine tool vibration was approaching towards the nanometer level during micro-machining operation. In addition. the amplitude was further reduced at higher cutting speed (rotational speed). The amplitude was lesser during machining with four flute milling cutter as compared two flute milling cutter due to lesser chip load. An average surface roughness of 100 nm has been achieved by high speed micro-milling operation with uniform tool feed marks on the machined surface of difficult-to-cut titanium alloy. Hence, the developed machine structure provided good static, dynamic stiffness and damping performance to the overall high-speed micro-machining center. The design approach was applied for vibration isolation without utilizing any vibration absorber.

After successful development of the micro-machining center high speed micro turning has been performed on lead free brass. However, promising result has not been achieved in terms of surface finish due to accumulation of chips on the tool tip and rapid heat generation at the chip-tool interface. Hence, it has opened a research area to utilize proper cooling condition like minimum quantity lubrication or cryogenic cooling to suppress the heat generation at high cutting speed.

4

High speed micro turning of lead free brass using minimum quantity lubrication

Present chapter describes the machinability of miniaturized lead free brass components in high speed micro turning. Machining operations have been performed varying the cutting speed, feed rate, and depth of cut. Minimum quantity lubrication (MQL) has been used for cooling and lubrication purposes. The surface topography, burr formation, chip formation, and the tool wear have been investigated for different process parameters. Additionally, statistical model has been developed to evaluate the contribution of the process parameters on average surface roughness, peak to valley height, and average burr height. Smoother surface finish has been achieved on the lead free brass component at higher cutting speed. The peak-to-valley height and burr height have been reduced as well. Additionally, the chip breaking was quite favorable at high cutting speed. Furthermore, the flank wear has been increased at elevated cutting speed.

4.1 Introduction

Requirement of miniaturization has promoted micro-machining in modern manufacturing. Singh et al. [21] revealed that low surface to volume ratio has promoted the versatile application of the miniaturized components which consequences favorable power consumption

and high heat transfer rate during the fabrication process. Mechanical micromachining processes have been preferred over nonconventional micromachining for their faster material removal capability and applicability to a variety of materials. However, rapid tool wear and tool breakage were the key issues faced during mechanical micromachining. Low stiffness of the micro tool or miniaturized workpiece leads to degradation in the dimensional accuracy in mechanical micromachining. Additionally, Das et al. [224] established the requirement of high speed micromachining technologies due to low material removal rate as well. High speed machining reduces the chip load on the tooltip which is subjected to lesser cutting force as well. Therefore, the deflection of the micro tool or miniaturized workpiece can be restricted in this process. Micro turning is a mechanical micromachining process used to fabricate miniaturized cylindrical components. However, low material removal rate, surface degradation at higher cutting speed, significant tool wear, and enhanced cutting force have restrained the implementation of mechanical micro turning for industrial and research purpose. The material removal rate can be improved incorporating high speed machining with micro turning.

Brass has been used extensively in electrical appliances and other industries due to its elevated thermal and electrical conductivity. In general, the alloys contain copper and zinc with some impurities which include lead. Toulfatzis et al. [225] showed that lead has improved the machinability of brass alloy facilitating favorable chip formation and lower tool wear; and reducing the cutting force as well. However, due to detrimental effect over living creatures and environments, the application of lead has been restricted by United Nations. Therefore, the requirement of lead free brass has been prompted from environmental aspect. However, the machinability has been significantly degraded excluding the lead content. Toulfatzis et al. [226] studied that the chip formation was very unstable for lead free brass due to rapid shear stability in the machining zone which further involved high power consumption during machining. Weak chip breakability has resulted in significant strain hardening of the chip component and plastic side flow of the work material. The power consumption could be somehow reduced by lowering the cutting speed, feed rate, and depth of cut. Schultheiss et al. [227] investigated that higher plasticity of lead free brass led to better surface generation during machining as compared to leaded brass; however, the cutting force was significantly higher for lead free brass due to higher tensile strength, yield strength and hardness. The improvement of the surface quality was attributed to higher ductility and strain hardening of the lead free brass alloy. Besides, this alloy was subjected to longer chips which were difficult to remove. Schultheiss et al. [228] depicted enhancing in machining time and manufacturing cost owing to poor machinability of lead free brass. In view of those critical issues, lead free brass has shown very low applicability in industrial and research purposes. Some researches have been performed in

order to improve the machinability of lead free brass alloys. Imai et al. [229] introduced graphite powder in the brass alloy to improve the machinability. However, the mechanical properties of brass alloys have been deteriorated incorporating the graphite particle. Additionally, heat treatment might be a solution to improve the machinability of lead free brass [230].

The present work determines the machining performance of miniaturized lead free brass component in high speed micro turning. High speed turning and micro turning have been combined to achieve the favorable effects. Machining operations have been performed incorporating four different levels of process parameters (cutting speed, feed rate, and depth of cut). Minimum quantity lubrication (MQL) has been incorporated considering its favorable effects and environmental point of view. The surface topography, burr formation, chip formation, and the tool wear have been investigated.

4.2 Workpiece materials

Amaral et al. [231] disclosed that conventional brass alloys contain 3% lead content which acts as a lubricant during machining reducing the friction between the cutting tool and the workpiece. Nobel et al. [197] studied that lead was insoluble in brass alloy and located in the grain boundaries. It reduced the shear strength of the material facilitating the chip formation. However, higher ductility and strength make the lead free brass alloy a difficult-to-machine material.

The workpiece material was commercially available lead free brass alloy (CW510L). The microstructure of the work material has been studied in FESEM (ZEISS make, model Supra 55) and shown in Fig. 4.1 (a). Additionally, EDS analysis has been performed on the workpiece sample to study the elemental composition of the brass alloy. Fig. 4.1 (b) shows the EDS spectroscopy of the workpiece. The microstructure shows that the brass alloy contains a mix of α and β phase. However, the percentage of α phase is much higher as compared to β phase resulting in higher ductility of the alloy. In general, the lattice structure of the α phase is responsible for low hardness and ductility of the brass alloys. Additionally, Nobel et al. [197] illustrated that the β phase having body-centered cubic (BCC) lattice structure was much harder compared to the α phase (Face-centered cubic lattice structure). The chemical composition of the brass alloy is highly responsible for the formation of α and β phases. The material contains 41% zinc content, and 59% copper content. Higher zinc content (above 39%) of the brass alloy led to higher percentage of β phases in the microstructure as compared to other lead free brass alloys. Toulfatzis et al. [226] investigated that higher hardness of the brass alloy compared to other lead free brass alloy could be attributed to higher β phase fraction in the microstructure of the brass alloy.

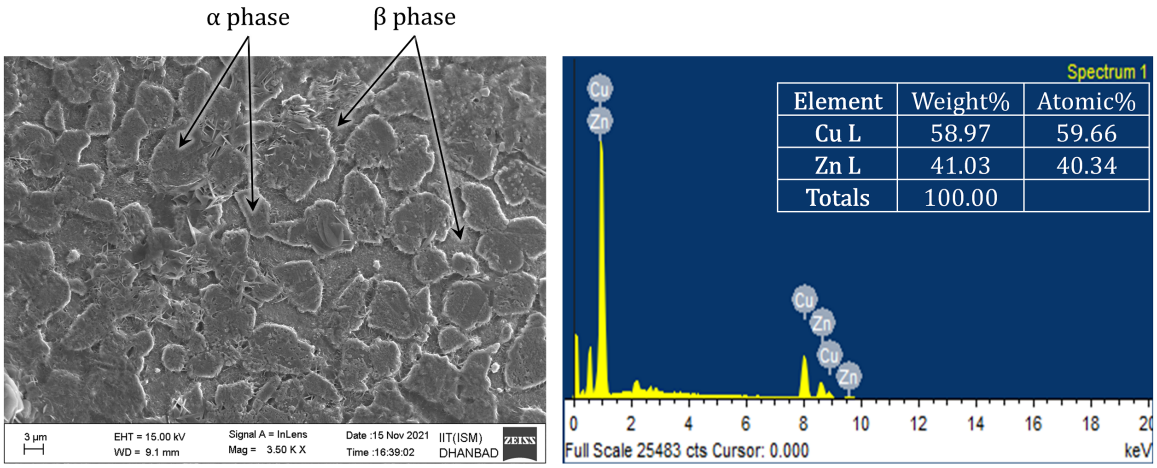

(a) (b)

Figure 4.1: (a) Micro structure of lead free brass; (b) Elementary analysis of the workpiece material

Moreover, existing β phase in the microstructure might result in favorable machinability of the brass alloy compared to other lead free brass alloys due to better chip fragmentation. It facilitates the shear band formation and micro crack generation in the lead free brass alloy [225]. Concurrently, the α phase in the microstructure increases the ductility and strength of the brass alloy. Therefore, increasing the fraction of the α phase enhances the cutting force during machining of the lead free brass alloys [232]. Table 4.1 depicts the mechanical properties of the workpiece material.

Table 4.1: Mechanical properties of the workpiece material (Lead free brass, CW510L)

Tensile strength (MPa)	Yield strength (MPa)	Hardness (HV)	Elongation to break (%)
478	310	136	25

4.3 Experimental procedure

4.3.1 Machining process

The machining experiments have been performed on cylindrical workpieces of lead free brass alloy. The diameter of the each workpiece was 3 mm with 40 mm length. The workpieces have been cut using wire-cut EDM process and turned in a mini lathe machine for final preparation. High speed micro turning operations have been performed in the high speed micromachining center (model V60) which was developed in the micro fabrication

laboratory of Indian Institute of Technology (ISM), Dhanbad. Fig. 4.2 shows the experimental setup for the micro turning experiment. The workpiece has been mounted using a pneumatic collet of the vertical spindle. The clamping length was 28 mm and the cantilever length was 12 mm for each workpiece. All the workpieces have been clamped with equal clamping and cantilever length so that the cantilever effect has not varied. The spindle was attached to the vertical linear stage (Z stage). A toolpost has been mounted on an acrylic container which further attached on the X-Y linear stage. The acrylic container was used to collect the lubricating fluid which was used during the machining operation. Longitudinal feed has been provided to the workpiece by controlling the movement of the Z stage. However, the cross movement (depth of cut) was generated by controlling the movement of the X-Y stage. Sandvik Coromant make TiAlN (PVD) coated cemented carbide inserts (MAFR 3 003 1105) have been used for micro turning operation. The insert contained sharp cutting edge of 5 μm edge radius. In general, negative rake angle reduces the load on the cutting edge of micro cutting tool, while it inflates the consumption of specific cutting energy. Besides, a negative rake angle cutting tool is subjected to longer tool life. In this experiment, the tool has a negative rake angle of -3^o.

The machining experiments have been carried out under minimum quantity lubrication (MQL) condition. This was preferred owing to ecofriendly lubricating condition due to smaller consumption of the hazardous cutting fluid. Additionally, the capability of MQL to reach the machining zone due to higher coolant pressure makes this superior over flood cooling. Moreover, the chips are easily lifted up from the rake surface due to high pressure coolant supply in MQL condition and reduced the chip-tool contact. Therefore, this reduces the accumulation of chips on the tool rake surface, especially during machining of highly ductile materials. Servocut S cutting fluid has been utilized as the base fluid of the lubricant solution. The typical kinematic viscosity of the cutting fluid was 20 cSt (at 40^oC). The cutting fluid has been mixed with distilled water at a ratio of 1:20 (volume percentage) to prepare a milky emulsion. The emulsion was incorporated in the machining operation with a mix of compressed air (pressure 2 bar). The flow rate of the emulsion was 400 ml/hour during the machining operations. The diameter of the nozzle was 0.5 mm. The nozzle was set at angle of 45^o with a standoff distance of 30 mm.

The process parameters have been selected based on the manufacturer's recommendation for the cutting tool. The rotational speed for the experiments have been varied from 10610 rpm to 18568 rpm. Four different levels of cutting speed, feed rate and depth of cut have been selected for the experiment. Taguchi L16 orthogonal array design was utilized to prepare the design of experiment. The machining length in each machining operation was 2.5 mm. Table 4.2 enlists the details of tool geometry and process parameters for the micro turning experiments. Each experiment has been repeated twice to check the repeatability

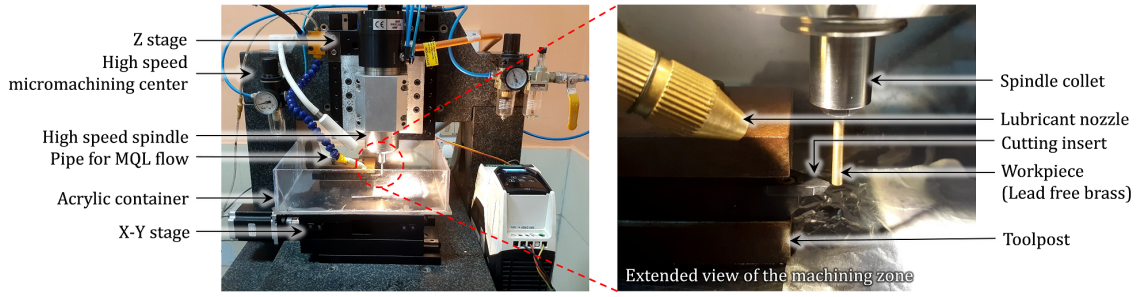

Figure 4.2: Experimental setup for the high speed micro turning operation

of the outcomes.

Table 4.2: Details of the tool geometry and process parameters for high speed micro turning experiment

Constant tool geometry		Variable process parameters				
Parameters	Values	Parameters	Level 1	Level 2	Level 3	Level 4
Side rake angle	-3^o	Cutting speed, V_c (m/min)	100	125	150	175
Back rake angle	3^o	Feed rate, f $(\mu m/rev)$	3	6	9	12
Side relief angle	3^o	Depth of cut, a_p (μm)	30	40	50	60
End relief angle	35^o					
End cutting edge angle	9^o					
Side cutting edge angle	0^o					
Nose radius (μm)	30					

4.3.2 Characterization

The surface topography of the machined sample has been determined in optical profilometer (Zygo make, model Newview 9000). The surface roughness and morphology have been included. Three different areas on each sample across the machining length have been chosen and the surface roughness has been measured on those areas. One measurement has been taken at the starting of the machining length followed by the center and the end of the machining length. 50X magnification has been taken for measuring the optical profilometry. The scanning length was 20 μm in each measurement.

The burr height has been measured from the surface profilometry on each sample determined by optical profilometer. The calculation of burr height is schematically shown in Fig. 4.3 (a). A number of linear slices have been drawn along the feed direction on the surface profile of the workpiece where the burrs have been observed. The peak height (R_p) along each slice has been measured. This was the height of the micro burr extended from the general profile. The linear surface roughness (R_a) along the slice of the profilometry

has been further measured. The difference between the peak height (R_p) and the linear average surface roughness (R_a) along each slice have been depicted as the burr height (B_{hp}). Based on Fig. 4.3 (a), the calculation of burr height can be mathematically represented as Equation 4.1, 4.2.

$$B_{hp_1} = R_{p_1} - R_a \tag{4.1}$$

$$B_{hp_2} = R_{p_2} - R_a \tag{4.2}$$

$$B_{hp} = \frac{(B_{hp_1} + B_{hp_2})}{2} \tag{4.3}$$

Based on the concept, the burr heights have been calculated and the average burr heights have been determined from Equation 4.3. Fig. 4.3 (b) depicts the measurement of burr height from the optical profilometry of the machined surface. The whole measurement procedure has been classified into two steps. The initial step included the identification of the burr. The burrs have been easily identified and distinguished from the arbitrary peaks formed on the surface profile. As burrs have been formed due to the involvement of the cutting tool on the machined surface, a little amount of material got deformed and piled up at the periphery of the tool indentation. Therefore, the propagation of the burrs is perpendicular to the feed direction. The positions of the burr can be identified from the Fig. 4.3 (a) and the burrs can be distinguished based on the position and propagation. The next step of burr measurement included the drawing of the linear slices and the measuring procedure as shown in Fig. 4.3 (b). The linear slices have been drawn in the spaces only where the burrs have been observed. The slice has been drawn as long as possible because the smaller slice has shown higher average surface roughness (R_a) due to strong influence of the burr. On the other way, the average surface roughness (R_a) along the longer slice was not much influenced by the burr height due to considering the average of long surface profiles and approximately same as the areal surface roughness value (S_a). Six measurements of burr height have been taken from each profilometry. Therefore, total number of measurements was eighteen from each machined surface and their average has been estimated. It is clear from the Fig. 4.3 (b) how the burrs have been distinguished from the arbitrary peaks and burrs have been calculated.

Additionally, the tool wear has been investigated in optical microscope (Olympus made, model BX51M). The microscopic images of flank wear on the turning inserts along with unworn one have been captured and analyzed. 50X magnification has been used to take the optical images of tool wear. Eventually, the chip formation and morphology have been studied in the optical microscope using 20X magnification. The data of the machined

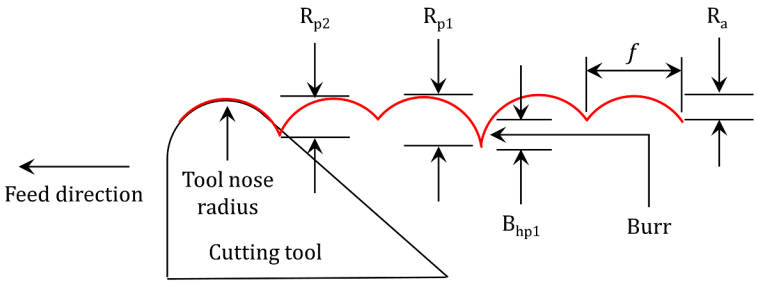

(a)

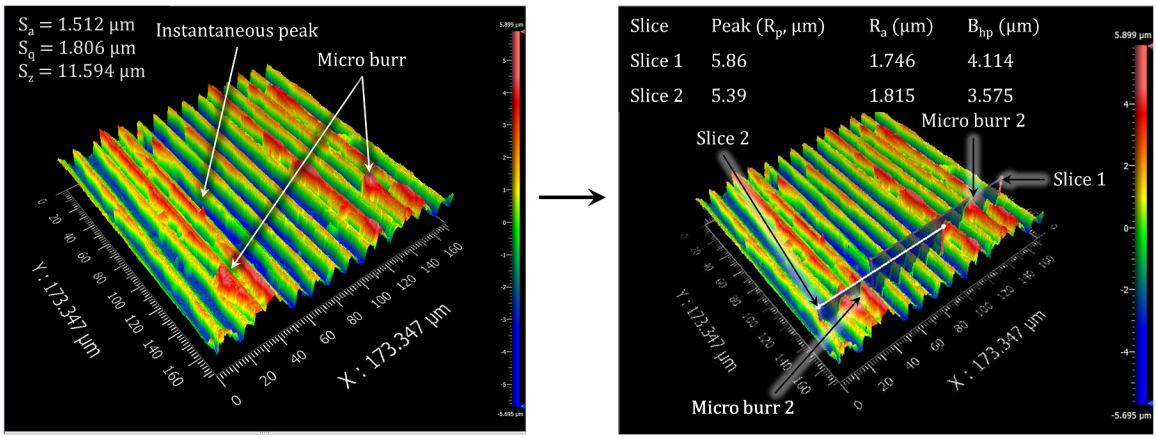

Step 1 Step 2

(b)

Figure 4.3: (a) Schematic diagram of calculating the burr heights from the turned surface profile; (b) Measurement of burr height from the optical profilometry

surface roughness, peak to valley height and average burr height have been analyzed in Minitab 17 software to determine the influence of the process parameters. Subsequently, Analysis of Variance (ANOVA) has been performed for parametric contribution and optimization. Eventually, the regression equations have been developed in Minitab.

4.4 Results and discussions

4.4.1 Surface topography

The surface finish is one of the most desirable quality characteristics in precision machining process. In this study, the optical profilometry of surface topography of the lead free brass samples have been determined after high speed micro turning. Due to higher plasticity of lead free brass, plastic side flow is quite significant in the surface generation during high speed micro turning. The theoretical surface roughness in precision turning can be estimated by Equation 4.4 and 4.5 developed by Grzesik [233], considering the elastic

recovery of the workpiece material.

$$R_t = \frac{5f^2}{8r_n} + \frac{h_{min}}{2}\left(\frac{r_n h_{min}}{f^2} - 1\right), f > \sqrt{r_n h_{min}} \tag{4.4}$$

$$R_t = \frac{4f^2}{8r_n} + \frac{h_{min}}{2}\left(\frac{r_n h_{min}}{4f^2} + 1\right), f \leq \sqrt{r_n h_{min}} \tag{4.5}$$

Here, f denotes the feed rate; and r_n and h_{min} denote the tool nose radius and minimum uncut chip thickness respectively. Fig. 4.4 (a) represents the incorporation of uncut chip thickness (h) and minimum uncut chip thickness (h_{min}) in the machining process which further depends on the cutting edge radius (r_e). V_c represents the cutting speed in the machining operation. Malekian et al. [234] developed a theoretical model to calculate the minimum uncut chip thickness as shown by Equation 4.6.

$$h_{min} = r_e(1 - cos\theta_m) \tag{4.6}$$

θ_m is the stagnation angle which has been represented in Fig. 4.4 (a). Malekian et al. [234] determined that the stagnation angle depends on either friction angle ($\theta_m = \beta_s$); or effective rake angle $\left(\theta_m = \frac{\pi}{2} - \alpha_e\right)$. β_s and α_e define the friction angle and effective rake angle respectively. Moreover, the friction angle (β_s) is influenced by cutting force (F_c) and thrust force (F_t) as the Equation 4.7.

$$\beta_s = \alpha + tan^{-1}\frac{F_c}{F_t} \tag{4.7}$$

It is clear from Equation 4.7 that the friction angle increases when the cutting force increases and subsequently, the minimum uncut chip thickness increases. Eventually, the machined surface roughness enhances as a function of the minimum uncut chip thickness. Hence, the cutting force directly influences the machined surface roughness. Fig. 4.4 (b) represents the formation of machined surface profile with the effect of different process parameters. Here, a_p defines the depth of cut and ϕ indicates the principal cutting edge angle.

The surface roughness has been evaluated in terms of areal surface roughness parameters. The surface roughness data i.e. the mean arithmetic surface roughness (S_a), and maximum peak to valley height (S_z) are enlisted in Table 4.3 for each experiment. It shows that the best quality surface has been found for experiment 5 (cutting speed = 125 m/min, feed rate = 3 $\mu m/rev$, depth of cut = 40 μm) where the mean area surface roughness (S_a) was 281 nm. The variation of mean surface roughness (S_a) was found from 281 nm (experiment 5) to 1.572 μm (experiment 4). The maximum peak to valley height (S_z) is much higher for all cases. This has been generated due to rapid plastic side flow of workpiece

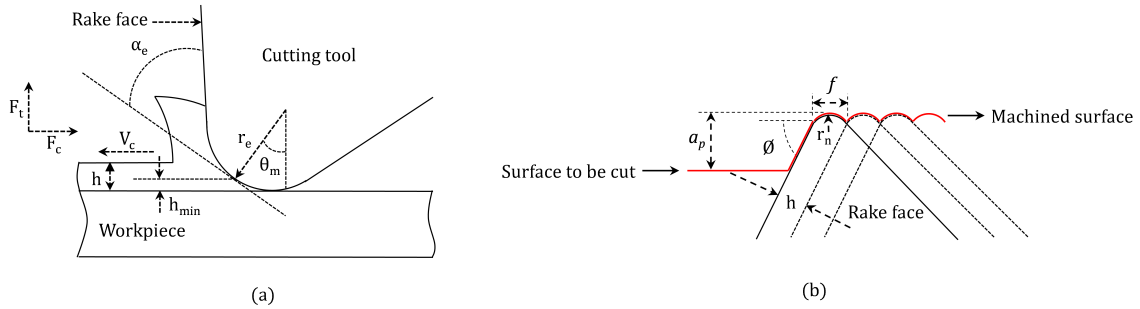

Figure 4.4: (a) Machining considering cutting edge radius and uncut chip thickness; (b) The cutting layers to form the machined surface

material during machining. This is the evidence of higher plasticity of lead free brass. A significant change in surface roughness over the machining length due to cantilever effect has not been observed. This was attributed to small machining length. The data of the average surface roughness (S_a) and peak to valley height (S_z) have been plotted in minitab 17 and the variations with the process parameters have been determined using Taguchi analysis.

Fig. 4.5 represents the SN ratio response plot for mean surface roughness (S_a) for different process parameters using Taguchi method. Fig. 4.6 depicts the analysis of the SN ratio response for maximum peak to valley height (S_z) with the process parameters based on Taguchi method. "Smaller is better" condition has been used for both the output parameters as the responses was expected to be minimized in both cases. In this condition, the higher value of the SN ratio indicates the lower value of the output response. Fig. 4.7 represents the surface profilometries of the machined surfaces achieved at a cutting speed of 125 m/min. Fig. 4.8 represents the surface profilometries of the machined surface achieved at constant feed rate (12 $\mu m/rev$) varying the cutting speed and depth of cut. Fig. 4.9 shows the FESEM images of the surface topography on lead free brass samples achieved at different process parameters.

It is clear from Fig. 4.5 that the mean surface roughness has been reduced rapidly when the cutting speed has been increased from 100 m/min to 125 m/min. As the cutting speed increased, the shear velocity has been increased as well which resulted in higher strain rate on the machining zone. Subsequently, the work hardening of the material has been occurred which reduced the level of shear deformation and plastic flow of material upto certain extent. In addition, the reduction in cutting force and frictional force has generated smaller friction angle as described in Equation 4.7. Consequently, the uncut chip thickness has become smaller at higher cutting speed (based on Equation 4.6). Therefore, the average surface roughness (S_a) has been reduced based on Equation 4.4 and 4.5. However, the mean surface roughness further increased when the cutting speed has been increased from

Table 4.3: The average surface roughness and maximum peak to valley height determined in experiment

Experiment	Cutting speed	Feed rate	Depth of cut	Average surface roughness (S_a)			Peak to valley height (S_z)		
No.	(m/min)	$(\mu m/rev)$	(μm)	Value 1	Value 2	Value 3	Value 1	Value 2	Value 3
1	100	3	30	0.699	0.647	0.653	9.063	9.932	10.589
2	100	6	40	0.645	0.701	0.842	10.688	11.613	11.524
3	100	9	50	0.87	0.847	0.892	8.834	9.29	13.835
4	100	12	60	1.512	1.572	1.568	11.594	12.023	17.071
5	125	3	40	0.281	0.305	0.295	6.121	3.797	3.491
6	125	6	30	0.331	0.341	0.322	2.907	2.924	3.269
7	125	9	60	0.389	0.429	0.43	4.821	4.725	4.145
8	125	12	50	0.556	0.519	0.532	6.54	4.613	4.668
9	150	3	50	0.778	0.734	0.742	6.602	6.661	7.554
10	150	6	60	1.117	1.164	1.195	6.865	11.544	11.929
11	150	9	30	0.766	0.737	0.727	10.804	7.4	10.822
12	150	12	40	0.697	0.701	0.695	8.061	9.178	7.736
13	175	3	60	0.531	0.544	0.535	4.477	6.509	4.343
14	175	6	50	0.354	0.38	0.371	2.921	4.637	4.175
15	175	9	40	0.385	0.39	0.405	4.032	4.024	4.653
16	175	12	30	0.535	0.538	0.544	5.421	6.135	8.876

125 m/min to 150 m/min. This is due to resonant condition of the machine tool with the spindle rotational speed as determined by previous experiments [224]. The corresponding spindle rotational speed was 15915 rpm which was equivalent to 265 Hz. This was very close to the resonant frequency (250 Hz) at which the vibration amplitude was maximum as shown in Fig. 3.11 and Fig. 3.12 in the previous chapter (Chapter 3). Hence, it is obvious that resonance has been taken place between the working spindle and the machine tool which induced some tool-work relative vibration. Consequently, a little amount of chatter has been developed. Therefore, the tool path has been deviated from its original position leading to deviated feed marks which resulted in the degradation of surface profile. The mean surface roughness further reduced when the cutting speed has been increased to 175 m/min. The influence of built-up edge (BUE) formation was negligible in this case as no significant trace of BUE has been observed on the cutting tool. It is obvious from previous findings [235] that the shear angle has been increased at higher cutting speed causing lesser cutting force and frictional force in the tool-work interface. Low friction at the tool-work interface has reduced the extent of plastic deformation on the machined surface leading to better finishing. Fig. 4.9 (b) shows the extent of plastic damage has been reduced as compared to Fig. 4.9 (a) as the cutting speed has been increased to 125 m/min to 175 m/min at similar feed rate. The plastic deformation induced in Fig. 4.9 (b) was governed by higher depth of cut.

Similar trend has been observed for peak to valley height as well. The peak to valley height (S_z) was mostly influenced by the plastic deformation of the machined surface. Due to rapid plasticity of lead free brass, the indentation of the cutting tool into the workpiece caused material pile up along the machined surface. Fig. 4.9 clearly indicates the material pile up over the machined surface. Therefore, instantaneous peaks have been observed on the machined surface. The tendency of burr formation has been observed as well on the machined surface which further enhanced the average peak height. Besides, the formation of pits and breaches like defects has originated deeper valleys on the machined surface. This has been attributed to chatter formation, depreciation of the lubricating interface, and the chemical affinity of the work material towards the cutting tool as well. The microscopic images of the tool wear clearly shows the sticking of the work material on the tool flank surface due to chemical affection. Owing to this phenomenon, overall peak to valley height has been increased. At higher cutting speed, the extent of plastic side flow slightly reduced. Additionally, the tool vibration at the cutting speed of 150 m/min caused fluctuation of cutting force and higher plastic deformation as well. This further led to enhancement in the peak to valley height.

A good quality surface has been observed on the machined samples of lead free brass in the high speed micro turning operation. The smaller workpieces possessed very low heat

dissipation area which subjected to higher heat generation at the chip-tool interface. The high speed micro turning operation could not be performed at dry condition due to rapid burning of the workpiece. This led to damage of the workpiece and the machine tool as well. However, the application of minimum quantity lubrication (MQL) has enabled the removal of cutting heat in an efficient manner. An improvement of 84% in the average surface roughness for CW510L lead free brass alloy [225] and 12% for silicon based lead free brass alloy [227] has been observed as compared to the previous researches. In addition, it was evident that the chips formed have been removed easily by the MQL flow due to high pressure coolant supply. Therefore, the chip accumulation on the tool rake surface which was evidenced in the preliminary experiments (discussed in Chapter 3) has been restrained in this case. Additionally, the improvements in surface finish with less amount of plastic damage on the machined surface confirmed that the application of MQL provided better lubricating interface which reduced the friction at the chip-tool interface as compared to preliminary experiments (Chapter 3) where dry environment has been used with cooled air as the coolant.

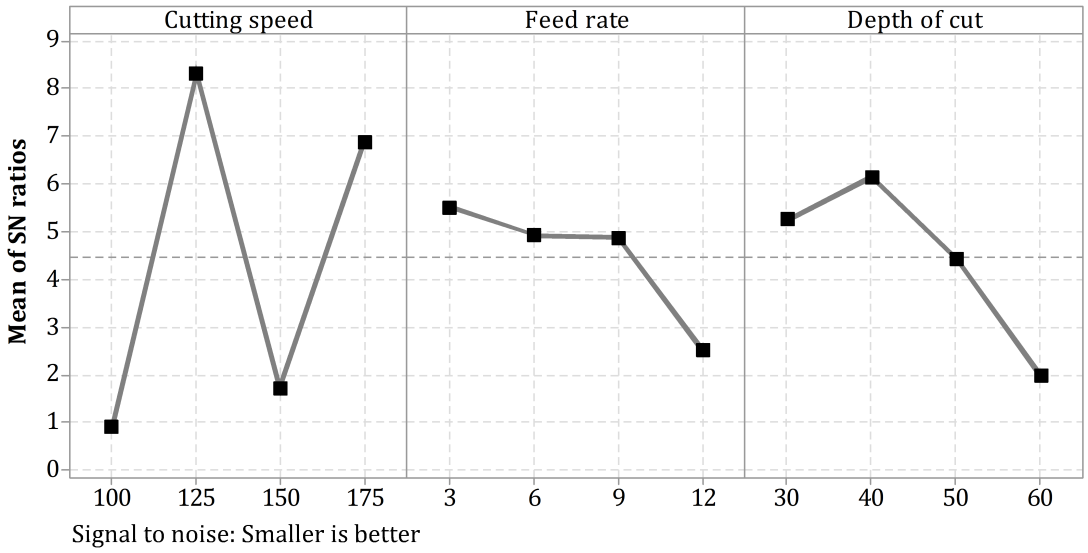

Figure 4.5: Analysis of mean plot for SN ratios for average surface roughness (S_a) for lead free brass

It is shown in Fig. 4.5 that the mean surface roughness (S_a) has been increased with increasing the feed rate. This has followed the general trend as the surface roughness is theoretically proportional to the square of the feed rate. As the feed rate increased, the friction between the cutting tool and the workpiece increased. However, substantial enhancement of mean surface roughness with feed rate was not observed upto 9 $\mu m/rev$. After that, the increment of mean surface roughness was quite rapid. It can be explained by the fact that

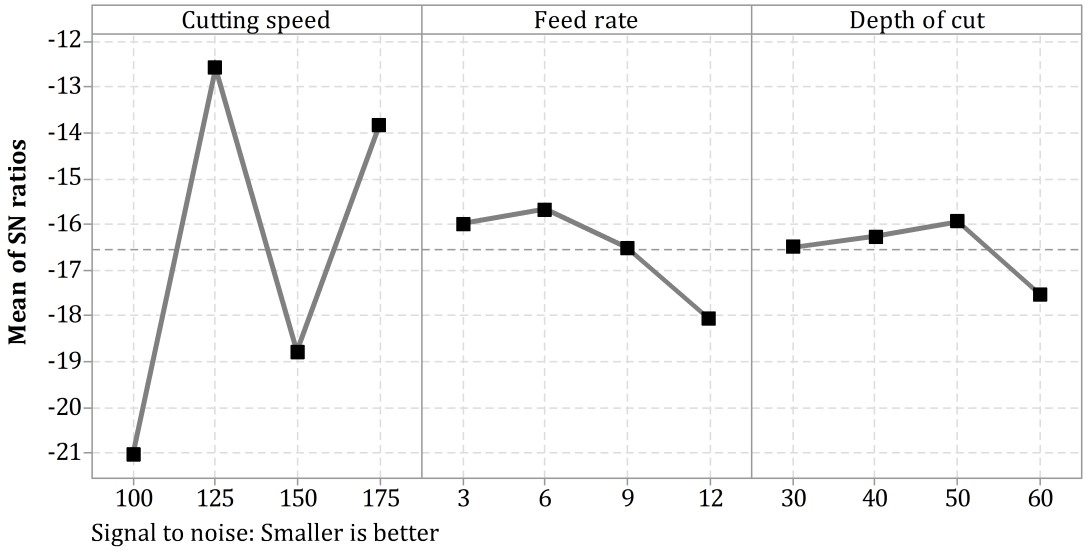

Figure 4.6: Analysis of mean plot for SN ratios for maximum peak to valley height (S_z) for lead free brass

the uncut chip thickness is directly proportional to the feed rate ($h = f sin\phi$). Therefore, the ratio of uncut chip thickness to the cutting edge radius becomes significantly high at higher feed rate. As a result, the stress in the primary shear zone increases. Subsequently, the elastic recovery and the material pile up increase during machining at very high feed rate considering higher ductility of workpiece material. Additionally, the lubricant may not have enough time to reach at the tool-work interface at higher feed rate and unable to create proper lubricating interface. Eventually, the frictional force increases rapidly. This may result in rapid growth of surface roughness as well. However, slightly different trend has been observed for the peak to valley height (S_z) with the feed rate as shown in Fig. 4.6. The peak to valley height initially decreased when the feed rate changes from 3 $\mu m/rev$ to 6 $\mu m/rev$. After that, this increased with feed rate. At lower feed rate (3 $\mu m/rev$), the effective rake angle became largely negative as calculated from Equation 4.5 discussed by Wu et al. [4].

$$\alpha_e = -sin^{-1}\left(1 - \frac{h}{r_e}\right) \tag{4.8}$$

For that reason, the required specific cutting energy was much higher. This enabled a certain amount of workpiece material ploughed over the machined surface. Consequently, the plastic side flow increased at lower feed rate which increased the peak height of the machined surface. Fig. 4.7 (a) clearly shows the effect of ploughing at lower feed rate. FESEM images presented in Fig. 4.9 confirmed the material pile up due to ploughing effect as well at lower feed rate (3 $\mu m/rev$). Significant plastic deformation in the near surface layer has been observed. Subsequently, clear material pile up has been occurred

evolving increased surface height from the original profile. When the feed rate changed from 3 $\mu m/rev$ to 6 $\mu m/rev$, shearing occurred rather than ploughing. This reduced the formation of peaks on the machined surface. Fig. 4.9 (c) clearly indicates the material pile up has been reduced significantly at the feed rate of 6 $\mu m/rev$ as compared to Fig. 4.9 (a) (which has been generated at 3 $\mu m/rev$) at similar cutting speed. When the feed rate further increased, rapid friction enabled higher amount of plastic deformation on the work material. This phenomenon led to formation of peaks on machined surface and increase in the S_z value.

Furthermore, the mean surface roughness (S_a) has been initially reduced (30 μm to 40 μm) and then increased rapidly with increasing the depth of cut (40 μm to 60 μm) as shown in Fig. 4.5. At lower depth of cut, ploughing over the machined surface was dominant over shearing. The best result has been obtained at depth of cut of 40 μm. As the depth of cut further increased, the involvement of the cutting tool into the workpiece material increased. Consequently, the cutting force and friction were enhanced. This phenomenon results in rapid heat generation at the chip-tool interface and more deposition of the workpiece material on the tool rake face due to plastic flow. Additionally, higher depth of cut leads to chatter formation which deteriorates the machined surface quality as well. Fig. 4.6 shows the peak to valley height has been reduced slowly with increasing the depth of cut upto 50 μm. It indicates favorable shearing has been occurred at higher depth of cut. This reduced the tendency of plastic deformation. Therefore, lower S_z value has been appeared at higher depth of cut. When the depth of cut increased beyond 50 μm, the plastic side flow has become higher due to higher indentation of the cutting tool into the workpiece. This resulted in slightly larger peak formation on the machined surface. Meanwhile, deeper grooves have been generated due to higher indentation as well at higher depth of cut. It is evident from Fig. 4.7 (c) and Fig. 4.8 (a) that the formation of deeper valley was significant at higher depth of cut. Subsequently, the S_z value has been increased.

Fig. 4.7 shows clear turning profile on the machine surface. The 2D surface profile clearly indicates precise replication of the tool feed over the machined surface which confirms the accuracy of the machine tool. However, the best quality surface has been seen in Fig. 4.7 (a) achieved at a feed rate of 3 $\mu m/rev$ and depth of cut of 40 μm. The surface profiles show some peaks and burrs on the machined surface of the lead free brass material. Higher plasticity of the lead free brass material accelerates the plastic flow on the machined surface and ameliorates the formation of peaks. Larger peaks have been observed at higher feed rate and depth of cut as shown in Fig. 4.7. Fig. 4.8 shows clear turning profile on the machined surface at the cutting speed of 100 m/min, 125 m/min and 175 m/min. However, the surface profile is slightly deviated from its original profile at the cutting speed of 150 m/min as shown in Fig. 4.8 (c). It indicates tool-work relative vibration during ma-

chining. Additionally, some pits and breaches like surface defects have been observed on the machined surface at this cutting speed which can be seen in Fig. 4.8 (c). Terabayashi and Yan [236] investigated that chatter developed microscale grain deformation leading to boundary step formation on the machined surface. The grains dislocations become more prominent at elevated temperature and some amount of grains or materials pulled out from the machined surface forming pit defects on the surface. Additionally, the deterioration of the lubricating interface at higher cutting speed attributed to some amount of the work-piece material adhered to the cutting tool and removed from the machined surface forming pits like defects. Fig. 4.9 shows the FESEM images of machined surfaces showing burr formation, material pile up, formation of peaks and valleys.

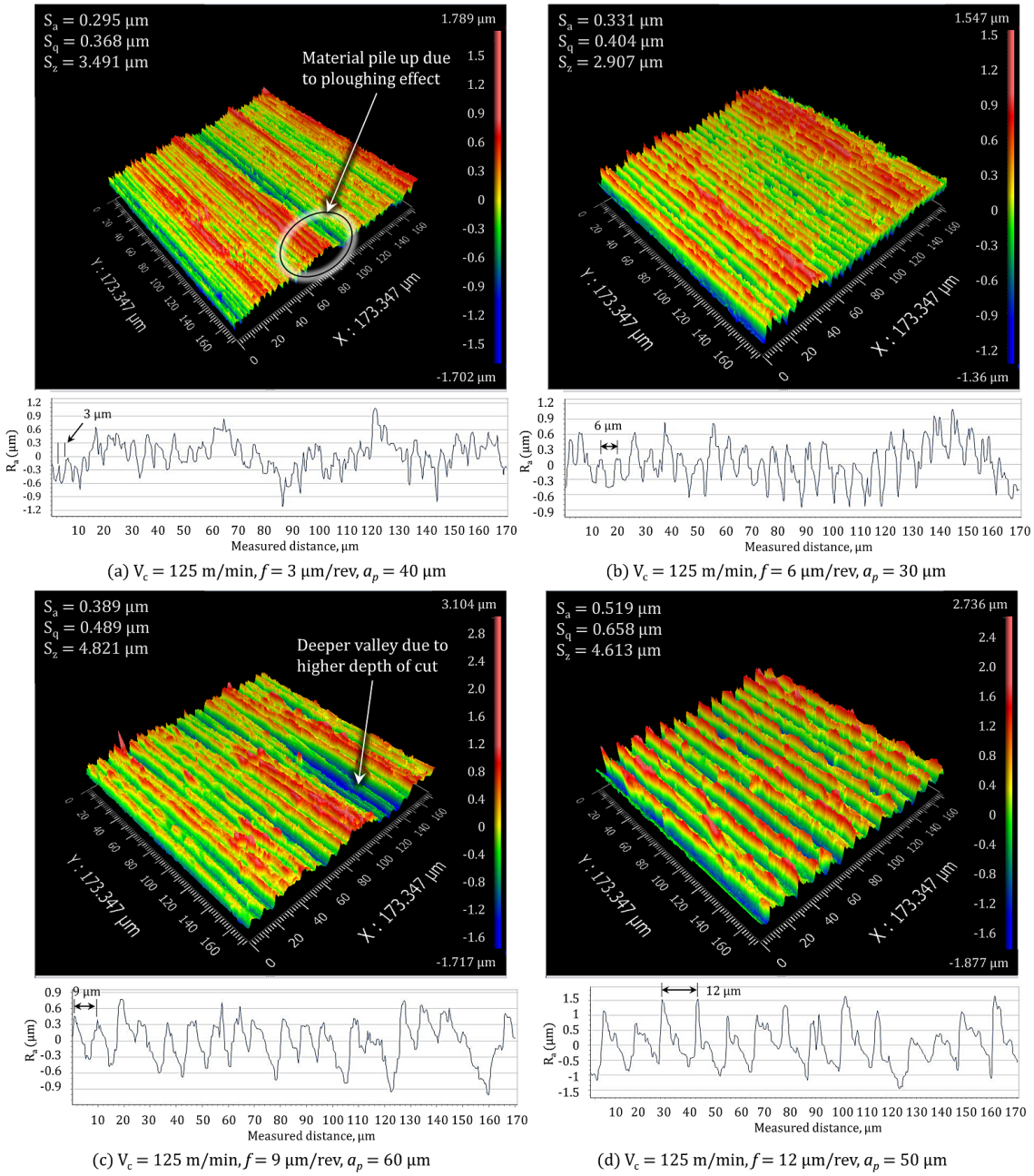

(a) $V_c = 125$ m/min, $f = 3$ µm/rev, $a_p = 40$ µm

(b) $V_c = 125$ m/min, $f = 6$ µm/rev, $a_p = 30$ µm

(c) $V_c = 125$ m/min, $f = 9$ µm/rev, $a_p = 60$ µm

(d) $V_c = 125$ m/min, $f = 12$ µm/rev, $a_p = 50$ µm

Figure 4.7: Surface profilometries on lead free brass samples obtained at cutting speed of 125 m/min

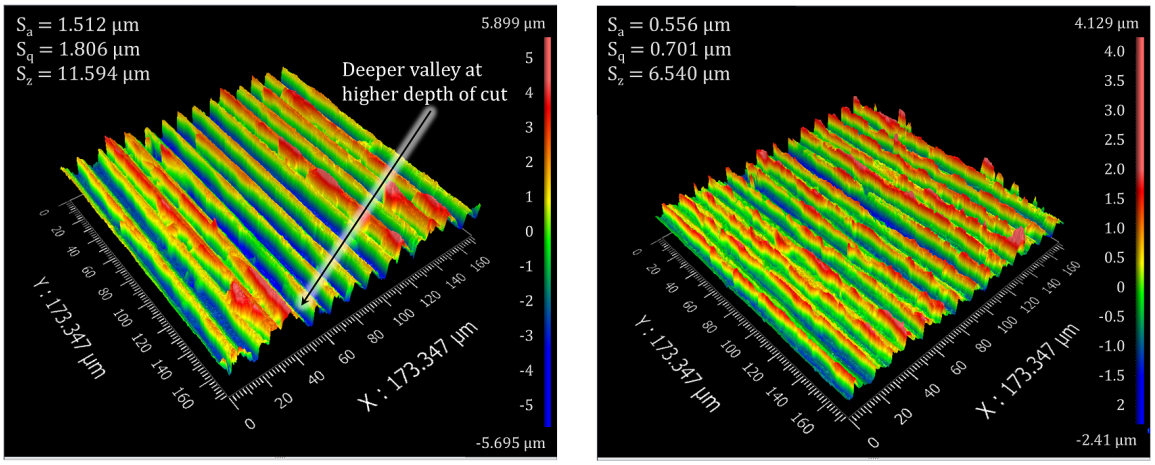

(a) $V_c = 100$ m/min, $f = 12$ µm/rev, $a_p = 60$ µm

(b) $V_c = 125$ m/min, $f = 12$ µm/rev, $a_p = 50$ µm

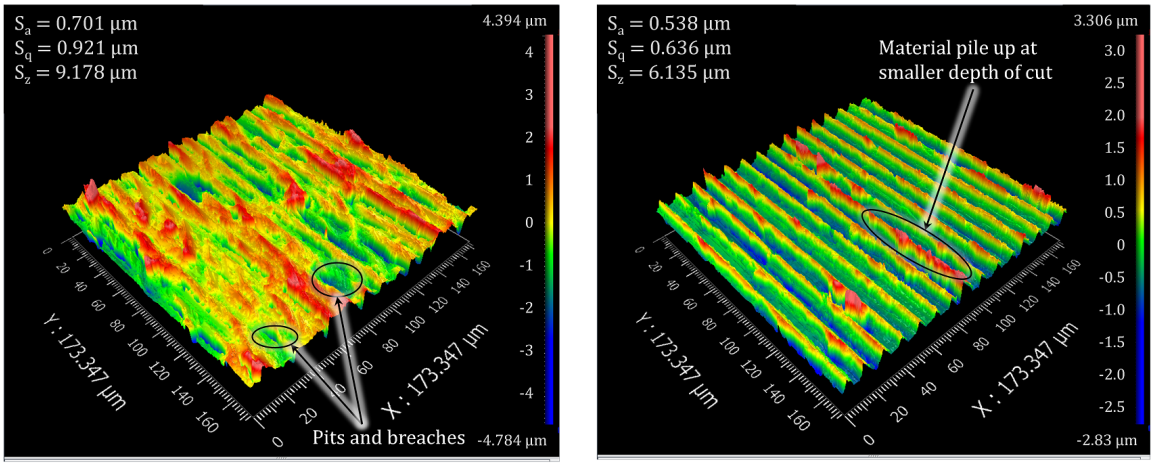

(c) $V_c = 150$ m/min, $f = 12$ µm/rev, $a_p = 40$ µm

(d) $V_c = 175$ m/min, $f = 12$ µm/rev, $a_p = 30$ µm

Figure 4.8: Surface profilometries on lead free brass samples achieved at a constant feed rate (12 $\mu m/rev$) varying cutting speed and depth of cut

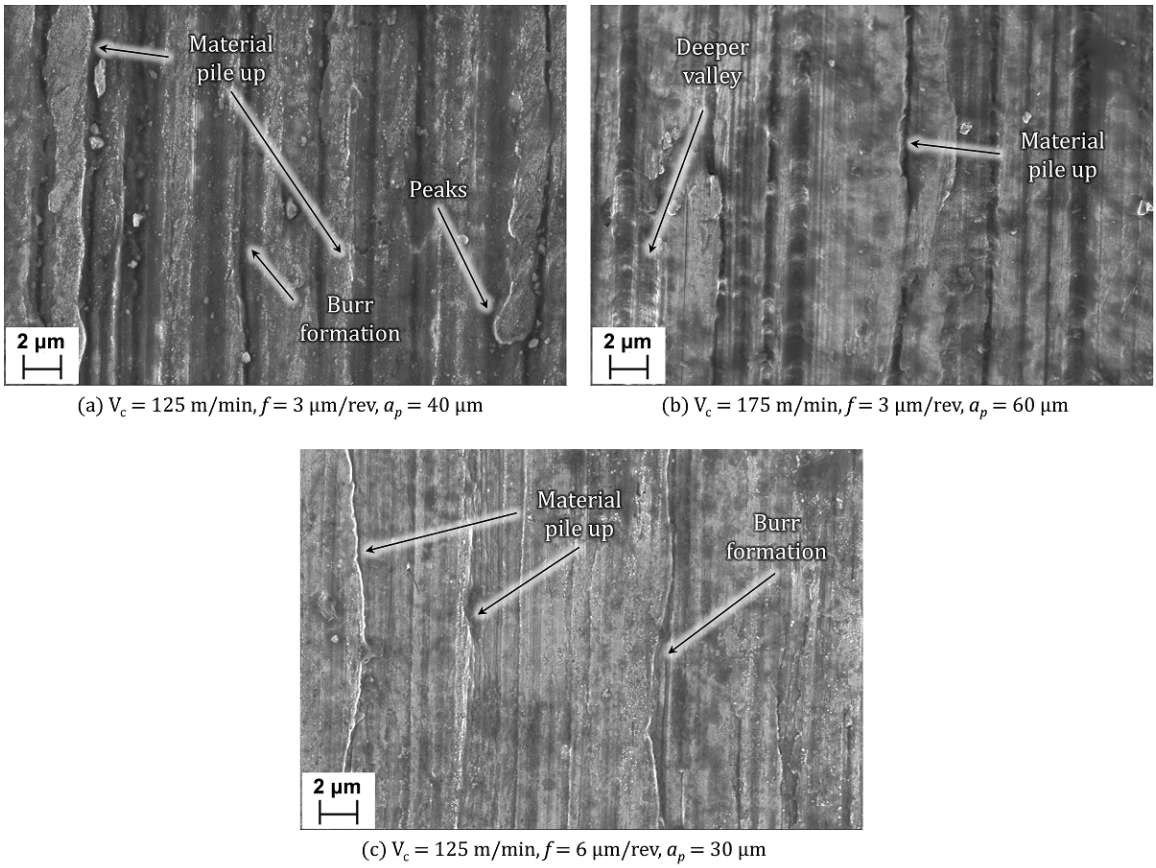

(a) $V_c = 125$ m/min, $f = 3$ µm/rev, $a_p = 40$ µm

(b) $V_c = 175$ m/min, $f = 3$ µm/rev, $a_p = 60$ µm

(c) $V_c = 125$ m/min, $f = 6$ µm/rev, $a_p = 30$ µm

Figure 4.9: FESEM images of the surface topography on lead free brass samples achieved at different process parameters

4.4.2 Burr formation on the machined surface

Burr formation is a challenging aspect in micromachining process especially for ductile materials. The burrs are commonly focused as exit burrs in most of the studies on turning operation. For example, Pang et al. [237] studied the Poisson exit burr formation on highly ductile copper based on cutting force model. However, the burrs on the machined surface are more detrimental as it directly increases the surface roughness. Additionally, these burrs are difficult to remove. The cutting insert exerted some compressive force on the workpiece material which enabled lateral plastic deformation of the workpiece. This led to lateral plastic side flow of the workpiece material as a form of micro burrs, specifically Poisson burrs. The micro burrs have been analyzed from the optical profilometry of the turned surface profile. Fig. 4.10 shows the micro burrs at different surface profiles obtained at different process parameters during the micro turning experiments. Some instantaneous small or large burr formation have been observed on each machined surface. Fig. 4.10 (a) shows significant burr formation at lowest cutting speed, feed rate, and depth of cut. As the feed rate and depth of cut has been increased, the tendency of burr formation initially

slightly reduced as shown in Fig. 4.10 (b). However, the tendency of burr formation has become higher on further increasing the feed rate and depth of cut at similar cutting speed as shown in Fig. 4.10 (c). Some scattered burrs have been found in Fig. 4.10 (b), while the formation of burrs was uniform in Fig. 4.10 (c). Additionally, the heights of the peaks have been found larger in Fig. 4.10 (c). Eventually, the average surface roughness (S_a) values have strongly agreed with the variation of burr height. The burr formation has been reduced by increasing the cutting speed as shown in Fig. 4.10 (d). The burr sizes were smaller in this surface as well.

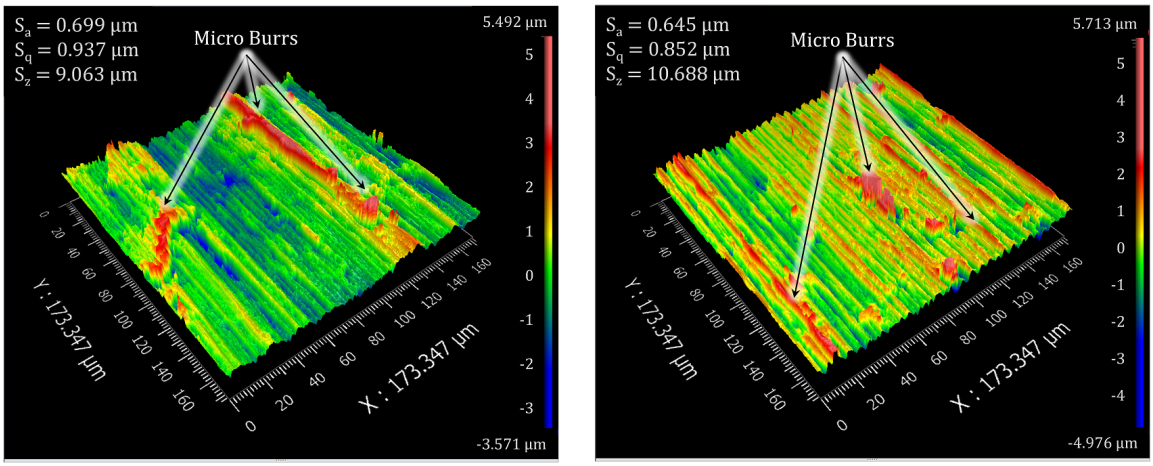

(a) $V_c = 100$ m/min, $f = 3$ µm/rev, $a_p = 30$ µm

(b) $V_c = 100$ m/min, $f = 6$ µm/rev, $a_p = 40$ µm

(c) $V_c = 100$ m/min, $f = 9$ µm/rev, $a_p = 50$ µm

(d) $V_c = 175$ m/min, $f = 6$ µm/rev, $a_p = 50$ µm

Figure 4.10: Micro burr formation on machined surface at different process parameters

Table 4.4 represents the absolute values of the burr height in each experiment calculated from the described phenomenon. Fig. 4.11 represents the variation of average burr heights with the process parameters determined by Taguchi method. In this case, "Smaller is better" condition has been used to minimize the average burr height. Hence, the higher value of the SN ratio indicates the lower value of average burr height. It is clear that the burr height is maximum at lowest cutting speed (100 m/min) and reduces on increasing the cutting speed.

The burr formation on the machined surface was mostly governed by plastic deformation, and material pile up due to plastic side flow. Kumar and Bajpai [62] showed that higher plastic strain and lower uncut chip thickness restrained the tendency of plastic deformation and reduced burr formation at higher cutting speed. Additionally, the micro burrs become uniform at a cutting speed of 125 m/min. However, it has been observed that the burr height further increased at 150 m/min. This speed corresponds to the resonant frequency of the machine tool with the working spindle originating cutting vibration. Hence, the exerted compressive force has been fluctuated due to tool vibration resulting in lateral plastic deformation of the workpiece material. Therefore, sudden peak like burrs have been formed at this cutting speed. The burr height further reduced when the cutting speed was increased to 175 m/min. Fig. 4.9 (a) shows higher tendency of plastic deformation on the machined surface at lower cutting speed as compared to the surface shown in Fig. 4.9 (b) generated at higher cutting speed.

Meanwhile, the average burr height initially decreases and then increases rapidly with increasing the feed rate. At low feed rate (3 $\mu m/rev$), ploughing of the cutting tool is significant on the machined surface. The chance of ploughing has been reduced at the feed rate of 6 $\mu m/rev$ which allows favorable material flow on the work surface reducing the burr height. Fig. 4.9 (a) clearly shows that the material pile up due to ploughing effect was significant at low feed rate (3 $\mu m/rev$) which facilitated the burr formation. However, the tendency of material pile up and burr formation has been reduced at higher feed rate (6 $\mu m/rev$) at similar cutting speed as shown in Fig. 4.9 (c). Further increase in feed rate resulted in enhanced uncut chip thickness. This led to enhancement of cutting force leading to high plastic side flow on the workpiece surface. Eventually, the burr height has been increased at higher feed rate. Similar phenomenon has been observed by Struzikiewicz et al. [238] during turning of aluminium, silicon and magnesium based sintered alloy. Additionally, the average burr height has been reduced initially and then increased on increasing the depth of cut. At the lowest depth of cut (30 μm), ploughing is dominant on machined rather than shearing. The tendency has been reduced on increasing the depth of cut to 40 μm. Further increase in depth of cut leads to larger volume involvement of the cutting tool evolving higher compressive force on the workpiece. Due to small sizes of workpiece, the material has very low area to restrain the deformation causing larger burrs.

Table 4.4: Absolute values of the burr height determined in each experiment

Experiment No.	Average burr height (μm)			Experiment No.	Average burr height (μm)		
	Value 1	Value 2	Value 3		Value 1	Value 2	Value 3
Experiment No. 1	2.128	2.396	1.922	Experiment No. 9	2.293	2.349	2.385
Experiment No. 2	2.139	1.912	2.361	Experiment No. 10	1.615	1.929	1.776
Experiment No. 3	2.191	2.397	2.167	Experiment No. 11	2.3	2.554	2.461
Experiment No. 4	3.097	3.556	3.682	Experiment No. 12	2.67	2.506	2.752
Experiment No. 5	0.759	0.764	0.667	Experiment No. 13	1.342	1.301	1.409
Experiment No. 6	0.849	0.88	0.779	Experiment No. 14	0.996	0.83	0.93
Experiment No. 7	1.172	1.158	1.452	Experiment No. 15	1.225	1.343	1.348
Experiment No. 8	1.568	1.757	1.863	Experiment No. 16	1.998	2.107	2.156

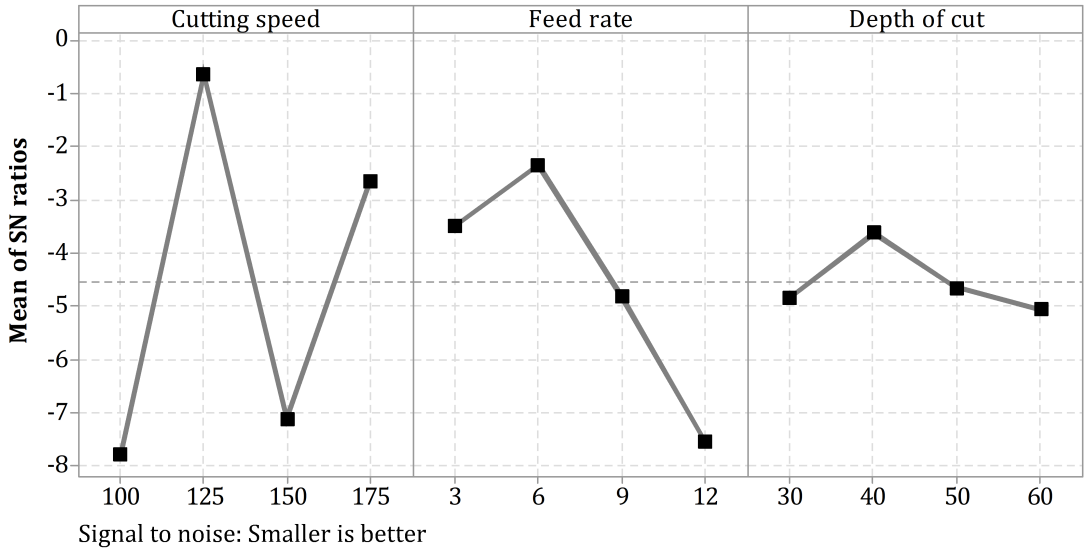

Figure 4.11: Analysis of mean plot for SN ratios for average burr height for lead free brass

4.4.3 Chip morphology

The chip formation is another influencing parameter to assess the machinability of lead free brass. The disappearance of lead content in the brass alloy increased the shear strength of the workpiece material and enhanced the ductility. Due to high ductility of lead free brass, the chip breakage was not much favorable. However, the presence of β phase in the microstructure facilitated the chip formation upto some extent. The shapes, sizes and the types of the chips have been varied depending on the process parameters. Fig. 4.12 represents some distinguished forms of the chips generated at different process parameters in the high speed micro turning experiments.

Table 4.5 depicts different types of chip formation observed in the high speed micro turning of lead free brass. It can be seen that longer chips have been formed at lower cutting speed. Laakso et al. [239] determined the dominance of thermal softening at lower cutting speed due to elevated temperature which further increased the ductility of the lead free brass. Additionally, strain hardening is dominant at higher cutting speed due to rapid strain rate. Therefore, the brittleness slightly increased and shorter chips have been formed at elevated cutting speed. Similar phenomenon has been observed by Laakso et al. [239]. It can be seen from Fig. 4.12 that the chips contain serrated edge at lower cutting speed. This is influenced by the dominance of thermal softening as well. Due to small workpiece, the heat dissipation area is quite lower which accelerates the thermal softening irrespective of higher thermal conductivity of the lead free brass alloy. Wang and Liu [240] discussed the micro shear formation at the primary shear zone followed by formation of adiabatic shear adjacent to the tool tip depending on the machining condition. This prompted serration of the chip edges at lower cutting speed. However, the tendency has been reduced at higher cutting speed. In addition, the chips were generally spiral or helical in nature at lower cutting speed; whereas a combination of helical chips, arc chips, cork screw chips and ribbon chips have been observed at higher cutting speed. The chip sizes have been reduced when the feed rate has been increased from 3 $\mu m/rev$ to 12 $\mu m/rev$. As the strain rate increases, the degree of plastic deformation is significant at higher feed rate. Therefore, material fracture occurs prior to adiabatic shear formation near the tool tip which exhibits shorter chips formation. Similar trend has been observed by Amaral et al. [231]. There is a tendency to form spiral or helical chips at lower feed rate which changes to arc or ribbon chips at higher feed rate. This variation is significant at higher cutting speed. The tendency of larger chip formation has been observed at lower depth of cut as well. The chips are generally spiral or helical in nature at lower depth of cut.

Table 4.5: Types of chip formation in high speed micro turning of lead free brass

Experiment No.	Type of chip formation	Experiment No.	Type of chip formation
Experiment No. 1	Long and spiral	Experiment No. 9	Short and snarled helical
Experiment No. 2	Long and snarled tabular	Experiment No. 10	Short and helical
Experiment No. 3	Long and snarled helical	Experiment No. 11	Long and flat spiral
Experiment No. 4	Long and conical spiral	Experiment No. 12	Short snarled; and Loose arc
Experiment No. 5	Long and spiral	Experiment No. 13	Short connected arc; and Flat spiral
Experiment No. 6	Long and spiral	Experiment No. 14	Short and snarled cork screw
Experiment No. 7	Long and snarler helical	Experiment No. 15	Short and snarled ribbon
Experiment No. 8	Short and conical spiral	Experiment No. 16	Short and snarled ribbon

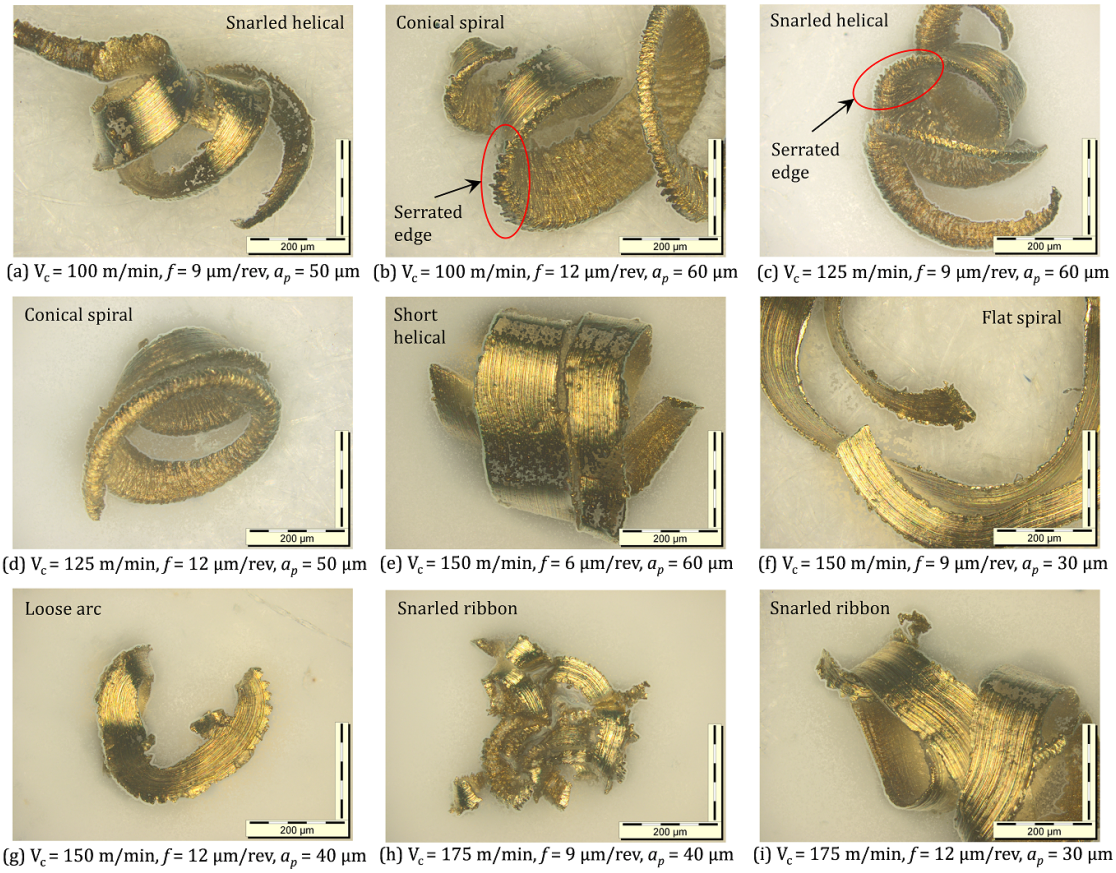

(a) V_c = 100 m/min, f = 9 µm/rev, a_p = 50 µm (b) V_c = 100 m/min, f = 12 µm/rev, a_p = 60 µm (c) V_c = 125 m/min, f = 9 µm/rev, a_p = 60 µm

(d) V_c = 125 m/min, f = 12 µm/rev, a_p = 50 µm (e) V_c = 150 m/min, f = 6 µm/rev, a_p = 60 µm (f) V_c = 150 m/min, f = 9 µm/rev, a_p = 30 µm

(g) V_c = 150 m/min, f = 12 µm/rev, a_p = 40 µm (h) V_c = 175 m/min, f = 9 µm/rev, a_p = 40 µm (i) V_c = 175 m/min, f = 12 µm/rev, a_p = 30 µm

Figure 4.12: Some distinguishing form of the chips produced in the high speed micro turning operation

4.4.4 Tool wear

The cutting tools have been subjected to tool wear analysis after machining of 10 *mm* machining length. Each insert has been used for a particular cutting speed. Fig. 4.13 illustrates the microscopic views of flank faces of the worn inserts along with an unworn one at different cutting speeds. The tool wear in this case was dominated by adhesion and diffusion due to chemical reaction between the chip and the cutting tool; and workpiece and the cutting tool. The adhesion of the brass contents on the tool surface was attributed to the chemical affinity of the workpiece towards the tool material as evidenced by the flank wear images shown in Fig. 4.13 (a) and Fig. 4.13 (d). Additionally, the strain hardening due to high speed machining resulted in moderately higher hardness of the workpiece which was responsible for the tool wear as well. Nonetheless, steady state performance of the cutting tool has been observed during the micro turning experiments. Moderate amount of flank wear and negligible crater wear has been observed on the cutting tool. This happened on account of small cutting length and machining of softer material.

The flank wear was mostly observed near the tool tip and along the major cutting edge as shown in Fig. 4.13. Maximum flank wear land width of 32 μm has been observed on the cutting tool used at 175 m/min. The flank wear mechanism is mostly influenced by adhesion, diffusion and microchipping. The friction at the chip-tool interface causes some localized heating at the tool tip. This phenomenon accelerates the formation of zinc oxide substrate from the brass material near the cutting zone. In general, the Zn present in the substrate is highly reactive with the cobalt binder present in tungsten carbide cutting tool. Due to reaction between zinc and cobalt, the binder diffuses. As a result, a lot of tungsten carbide substrate lose its binder strength. Therefore, the non-bounded WC grains are plucked out leading to diffusion wear. Bushlya et al. [241] described the phenomenon of diffusional wear during machining of lead free silicon brass. Additionally, high strain rate induced a variation of stress field on the cutting edge due to high cutting speed. However, the strength is lower due to sharp cutting edge. Therefore, fracture occurs on the cutting edge followed by formation of micro cracks leading to microchipping near the cutting edge. Fig. 4.14 indicates the variation of flank wear land width and flank wear length with the cutting speed. Flank wear length describes the propagation of flank wear along the cutting edge. It can be seen that the flank wear land width has been increased almost linearly with the cutting speed. This illustrates that the flank wear land width was mostly influenced by the cutting speed; and the effect of combined variation between feed rate and depth of cut was almost negligible. It is clear that the flank wear has been increased with the cutting speed. Strain hardening dominates over thermal softening at higher cutting speed causing increase in hardness of the workpiece material. High cutting speed resists the cutting fluid to reach at the tool-work interface deteriorating the lubricating film at the tool-work

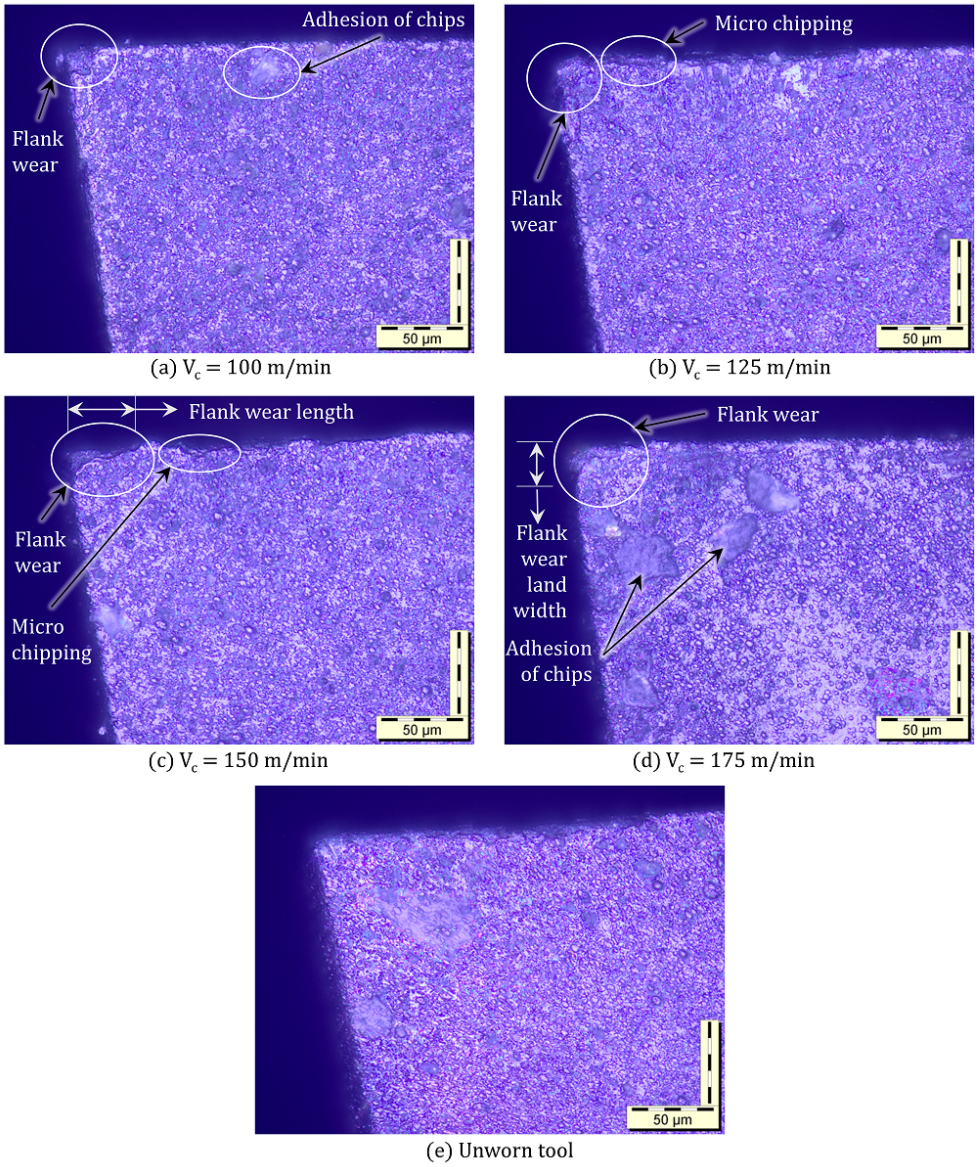

Figure 4.13: Flank wear on the cutting inserts at different cutting speeds

interface. The adhered particles might pull out the coating substrate from the tool surface resulting in certain flank wear.

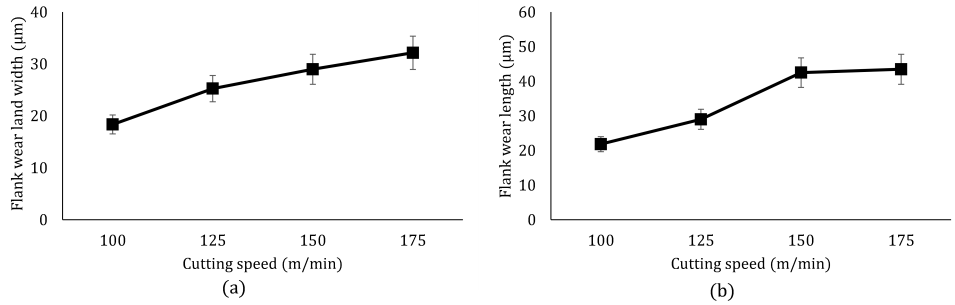

Figure 4.14: (a) Variation of flank wear land width with cutting speed; (b) Variation of flank wear length with cutting speed

4.5 Statistical analysis and prediction model

The experimental values of average surface roughness (S_a), maximum peak to valley height (S_z) and average burr height have been analyzed by analysis of variance (ANOVA) to check the significance of the parameter. The three process parameters have been selected as the source factor. The interactions of the process parameters were not significant as determined in ANOVA. The confidence interval has been taken as 95% for every analysis. Table 4.6 depicts the ANOVA model for average surface roughness (S_a). It can be seen that the cutting speed is the most contributing process parameter affecting the average surface roughness followed by depth of cut and feed rate. The cutting speed is significant parameter for average surface roughness as the P-value is less than the level of significance (0.05). However, the feed rate and depth of cut are not significant for the average surface roughness.

Table 4.6: ANOVA model for average surface roughness (S_a) of lead free brass

Parameter	DF	Adj SS	Adj MS	F-Value	P-Value	Contribution
Cutting speed	3	0.9158	0.30528	11.35	0.007	56.86%
Feed rate	3	0.1675	0.05585	2.08	0.205	10.40%
Depth of cut	3	0.3660	0.12199	4.54	0.055	22.72%
Error	6	0.1613	0.02689			10.02%
Total	15	1.6107				100%

The ANOVA model for maximum peak to valley height (S_z) and average burr height on the machined surface are depicted in Table 4.7 and Table 4.8 respectively. It is clear that the cutting speed is very highly contributing process parameter affecting the maximum peak to valley height followed by feed rate and depth of cut. However, the contributions of feed rate and depth of cut are very less as compared to cutting speed for S_z. The cutting speed is significant parameter for maximum peak to valley height as the P-value is less than the level of significance (0.05). For average burr height, the cutting speed is the most contributing process parameter followed by feed rate. The depth of cut has very less

contribution on the average burr height. Both the cutting speed and feed rate are significant parameters for the burr height as the P-values are less than the level of significance (0.05). The ANOVA result confirms that surface roughness in case micromachining not only depends on the feed marks and depth of the cutting tool involved into the workpiece which is observed in conventional turning. However, the strain hardening phenomenon, chattering of the cutting tool, surface plastic deformation, and the extent of uncut chip thickness are significant influencing the surface roughness. A little variation in those factors may deteriorate the surface finish of the micro components. Cutting speed is the most influencing parameter governing those factors. Therefore, the contribution of cutting speed is maximum for the surface parameters. Apart from this, feed rate and depth of cut also influence the surface deformation, ploughing effect etc. Therefore, these are also responsible for surface roughness, peak to valley height, and burr formation.

Table 4.7: ANOVA model for maximum peak to valley height (S_z) of lead free brass

Parameter	DF	Adj SS	Adj MS	F-Value	P-Value	Contribution
Cutting speed	3	129.732	43.244	33.45	0.00	85.79%
Feed rate	3	7.807	2.602	2.01	0.214	5.16%
Depth of cut	3	5.915	1.972	1.52	0.302	3.91%
Error	6	7.758	1.293			5.13%
Total	15	151.212				100%

Table 4.8: ANOVA model for average burr height of lead free brass

Parameter	DF	Adj SS	Adj MS	F-Value	P-Value	Contribution
Cutting speed	3	5.1859	1.72864	32.66	0.00	64.61%
Feed rate	3	2.3839	0.79464	15.01	0.003	29.70%
Depth of cut	3	0.1389	0.04631	0.87	0.505	1.73%
Error	6	0.3176	0.05293			3.96%
Total	15	8.0264				100%

Equation 4.6, 4.7 and 4.8 describe the regression equations to predict the average surface roughness (S_a), maximum peak to valley height (S_z) and the average burr height (B_{hp}). One dimensional linear models have been applied to generate the regression equations.The subscripts on the process parameters in the equations indicate the level of the parameters. Each numeric coefficient corresponding to the process parameter indicates the constant values of the equation for the particular process parameters. Each equation is a conditional equation where a set of equations can be generated based on the variation of the process parameters.

$$S_a = 0.6613 + 0.2927V_{c1} - 0.2671V_{c2} + 0.1764V_{c3} - 0.2020V_{c4} - 0.0993f_1 - 0.0144f_2 - 0.0557f_3 + 0.1694f_4 - 0.0913a_{p1} - 0.1328a_{p2} - 0.0301a_{p3} + 0.2542a_{p4} \quad (4.9)$$

$$S_z = 7.363 + 3.975V_{c1} - 3.028V_{c2} + 1.400V_{c3} - 2.346V_{c4} - 0.768f_1 - 0.280f_2 - 0.081f_3 + 1.130f_4 - 0.018a_{p1} - 0.287a_{p2} - 0.669a_{p3} + 0.974a_{p4} \quad (4.10)$$

$$B_{hp} = 1.8338 + 0.6588V_{c1} - 0.6938V_{c2} + 0.4538V_{c3} - 0.4188V_{c4} - 0.1913f_1 - 0.4162f_2 - 0.0138f_3 + 0.6213f_4 + 0.0462a_{p1} - 0.1412a_{p2} - 0.0163a_{p3} + 0.1113a_{p4} \quad (4.11)$$

For example, the average surface roughness (S_a) for a particular set of process parameters (V_c) = 100 m/min (V_{c1}), f = 3 $\mu m/rev$ (f_1), a_p = 30 μm (a_{p1}) can be calculated from Equation 4.6 as,($S_a = 0.6613 + 0.2927 - 0.0993 - 0.0913 = 0.7634$ μm).

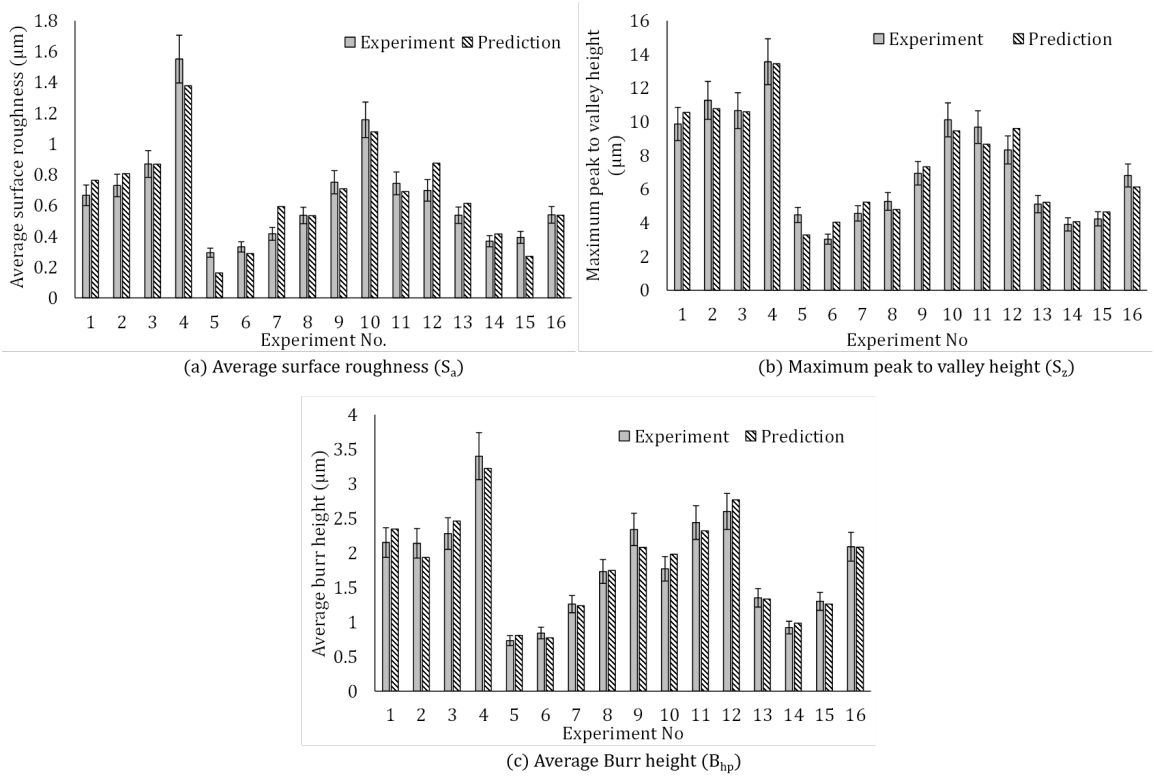

(a) Average surface roughness (S_a)

(b) Maximum peak to valley height (S_z)

(c) Average Burr height (B_{hp})

Figure 4.15: Comparison of experimental and statistically predicted results

The linear models have shown better prediction compared to other models. The R^2 values of all the three equations were 89.98%, 94.87%, and 96.04% respectively. Based on the regression equations, the values of the output parameters can be predicted. Fig.

4.15 (a), (b), and (c) represents the comparison of experimental and predicted values of average surface roughness (S_a), maximum peak to valley height (S_z) and the average burr height (B_{hp}). The predicted results have shown good similarity with the actual results. It was evident that most of the residues were approaching towards mean position which is subjected to zero. Based on those outcomes, the parameters have been optimized using Desirability Function. The desirability function D_i lies between 0 to 1 for each output response $Y_i(x)$ that depicts the predicted output response for a given operating condition x. $(D_i = 0)$ indicates completely undesirable response value, while $(D_i = 1)$ indicates completely desirable response. In this analysis, all the three parameters need to be minimized. Hence, the desirability function has been defined as Equation 4.9.

$$D_i = \begin{cases} 1, & \text{if} Y_i(x) < T_i \\ \left(\frac{Y_i(x)-U_i}{T_i-U_i}\right)^s, & \text{if} T_i \leq Y_i(x) \leq U_i \\ 0, & \text{if} Y_i(x) > U_i \end{cases} \tag{4.12}$$

Here, U_i represents the upper value of the output response and T_i represents the target value of the response. s indicates the exponent of importance to achieve the target value. The individual desirability (D_i) has been calculated prior to evaluate the overall or composite desirability (D). The composite desirability can be calculated based on the Equation 4.10.

$$D = \left(\prod_{i=1}^{n} D_i\right)^{\frac{1}{n}} \tag{4.13}$$

Here, n is the total number of responses to be optimized. The value of composite desirability need to be maximized to achieve the desirable output response. Based on the analyses, the most efficient combination of process parameters has been defined as, $V_c = 125\ m/min$, $f = 3\ \mu m/rev$, $a_p = 40\ \mu m$, to minimize the average surface roughness, peak to valley height and burr height. The desirability functions (D_i) for S_a, S_z, and B_{hp} have been calculated as 1, 0.976, and 0.971 respectively. The composite desirability D has been calculated as 0.982.

4.6 Summary

This chapter presents the machining performance of miniaturized lead free brass component in high speed micro turning. High speed turning and micro turning have been combined to achieve the favorable effects. Four different levels of cutting speed, feed rate, and depth of cut have been incorporated in the experiments. Machining has been performed in

MQL condition for its favorable effects and environmental aspect. The surface topography, burr formation, chip formation, and the tool wear have been investigated. The influences of the process parameters on the outcomes have been investigated. Additionally, the contribution of the process parameters on average surface roughness, peak to valley height, and average burr height have been determined based on analysis of variance (ANOVA). Eventually, regression equations have been developed which can successfully predict the average surface roughness, maximum peak to valley height, and average burr height with minimum error.

The average surface roughness (S_a) has been decreased on increasing the cutting speed. However, it further increased due to resonance condition in the machine tool. Although, a decreasing trend has been determined at upper level of cutting speed. Meanwhile, the average surface roughness has been increased with feed rate. However, S_a has been initially reduced and then increased with depth of cut. Mean surface roughness (S_a) of 281 nm has been achieved at cutting speed of 125 m/min, feed rate of 3 $\mu m/rev$, and depth of cut of 40 μm. The maximum peak to valley height (S_z) has shown similar trend as average surface roughness with the cutting speed. However, S_z has been initially decreased and then increased with feed rate as well as depth of cut.

The burr formation was significant on the machined surface especially at lower cutting speed; higher feed rate and depth of cut. The average burr height has shown the similar trend as the maximum peak to valley height (S_z) with the process parameters.

Longer chips have been formed at lower cutting speed during the machining experiments. However, the chip size was smaller at higher cutting speed. Additionally, shorter chips have been formed at higher feed rate. The tool wear was moderate and increased with the cutting speed.

Based on the ANOVA model, the cutting speed was the most contributing process parameter affecting average surface roughness followed by depth of cut and feed rate. Whereas, the most substantial parameter affecting maximum peak to valley height and burr height was cutting speed followed by feed rate and depth of cut. Based on the analysis, the most efficient combination of process parameters is cutting speed = 125 m/min, feed rate = 3 $\mu m/rev$, depth of cut = 40 μm.

Present study focused on combining high speed turning and micro turning and achieved favorable effects like improved material removal rate without sacrificing the product accuracy, good quality surface finish, favorable chip formation, better tool wear behavior upto a certain extent which established the accomplishment of the proposed hypothesis. Additionally, a favorable machining condition has been established for a highly difficult-to-machine material lead free brass. Moreover, the challenging issues involved in the high speed micro turning technology such as heat accumulation and burning of workpiece have been

restrained which facilitated the applicability of high speed micro turning in the manufacturing domain.

5

Enhancing machinability of lead free brass in high speed micro turning using hybrid cryogenic cooling technique

This chapter presents an approach to enhance the machinability of lead free brass in high-speed micro turning incorporating hybrid cryogenic cooling. A simultaneous flow of liquid nitrogen and vegetable oil-based MQL has been supplied to the machining interface. The performance has been compared with cutting oil-based MQL, and cryogenic cooling. Three different levels of cutting speed have been incorporated at constant feed rate and depth of cut in the machining experiments. The surface topography, microhardness, burr formation, chip formation, and tool wear have been investigated. The hybrid cooling strategy has shown steady state performance as the surface quality, burr formation, and tool wear behavior have been improved significantly. Moreover, the technique was economically and environmentally sustainable as well.

5.1 Introduction

Micro-machining is applicable to produce miniaturized components in several industries such as aerospace, automobile, electronics, and biomedical. However, low stiffness of

the micro components or the micro tools and low material removal rate are the common problem in mechanical micro-machining which stimulated the requirement of high speed micromachining technologies [224]. The researches on micro turning were mostly reported in the last decade. These researches have been performed at very low cutting speed to resist the surface degradation, tool wear, and elevation of cutting force [20, 21, 22, 23]. This prompted substantially lower productivity of micro turning operation. Owing to those challenging issues, the application of mechanical micro turning has been restrained for commercial and research purposes.

High speed machining can be a comprehensive mean to improve the material removal rate. However, higher cutting speed expedited the generation of elevated cutting temperature in high speed turning followed by significant tool wear. Previous study described in Chapter 4 revealed that high speed micro turning with minimum quantity lubrication (MQL) was able to reduce the surface roughness. However, tool wear has been reported in this study upto certain extent which is required to be minimized. This was mainly due to the ineffectiveness of the MQL to reach the chip-tool interface at high cutting speed causing localized heating. Even cryogenic cooling was failed to reach the tool-work interface at high cutting speed [78]. On the other hand, Yıldırım [242] incorporated cryogenic cooling with MQL which considerably reduced the cutting temperature at the machining zone. This hybrid technique was able to improve the surface quality and tool life during machining of nimonic alloy. A simultaneous supply of electrostatic MQL and cryogenic liquid at the tool face during machining was profitably able to improve the tribological performance of nimonic alloy [243]. This technique was economical and substantially able to improve the machinability of Inconel 718.

In this study, hybrid cryogenic cooling has been incorporated to improve the machinability of lead free brass by high speed micro turning. Machining has been performed applying three different cooling strategies i.e. cutting oil based MQL, cryogenic cooling (LN2), and hybrid cryogenic cooling technique (LN2 + MQL). In case of hybrid cryogenic cooling, a simultaneous flow of liquid nitrogen and vegetable oil (groundnut) based MQL have been supplied. The purpose was to achieve the cooling performance of liquid nitrogen and lubricating performance of vegetable oil in a combined manner. Three different levels of cutting speed have been incorporated at constant feed rate and depth of cut in the machining experiments. The surface topography, microhardness, burr formation, chip formation, and the tool wear have been investigated.

5.2 Experimental procedure

5.2.1 Preparation and application of the lubricant

Machining experiments have been carried out using three different types of lubricating/ cooling environments. Initially, cutting oil based minimum quantity lubrication (MQL) has been used to perform the machining experiments. The application of MQL was adopted over flood cooling considering its ecofriendly nature due to smaller consumption of the hazardous cutting fluid. Additionally, flood cooling is unable to reach the machining zone due to inadequate pressure and flow rate [244]. Moreover, MQL enables the flushing out of the chips up from the rake surface due to high pressure coolant supply. Therefore, this phenomenon reduces the accumulation of chips on the tool rake surface. Servocut S cutting fluid has been utilized as the base fluid of the cutting oil based MQL solution. The typical kinematic viscosity of the base fluid was 20 cSt (at 40^o). The cutting fluid has been mixed with distilled water at a ratio of 1:20 (volume percentage) to prepare a milky emulsion. The viscosity of the emulsion has been studied in a Vibro viscometer (A&D Co. Ltd. made, Model: SV - 10). The properties of the cutting oil based MQL are depicted in Table 5.1. Further, the emulsion was incorporated in the machining operation with a mix of highly compressed air (pressure 2 bar). The flow rate of the emulsion was 400 ml/hour during the machining operations. A syringe pump has been utilized for MQL supply and to maintain the flow of the lubricant.

Liquid nitrogen (LN2) has been utilized in the next step of the machining operations. The cryogenics have the ability to evaporate quickly leaving no residues on the machined surface contaminating the final product [245]. Additionally, it has the ability to improve the surface quality as well as the tool wear performance. Moreover, the application of cryogenics enables the transformation of materials property from ductile to brittle due to very low machining temperature [246]. This phenomenon may facilitate better chip breakage of highly ductile lead free brass alloys. In this experiment, liquid nitrogen has been stored in a cryogenic container (BA-35). The maximum output pressure that can be sustained by the container was 1 bar. The output pressure was maintained at 0.5 bar during the machining operation. The spraying angle was maintained at 45^o with a standoff distance of 50 mm.

Eventually, hybrid cryogenic cooling has been utilized in the machining operation incorporating simultaneous supply of crude vegetable oil based MQL and liquid nitrogen. This has been applied to achieve the favorable effect of liquid nitrogen as well as the lubricating properties of MQL. Crude groundnut oil has been adopted as the fluid of MQL due to its better lubricating properties. The viscosity of the crude groundnut oil has been measured using a Vibro viscometer (A&D Co. Ltd. made, Model: SV - 10). The properties of the groundnut oil are presented in Table 5.1. During hybrid cryogenic cooling supply,

the MQL flow and pressure have been maintained at 150 ml/hour and 2 bar. Meanwhile, the liquid nitrogen supply pressure was maintained at 0.5 bar. Syringe pump was used for the MQL supply.

Table 5.1: Properties of the coolant/lubricant used in the experiment

Sl No.	Coolant type	Coolant used	Temperature	Dynamic viscosity	Thermal conductivity
1	Cutting oil based MQL (MQL)	Emulsion of Servo-cut Oil with water at a ratio of 1:20	25^oC	10.25 mPa.S	0.565 W/mK
2	Cryogenic (LN2)	Liquid nitrogen	-196^oC		
3	Hybrid cryogenic cooling (LN2 + MQL)	Crude groundnut oil (MQL) and Liquid nitrogen simultaneously	28^oC	59.9 mPa.S	9.418×10^{-4} W/mK

5.2.2 Machining process

The workpiece was lead free brass (CW510L) in this experiment. The properties of the material has been discussed in the previous chapter (Chapter 4, section 4.2). The cylindrical workpieces have been cut using a WEDM machine and turned in a mini lathe machine to ensure the uniform cylindricity. The diameter and length of each workpiece were 3 mm and 40 mm respectively. The high speed micro turning operations have been performed in the high speed micromachining center (model V60) which was indigenously developed in micro fabrication laboratory of Indian Institute of Technology (ISM), Dhanbad. Fig. 5.1 represents the experimental setup along with the extended view of the machining zone. The vertical spindle has an ability to rotate from 10000 to 60000 rpm. The workpieces have been mounted vertically by the pneumatic collet mounted on the spindle. Initially the clamping length of the workpiece was 28 mm and cantilever length was 12 mm. The machining length was 10 mm in that case. However, significant tool vibration deteriorated the machined surface. Therefore, the machining length was reduced to 3 mm. In this case, the cantilever length was 6 mm for each workpiece. The machine tool consists of a X-Y linear stage which carried the whole tool holding devices. A t-slot was attached on the X-Y stage. A toolpost along with the cutting tool and tool holder have been mounted on t-slot. There was proper fluid extraction facility in the t-slot and hence, no lubricant was stored on the passages of the t-slot. The longitudinal feed has been provided to the workpiece by the Z stage, while the cross movement (depth of cut) was generated by the X-Y stage. TiAlN (PVD) coated cemented carbide inserts (Sandvik Coromant made, Model: MAFR 3 003 1105) have been used for the machining operation. The insert contained sharp cutting edge

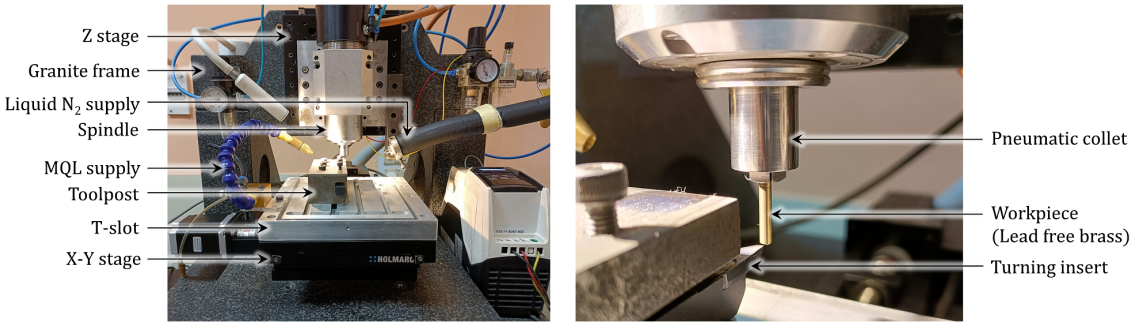

Figure 5.1: Experimental setup for the high speed micro turning operation

of 5 μm edge radius. The rake angle of the cutting tool was 0^o following the general state of the art to machine lead free brass. One cutting insert has been used for each machining operation at a particular cutting speed and cutting environment. The process parameters have been selected based on the permissibility of the cutting tool and the optimum results of the previous experiments. Three different levels of cutting speeds have been utilized in the experiments. The depth of cut and feed rate were constant for all the machining operations. The values of feed rate and depth of cut have been chosen based on the optimum results of the previous experiments described in chapter 4. Table 5.2 enlists the details of tool geometry and process parameters for the machining operations. All the experiments have been carried out under MQL, LN2, and LN2 + MQL conditions. Each experiment has been repeated twice to check the repeatability of the outcomes.

Table 5.2: Details of the tool geometry and process parameters

Tool geometry		Process parameters			
Parameters	Values	Parameters	Level 1	Level 2	Level 3
Side rake angle	0^o	Cutting speed, V_c (m/min)	120	180	240
Back rake angle	3^o	Feed rate, f $(\mu m/rev)$	3		
Side relief angle	3^o	Depth of cut, a_p (μm)	40		
End relief angle	35^o				
Principal cutting edge angle	90^o				
End cutting edge angle	9^o				
Nose radius (μm)	30				

5.2.3 Characterization

Surface topography

The surface topography of the workpiece after machining has been investigated in optical profilometer (Zygo make, model: Newview 9000). The areal surface roughness (Mean

surface roughness, S_a; and Root mean square surface roughness, S_q) has been determined. The measurements have been taken at a distance of 1 mm along the machining length. Therefore, three measurements have been taken on each samples and their average has been calculated. 50X magnification has been used for measuring the optical profilometry. The scanning length was 20 μm in each measurement. Additionally, the defects on the surface topography due to machining have been investigated in FESEM (ZEISS make, model Supra 55) using a scale of 1 μm.

Microhardness

The microhardness of each machined surface has been measured using a Vickers microhardness tester (Mitutoyo made, Model: HM220). The load given on the samples was 50 gm-f. The dwell time was 10 sec. The indentation of the diamond indenter was measured using in-build microscope in the hardness testing machine with 50X magnification. 5 measurements have been taken on each machined sample at equal distance along the machining length and their average has been calculated.

Burr formation

The burr height has been measured from the surface profilometry on each sample determined by optical profilometer. The procedure of burr height calculation has been already represented in previous chapter (Chapter 4). A number of linear slices have been drawn on the surface profile of the workpiece where the burrs have been observed. The peak height (R_p) along each slice and the linear surface roughness (R_a) along the slice have been measured. The arithmetic difference between the peak height (R_p) and the linear average surface roughness (R_a) along each slice have been depicted as the burr height (B_{hp}). Six measurements of burr height have been taken from each profilometry. Therefore, total number of measurements was eighteen from each machined surface and their average has been estimated.

Chip morphology and Tool wear

The chip morphologies after machining have been studied in optical profilometer (Zygo make, model Newview 9000) using 50X magnification. Additionally, the tool wear has been investigated in the optical profilometer. The microscopic profilometries of flank wear have been captured with 50X magnification and analyzed. The scanning length was 65 μm in this case. Eventually, the flank wear width and length have been determined based on each profilometry of the tool flank surface.

5.3 Results and discussions

5.3.1 Surface topography

The variation of surface roughness with the cutting speed at different machining environments is depicted in Fig. 5.2. It can be seen that both the mean arithmetic surface roughness (S_a), and root mean square surface roughness (S_q) have been reduced on increasing the cutting speed. Similar trend has been found for maximum peak to valley height (S_z) as well. In addition, better performance has been observed for cryogenic cooling (LN2) as compared to cutting oil based MQL. Moreover, hybrid cryogenic cooling has shown superior performance as compared to other cooling strategies. The best quality surface has been achieved by cryogenic cooling at a cutting speed of 240 m/min. The best surface roughness was 0.181 μm (S_a). The effect of workpiece vibration was taken into account in this study. The variation of surface roughness with the machining length (10 mm) is presented in Fig. 5.3. In this figure, the cutting length 0 indicates the free end of the workpiece where the cantilever length was maximum. The cutting length 10 mm indicates the end of the cutting length where the cantilever length was minimum. The surface roughness has been varied significantly with the machining length due to higher cantilever effect as illustrated in Fig. 5.3. The variation of surface roughness was larger with the cutting length when the measurement has been taken from the free end to the cutting length of 7 mm. Additionally, stable surface roughness results have been observed for the last 3 mm machining length (Cutting length of 7 mm to 10 mm) due to lesser cantilever length as shown in the Fig 5.3. On the basis of the findings, the machining length has been reduced to 3 mm for establishing stable machining performance eliminating workpiece vibration.

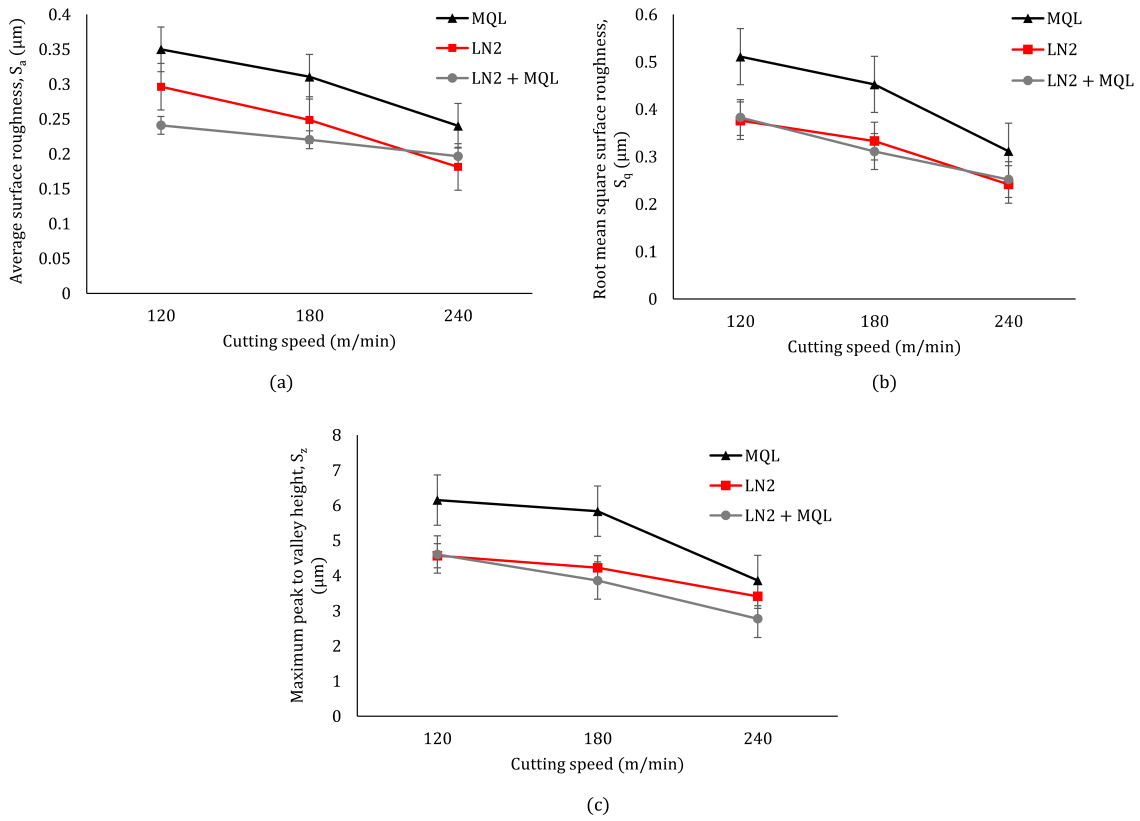

Figure 5.2: Variation of (a) mean surface roughness (S_a); (b) root mean square surface roughness (S_q); (c) maximum peak to valley height (S_z) with cutting speed at different machining environments

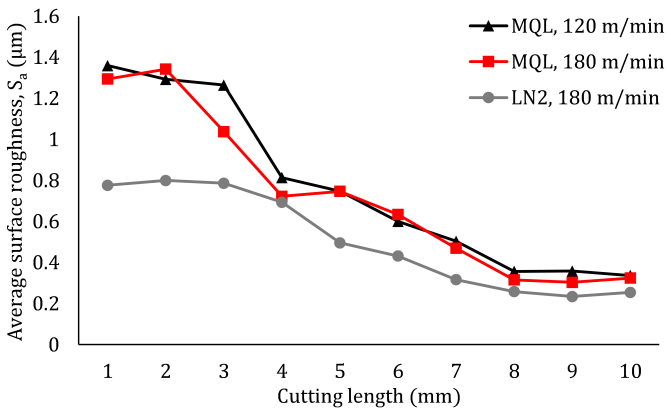

Figure 5.3: Variation of mean surface roughness (S_a) with machining length considering workpiece vibration

Effect of machining environment on surface topography

It is evident from Fig. 5.2 that the surface roughness has been improved using cryogenic cooling (LN2) as compared to cutting oil based MQL. The minimum average surface roughness (S_a) was 0.24 μm during machining with cutting oil based MQL at higher cutting speed. While the minimum average surface roughness was 0.18 μm during machining with cryogenic cooling at higher cutting speed. Therefore, a reduction of 32.5% in average surface roughness was observed when the cooling strategy has been changed from cutting oil based MQL to cryogenic cooling. Meanwhile, a steady state and better surface quality has been observed for hybrid cryogenic cooling (LN2 + MQL) irrespective of cutting speed. At higher cutting speed (240 m/min), the performance of cryogenic cooling and hybrid cryogenic cooling was almost similar, although the performance of cryogenic cooling was slightly better at this cutting speed.

The application of cryogenic cooling significantly improved the work hardening of the machined surface. Therefore, the plastic side flow of the work material due to higher plasticity was somehow restricted to certain extent. Consequently, the surface quality has been improved. Meanwhile, the application of vegetable oil based MQL has created a favorable lubricating interface at the machining zone. This reduced the friction at the chip-tool interface in addition with the work hardening effect due to cryogenic cooling. As a result, the plastic deformation of the surface has been reduced significantly. Consequently, improved surface quality has been observed during hybrid cryogenic cooling. The root mean square surface roughness (S_q) has shown almost similar trend like (S_a). Although, there was very negligible difference between the surface quality achieved in cryogenic cooling and hybrid cryogenic cooling. The tendency of forming larger peaks has been reduced significantly by the application of cryogenic cooling and hybrid cryogenic cooling. The surface profilometries presented in Fig. 5.5 clearly shows that the peaks which has been found in a large extent under cutting oil based MQL condition (Fig. 5.5 (a) and (b)) has been reduced by cryogenic and hybrid cryogenic cooling. This was attributed to the work hardening of the work material restraining the plastic side flow. On the other hand, low depth of cut and elevated hardness of the work material restricted the formation of valley during cryogenic cooling as shown in the surface profilometries presented in Fig. 5.5 as well as the FESEM images of the surface topographies shown in Fig. 5.6. In addition, the favorable lubricating interface in hybrid cryogenic cooling created a lubricating film between the cutting tool and workpiece reducing the chemical reaction in between them. Thus the plucking out of work material has been reduced in this case restraining the formation of pits like valleys on the machined surface which was significant under MQL condition as shown in Fig. 5.5 (a). Subsequently, the peak to valley height has been decreased on the machined surface as shown in Fig. 5.2 (c) reducing the overall root mean square surface roughness.

Effect of cutting speed on surface topography

Cutting speed is one of the most influencing process parameters for surface roughness. It is clear from Fig. 5.2 that the surface roughness has been reduced at higher cutting speed. Both average surface roughness (S_a) and root mean square surface roughness (S_q) have shown similar trend with the variation of cutting speed. Fig. 5.4 represents the fundamental mechanism of surface generation in high speed micro turning. It is clear that the elastic recovery and plastic side flow are the major factor dominating the surface generation. It can be seen from Fig. 5.4 that the effect of elastic recovery on the machined surface caused continuous variation of the actual depth of cut (a_p) along infeed direction. A theoretical relationship between the actual depth of cut, uncut chip thickness (h_{min}), and elastic recovery (h_e) has been represented by Equation 5.4 [3].

$$h_e = \begin{cases} a_p, & \text{if} a_p < a_e \\ \frac{(1-\varepsilon_p)h_{min}}{h_{min}-a_e}(a_p - a_e), & \text{if} a_p \in [a_e, h_{min}] \\ a_e, & \text{if} a_p > h_{min} \end{cases} \tag{5.1}$$

In this equation, ε_p represents the plastic strain of the work material. a_e illustrates the limiting value of depth of cut required for pure elastic deformation of the work material. The value of a_e can be determined as $a_e = kr_e\frac{H}{E}$ [247], where H and E denote the hardness and elastic modulus of the work material respectively. k is a constant and r_e denotes the cutting edge radius.

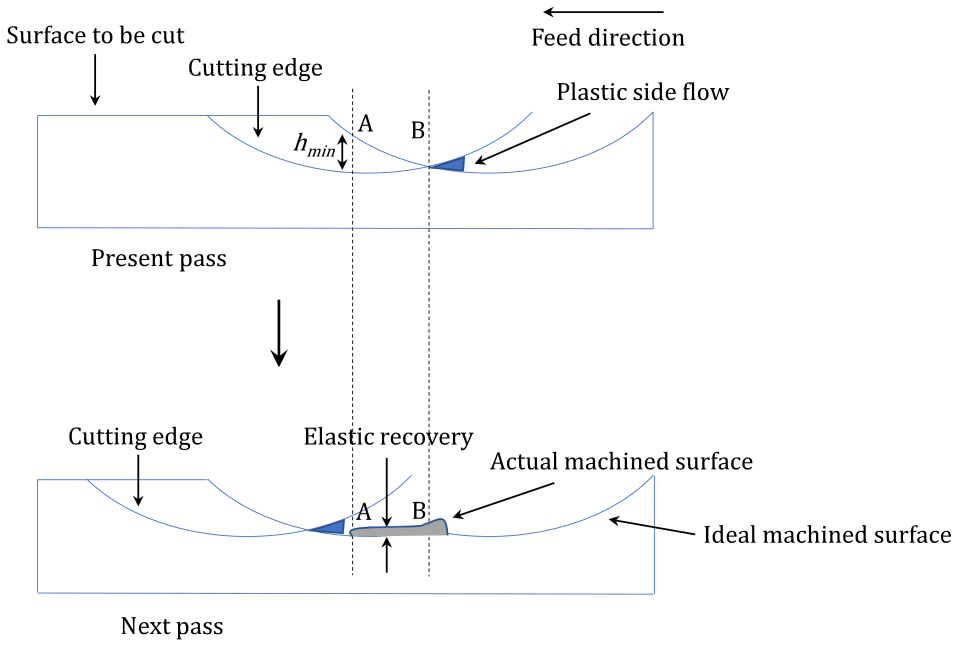

Figure 5.4: Surface generation mechanism on lead free brass in high speed micro turning

As shown in Fig. 5.4, there is a zone AB where the depth of cut was significantly smaller as compared to the minimum uncut chip thickness. This results in ploughing of the cutting tool on the machined surface rather than shearing. Consequently, large amount of elastic recovery has been observed in that zone rather than material removal. Additionally, the stress concentration has been developed near the cutting edge resulting in plastic side flow of the work material. High plasticity of lead free brass expedited the plastic side flow. The ploughing phenomenon and the material pile up was clearly observed in the optical profilometry presented in Fig. 5.5 and the FESEM images of the machined surface presented in Fig. 5.6.

The uncut chip thickness varies inverse proportionally with the cutting velocity in machining operation. As the cutting speed increased, the minimum uncut chip thickness has been reduced which in turn reduced the surface roughness. It can be explained in another way. Warsi et al. [235] proposed that the shear angle has been increased at higher cutting speed. Therefore, the cutting force is reduced at higher cutting speed in micromachining. Subsequently, the friction angle has been reduced based on Equation 4.4. As a result, the minimum uncut chip thickness has been reduced as a function of friction angle (based on Equation 4.3). Consequently, the theoretical surface roughness has been reduced based on Equation 4.1 and 4.2 (Described in Chapter 4). Additionally, the dominance of strain hardening has been observed at higher cutting speed. The plastic side flow has been drastically reduced at higher cutting speed as an influence of that phenomenon. Consequently, the surface quality has been improved at higher cutting speed.

The appearance of coarse grains in the workpiece microstructure (Presented in Fig. 4.1 (a) in Chapter 4) has been subjected to severe grain dislocations during machining. Therefore, rapid plastic deformation has been taken place on the workpiece surface resulting in strain hardening phenomenon. On the contrary, the presence of β phase in a significant amount in the workpiece microstructure as shown in Fig. 4.1 (a) in Chapter 4 resulted in elevated material hardness. Additionally, the application of coolant during MQL or cryogenic led to some quenching treatment of the workpiece. Consequently, the amount of β phase has been slightly enhanced in the microstructure causing work hardening of the surface layer. Moreover, a marginal amount of embrittlement has been occurred on the workpiece surface. This phenomenon resulted in formation of micro cracks and tearing of the machined surface due to interaction with the cutting tool during machining. However, smooth interaction of the cutting tool with the workpiece surface during application of hybrid cryogenic cooling has led to lesser defects on the machined surface. During machining operation, the α and β phases were favorably oriented along the direction of cutting. The β phase allowed the development of cracks or fracture along the direction of cutting under the action of the compressive stress exerted by the cutting tool. While the

α phase restricted the formation of cracks and allowed plastic deformation due to ductile nature. Therefore, the cracks or fracture like defects have been propagated through the β phase along the grain boundaries towards the cutting direction. The formation of cracks over the machined surface and its propagation along the cutting direction were shown in Fig. 5.6. In contrast, smooth surfaces, slight material pile up has been appeared on the machined surface through the α phase towards the cutting direction. Hence, an inhomogeneous behavior in the surface formation has been observed on the machine surface due to bi-phasic nature of the lead free brass.

Small size of the workpieces possessed very low heat dissipation area irrespective of higher thermal conductivity. Therefore, slightly localized heating has been developed at the tool-work interface resulting in slightly thermal softening at lower cutting speed. This accelerated the plastic side flow of the work material causing some surface roughness especially during machining with cutting oil based MQL. Further ploughing effect was also responsible for more rubbing over the machined surface and heat generation leading to material pile up. Fig. 5.6 (a) clearly shows the material pile up over the machined surface under MQL condition. During application of cryogenic cooling and hybrid cryogenic cooling, the machining temperature has been drastically reduced. Therefore, the effect of thermal softening completely eliminated during machining with these cooling strategies. Additionally, the work hardening effect due to machining at very low temperature reduced the elastic recovery as well as plastic side flow. The combination of high cutting speed and cryogenic or hybrid cryogenic cooling significantly improved the surface quality on the lead free brass. Hybrid cryogenic cooling (LN2 + MQL) exhibits the best cooling action during the machining process as the heat generated due to friction was further minimized in this technique. Therefore, the tendency of elastic recovery was further reduced.

Fig. 5.5 represents the profilometries of the machined surface at different cutting speeds and different machining environments. There were some tendencies of generating pits like defects on the machined surface at lower cutting speed during machining with cutting oil based MQL (Fig. 5.5 (a)). At lower cutting speed, material plucking out has been observed on the machined surface causing pits like defects. However, the tendency has been diminished at higher cutting speed (240 m/min) as shown in Fig. 5.5 (b). Additionally, higher material pile up has been observed at lower cutting speed (120 m/min) during turning with cryogenic cooling as depicted in Fig. 5.5 (c). The formation of periodic burrs on the machined surface has been observed as well in this case. This might be caused due to non-uniform hardening of the material at different locations by cryogenic cooling, resulted in fluctuation of cutting force. However, such defects have been diminished at higher cutting speed (Fig. 5.5 (d)). The surfaces were mostly clean under hybrid cryogenic cooling as observed in Fig. 5.5 (e) and (f). Moreover, Fig. 5.6 represents some closed view of the

machined surface at different cutting conditions captured in FESEM. The closed view of the machined surface revealed that there was a tendency of cracks and cavities formation on the machined surface during machining with cutting oil based MQL as shown in Fig. 5.6 (a). However, the tendency of cavities has been diminished by cryogenic cooling at the same cutting speed. Although some laps and tearing have been observed as well on the machined surface in this case (Fig. 5.6 (b)). At high speed (240 m/min), the surface was almost defect free during machining with cryogenic cooling. However, the laps like defects were present during machining with hybrid cryogenic cooling at the same cutting speed (240 m/min).

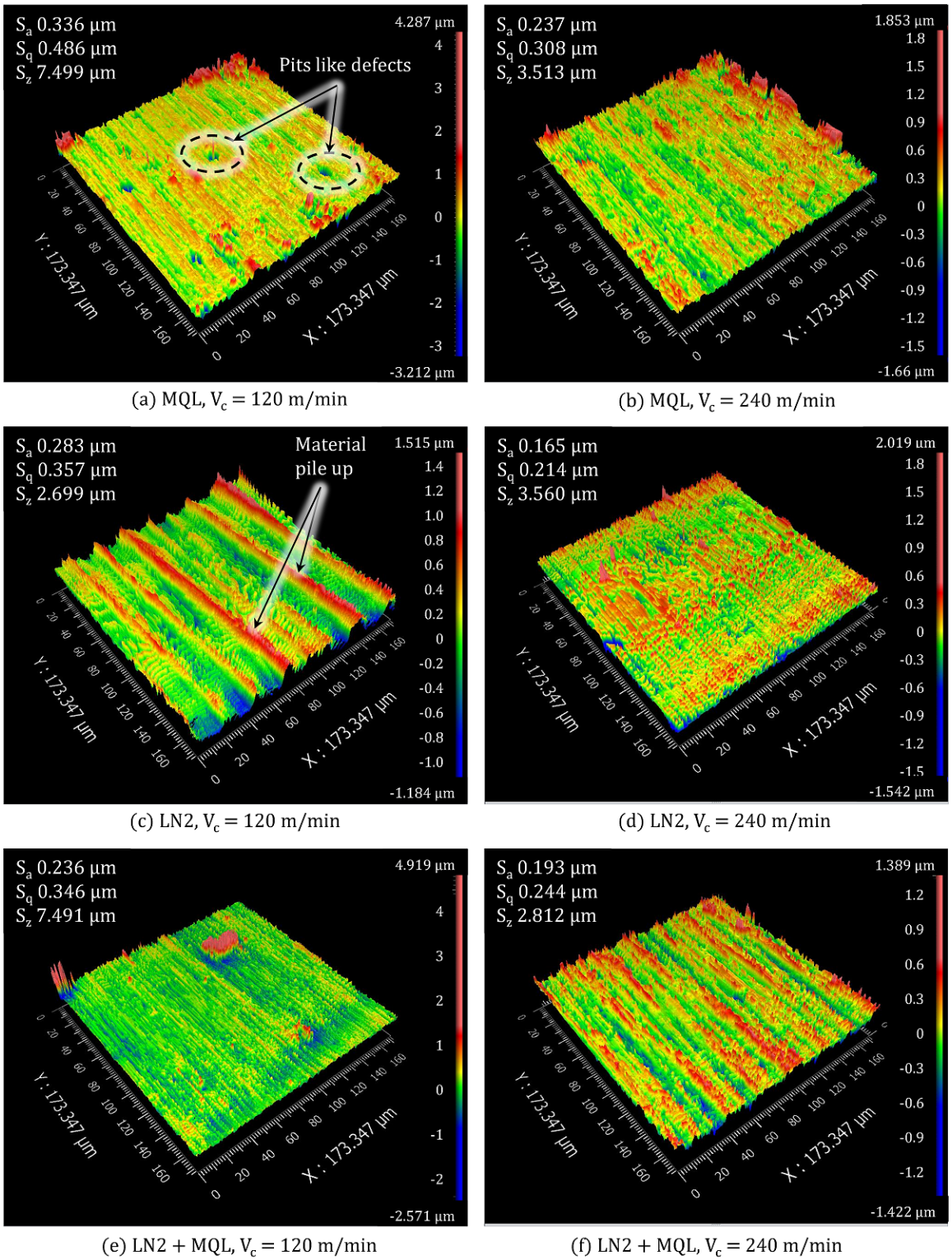

(a) MQL, $V_c = 120$ m/min

(b) MQL, $V_c = 240$ m/min

(c) LN2, $V_c = 120$ m/min

(d) LN2, $V_c = 240$ m/min

(e) LN2 + MQL, $V_c = 120$ m/min

(f) LN2 + MQL, $V_c = 240$ m/min

Figure 5.5: Surface profilometries on lead free brass samples achieved at different cutting speeds and machining environments

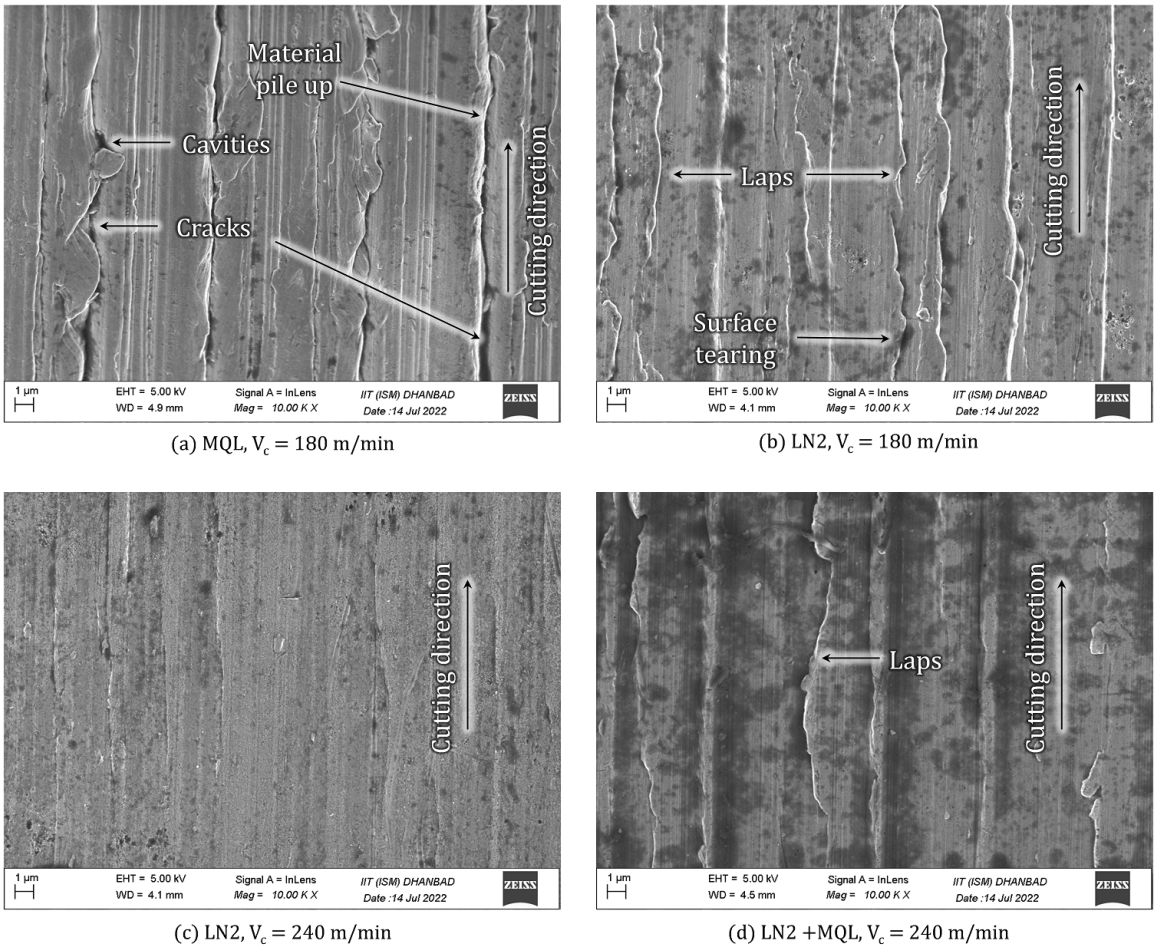

(a) MQL, $V_c = 180$ m/min

(b) LN2, $V_c = 180$ m/min

(c) LN2, $V_c = 240$ m/min

(d) LN2 +MQL, $V_c = 240$ m/min

Figure 5.6: Closed view of the machined surface at different cutting conditions determined in FESEM

5.3.2 Microhardness

The microhardness of each machined surface has been measured with $\pm 0.5\%$ repeatability. Fig. 5.7 (a) represents the variation of microhardness with the cutting speed at different machining conditions. The microhardness of the workpiece material has been measured as 136 HV before machining. The extent of strain hardening induced subsurface plastic deformation during machining can be quantified from the enhancement of surface microhardness after machining than the hardness of the bulk material. Additionally, it has been observed that the microhardness was maximum for cryogenic cooling (LN2) as compared to MQL and hybrid cryogenic cooling. Similar phenomenon has been observed in previous research as well [119]. The cryogenic cooling induced rapid amount of work hardening and very low thermal softening on the machined surface. This led to higher hardness of the machined surface. The microhardness has been reduced by a great extent during machining with hybrid cryogenic cooling (LN2 + MQL). In this case, the application of liquid

nitrogen was responsible for work hardening of the machined surface. Meanwhile, the application of vegetable oil based MQL has created a superior lubricating interface at the machining zone. Therefore, the friction in the chip-tool interface has been reduced facilitating a smooth chip flow. This phenomenon restrained the work material to adhere at the tool surface. Lesser adhesion between the work material and cutting tool has reduced the extent of plastic deformation on the machined surface. Thus the microhardness has been reduced. The flank wear images presented in Fig. 5.12 (g), Fig. 5.12 (h) and Fig. 5.12 (i) confirm lesser adhesion of the chip particles to the tool surface. Minimum microhardness has been observed during machining with cutting oil based MQL. The chances of work hardening was significantly lesser as compared to other two techniques. The difference in microhardness achieved after machining under different cooling conditions with the microhardness of the parent material indicates the extent of work hardening. This specified highest work hardening achieved during machining with cryogenic cooling (LN2) followed by hybrid cryogenic cooling (LN2 + MQL) and cutting oil based MQL.

The variation of microhardness with the cutting speed has shown similar trend for all the three machining environments. Fig. 5.7 (a) shows that the microhardness of the machined surface has been increased with the cutting speed. Being a highly plastic material, the effect of strain hardening was dominant over thermal softening at high cutting speed. Higher thermal conductivity of the workpiece material allows the cutting heat to dissipate rather than accumulation. This in turn restricts the thermal softening of the workpiece. Low feed rate and depth of cut evolved the ploughing effect over shearing on the machined surface. This may induced the strain hardening of the machined surface as well. Subsequently, the surface microhardness has been increased at higher cutting speed. Fig. 5.7 (b) represents the indentation of the diamond indenter on the machined surface during the microhardness testing.

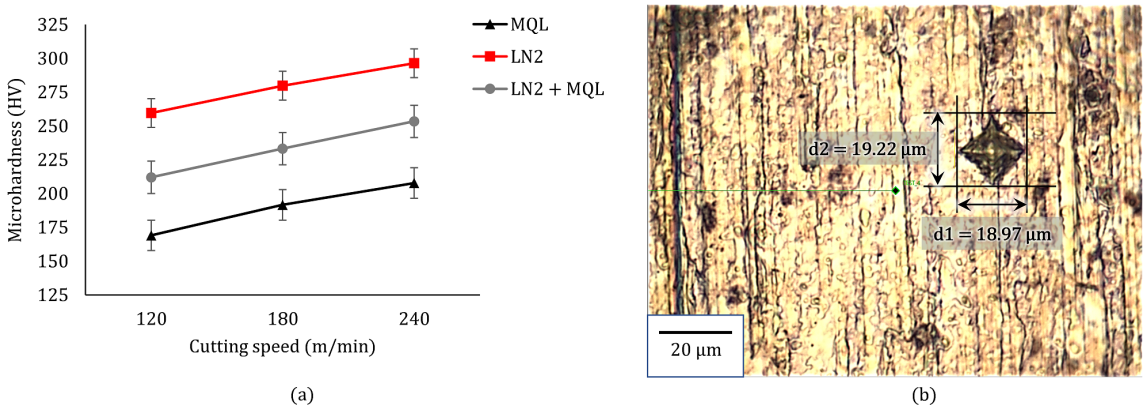

Figure 5.7: (a) Variation of microhardness with cutting speed at different machining environments; (b) Indentation of the micro indenter on the machined surface during microhardness testing

5.3.3 Burr formation on the machined surface

Burrs are inevitable on the machined surface. They are very hard to remove in micromachining process due to size effects. Therefore, they are focused to minimized in micromachining operation. In turning operation, burrs are mostly focused as the exit burrs. However, the burrs on the machined surface are more detrimental as it directly increases the surface roughness. The compressive force exerted by the cutting insert on the machined surface resulted in plastic side flow of the work material during ductile machining. The lateral flow of the work materials led to formation of instantaneous peaks like micro burrs on the machined surface. Fig. 5.8 represents the variation of height of the micro burrs on the machined surface at different cutting speed and cutting environment. It was observed that the burr height was maximum during machining with cutting oil based MQL in all cutting speeds. The burr height has been reduced significantly during machining with cryogenic cooling. The application of cryogenic cooling was able to restrict the plastic side flow of the work material enabling substantial work hardening. Meanwhile, the reduction of burr height was not significant at lower cutting speed (120 m/min) during hybrid cryogenic cooling as compared to cutting oil based MQL. The burr height was larger in this case as compared to cryogenic cooling. However, the burr height has been reduced rapidly at higher cutting speed under hybrid cryogenic cooling and the best performance has been observed in this case. The application of liquid nitrogen in hybrid cryogenic cooling induced work hardening of the machined surface and restrained the plastic side flow of the material. Meanwhile, the application of vegetable oil based MQL reduced the friction at the tool-work interface. Therefore, the friction induced plastic deformation of the machined surface has been decreased. Additionally, lesser adherence of work material to the cutting tool which can be seen in the flank wear images at Fig. 5.12 (g), Fig. 5.12 (h) and Fig. 5.12

(i), has reduced the plastic deformation deformation as well. All these phenomenon was responsible to reduce the burr height in hybrid cryogenic cooling technique. Altogether it can be said from Fig. 5.8 that both cryogenic cooling and hybrid cryogenic cooling were effective to reduce the burr height at high cutting speed.

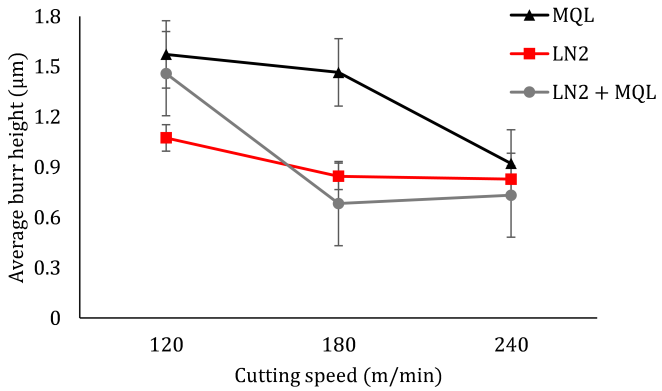

Figure 5.8: Variation of burr height on the machined surface at different cutting speeds and machining environments

It has been observed that the burr height has been reduced at higher cutting speed for all the machining environments. Kumar and Bajpai [62] revealed that the reduction of burr formation at higher cutting speed was attributed to higher plastic strain and lower uncut chip thickness. This phenomenon restrained the tendency of plastic deformation at higher cutting speed. Fig. 5.9 represents the burr formation on the machined surface at different cutting speeds and machining environments. It was evident that some instantaneous larger peaks have been appeared at lower cutting speed (120 m/min) with cutting oil based MQL (Fig. 5.9 (a)). However, this tendency has been reduced slightly at higher cutting speed of 240 m/min (Fig. 5.9 (b)). Meanwhile, the burr formation has been reduced significantly by the application of liquid nitrogen as coolant resulting in smaller number of peaks (Fig. 5.9 (c)). The burr formation was almost diminished applying hybrid cryogenic cooling (LN2 + MQL) at 240 m/min (Fig. 5.9 (d)) resulting in very few number of peaks and smooth machined profile. In the present study, the burrs were less propagated along the cutting direction. Therefore, most of the burrs have been found as intermittent burrs, especially in cryogenic cooling and hybrid cryogenic cooling as shown in Fig. 5.9 (c) and (d). Meanwhile, the propagation of burrs was comparatively larger in MQL condition. Therefore, continuous burrs have been found in this condition as shown in Fig. 5.9 (b).

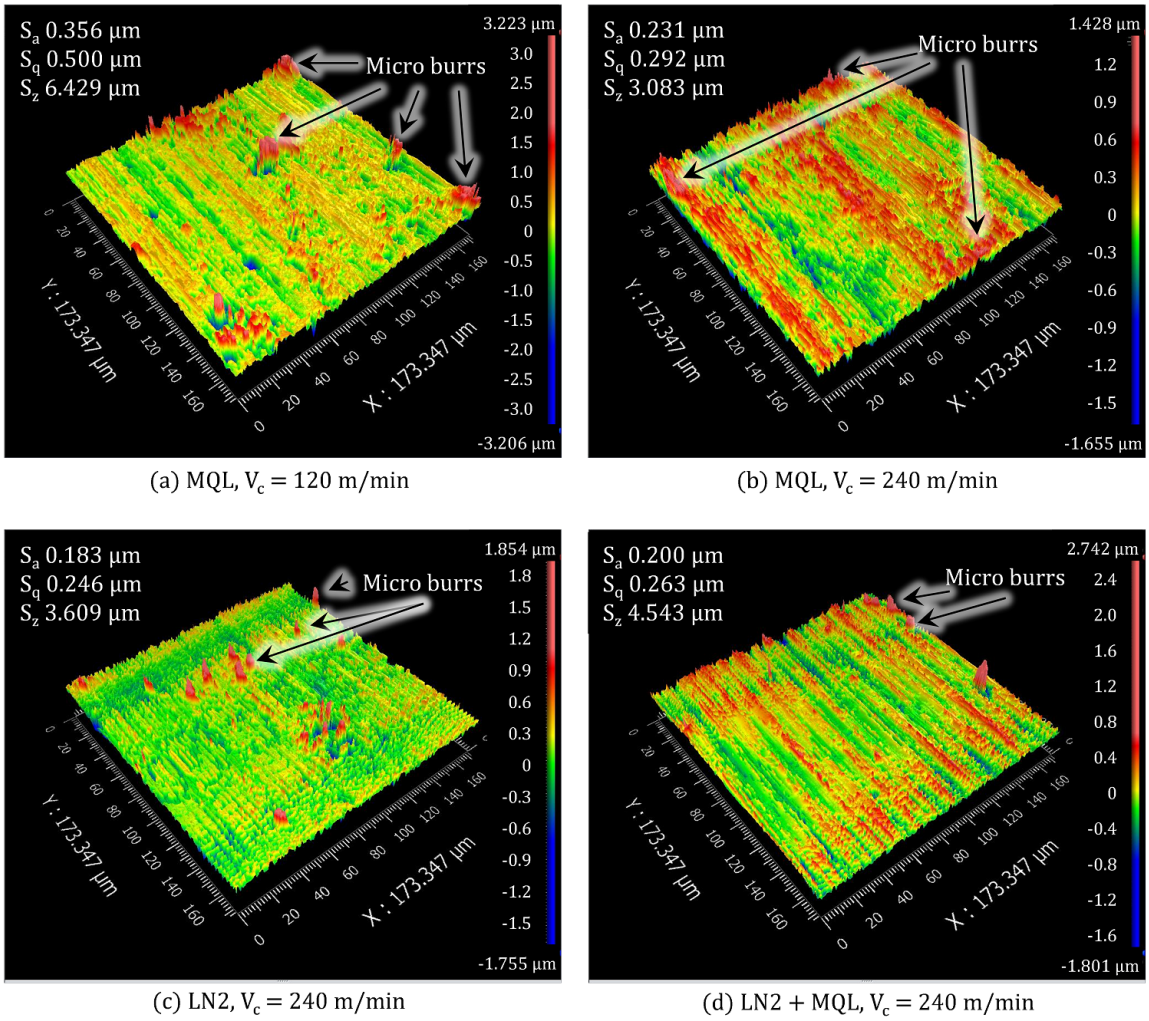

(a) MQL, $V_c = 120$ m/min

(b) MQL, $V_c = 240$ m/min

(c) LN2, $V_c = 240$ m/min

(d) LN2 + MQL, $V_c = 240$ m/min

Figure 5.9: The surface profilometry showing the micro burrs formed on the machined surface at different cutting speeds and machining environments

5.3.4 Chip morphology

The chip formation is one of the most effective parameters determining the machinability of lead free brass. The absence of lead content in the brass alloy increased the shear strength of the workpiece material and enhanced the ductility. As a result, the chip breakage was not much favorable. However, the application of cryogenics reduced the ductility of the chips and improved the chip breaking mechanism. Fig. 5.10 represents different types of chip formation at different cutting speeds and cutting environments during high speed micro turning of lead free brass.

The micro chips formed were mostly ribbon in shape. The chips were long in size at lower cutting speed especially during machining with cutting fluid based MQL. However, the size of the chips became smaller at higher cutting speed. This may be attributed to the dominance of strain hardening over thermal softening at higher cutting speed due to higher

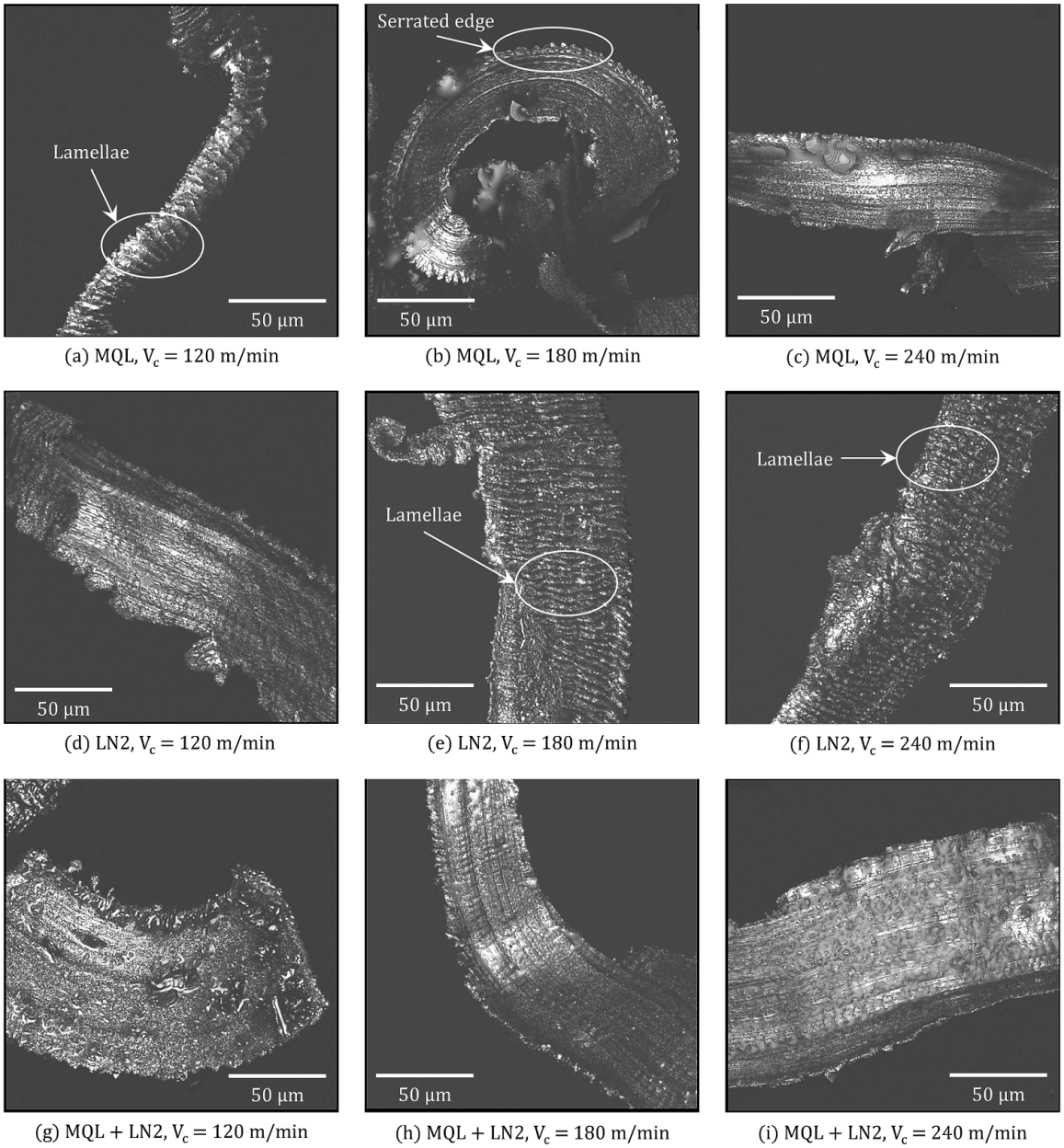

Figure 5.10: Optical images of chip morphologies at different cutting speeds and machining environments generated in the high speed micro turning operation

strain rate [239]. This phenomenon slightly improved the brittleness of the chips and eased the chip breakage at higher cutting speed. Additionally, the chip sizes were small for LN2 and hybrid cryogenic cooling. The lower temperature due to cryogenics resulted in embrittlement of the brass chips. Consequently, the chips were fractured rather than deformed due to presence continuous shear force and shorter chips have been observed. Lamellar chips have been formed in some cases during machining under cutting oil based MQL and liquid nitrogen as shown in Fig. 5.11. The formation of lamellae was attributed to the variation of shear stress and heat generation within the shear bands. Due to high cutting speed, the cutting oil based coolant or liquid nitrogen were unable to reach at the exact chip-tool interface. Therefore, the temperature at the chip-tool interface was slightly higher as compared to the surroundings. On the other way, the chip suddenly moved from the chip-tool contact zone to the surrounding due to continuous movement and became cooled by the cooling action. As a result, a variation of thermal stress field has been generated on the chips. This phenomenon develops a periodic cycle based on variation of thermal stress for repeated shear band formation. Consequently, the periodic lamellar chip formation has been taken place. Jiang and Dai [248] observed similar phenomenon during machining of bulk metallic glasses. However, the friction at chip-tool interface significantly reduced by hybrid cryogenic cooling due to application of vegetable oil based MQL. Therefore, the development of cutting heat was not significant during turning with hybrid cryogenic cooling. Consequently, the tendency of lamellae formation has been diminished in this case. Additionally, some of the chips contain serrated edge during machining with cutting oil based MQL, especially at lower cutting speed since thermal softening of the workpiece. This accelerated micro shear formation at the primary shear zone followed by adiabatic shear near the tool tip [240]. Consequently, the serration of the chips has taken place. However, this trend has been diminished at higher cutting speed and other machining environments.

5.3.5 Tool wear

All the cutting tools have been subjected to tool wear analysis after machining of 20 *mm* machining length. Fig. 5.11 represents the variation of tool flank wear with the cutting speed at different machining environment. The variation of flank wear width (V_B) is depicted in Fig. 5.11 (a). Fig. 5.11 (b) shows the variation of flank wear length (b). Flank wear length defines the amount of flank wear propagated along the cutting edge. Moderate amount of tool wear has been observed during turning under cutting oil based MQL condition. The flank wear width was 30.4 μm at the cutting speed of 120 m/min. However, the flank wear width has been increased at higher cutting speed. Similar trend has been observed for flank wear length as well. The dominance of strain hardening was significant at higher cutting speed. Additionally, the heat generation was slightly higher at the

chip-tool interface during higher cutting speed. Therefore, slightly higher localized cutting temperature has been observed at the chip-tool interface. This accelerated the flank wear at higher cutting speed. The flank wear has been reduced at lower cutting speed (120 m/min) using liquid nitrogen. This may be due to shorter chip formation resulting in smaller amount of chips accumulated at the chip-tool interface. However, the flank wear has been increased rapidly at higher cutting speed during machining with cryogenic cooling (LN2). This may be due to combined effect of work hardening by cryogenic cooling and strain hardening at higher cutting speed. Additionally, high cutting speed restrained the coolant/lubricant to reach at the tool-work interface deteriorating the lubricating film at the machining zone. Moreover, uniform steady state performance has been observed by the cutting tool during turning with hybrid cryogenic cooling. The flank wear was independent of cutting speed during application of hybrid cryogenic cooling (LN2 + MQL). This indicated a clear lubricating interface at the machining zone protecting the cutting tool from tool wear. Additionally, the tool strength might be increased under the action of cryogenic cooling.

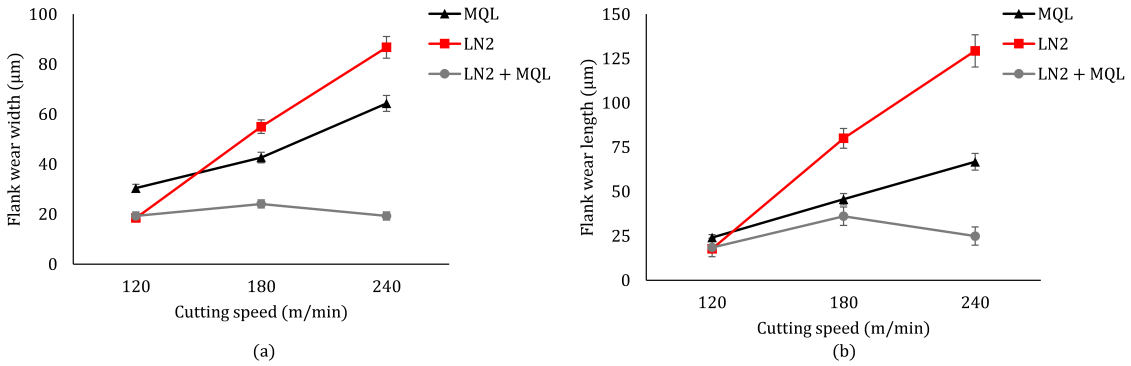

Figure 5.11: (a) Variation of flank wear width with cutting speed at different machining environments; (b) Variation of flank wear length with cutting speed at different machining environments

The tool wear mechanism was dominated by adhesion and diffusion due to chemical reaction between the chip and the cutting tool. Sometimes, longer chip formation resulted in accumulation of chips at the chip-tool interface. As discussed in section 5.3.4, longer chips have been found under cutting oil based MQL condition which has a tendency to accumulate at the tool tip. This tendency was quite severe at lower cutting speed. Additionally, the flank wear image presented in Fig. 5.12 (a) shows the chip adhesion at the tool tip which confirms the same. The accumulation of chips at the tool tip elevated the friction at the chip-tool interface. Additionally, the hardness of workpiece was responsible as well for the tool wear. Slightly higher localized cutting temperature at the chip-tool interface led to formation of zinc oxide substrate from the brass material near the cutting zone. The

zinc oxide substrate is highly reactive to the cobalt binder present in the cutting tool. Subsequently, the diffusion of the binder has been taken place in tungsten carbide substrate. Hence, the non-bounded WC grains were plucked out due to the diffusional wear. The mechanism of diffusional wear has been described by Bushlya et al. [241]. The adhesion of chips at the cutting tool surface as shown in Fig. 5.12 (e) and Fig. 5.12 (f) confirm the chemical phenomenon which is caused due to localized heating at elevated cutting speed.

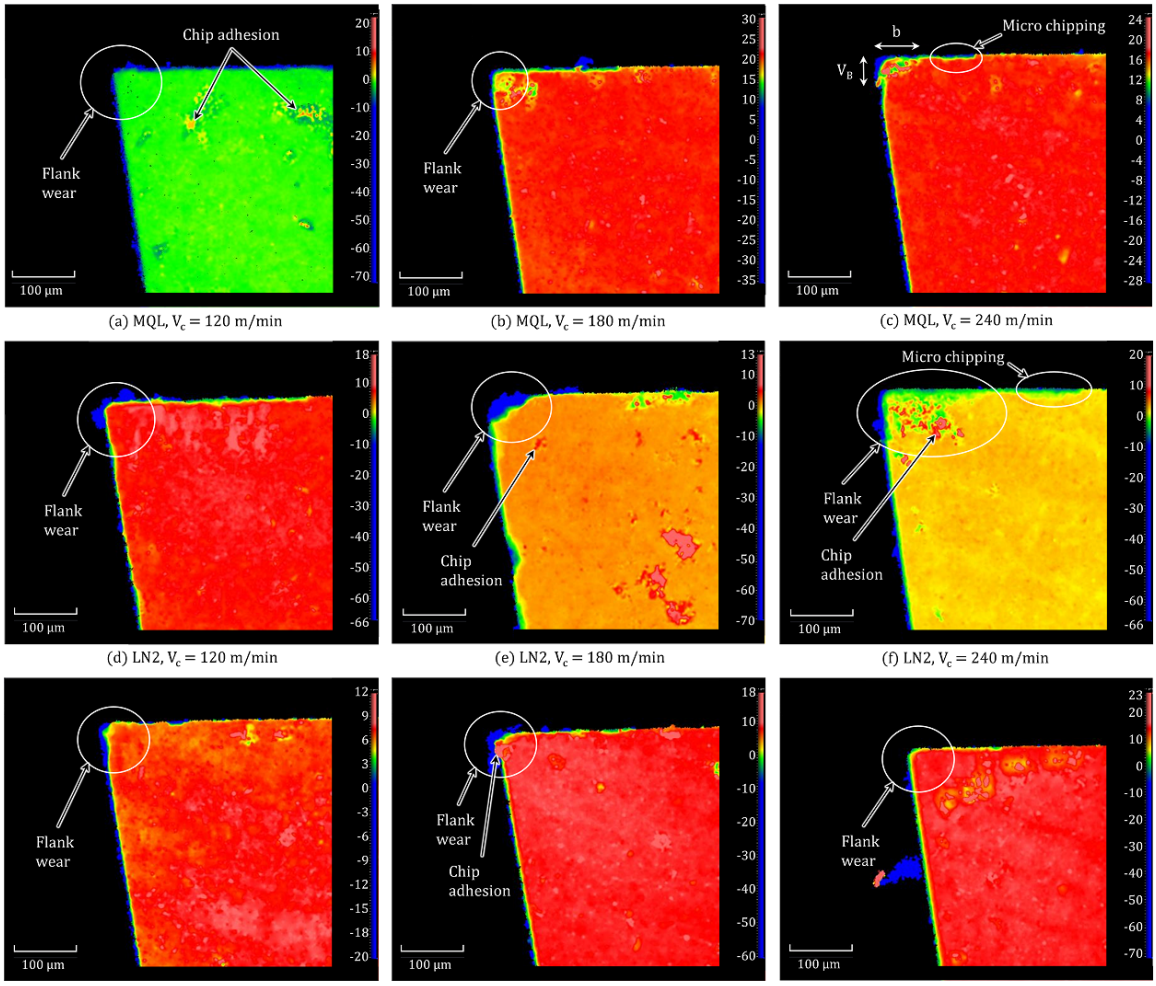

Figure 5.12: Microscopic images of tool flank surfaces showing flank wear including micro chipping near the cutting edge and chip adhesion at different cutting speeds under different machining conditions

In addition, High cutting speed developed high strain rate followed by stress field variation on the cutting edge. Therefore, fracture occurred on the cutting edge immediately as it possessed lower strength. This phenomenon led to micro cracking followed by microchipping near the cutting edge. The tendency of microchipping has been observed at higher cutting speed (240 m/min) during machining with cutting oil based MQL and liquid nitrogen. However, the tendency has been diminished during turning with hybrid cryogenic

cooling. Fig. 5.12 represents the microscopic images of tool flank wear at different cutting speed and machining environments. There was an evident of adhering chips to the flank surface during machining with cutting oil based MQL and liquid nitrogen. However, clean flank surfaces have been observed during machining with hybrid cryogenic cooling confirming steady state lubricating interface at the chip-tool interface.

5.4 Economical and environmental sustainability

5.4.1 Economical assessment

Economy is a major aspect to determine the sustainability of a process. In this case, the total economy involved in each process has been divided into two subcategory. One is fixed cost and another is variable cost. The fixed cost involved the machine tool cost, the labour cost, and the cost due to energy consumption for a particular running condition. These costs are same for all the cooling conditions during machining. Besides, the variable cost involved the cost due to cutting fluid consumption, cost of cutting tool, and the cost involved in waste management. The variable cost has been compared for three different machining environments, i.e. cutting oil based MQL, cryogenic cooling (LN2), and hybrid cryogenic cooling (LN2 + MQL).

The cost involved in cutting fluid has considered the loses due to leakage, vaporization, machined parts handling etc. Meanwhile, the consumption of cutting fluid was much lesser due to application of MQL. However, the recycling was not possible in this case due to mixing of chips and other wastes. The cost involved in recycling the cutting fluids are much higher rather than disposing it because the quantity was much lesser. Therefore, the recycling of the cutting fluid was not focused in this case. The reuse of liquid nitrogen was not possible because it is completely vaporized in open environment. Although liquid nitrogen is easily and economically available in market as a byproduct of oxygen plant, the loss involved in liquid nitrogen was much higher. Therefore, the cost of cryogenic cooling was higher as compared to MQL. After performing 30 mm cutting, the cost involved for consumption of cutting fluid in cutting oil based MQL was 0.063 $. While, the cost involved for cryogenic cooling due to the consumption of liquid nitrogen after cutting equal length was 1.982 $. Meanwhile, the cost involved in vegetable oil (groundnut oil) was 4.506 $ per litre. Therefore, the lubricant cost involved for hybrid cryogenic cooling after cutting 30 mm length was 2.207 $ incorporating the cost of liquid nitrogen with vegetable oil.

The average flank wear was three times for cryogenic cooling (LN2) as compared to hybrid cryogenic cooling (LN2 + MQL). While it was almost two times for cutting oil

based MQL as compared to hybrid cryogenic cooling. Therefore, it can be considered that almost three fresh cutting tools (nose) have been required after cutting a standard length during machining with cryogenic cooling, while the requirement of cutting tool (nose) is only one for hybrid cryogenic cooling. Meanwhile, two cutting tools (nose) have been required for cutting oil based MQL. Each cutting insert contains two different cutting nose. Therefore, the cost involved in each cutting tool has been considered as half of the price of the actual insert (43.813 $). Meanwhile, it has been observed that minimal amount of flank wear has been reported for hybrid cryogenic cooling. Therefore, the tools can be reused depending on the desired grade of finishing.

The wastes involved in cutting oil based MQL incorporated chips and the used cutting fluid. While there was no residual coolant on the machined zone during machining with cryogenic cooling. The wastes only included chips in this case. Furthermore, the lubricants and the chips have been included in the wastes during machining with hybrid cryogenic cooling. Therefore, some additional cost has been involved to dispose the lubricant or coolant in MQL and LN2 + MQL techniques. The lubricating oil has been disposed by means of an air gun through the disposing channel in the t-slot.

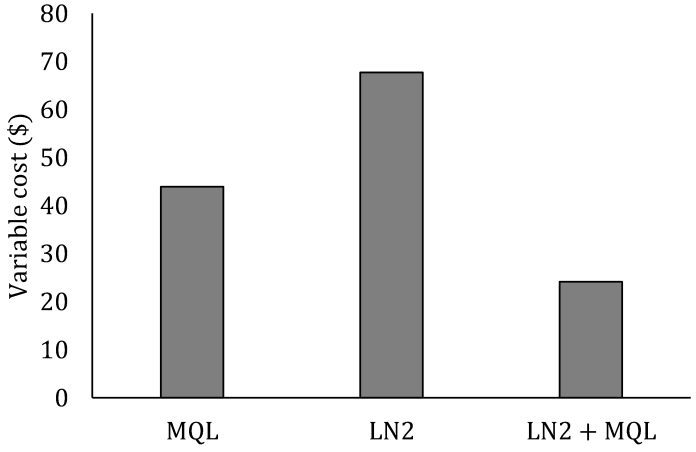

Figure 5.13: Total variable costs involved in different cooling strategies in the machining experiments

Total variable cost has been calculated by summing the costs involved in cutting fluid consumption, the tool cost, and the cost involved in disposing wastes. The total variable costs involved in all three lubricating strategies have been plotted and depicted in Fig. 5.13. It can be seen that the variable cost was minimum for hybrid cryogenic cooling as compared to other two machining environments. It has been reduced by 64% as compared to cryogenic cooling and 45% as compared to cutting oil based MQL. Therefore, hybrid cryogenic cooling has been considered as the most economically sustainable cooling technique as compared to the others.

5.4.2 Environmental assessment

Irrespective of having poor machinability, lead free brass has been promoted for the versatile application due to environmental exposure. The machinability of the lead free brass alloy has been improved in this study focusing on the machining environment. Furthermore, it has been emphasized in this research to reduce the utilization of hazardous lubricant by applying MQL and cryogenic cooling. From environmental aspect, the sustainability depends on the extent of applying hazardous cutting fluid as coolant/ lubricant, the amount of waste generated, the amount of carbon emission. The application of hybrid cryogenic cooling has eliminated the application of detrimental cutting fluid by utilizing vegetable oil (groundnut oil) as the lubricant. Additionally, the use of liquid nitrogen did not leave any residual wastes on the machined surface as it was vaporized completely. It did not generate any harmful emission in the atmosphere. The wastes only involved the vegetable oil and the chips which were very small in amount. Additionally, they were easily disposable. Hence, it did not create any contamination to the environment. The amount of carbon emission was negligible. Especially the application of liquid nitrogen as cryogenic has eliminated the emission of carbon content during the machining experiments. Therefore, the application of hybrid cryogenic cooling has been considered as environmentally sustainable. The environmental sustainability of hybrid cryogenic cooling (LN2 + MQL) strategy is shown in Fig. 5.14.

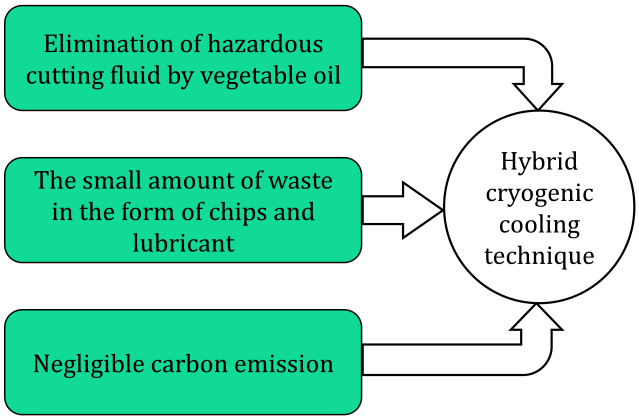

Figure 5.14: Environmental sustainability of hybrid cryogenic cooling technique

5.5 Summary

This study incorporated hybrid cryogenic cooling to improve the machinability of lead free brass by high speed micro turning. Machining has been performed applying three different cooling strategies i.e. cutting oil based MQL, cryogenic cooling (LN2), and hybrid cryogenic cooling technique (LN2 + MQL). For hybrid cryogenic cooling, a simultaneous flow

of liquid nitrogen and vegetable oil (groundnut) based MQL have been supplied at the chip-tool interface. Three different levels of cutting speed have been incorporated at constant feed rate and depth of cut in the machining experiments. The surface topography, microhardness, burr formation, chip formation, and the tool wear have been investigated. The average surface roughness (S_a) was significantly low during machining with hybrid cryogenic cooling (LN2 + MQL) as compared to cutting oil based MQL and cryogenic cooling (LN2). The average surface roughness (S_a) achieved in this condition was in the order of 200 nm. However, the average surface roughness was in the order of 250 nm and 300 nm in cryogenic cooling and cutting oil based MQL respectively. Although the minimum value of S_a has been found during machining with cryogenic cooling at 240 m/min; and the value was 165 nm. The value of S_a has been reduced at higher cutting speed in all machining conditions. S_q has shown similar trend as average surface roughness. The microhardness has been considerably increased during machining with cryogenic cooling as compared to cutting oil based MQL owing to rapid work hardening. During hybrid cryogenic cooling, the microhardness values were almost intermediary of the other two conditions. Additionally, microhardness has been increased at higher cutting speed for strain hardening of the work surface. The burr formation has been reduced significantly on the machined surface during turning at higher cutting speed with cryogenic and hybrid cryogenic cooling technique. The chip breaking was not favorable during machining at lower cutting speed. However, it has been improved at higher cutting speed specially under cryogenic and hybrid cryogenic cooling. In addition, the tendency of lamellar chip formation was prominent during machining with cutting oil based MQL and cryogenic cooling. Steady state performance of the cutting tool has been observed in hybrid cryogenic cooling irrespective of the cutting speed. Very low flank wear has been determined during this condition. However, the flank wear was significant in cryogenic cooling especially at higher cutting speed. It has been observed that the flank wear width was almost 2 to 3 times in cutting oil based MQL and 3 to 5 times in cryogenic cooling as compared to hybrid cooling technique in higher cutting speed. Based on the amount of cutting fluid application, cutting tool wear, waste development and management cost, hybrid cryogenic cooling technique has been considered as economically and environmentally sustainable compared to other two cooling techniques.

6

Feasibility of cost-effective ultra-precision diamond turning using ceramic bearing spindle

The present chapter reveals a cost-effective methodology of producing mirror finish on difficult-to-machine lead free brass by ultra-precision diamond turning. Ultra-precision face-turning has been performed in an economically developed machine tool comprised of ceramic bearing spindle. Mirror surface finish has been achieved on the workpiece with average surface roughness from 7 nm to 51 nm. The axial spindle drift was small; however, a marginal spindle drift has induced small amplitude periodic fluctuation of surface profile and center groove on the machined surface. Additionally, the amplitude of machine tool vibration has been appeared in the nanometer level. Negligible tool wear has been observed as well. Moreover, the ultra-precision machining performed in the present study was economically and environmentally sustainable.

6.1 Introduction

The requirement of high precision components with nanometric surface finish is growing continuously in various fields such as optical, semiconductors and telecommunication

industries. Ultra-precision diamond turning is an efficient material removal technology capable to produce super finished components with nanoscale features [249, 158]. This technology has been extensively applied to fabricate optical components such as different optical lenses, scanners, computer memory disks, optical molds, infrared imaging optics etc. The predominant advantage of the ultra-precision diamond turning is the redundancy of expensive post-machining techniques such as polishing. However, exorbitant development cost of the ultra-precision diamond turning machine tool has limited the the number of industrial and research organization to develop the machine tool.

The dynamic characteristic of a machine tool substantially influenced the surface generation in machining. Meanwhile, the dynamic characteristic of the machine tool depends on the spindle dynamics, and machine tool dynamics. The researchers have focused on using ultra-precision spindle based on aerostatic bearing for minimized friction, low viscosity resulting in thermal stability during high speed operation [250]. However, a marginal amount of tilting motion have resulted in periodic fluctuation of the tool profile on the machined surface inducing surface roughness. The tilting motion has been generated by dynamic unbalancing of the air bearing spindle which resulted in whirling and forced vibration [163]. Consequently, lobes-star error has been formed over the machined surface. Elevated compressibility of air led to low stiffness and damping performance of the air bearing causing significant difficulties in dynamic balancing. Owing to this problem, hydrostatic bearing spindle has been utilized as well for ultra-precision machining which exhibited higher stiffness as compared to aerostatic bearing spindle. However, both these spindles are highly expensive.

On the contrary, ceramic bearing spindle exhibits significantly low cost. Meanwhile, it shows higher stiffness, thermal stability, and superior dynamic performance which make it suitable for high speed operation [251, 252]. Additionally, a little reduction in preloading force may reduce the thermal deformation during high speed operation in case of ceramic bearing and improve the dynamic stability [253]. Therefore, the ceramic bearing is able to sustain extreme temperature fluctuation due to its low deformation tendency. For these reason, the ceramic bearing was dynamically stable during utilization of cryogenic cooling as well [254].

The dynamic stability of the machine tool has largely influenced the surface formation in ultra-precision diamond turning. A marginal vibration may substantially affect the surface finish in diamond turning.

This study reveals a cost-effective methodology of producing mirror finish on difficult-to-machine lead free brass by ultra-precision diamond turning. Ultra-precision face turning operation has been performed in an economically developed machine tool comprised of ceramic bearing spindle. The spindle rotational speed has been varied from 10000 to 30000

rpm during the machining operation. The spindle drift, machine tool vibration, surface topography, chip formation, and tool wear have been determined. Eventually, a comparative analysis has been performed to evaluate the economical and environmental sustainability of the presented methodology.

6.2 Experimental procedure

The ultra-precision diamond turning operations have been performed in the high-speed ultra-precision micromachining center (model V140) which was indigenously developed in micro fabrication laboratory of Indian Institute of Technology (ISM), Dhanbad. Fig. 6.1 represents the experimental setup along with the extended view of the machining zone. Vertical face turning operations have been performed in the machine tool. The spindle comprised of ceramic ball bearing which was dedicated for ultra high speed operation (Ibag made, Model: HT 45 S 140). The range of the spindle rotational speed was 10000 to 140000 rpm. The technical specifications of the spindle are depicted in Table 6.1. The bearing of the spindle possessed significant damping capability which improved the dynamic stability of the spindle. The material of the spindle holder was mild steel. Additionally, Newport make ultra-precision linear stages (X-Y stage: One XY100, Z stage: GTS 30 V) have been used to provide the linear motions during the machining operations. The technical specifications of the linear stages are presented in Table 6.1. The workpiece has been gripped by the pneumatic collet mounted on the spindle. The workpiece was cylindrical rod of lead free brass (CW510L). The workpiece material contained 59% copper and 41% zinc. Disappearance of lead content has resulted in rapid ductility of the material and made it a difficult-to-machine material [227]. The diameter and length of each workpiece were 3 mm and 30 mm respectively. The sample preparation involved cutting of the cylindrical workpieces using a WEDM machine followed by turning and facing in a mini lathe machine. The clamping length of the workpiece was 27 mm. Single point diamond turning insert (DCGT11T3, Halnn made) has been used to perform the ultra-precision machining. The details of the tool geometry are depicted in Table 6.2. The diamond insert contained sharp cutting edge of 0.05 μm radius. A toolpost along with the cutting tool and tool holder have been mounted on X-Y stage. The spindle system has been fixed in the machine tool and the motions have been provided by the linear stages. The feed has been provided to the workpiece by the X-Y stage, while the axial depth of cut has been provided by the Z stage. The process parameters have been selected based on the permissibility of the cutting tool and the motion capability of the linear stages. The rotational speed of the spindle has been varied from 10000 rpm to 30000 rpm at an interval of 2500. The depth of cut and feed rate were constant for all the machining operations. The details of the process parameters for

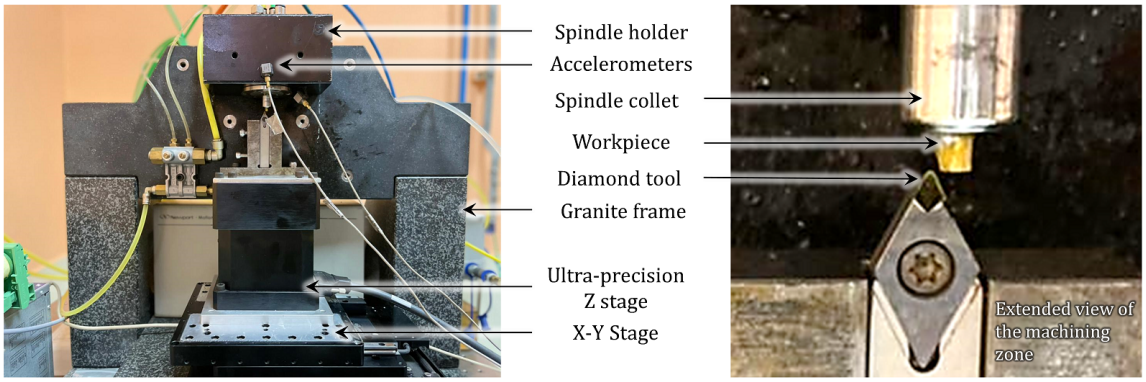

Figure 6.1: Experimental setup for the ultra-precision diamond turning operations

the machining operations are enlisted in Table 6.2. All the experiments have been carried out under dry condition. Each experiment has been repeated twice to check the repeatability of the outcomes. Two piezoelectric accelerometers (Bruel & Kjaer made, Type 4507 CCLD) have been mounted in the spindle holder to measure the machine tool vibration. The sensitivity of the accelerometers was 10.14 mV/ms^{-2}. The major source of vibration in the machine tool was the high-speed spindle. Therefore, the accelerometers have been mounted in the spindle holder along axial and radial direction.

Table 6.1: Technical specifications of Spindle and linear stages

Spindle		Linear stages		
			X-Y stage	Z stage
Rotational speed (rpm)	10000 - 140000	Travel range (mm)	90	30
Bearing type	Ceramic	Maximum speed (mm/sec)	200	10
Torque (N.m)	0.043	Minimum incremental motion (nm)	50	100
Motor power (W)	630	Load capacity (N)	10	40
Cooling system	Liquid	Accuracy (μm)	$\pm$0.5	$\pm$0.37
Mass (kg)	1.013	Bi-directional repeatability (nm)	40	70
Axial stiffness ($N/\mu m$)	21	Straightness (μm)	1	0.75
Radial stiffness ($N/\mu m$)	24	Drive system	Linear motor	DC motor with low-friction lead screw system

The signal of the vibration, captured by the accelerometers have been amplified by a data acquisition system (Bruel & Kjaer made) and converted from time domain function to frequency domain functions using RT Pro Photon+ software. The FFTs have been analysed using ME'Scope Ves software. All the FFTs generated for every machining op-

Table 6.2: Details of the tool geometry and process parameters

Tool geometry		Process parameters	
Side rake angle	0^o	Spindle rotational speed, N (rpm)	10000, 12500, 15000, 17500, 20000, 22500, 25000, 27500, 30000
Back rake angle	0^o	Feed rate, f ($\mu m/rev$)	1.5
Clearance angle	7^o	Depth of cut, a_p (μm)	5
Tool wedge angle	55^o		
Nose radius (mm)	0.5		

erations have been superimposed over each other; and the final frequency vs amplitude spectrum for axial and radial vibration have been generated. The surface topography of the workpiece generated after each machining operation has been investigated in optical profilometer (Zygo made, model: Newview 9000). The areal surface roughness (Mean surface roughness, S_a) has been determined using 5.5X and 100X magnifications. Measurements have been taken at different location of the machined surface as well as the center of the workpiece. Based on the surface profile generated on the workpiece surface, the spindle drift has been determined. Additionally, the surface topography on the workpiece have been investigated in FESEM (ZEISS make, model Supra 55) using a scale of 1 μm. Further, the elementary analysis has been performed on the machined surface using EDS spectroscopy (Oxford make, Model: SDD X MAX 50). The chip morphologies after machining have been studied in optical microscope (Olympus made, Model: BX51M) using 5X magnification. Additionally, the diamond tool wear has been investigated in the optical microscope. The microscopic images of flank wear have been captured using 20X magnification and analyzed. The tool wear of the used insert has been compared with an unworn insert.

6.3 Calculation of spindle drift

The spindle drift causes the positional fluctuation of the rotational axis. Spindle drift is a common phenomenon irrespective of the type of bearing [161, 9]. In general, the axis of the spindle exhibits three types of motions which include axial, radial, and tilting. These motions resultantly forms the drift error of the rotating spindle. The schematic diagram of the mechanical system of the spindle is shown in Fig. 6.2 (a). This spindle system has been deviated from the inertial co-ordinate system (XYZ) due to drift motion and positioned in the reference co-ordinate system (X'Y'Z'). The origin of the inertial co-ordinate system O has been shifted to O' for the reference co-ordinate system. The translational motions of the point O' along the X, Y, Z axes are depicted as x, y, and z respectively from the point

O. Similarly, the rotational motions of O' with respect to the X', Y', Z' axes are depicted as R_x, R_y, and R_z respectively. The axis of the spindle (Z') is supposed to be rotated by an angle θ from its original axis. For a spindle without eccentricity (balanced spindle), the geometric center of the spindle lies at point O'. It is supposed that there is a very small eccentric mass m in the spindle lies at a distance a from the center (AO'), b from the Z' axis (AB), and c from the X' axis (AC). Due to the presence of the unbalanced mass m, a moment has been generated with respect to the Z' axis and the vertical axis of the spindle rotates around Z'. The center of gravity is assumed to be at point O' as the amount of the unbalanced mass (m) is very small.

The radial and axial stiffness of the spindle bearing are regarded as k_r and k_a. For representing this, two spring elements have been considered at the radial direction having stiffness of k_1 and k_2 respectively. Additionally, two spring elements have been considered at the direction having stiffness of k_3 and k_4 respectively. Therefore, the radial stiffness k_r can be defined as the summation of k_1 and k_2 ($k_r = k_1 + k_2$). Therefore, the axial stiffness k_a can be defined as the summation of k_3 and k_4 ($k_a = k_3 + k_4$). The rotational stiffness of the spindle along the radial direction $k_{r\theta}$ can be represented as, $k_{r\theta} = k_1 l_1^2 + k_2 l_2^2$. The linear displacement along the radial direction due to drift motion can be expressed as, $Z = x + jz$. M and I are supposed to be the mass and the rotational moment of inertia of the spindle. The damping effect of the spindle bearing has been neglected. Therefore, considering the motion around the axis of the spindle at the X'Z' plane, the equation of translational and rotational motion can be expressed as Equation 6.1 [255, 9].

$$\begin{bmatrix} M & 0 \\ 0 & I \end{bmatrix} \begin{bmatrix} \ddot{Z} \\ \ddot{\theta} \end{bmatrix} + \begin{bmatrix} k_r & 0 \\ 0 & k_{r\theta} \end{bmatrix} \begin{bmatrix} Z \\ \theta \end{bmatrix} = \begin{bmatrix} 1 \\ c \end{bmatrix} m\omega^2 b e^{j\omega t} \tag{6.1}$$

The solution of the Equation 6.1 are follows [255, 9]:

$$Z = \frac{mb\lambda^2}{M\sqrt{(1-\lambda^2)^2 + (2\zeta\lambda)^2}} e^{-j\phi} \tag{6.2}$$

$$\theta = \frac{-mbc\omega^2}{I(f_2^2 - \omega^2)} e^{-j\phi} \tag{6.3}$$

Here, ζ is the angular damping ratio, and $\lambda = \frac{\omega}{f_1}$. f_1 and f_2 are the translational and tilting frequency of the spindle around its axis.

$$f_1 = \sqrt{\frac{k_r}{M}} \tag{6.4}$$

$$f_2 = \sqrt{\frac{k_{r\theta}}{I}} \tag{6.5}$$

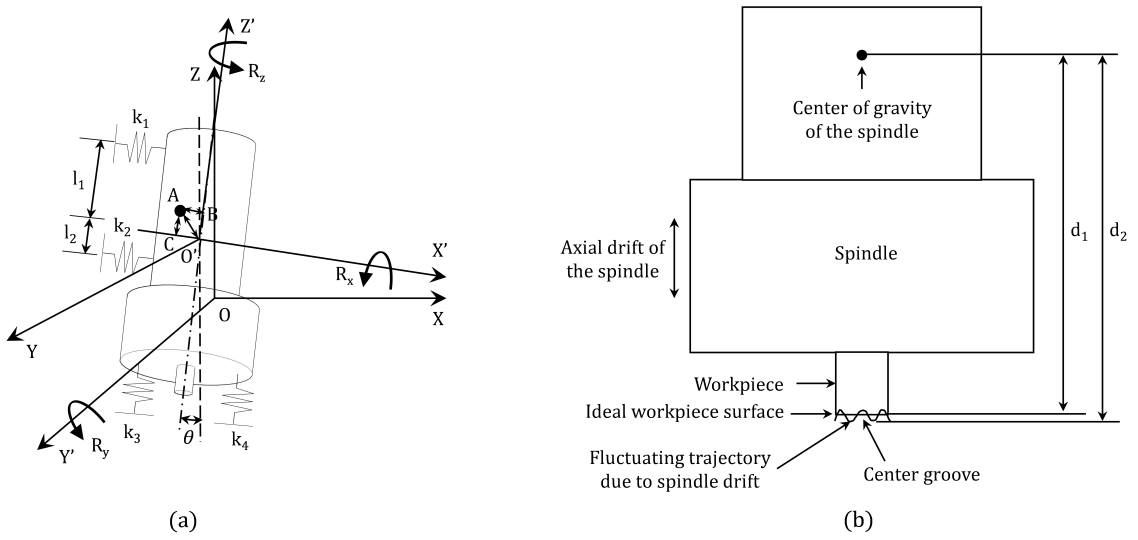

Figure 6.2: (a) The schematic diagram of the spindle system [9]; (b) Fluctuation of the workpiece trajectory due to axial drift of the spindle

It is clear that the equation 6.2 and 6.3 describe the whirling motion of the spindle around its axis. The whirling consists cylindrical whirling (Equation 6.2) as well as conical whirling (Equation 6.3). The whirling motion of the spindle generates low frequency vibration of the spindle affecting the surface geometry and waviness [9]. Due to the combination of cylindrical and conical whirl, a tapering whirl with periodic axis movement is generated. The periodic fluctuation of the spindle axis is superimposed over the workpiece surface. Subsequently, the axial depth of cut is fluctuated. Fig. 6.2 (b) describes the fluctuation of the workpiece trajectory due to spindle drift. d_1 represents the distance between the workpiece surface from the center of gravity of the spindle during no vibration. d_2 represents the distance between the outer point of the workpiece surface from the center of gravity of the spindle during axial vibration due to spindle drift. The amplitude of the periodic axial vibration is D. Other mechanical factors such as tool vibration, material deformation are neglected in the calculation.

$$D = |d_2 - d_1| \tag{6.6}$$

In ideal face turning operation, the cutting tool produces Archimedean spiral trajectory on the workpiece surface. However, the periodic fluctuation of the depth of cut due to axial drift of the spindle causes periodic trajectory of the cutting tool over the workpiece surface. The trajectory of the cutting tool on the workpiece surface can be defined using Equation 6.7. Here, N denotes the rotational speed of the spindle (rpm) and t denotes processing time (sec). ω is the angular velocity of the spindle axis during axial vibration. D is calculated from Equation 6.6. f denotes the feed rate in ($\mu m/rev$). x, y, z are the

translation displacement of the workpiece surface along X, Y, Z direction respectively. α is the real number to convert the rpm to angular velocity (rad/s).

$$\begin{cases} x = \frac{fNt}{60} cos \frac{2\pi Nt}{60} \\ y = \frac{fNt}{60} sin \frac{2\pi Nt}{60} \\ z = Dsin\omega t \\ \omega = 2\pi N.\alpha \end{cases} \tag{6.7}$$

Due to spindle drift, a periodic waviness can be observed on the workpiece surface along the circular profile concentric to the workpiece center. This is called lobes-star waviness [9]. Additionally, a groove-like valley may be formed at the center of the workpiece for the presence of spindle drift as shown in Fig. 6.2 (b). This defect is known as center groove and formed due to the fluctuation of axial depth of cut for spindle drift. Due to the presence of the unbalanced mass, the lobes-star waviness may be subjected to large period of fluctuation. By balancing the mass of the spindle system, the period of fluctuation can be reduced. Eventually, an improved and balanced mechanical system of a spindle may resulted in elimination of the lobes-star as well as the valley at the workpiece center.

6.4 Results and discussions

6.4.1 Estimation of spindle drift

The surface topography of the workpiece during face turning at 10000 rpm is presented in Fig. 6.3. The surface has been measured at the center of the workpiece. The measurement location has been selected along a circle of 0.05 mm radius concentric to the center of the workpiece. It is clear from Fig. 6.3 that the lobes-star error that could be caused by the axial drift of the spindle due to unbalanced mass was not present on the workpiece surface profile. However, the periodic fluctuation of the surface profile along the circle of the measurement was still appeared. The amplitude of fluctuation was in the order of 20 nm to 40 nm as shown in Fig. 6.3. Although, large amplitude periodic fluctuation was not observed observed on the surface profile. In addition, a trace of circular groove at the center of the workpiece surface has been observed. This was an evidence of little amount of drift motion present in the current spindle.

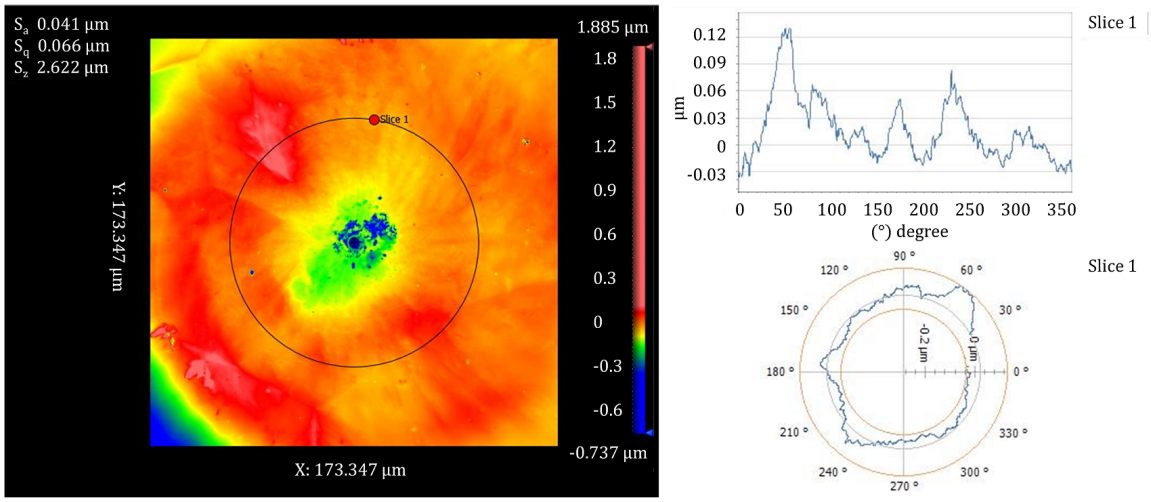

Figure 6.3: The surface topography of the workpiece center generated by face turning at 10000 rpm

The amount of the unbalanced mass can be approximated from the formulation of spindle drift described in section 6.3 and using the Fig. 6.3. The amplitude of the periodic fluctuation can be expressed as Equation 6.2. Due to metal to metal inside the spindle component, the damping ratio ζ has been taken as 0.04. The mass (M) and radial stiffness (k_r) of the spindle have been already mentioned in Table 6.1. Therefore, the translational frequency (f_1) can be calculated as 4867.44 Hz. Meanwhile, the angular velocity of the spindle at 10000 rpm was 1047.2 rad/s. Therefore, the value of λ can be approximated as 0.215. Hence, considering all the values, the amplitude of the periodic fluctuation can be represented as, $Z_a = 0.048mb$. Now, the amplitude of the fluctuation can be approximated from the plot presented in Fig. 6.3 which was approximately 35 nm as measured. Therefore, considering the radial eccentricity (b) of the unbalanced mass as 1 mm, the unbalanced mass (m) can be approximated as 0.732 gm.

The phenomenon of periodic fluctuation of surface profile has been observed at higher spindle rotational speed as well. Fig. 6.4 represents the surface topography of the workpiece during face turning at 27500 rpm. The measurement has been taken along a circle of 0.05 mm radius concentric to the center of the workpiece. Although, a little amount of lobes-star error has been appeared at the workpiece surface, the amplitude of periodic fluctuation was significantly smaller as compared to the surface generated at 10000 rpm. The amplitude of the periodic fluctuation was in the order of 10 nm to 25 nm in this case. Moreover, the large periodic fluctuation of the surface profile has not been observed in this case. It is certain that the periodic fluctuation of the depth of cut due to the axial vibration generated from spindle drift has been reduced significantly at higher rotational speed. The amount of unbalanced mass present in the spindle has been approximated as 0.048 gm for a radial eccentricity of 1 mm at 27500 rpm. Therefore, the ceramic bearing spindle has

been well-balanced at higher rotational speed during its utilization for ultra-precision machining. However, the center groove has been observed in this case as well. Additionally, a conical portion has been observed at the center of the workpiece surface underlying by the centering error of the workpiece.

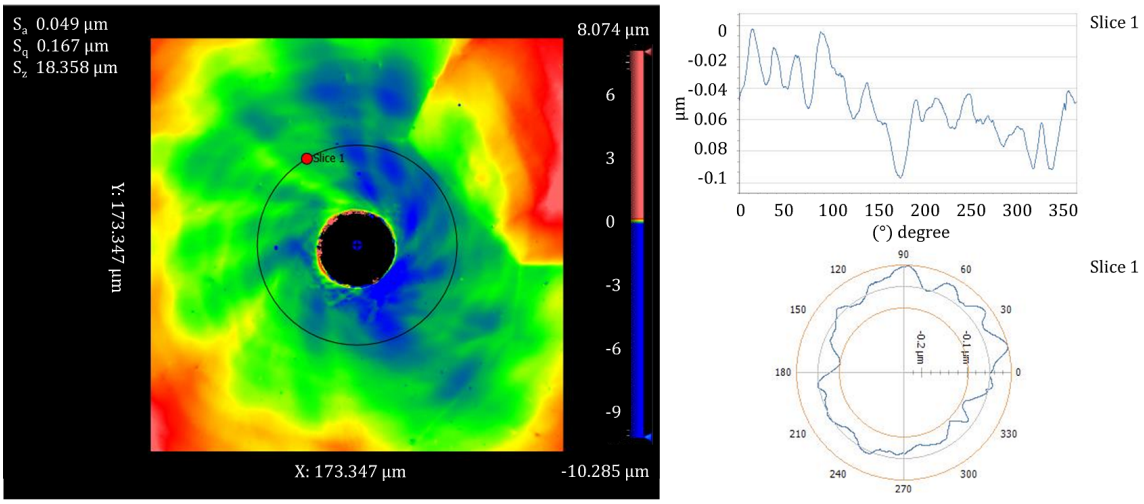

Figure 6.4: The surface topography of the workpiece center generated by face turning at 27500 rpm

The surface quality of the workpiece has been improved as large amplitude periodic fluctuation of the formed profile was not observed on the machined surface. However, uniform periodic fluctuation of shorter amplitude over the surface profile and center groove have been exhibited as a residue of modest spindle drift. This need to be compensated for further improvement of the surface quality. Therefore, the dynamic balancing system of the rotating spindle should be further improved which can be included in future research.

6.4.2 Machine tool vibration

The amplitude of vibration of the machine tool has been approached towards the nanometer level along the axial and radial direction. Fig. 6.5 represents the amplitude vs frequency spectrum of the machine tool along axial and radial directions. The accelerometers can sense the displacement in the nanometer level and measure minimum amplitude of 1 nm. The ME'Scope Ves software initially plotted the amplitude vs frequency spectrum in terms of acceleration. Further integrating twice the signal, the displacement spectrum has been achieved and shown in Fig. 6.5. The frequency indicates corresponding rotational speed (rpm) of the spindle. The formation of peaks has started at the frequency of 166.6 Hz as the machining starts from 10000 rpm. After that, distinguished peaks have been formed at each operating frequency at which the machining has been performed. Fig. 6.5 shows the combination of all the peaks for simplified analysis of the amplitudes. The largest peak has

been observed at 166.6 Hz for axial vibration and the corresponding amplitude was 36 nm. Similarly, the largest peak has been observed at the same frequency for radial vibration as well; and the corresponding amplitude was 16 nm. Hence, the resonant frequency of the ultra-precision machine tool was 166.6 Hz. It has been observed that the amplitude of vibration has been reduced at higher operating frequencies. This has been attributed to the fact that the cutting force has been reduced at higher rotational speed (higher operating frequency) in case of high speed machining [224]. Therefore, the force transmitted to the structure was lesser at higher operating frequency resulting in lower vibration. In addition, the machine structure was highly rigid to absorb the vibration at higher operating frequency. Probable occurrence of second order frequency of resonance has resulted in instantaneous larger peak at 333.3 Hz. The amplitude of axial vibration has been observed to be slightly higher as compared to the radial vibration. In general, the axial thrust force has been appeared in this direction which dominated the transmitted force to the machine tool. Moreover, the axial vibration of the machine tool directly influenced the formation of roughness on the machined surface. Eventually, the amplitudes of vibration within the working range of the operating frequencies have been found to be in nanometer range. Therefore, the machine tool has shown superior dynamic stability even during high speed operation. Hence, the machine tool has fulfilled the criteria to be used as an ultra-precision machine tool.

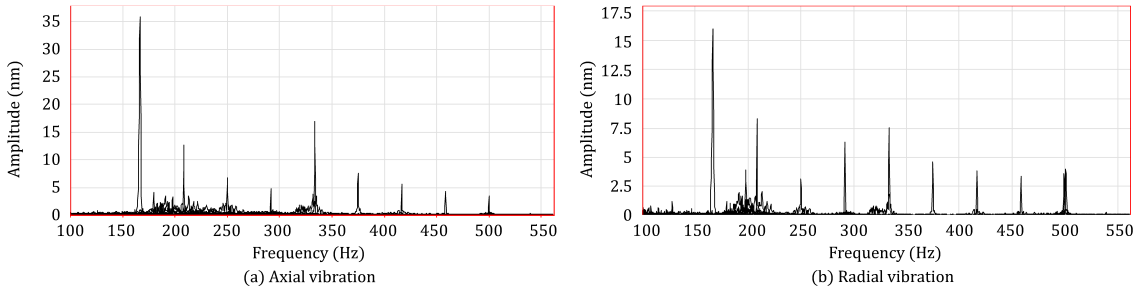

Figure 6.5: Amplitude vs Frequency spectrum of the machine tool along axial and radial direction

6.4.3 Surface topography

The surface finish is the most significant output parameter to determine the product quality in ultra-precision machining. All the measurements of surface topography have been taken based on ISO standard (ISO 4288-1996). Based on the measurement, the variation of average surface roughness (S_a) at different spindle rotational speed is depicted in Fig. 6.6. It is clear from Fig. 6.6 that the surface roughness was not much influenced by the spindle rotational speed. No significant trend has been observed for the average surface roughness

with the variation of cutting speed. The S_a values have been varied from 7 nm to 51 nm at different locations of the workpiece surfaces. However, the minimum surface roughness has been achieved at 10000 rpm. Regardless of high cutting speed (Spindle rotational speed 10000 to 30000 rpm), the average surface roughness has been found in the nanometer level for all the samples. Additionally, super finished range of surface roughness has been achieved on the machined surface even on difficult-to-machine lead free brass.

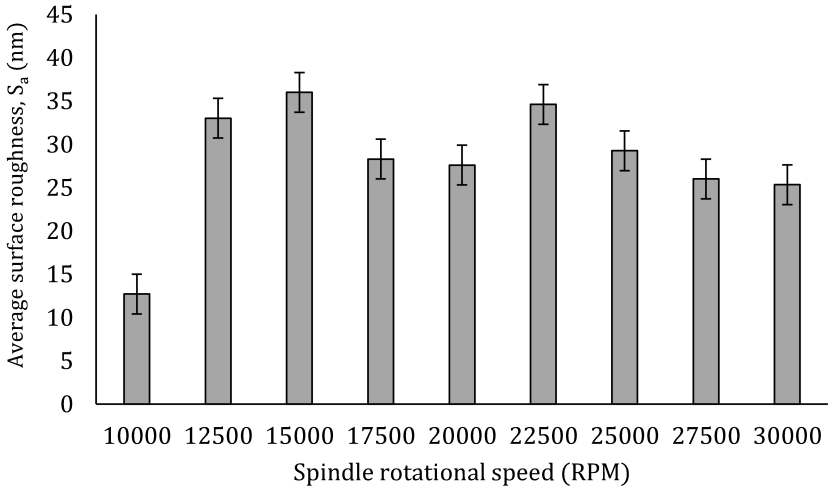

Figure 6.6: Variation of average surface roughness (S_a) at different spindle rotational speed

Apart from the spindle rotational speed, the surface topography has been substantially influenced by some uncontrollable parameters such as workpiece centering error, spindle drift, and material properties. A marginal workpiece centering error may led to some residual amount of workpiece material present at the center of the machined surface. Fig. 6.7 shows the formation of the center residual part of the workpiece due to workpiece centering error. As the machining progresses, the uncut area of workpiece is reduced towards the center. Due to centering error, a small portion remains uncut at the center of the workpiece forming the residual center cone. The residual parts are mostly cylindrical or conical in shape [256]. However, this is completely undesirable in case of ultra-precision machining. This phenomenon was responsible for slightly elevated surface roughness on the machined surface. To compensate the problem, an advanced microscopic camera having high resolution with a proper coordinate measuring system needs to be attached to detect the exact tool-work control monitoring and position control. It should detect the exact coordinate of the workpiece surface and determine the center of the workpiece. Fig. 6.8 (a) shows the original machined surface on the lead free brass sample. Mirror finish has been achieved on the machined surface which shows a clear reflection of the paper sheet on which the sample has been located. Even the wrinkle marks present on the paper sheet has been reflected

on the machined surface. However, the center cone was still appeared on the workpiece surface as shown in the two-dimensional topography of the surface presented in Fig. 6.8 (b). This induced a variation of surface roughness on the machined surface at different location. Fig. 6.8 (b) shows the roughness has been increased at a particular distance from the center. This was caused by adhesion of small chip particles on the surface at a particular position concentric to the workpiece center. The FESEM image presented in Fig. 6.10 confirms the tendency of small chip adhesion on the machined surface.

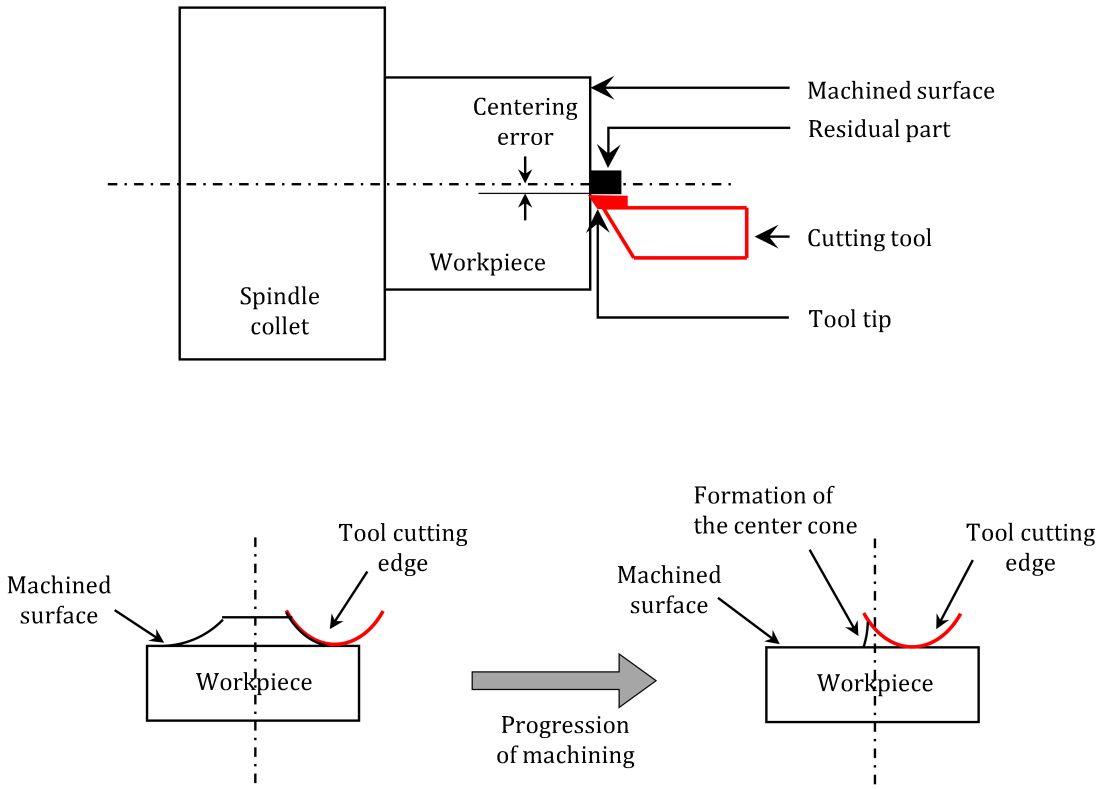

Figure 6.7: Mechanism of forming the center cone at the workpiece center due to workpiece centering error

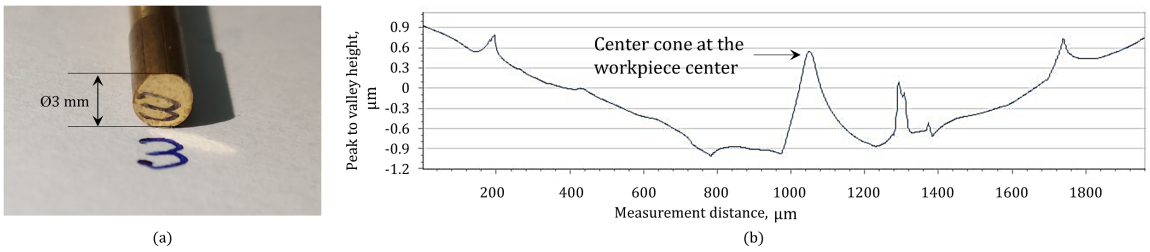

Figure 6.8: (a) Original machined surface generated on lead free brass sample by ultra-precision diamond turning; (b) Two-dimensional surface topography of the machined surface showing the center cone

High amplitude periodic fluctuation of depth of cut due to axial spindle drift was disap-

peared in this case. Nevertheless, lower amplitude periodic fluctuation has been observed on the machined surface due to spindle drift which induced some surface roughness. In addition, a little amount of spindle drift has resulted in formation of center grooves on the machined surface. This phenomenon further induced a small amount of surface roughness on the machined surface. As shown in Fig. 6.3 and Fig. 6.4, the center grooves have been visible on the machined surface generated in all spindle rotational speeds. Therefore, a deeper valley has been generated at the center of the workpiece as compared to the outer peripheral zone of the machined surface under this circumstances. Consequently, a variation of surface roughness has been perceived at different location of the workpiece surface.

The workpiece material property has significant influence on the surface roughness of the workpiece. The chip formation was not favorable for lead free brass during the face turning operation due to its rapid ductility. Long chip formation was a widespread challenging issue during machining of lead free brass [226]. The long chips formed during the machining experiments have accumulated at the tip of the diamond insert and rubbed over the machined surface as the machining progressed. Consequently, some scratches or valleys have been generated on the machined surface after a while of starting the machining. This phenomenon resulted in some variation of surface roughness on the workpiece as well. Fig. 6.9 represents the surface profilometry of the machined surface generated at 10000 rpm measured at the workpiece center. The valleys generated by center grooves due to spindle drift and scratches due to rubbing with longer chips have been observed on the profilometry. The long continuous chips have been already presented in Fig. 6.13 which was clearly observed to accumulate at the tool tip during the machining process. As nanometric mirror finish was generated on the machined surface, a little amount of rubbing of the chips induced some scratches or valleys leading to higher surface roughness. The scratches and valleys were found especially after a while of starting the machining or at the end position which was at the center of the workpiece as shown in Fig. 6.9. This phenomenon confirms the rubbing of the chips on the machined surface which was formed and accumulated on the tool tip after a while of starting the machining. Additionally, the continuous interaction between diamond insert and the workpiece has resulted in marginal abrasion on the tool flank surface. Subsequently, a little amount of carbon particles have lost their bond strength and deposited over the machined surface. Furthermore, a marginal amount of cutting heat has been generated at the chip-tool interface due to high speed machining under dry condition. This phenomenon led to oxidation of zinc content in the brass alloy in open environment. The ZnO further reacted with the carbon atom present in the diamond tool. Therefore, a little amount of carbon diffused from the tool material and combined with the Zn content on the workpiece surface. Fig. 6.10 shows FESEM

micrograph of machined surface and the EDS analysis with elementary mapping of the machined surface. The EDS analysis clearly shows that the amount of carbon over the machined surface was approximately 9% in terms of weight. The elemental mapping further confirms the presence of carbon particles over the machined surface. Moreover, the scattering of carbon particles has induced little amount of surface roughness on the workpiece and influenced the variation of the surface roughness at different locations of the machined surface. The FESEM micrograph of the machined surface presented in Fig. 6.10 shows that the deposition of carbon particles induced a slight amount of surface roughness over the clean surface. Additionally, the adhesion of small chip particles shown in the FESEM micrograph presented in Fig. 6.10 confirms the rubbing of chips on the machined surface inducing surface roughness.

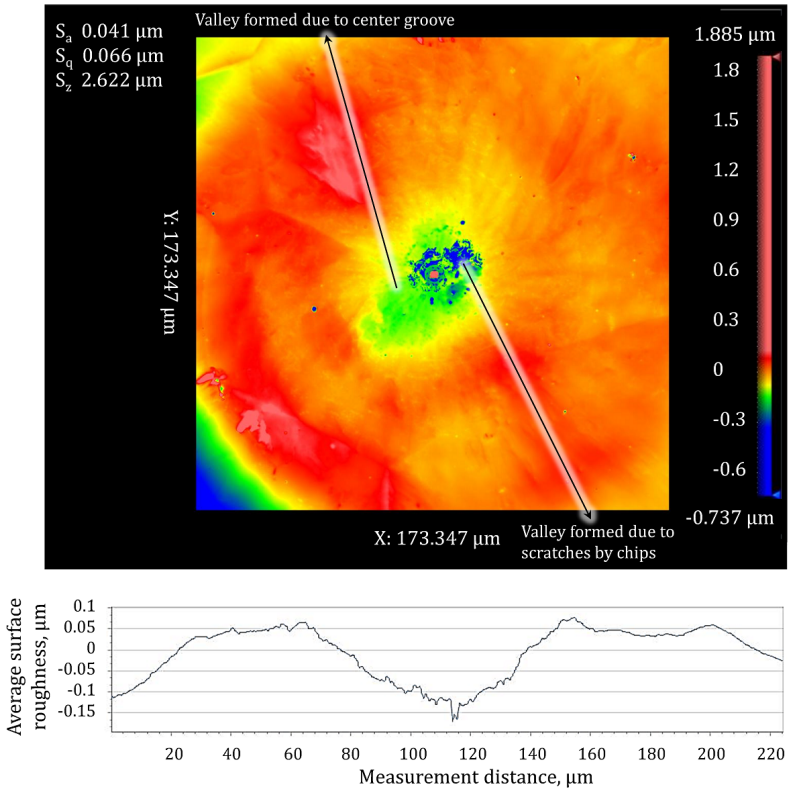

Figure 6.9: The surface profilometry of the machined surface at 10000 rpm measured at the center of the workpiece

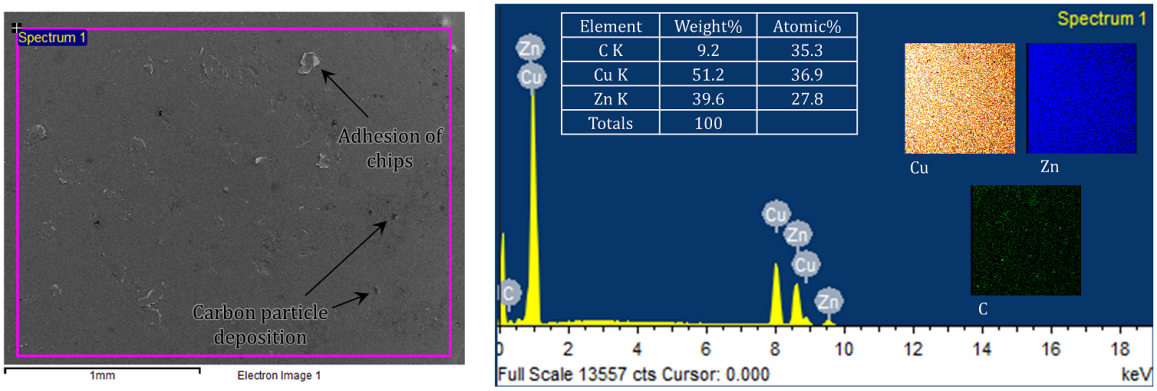

Figure 6.10: FESEM micrograph of machined surface and EDS analysis with elemental mapping of the machined surface

Moreover, nano finishing has been achieved over all the machined surfaces. Fig. 6.11 represents the surface profilometries of the machined surfaces achieved at different spindle rotational speed. Clean feed marks have been found over the machined surface with very negligible surface defects. Additionally, a tendency of lay marks have been found over the machined surface as shown in Fig. 6.11. In the present study, the machining operation has been performed at a combination of high spindle speed and low depth of cut. Due to the ultra-fine feed rate, the feed marks are very dense. Additionally, high spindle speed was responsible for a small amount of tool interference. Therefore, a tendency of irregular feed marks has been found over the machined surface as lay marks. Very few peaks and valleys have been observed over the machined surface apart from the machining marks. Some deep valleys have been observed on the machined surfaces generated due to diffusion of Zn atoms from the brass alloy. This has been attributed to ZnO formation at the machined surface. Furthermore, continuous super finished surface has been observed even at very high spindle rotational speed. Further, the machined surfaces have been investigated in FESEM. Fig. 6.12 represents the FESEM images of the machined surfaces achieved at different spindle rotational speed. No significant defects over the machined surfaces have been found in FESEM. At most feed marks and cutting marks have been observed on the machined surface. Apart from that, the surfaces were mostly smooth in nature. A marginal amount of foreign particles deposition have been observed. These might be the carbon particles appeared over the machined surface. Hence, the developed machine tool with ceramic bearing spindle was very much able to generate mirror finished surfaces in diamond turning even on difficult-to-machine materials. Therefore, the machine tool with the ceramic bearing spindle was capable to be used as an ultra-precision machine tool for producing super-finished surfaces.

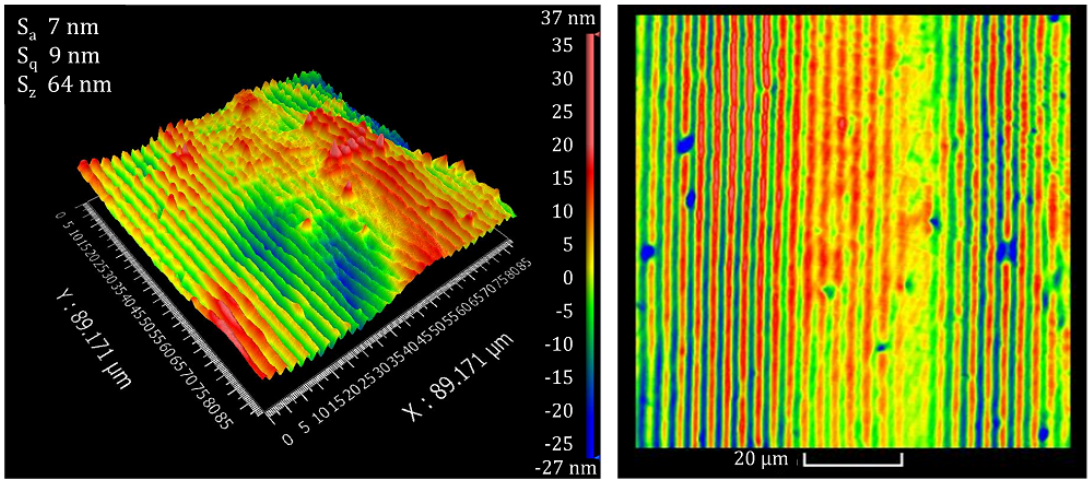

(a) Spindle rotational speed: 10000 rpm

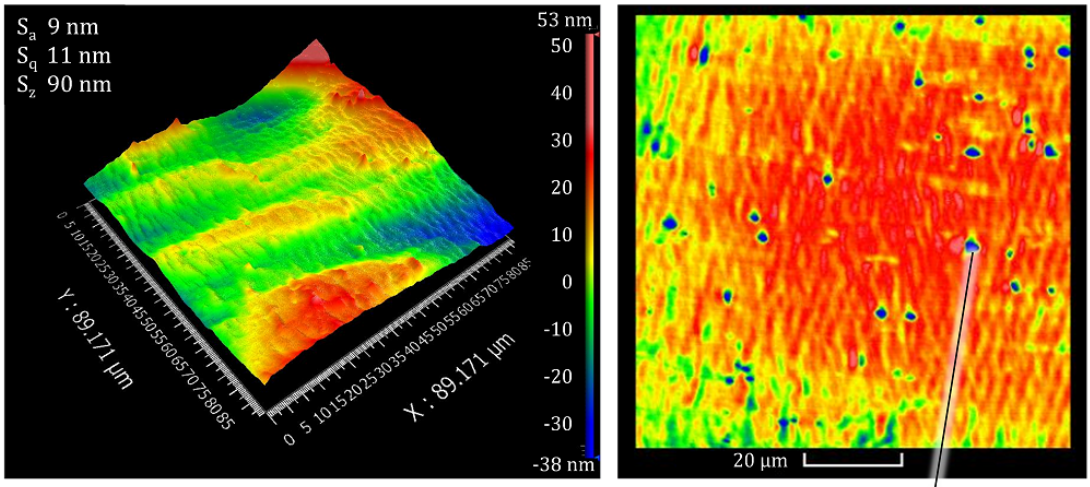

(b) Spindle rotational speed: 17500 rpm

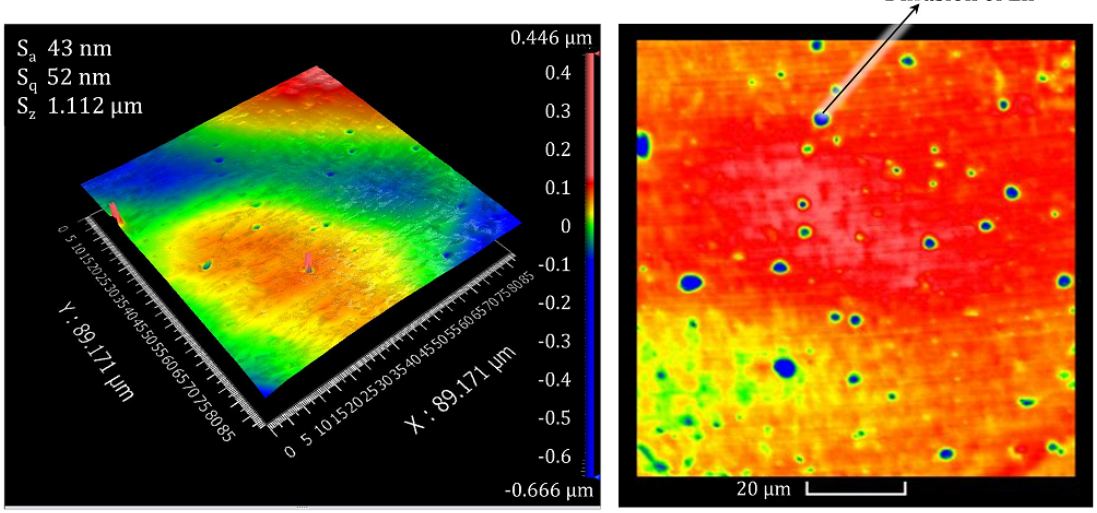

(c) Spindle rotational speed: 27500 rpm

Figure 6.11: Surface profilometries of the machined surfaces generated at different spindle rotational speeds in ultra-precision diamond turning

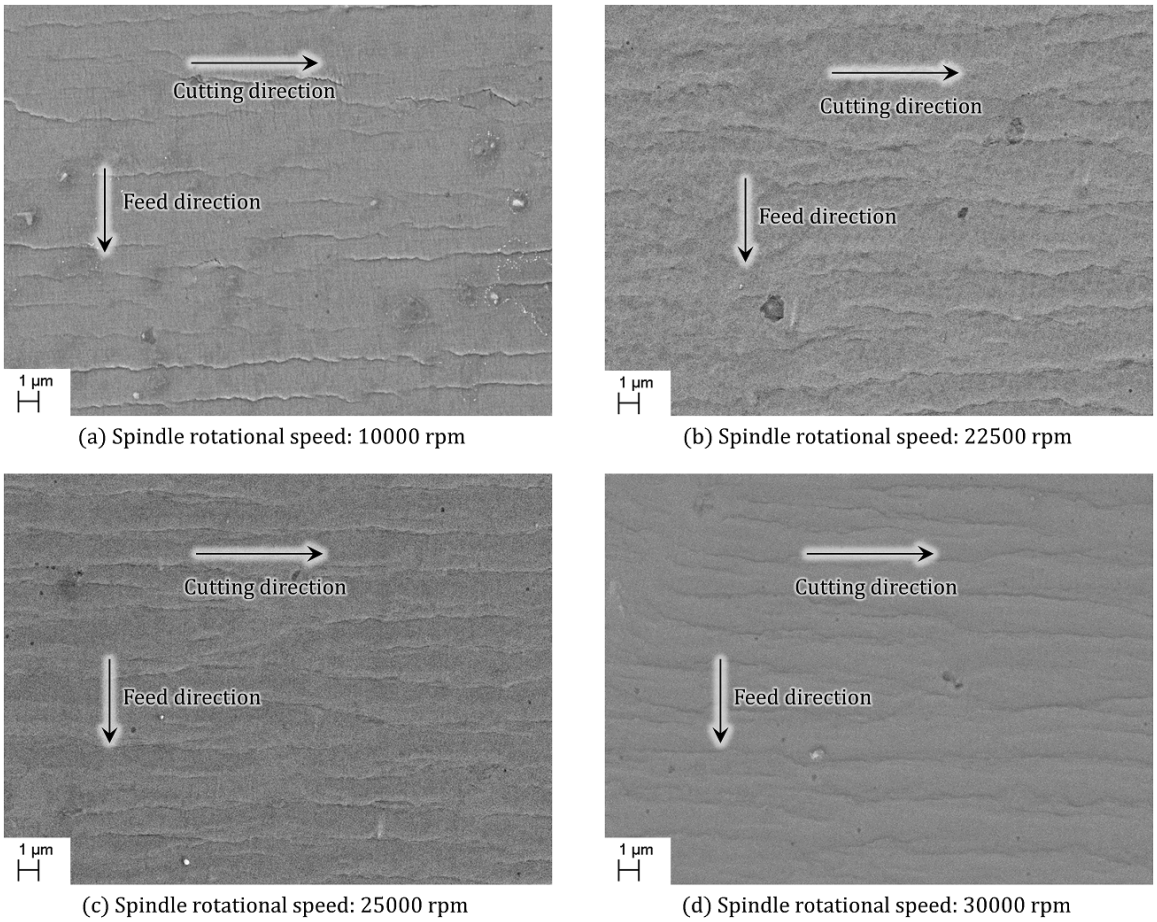

Figure 6.12: FESEM images of the machined surfaces generated at different spindle rotational speeds

6.4.4 Chip morphology and tool wear

The chip formation is a significant parameter to determine the tribological performance of the workpiece. The shear strength of the brass alloy has been increased owing to the disappearance of lead. This phenomenon has resulted in enhancement of ductility. Therefore, the chip breakage was not favorable during the ultra-precision machining. Similar type of chips has been formed during the machining operation at different rotational speeds. Fig. 6.13 represents the microscopic view of the chip morphology generated during the machining operation. In general, ribbon type chip has been formed. The chip was long and continuous. Therefore, the chip has been accumulated at the tip of the cutting tool as the machining has been progressed. As a result, the chip has started rubbing over the machined surface and formed scratches and valleys as shown in Fig. 6.9 inducing some surface roughness. Additionally, the FESEM micrograph presented in Fig. 6.10 confirms the presence of small chip particles adhered on the machined surface which ascertains the

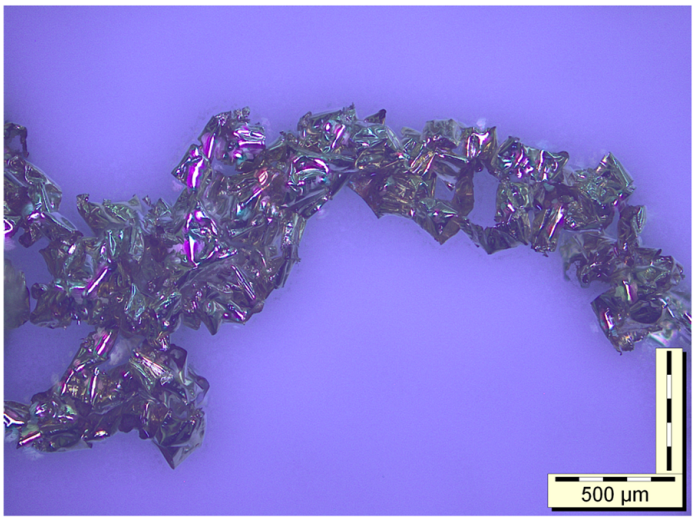

Figure 6.13: Long and continuous chip formation during the machining operations

rubbing phenomenon of the chips. As mirror finish was generated (within 50 nm), it was highly vulnerable to surface roughness as the hardness of the workpiece material was moderate (136 HV). The rubbing phenomenon of the chips induced a little amount of roughness on the machined surface. Due to low feed rate and low depth of cut, the amount of heat generation was small during the machining operation. Consequently, the formation of adiabatic shear band has been restricted. Therefore, both the surfaces of the chip was shiny and smooth in nature.

All the machining experiments have been performed with a single diamond insert. After completing all the experiments, the diamond insert has been subjected to tool wear analysis. Fig. 6.14 depicts the microscopic view of the flank surfaces of the used and a new tool. It is clear from Fig. 6.14 that the diamond insert has comprised of the sharp cutting edge even after machining 54 mm at different cutting speeds. Negligible flank wear has been observed on the diamond insert. This phenomenon has been attributed to very high hardness of the cutting tool as compared to the workpiece material. Additionally, elevated thermal conductivity of the workpiece material has led to minimize the thermal load on the cutting edge of the tool. Moreover, high thermal resistance of diamond has made the diamond insert less susceptible to thermal loading [257]. The micro craters like defects present on the flank surface of the new diamond insert has been disappeared in case of the used tool. This may be due to continuous interaction between the cutting tool and the workpiece during machining led to surface modification of the cutting tool. Some traces of the chip particles have been found adhered to the flank surface of the diamond insert. The reason was continuous accumulation of the chip at the tool tip. However, due to abrasion, a little amount of carbon particles have lost their bond strength and deposited over the machined surface. Additionally, diffusion of carbon atom has been occurred as well react-

ing with the ZnO on the machined surface. The EDS analysis presented in Fig. 6.10 has confirmed the appearance of carbon particles over the machined surface. Moreover, steady state performance has been observed by the diamond insert during the ultra-precision diamond turning of the lead free brass.

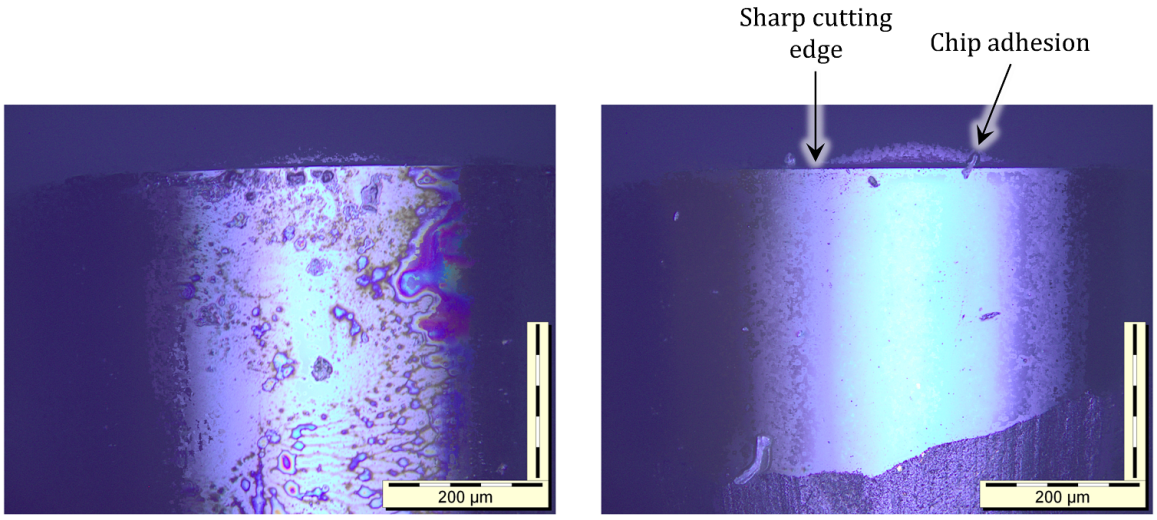

(a) New diamond insert (b) Used diamond insert

Figure 6.14: The microscopic images of the flank surface of (a) the unused diamond insert; and (b) the diamond insert used for machining operating

6.5 Economical and environmental sustainability

6.5.1 Economical assessment

The machine tool was capable to generate super finished surfaces on lead free brass which is a difficult-to-machine material. Fig. 6.15 shows the different range of surface roughness achieved on brass alloys in previous literatures [171, 258, 259] and the present study using ultra-precision diamond turning. It can be seen that the range of the average surface roughness achieved in the present study was quite comparable with the previous studies performed in expensive ultra-precision machine tool. The present experiment has precipitated even better results as compared to some previous studies as shown in Fig. 6.15. Therefore, the machine tool including a ceramic bearing spindle can be considered as a ultra-precision machine tool.

Economy is a major aspect to determine the sustainability of a process. In this study, the total economy has been divided into several subcategory. These are the machined tool development cost, cost involved in cutting tool consumption, labour cost, energy consumption. Besides, the cost involved in waste management has been incorporated to calculate

the overall cost. However, the cost involved in cutting tool consumption, labour cost, and waste management are same for all the machine tools irrespective of its precision. Negligible difference in energy consumption has been considered in this economical analysis. However, the difference was significantly observed in the machine tool development cost.

The machine tool development cost incorporated the cost of the spindle and its controller, the cost of the linear stages and its controller, cost of the machine structure, and the cost for other accessories like compressor. As the present machine tool incorporated ceramic bearing spindle, the cost involved in the spindle and controller was 11500 USD. This was significantly lower as compared to the air bearing spindle used in conventional ultra-precision machine tool. Table 6.3 shows an approximation of the costs involved in the machine tool. It can be observed that the cost involved in the spindle and linear stages are approximately 6 times higher for the conventional ultra-precision machine tool as compared to present machine tool. Subsequently, the total cost involved in the development of the present machine tool has become 4 times smaller as compared to the conventional one.

Table 6.3: An approximation of the costs involved in the present machine tool and conventional ultra-precision machine tool

	Present machine tool		Conventional ultra-precision machine tool	
Machine components	Type	Cost (USD)	Type	Cost (USD)
Spindle and controller	Ceramic bearing spindle	11500	Air bearing spindle	70000
Linear stages and controller	Linear motor drive and Lead screw drive	35000	Hydrostatic bearing slideways with linear motor drives	200000
Machine structure	Granite frame with shock absorber stand	10000	High precision frame with granite bed	10000
Computational facilities		6000		6000
Other accessories like compressors		10000		10000
Total		72500		296000

The air bearing spindle have high technical merit such as nanometric rotational accuracy (in the order of 25 nm). Meanwhile, the present ceramic bearing spindle has a rotational accuracy of 1 μm which is high enough as compared to air bearing spindle. However, the comparison should be based on output parameter such as surface roughness and the present ceramic bearing spindle was able to generate 7 nm surface roughness on lead free brass. The challenging issue with this ceramic bearing spindle is the rotational accuracy which can be focused in future study. If the rotational accuracy can be enhanced, the present ceramic bearing spindle can be commercialized for diamond turning operation

in a cost-effective way. Additionally, the present machine tool with ceramic bearing spindle can be a cost-effective alternate of the expensive ultra-precision machine tool consuming one-fourth development cost of the conventional ultra-precision machine tool. Some additional facilities such as laser based tool-work contact monitoring technology, fast-tool servo mechanism (FTS) can be incorporated in the present machine to make it more precise and efficient in generating the super-finished surfaces. This may further assist to generate several nano features on the workpiece surface with nano finishing as well.

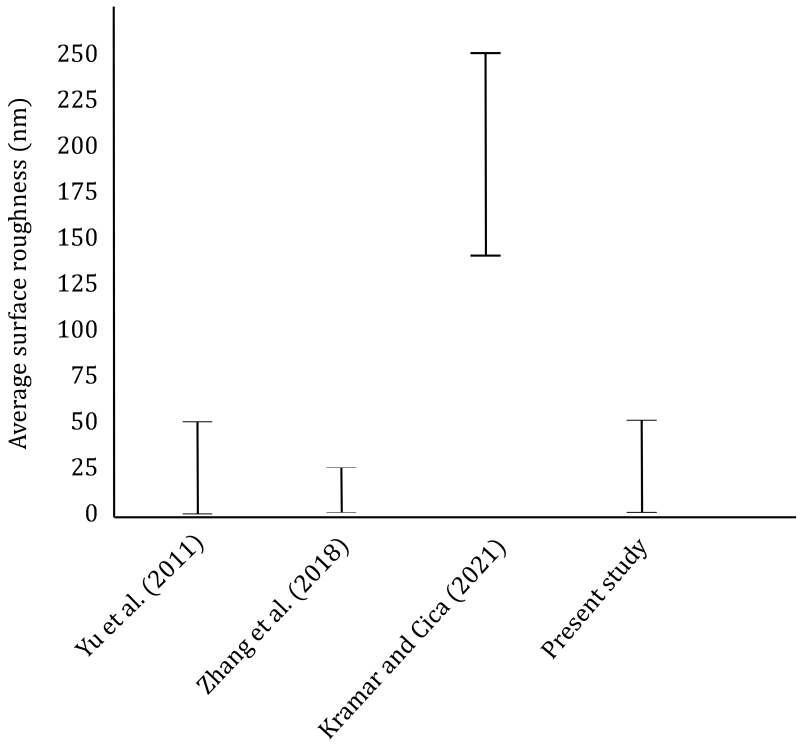

Figure 6.15: The range of average surface roughness on brass alloys found from previous literatures and the present study in ultra-precision diamond turning

6.5.2 Environmental assessment

The environmental sustainability of this study has been determined by calculating the CO_2 emissions. LCA (Life cycle assessment) method has been utilized to estimate the CO_2 emissions. Narita et al. [260] proposed this technique to analyse the environmental impact of a machine tool operation. This technique incorporated the CO_2 emissions from several parameters, such as electricity for the machining operation, consumption of coolants, consumption of the lubricants, utilization of cutting tool utilization, and chip formation. All the calculations have been performed based on the numerical methods proposed by Narita et al. [260]. Table 6.4 enlists the CO_2 emission intensity (EI) from several parameters involved in the present study.

For two hours running of the machine tool including the machining time and the idle time, total electrical energy of 2.02 kWh (EC) has been consumed. The power required for spindle motor, lubricating unit, compressor unit, linear motor drives have been incorporated in the calculation. Machining operations have been performed under dry condition in this experiment. Therefore, the emission involved in the consumption of cutting fluid has been neglected. The lubricating oil has been supplied only to the spindle in the machine tool during operation. For two hours running of the spindle, total discharge of the lubricating oil was 0.008 L. In this experiment, one cutting insert has been used throughout the machining operations. The weight of the insert was 4.15 gm. The mass of the chip was in the order of micro grams and negligible in this study.

Table 6.4: CO_2 emissions from different parameters involved in the ultra-precision machining operations for two hours

Parameter for EI	Total CO_2 emissions (g-CO_2)
Machine tool operation	769.6
Coolant	Not applicable
Lubricating oil	3.8
Cutting tool	140.1
Metal chip	1.88×10^{-5}
Total	976

To evaluate the environmental sustainability of the present study, the calculated data of the CO_2 has been compared with previous literature. Kim et al. [261] investigated a sustainable machining technology and the CO_2 emissions have been evaluated for each parameters. To compare with the previous literature, the results of the present investigation have been scaled for the same operation time as the previous one. Fig. 6.16 shows the comparison of CO_2 emissions from different parameters in the present study and previous literature. It can be seen that the CO_2 emission in the present study was significantly lower (approximately 13 times) as compared to the previous sustainable technology. Hence, it can be said that the present machining technology was environmentally sustainable as well.

In addition, the present study investigated the generation of super finished surfaces on lead free brass by ultra-precision machining. Irrespective of having poor machinability, lead free brass has been promoted to eliminate the detrimental effect of highly toxic lead content on the living beings. Furthermore, dry machining has been performed to minimize the application of hazardous coolant. From environmental aspect, the present technology is highly sustainable in terms of decrement in CO_2 emission, elimination of toxic contents, and reduction in hazardous coolant.

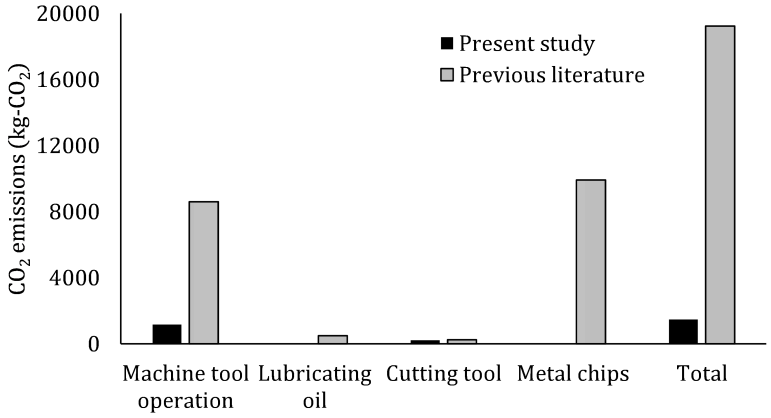

Figure 6.16: Comparison in CO_2 from different parameters in the present study and previous literature

6.6 Summary

The present chapter reveals a cost-effective methodology of producing mirror finish on difficult-to-machine lead free brass by ultra-precision diamond turning. Ultra-precision face turning operation has been performed in an economically developed machine tool comprised of ceramic bearing spindle. The spindle rotational speed has been varied from 10000 to 30000 rpm during the machining operation. The spindle drift, machine tool vibration, surface topography, chip formation, and tool wear have been determined. Eventually, a comparative analysis has been performed to evaluate the economical and environmental sustainability of the presented methodology. Based on the investigations, it has been found that the axial drift was smaller in the ceramic bearing spindle used in this study due to high stiffness. Therefore, large periodic fluctuation of the surface profile was not observed with a marginal formation of lobes-star error on the machined surface. However, small periodic fluctuation of the surface profile and the center groove on the machined surface confirmed a slight amount of spindle drift appeared in the spindle. The amplitude of machine tool vibration was appeared in the nanometer level. The maximum amplitudes of axial and radial vibration were 36 nm and 16 nm at a frequency of 166.6 Hz. Hence, the machine tool was dynamically stable for ultra-precision machining. Mirror surface finish was achieved on lead free brass with an average surface roughness (S_a) varies from 7 nm o 51 nm. The locational variation of S_a was attributed to marginal spindle drift, workpiece centering error, rubbing of longer chips on the machined surface, deposition of carbon particles from the cutting tool. Long and continuous chips have been formed throughout the machining process without chip breakage since rapid shear stability of lead free brass. In addition the flank wear of the diamond insert was negligible after performing all the machining operations. The development cost of the machine tool was approximately 4 times lesser than the

conventional ultra-precision diamond turning machine tool. Therefore, the present machine tool can be a cost-effective alternate of the highly expensive machine tools used to produce super-finished surfaces. Moreover, the carbon emission in the present methodology was significantly less which confirmed the environmental sustainability of this technology as well. Further improvement of the machine tool can be possible by improving the dynamic balancing of the spindle and its rotational accuracy; introducing advanced tool-work contact monitoring and Fast tool servo (FTS) mechanism.

7

Conclusion and Future Scope

The present research work describes the development of a high speed micromachining center and its performance in micro and diamond turning. The work was mostly focused on machining of miniaturized cylindrical components made of ductile materials. In this regard, a dynamically stable high speed micromachining center has been developed to improve the material removal rate in micro turning and achieve the favorable effects of high speed machining. Further, high speed micro turning has been performed on lead free brass components using minimum quantity lubrication and the machinability has been determined. The machinability has been further improved by incorporating hybrid cryogenic cooling. Eventually, an economic diamond turning technology has been proposed using ceramic bearing spindle. This was capable to produce nano finishing on difficult-to-machine lead free brass alloy.

7.1 Key conclusions of the thesis

Based on the modelling and experimental analysis, the following conclusions can be drawn:

7.1.1 Development of a dynamically stable high speed micromachining center

- The design approach was focused on developing a rigid vibration free machine structure to support the high speed spindle. The developed machine structure provided good static, dynamic stiffness and damping performance to the high speed micromachining center. The amplitude of machine tool vibration was approaching towards nanometer level during machining operation. Therefore, the machine tool vibration was reduced significantly utilizing this machine structure. The design approach is appropriate for vibration isolation without utilizing any vibration absorber.

- Natural granite has shown better stiffness, rigidity and damping performance as compared to cast iron. Therefore, the machine structure made of natural granite has shown better performance than structure made of cast iron to reduce structural vibration.

- The amplitude of vibration was reduced with increasing the cutting speed (rotational speed). This was due to lower force transmission at higher cutting speed. Hence, the developed machine structure can be utilized for ultra-high speed machining as well.

- The amplitudes of vibration in the machine tool were reduced by 20% and 19% along Y and Z axis respectively during machining with a four flute milling cutter as compared to two flute milling cutter under similar machining condition. Machining with four flute milling cutter precipitated lower chip load resulted in lower cutting force. Therefore, force transmission to the machine tool was reduced utilizing four flute milling cutter.

- The design of the machine structure was best within the experimental range to minimize the vibration. The thickness, height and width of all components of the structure were determined considering vibration point of view; and to reduce cantilever effect, and to improve structural stiffness.

- Preliminary experiments of high speed micro turning precipitated a large variation of average surface roughness (R_a) and mostly in the order of 2 μm on miniaturized lead free brass samples. This was attributed to tool vibration due to significant overhang, rubbing of chips accumulated on the tool tip with the machined surface, rapid plastic deformation of the machined surface due to cutting heat generated at higher cutting speed.

7.1.2 Machinability assessment of lead free brass in high speed micro turning using minimum quantity lubrication

- The average surface roughness (S_a) has been decreased on increasing the cutting speed due to lower friction, smaller uncut chip thickness, and work hardening. However, it further increased due to resonance condition in the machine tool. Meanwhile, the average surface roughness decreased at upper level of cutting speed. Additionally, the average surface roughness has been increased with feed rate due to higher friction. However, S_a has been initially reduced and then increased with depth of cut. Significant ploughing has dominated at lower level of depth of cut influencing surface roughness. S_a of 281 nm has been achieved in this experiment.

- The maximum peak to valley height (S_z) has shown similar trend as average surface roughness with the cutting speed. However, S_z has been initially decreased and then increased with feed rate as well as depth of cut. This is due to significant ploughing at lower feed rate and depth of cut which accelerated the plastic deformation of the workpiece surface. At higher feed rate and depth of cut, the frictional and compressive force have been increased at the tool-work interface leading to rapid plastic side flow.

- The burr formation was significant on the machined surface especially at lower cutting speed; higher feed rate and depth of cut. The average burr height has shown the similar trend as the maximum peak to valley height (S_z) with the process parameters.

- The chip formation was not favorable due to rapid plastic behavior of lead free brass. Longer chips have been formed at lower cutting speed. However, the chip sizes have become smaller at higher cutting speed due to the dominance of strain hardening. Additionally, shorter chips have been formed at higher feed rate.

- The cutting tools have shown steady state performance with moderate flank wear and negligible crater wear. However, the tool wear rate has been increased with the cutting speed. Both the flank wear land width and flank wear length have been increased at higher cutting speed.

- Based on the ANOVA model, the cutting speed was the most contributing process parameter affecting average surface roughness followed by depth of cut and feed rate. Whereas, the most substantial parameter affecting maximum peak to valley height and burr height was cutting speed followed by feed rate and depth of cut. Based on the analysis, the most optimum combination of process parameters is cutting speed = 125 m/min, feed rate = 3 $\mu m/rev$, depth of cut = 40 μm.

7.1.3 Enhancement in machinability of lead free brass in high speed micro turning incorporating hybrid cryogenic cooling

- The average surface roughness (S_a) was significantly low during machining with hybrid cryogenic cooling (LN2 + MQL) as compared to cutting oil based MQL and cryogenic cooling (LN2). Although the minimum S_a has been found by cryogenic cooling during machining at 240 m/min (S_a = 165 nm). However, constant good quality surface has been achieved by the hybrid cooling technique. This was attributed to combined effect of cryogenic cooling and vegetable oil as lubricant resulted in reduction in plastic side flow of the work material as well as lower friction at the chip-tool interface. The value of S_a has been reduced at higher cutting speed. S_q has shown similar trend as average surface roughness.

- The microhardness has been considerably increased during machining with cryogenic cooling as compared to cutting oil based MQL. This was attributed to higher work hardening of the machined surface due to cryogenic cooling. Additionally, the microhardness has been reduced by some extent during machining with hybrid cryogenic cooling. This was because of lesser adherence of the work material to the cutting tool reduced the level of plastic deformation. Additionally, microhardness has been increased at higher cutting speed owing to strain hardening of the work surface.

- The burr has been reduced significantly on the machined surface during turning at higher cutting speed with hybrid cryogenic cooling technique. Very few instantaneous peaks have been observed on the machined surface generated at high cutting speed with the hybrid cooling technique.

- Longer chips have been observed at lower cutting speed, while shorter chip formation was observed at higher cutting speed. Additionally, the tendency of lamellar chip formation was prominent during machining with cutting oil based MQL and cryogenic cooling. The variations of shear stress field and heat generation within the shear band were responsible for the lamellar chip formation. However, this tendency has been completely diminished under hybrid cryogenic cooling.

- Favorable lubricating interface at the chip-tool contact area has reduced the flank wear during micro turning with hybrid cryogenic cooling irrespective of the cutting speed. However, a tendency of higher flank wear has been observed at higher cutting speed during machining with cutting oil based MQL as well as cryogenic cooling. Significant tool wear has been observed for cryogenic cooling as a result of increased hardness of the work surface.

- Based on the amount of cutting fluid application, cutting tool wear, waste development and management cost, hybrid cryogenic cooling technique has been considered as economically and environmentally sustainable compared to other two cooling techniques. This technique has eliminated hazardous cutting fluid by vegetable oil, and generated very small amount of wastes with negligible carbon emission.

7.1.4 Feasibility of economical diamond turning using ceramic bearing spindle

- The axial drift was small in the ceramic bearing spindle used in this study. Therefore, large periodic fluctuation of surface profile was not observed on the machined surface. However, a marginal amount of spindle drift was still present due to dynamic imbalance causing small amplitude periodic fluctuation of the surface profile, a little amount of lobes-star error formation and center groove on the machined surface. The amplitude of periodic fluctuation has been reduced at higher rotational speed.

- The amplitude of machine tool vibration was appeared in the nanometer level. The maximum amplitudes of axial and radial vibration were 36 nm and 16 nm at a frequency of 166.6 Hz. The amplitude of vibration has been further reduced at higher operating frequency. Therefore, the machine tool has fulfilled the criteria to be used as an ultra-precision machine tool.

- Mirror surface finish was achieved on lead free brass with an average surface roughness (S_a) varies from 7 nm o 51 nm. The surface roughness was not much influenced by spindle rotational speed. However, a variation of S_a was found at different locations of the workpiece surface. This was attributed to marginal spindle drift, workpiece centering error, rubbing of longer chips on the machined surface, deposition of carbon particles from the cutting tool. Moreover, super-finished surface was achieved with minimum defects by the diamond turning experiment.

- The chip formation was not favorable due to rapid ductility of lead free brass. Long and continuous chip formation was observed throughout the machining process without chip breakage. The longer chip was accumulated over the tool tip and subjected to rubbing on the machined surface.

- Negligible tool wear has been observed on the flank surface of the diamond insert after performing the machining operations. The cutting edge retained its sharpness after the machining. This was attributed to very high hardness of the tool material, and high thermal resistance of diamond. However, due to abrasion and diffusion,

a few amount of carbon particles lost their bond strength and deposited over the machined surface.

- The present machine tool with ceramic bearing spindle was able to generate super-finished surfaces by ultra-precision diamond turning in an economical manner. The surface finish achieved in the present study was comparable with the previous studies and some times even better. The development cost of the machine tool was approximately 4 times lesser than the conventional ultra-precision diamond turning machine tool. Therefore, the present machine tool can be a cost-effective alternate of the highly expensive machine tools used to produce super-finished surfaces. In addition, the carbon emission in the present methodology was significantly less which confirmed the environmental sustainability of this technology as well.

7.2 Contribution

The present work provides the following contributions to the research field:

- Development of a dynamically stable high speed micromachining center which was able to machine complex micro components even of difficult-to-machine materials. (Described in Chapter 3)
- Introducing high speed micro turning to improve the productivity of cylindrical micro components. (Described in Chapter 4 and 5)
- Presenting favorable machining techniques and process parameters to achieve superior surface quality and machinability of difficult-to-machine lead free brass having industrial and research significance. (Described in Chapter 4 and 5)
- Development of a cost-effective diamond turning technology using ceramic bearing spindle able to generate nano finished surfaces. (Described in Chapter 6)

7.3 Future scope

The present research work opens the following research scopes which can be explored in future:

- Applicability of high speed micro turning on difficult-to-machine superalloys having elevated hardness and low thermal conductivity can be explored. It is very difficult to control the heat accumulation at the chip-tool interface for those alloys which further

degrades the machining performance. Therefore, minimization of the cutting heat at the chip-tool interface during high speed micro turning of those superalloys need to be focused in future research.

- MEMS (Micro-Electro-Mechanical System) based devices are highly applicable for electronic and biomedical implants comprising components of submillimeter range. Fabrication of those submillimeter miniaturized components can be explored in high speed micro turning for improved productivity without affecting the dimensional accuracy.

- The rotational accuracy of the ceramic bearing spindle was in the order of 1 μm. Further research needs to be focused on enhancing the rotational accuracy by applying improved dynamic balancing which will ameliorate the surface quality and dimensional accuracy of the components in diamond turning.

- Accurate monitoring of the tool-work contact was very difficult during the diamond turning operation. Therefore, an automated sensor-based tool-work contact monitoring technology can be developed to incorporate in the developed cost-effective diamond turning machine tool which will further enhance the monitoring accuracy and reduce the time consumption.

- A combined operational interface can be developed for the linear stages and the spindle of the ultra-precision machine tool by combining the IP addresses of the controllers of both devices. It will prompt more user-friendly and expeditious operation of those devices. In addition, it will make the machine tool more compact and suitable for the application in Industry 4.0.

- Technologies need to be developed for reducing the tool wear of diamond inserts during diamond turning of ferrous alloys.

References

[1] A. Asad, T. Masaki, M. Rahman, H. Lim, Y. Wong, Tool-based micro-machining, Journal of Materials Processing Technology 192 (2007) 204–211.

[2] B. Boswell, M. Islam, I. J. Davies, A review of micro-mechanical cutting, The International Journal of Advanced Manufacturing Technology 94 (2018) 789–806.

[3] W.-L. Zhu, F. Duan, X. Zhang, Z. Zhu, B.-F. Ju, A new diamond machining approach for extendable fabrication of micro-freeform lens array, International Journal of Machine Tools and Manufacture 124 (2018) 134–148.

[4] X. Wu, L. Li, M. Zhao, N. He, Experimental investigation of specific cutting energy and surface quality based on negative effective rake angle in micro turning, The International Journal of Advanced Manufacturing Technology 82 (2016) 1941–1947.

[5] P. Cui, Z. Shi, X. Li, N. Duan, Evaluation of specific cutting energy considering effects of cutting tool geometry during micro-machining process, The International Journal of Advanced Manufacturing Technology 102 (2019) 1127–1139.

[6] K. Liu, S. N. Melkote, Effect of plastic side flow on surface roughness in micro-turning process, International Journal of Machine Tools and Manufacture 46 (2006) 1778–1785.

[7] E. O. Ezugwu, J. Bonney, R. B. Da Silva, O. Çakir, Surface integrity of finished turned ti–6al–4v alloy with pcd tools using conventional and high pressure coolant supplies, International Journal of Machine Tools and Manufacture 47 (2007) 884–891.

[8] Q. Zhang, N. Guo, Y. Chen, Y. Fu, Q. Zhao, Simulation and experimental study on the surface generation mechanism of cu alloys in ultra-precision diamond turning, Micromachines 10 (2019) 573.

[9] Q. Wu, Y. Sun, W. Chen, G. Chen, Theoretical and experimental investigation of spindle axial drift and its effect on surface topography in ultra-precision diamond

turning, International Journal of Machine Tools and Manufacture 116 (2017) 107–113.

[10] J. Yang, X. Wang, M. Kang, Finite element simulation of surface roughness in diamond turning of spherical surfaces, Journal of Manufacturing Processes 31 (2018) 768–775.

[11] L. Zou, Y. Huang, M. Zhou, Y. Yang, Effect of cryogenic minimum quantity lubrication on machinability of diamond tool in ultraprecision turning of 3cr2nimo steel, Materials and Manufacturing Processes 33 (2018) 943–949.

[12] G. Yingfei, X. Jiuhua, Y. Hui, Diamond tools wear and their applicability when ultra-precision turning of sicp/2009al matrix composite, Wear 269 (2010) 699–708.

[13] S. Zhang, S. To, G. Zhang, Diamond tool wear in ultra-precision machining, The International Journal of Advanced Manufacturing Technology 88 (2017) 613–641.

[14] C. He, W. Zong, J. Zhang, Influencing factors and theoretical modeling methods of surface roughness in turning process: State-of-the-art, International Journal of Machine Tools and Manufacture 129 (2018) 15–26.

[15] D. Huo, K. Cheng, F. Wardle, Design of a five-axis ultra-precision micro-milling machine—ultramill. part 1: holistic design approach, design considerations and specifications, The International Journal of Advanced Manufacturing Technology 47 (2010) 867–877.

[16] S. Leo Kumar, D. Avinash, Influence of cutting conditions on surface characteristics in micro-milling of ti-6al-7nb alloy, Materials and Manufacturing Processes 34 (2019) 1783–1791.

[17] S. Z. Chavoshi, X. Luo, Hybrid micro-machining processes: a review, Precision Engineering 41 (2015) 1–23.

[18] D. Germain, G. Fromentin, G. Poulachon, S. Bissey-Breton, From large-scale to micromachining: A review of force prediction models, Journal of Manufacturing Processes 15 (2013) 389–401.

[19] W. Grzesik, Advanced machining processes of metallic materials: theory, modelling and applications, Elsevier, 2008.

[20] S. L. Kumar, Measurement and uncertainty analysis of surface roughness and material removal rate in micro turning operation and process parameters optimization, Measurement 140 (2019) 538–547.

[21] S. Singh, V. Ghai, A. Agrawal, H. Singh, Effect of machining parameters on cutting force during micro-turning of a brass rod, Materials and Manufacturing Processes 34 (2019) 1816–1823.

[22] T. Jagadesh, G. Samuel, Mechanistic and finite element model for prediction of cutting forces during micro-turning of titanium alloy, Machining Science and Technology 19 (2015) 593–629.

[23] J. V. Elias, S. Asams, J. Mathew, Worn tool geometry–based flank wear prediction in micro turning, Proceedings of the Institution of Mechanical Engineers, Part B: Journal of Engineering Manufacture 234 (2020) 710–719.

[24] G. Kibria, B. Doloi, B. Bhattacharyya, Experimental analysis on nd: Yag laser micro-turning of alumina ceramic, The International Journal of Advanced Manufacturing Technology 50 (2010) 643–650.

[25] A. Das, D. Kumar, M. Kumar, V. Bajpai, Experimental investigation of electrochemical micro turning of ti6al4v with naoh solution, in: International Manufacturing Science and Engineering Conference, volume 84263, American Society of Mechanical Engineers, p. V002T08A007.

[26] Z. F. Rad, P. D. Prewett, G. J. Davies, An overview of microneedle applications, materials, and fabrication methods, Beilstein Journal of Nanotechnology 12 (2021) 1034–1046.

[27] G. Quintana, J. Ciurana, Chatter in machining processes: A review, Int J Mach Tools Manuf 51 (2011) 363–376.

[28] N. Ikawa, R. Donaldson, R. Komanduri, W. König, P. McKeown, T. Moriwaki, I. Stowers, Ultraprecision metal cutting—the past, the present and the future, CIRP annals 40 (1991) 587–594.

[29] A. Dodmani, S. Subbiah, Theoretical cutting edge radius on single crystal diamond tool.

[30] T. Otieno, K. Abou-El-Hossein, Surface roughness analysis when diamond turning optical grade rapidly solidified aluminium rsa 905, Journal of Optics 46 (2017) 446–455.

[31] Z. Wang, J. Zhang, G. Li, Z. Xu, H. Zhang, J. Zhang, A. Hartmaier, F. Fang, Y. Yan, T. Sun, Anisotropy-related machining characteristics in ultra-precision diamond cutting of crystalline copper, Nanomanufacturing and Metrology 3 (2020) 123–132.

[32] C. Evans, J. Bryan, Cryogenic diamond turning of stainless steel, CIRP annals 40 (1991) 571–575.

[33] T. Chabot, D. Brousseau, H. Auger, S. Thibault, Diamond turning of aluminum image slicers for astronomical applications, in: Optifab 2019, volume 11175, SPIE, pp. 392–401.

[34] D. Fedorynenko, R. Kirigaya, Y. Nakao, Dynamic characteristics of spindle with water-lubricated hydrostatic bearings for ultra-precision machine tools, Precision Engineering 63 (2020) 187–196.

[35] S. Zhang, S. To, A theoretical and experimental investigation into multimode tool vibration with surface generation in ultra-precision diamond turning, International Journal of Machine Tools and Manufacture 72 (2013) 32–36.

[36] S. Jahanmir, Surface integrity in ultrahigh speed micromachining, Procedia Engineering 19 (2011) 156–161.

[37] E. Kuram, B. Ozcelik, Micro Milling, Springer Berlin Heidelberg, Berlin, Heidelberg, pp. 325–365.

[38] D. Huo, K. Cheng, F. Wardle, Design of a five-axis ultraprecision micro-milling machine—ultramill. part 2: integrated dynamic modelling, design optimization and analysis, Int J Adv Manuf Technol 47 (2010) 879–890.

[39] R. K. Mittal, S. S. Kulkarni, R. K. Singh, Effect of lubrication on machining response and dynamic instability in high-speed micromilling of ti-6al-4v, Journal of Manufacturing Processes 28 (2017) 413–421.

[40] Z. Lu, T. Yoneyama, Micro cutting in the micro lathe turning system, International Journal of machine tools and manufacture 39 (1999) 1171–1183.

[41] I. Piotrowska, C. Brandt, H. R. Karimi, P. Maass, Mathematical model of micro turning process, The International Journal of Advanced Manufacturing Technology 45 (2009) 33–40.

[42] M. Durairaj, S. Gowri, Parametric optimization for improved tool life and surface finish in micro turning using genetic algorithm, Procedia Engineering 64 (2013) 878–887.

[43] R. M'saoubi, H. Chandrasekaran, Investigation of the effects of tool micro-geometry and coating on tool temperature during orthogonal turning of quenched and tem-

pered steel, International Journal of Machine Tools and Manufacture 44 (2004) 213–224.

[44] T. Jagadesh, G. Samuel, Investigations into cutting forces and surface roughness in micro turning of titanium alloy using coated carbide tool, Procedia materials science 5 (2014) 2450–2457.

[45] T. Jagadesh, G. Samuel, Finite element simulations of micro turning of ti-6al-4v using pcd and coated carbide tools, Journal of The Institution of Engineers (India): Series C 98 (2017) 5–15.

[46] K. Aslantas, M. Danish, A. Hasçelik, M. Mia, M. Gupta, T. Ginta, H. Ijaz, Investigations on surface roughness and tool wear characteristics in micro-turning of ti-6al-4v alloy, Materials 13 (2020) 2998.

[47] J. A. de Oliveira, S. L. M. Ribeiro Filho, C. H. Lauro, L. C. Brandão, Analysis of the micro turning process in the ti-6al-4v titanium alloy, The International Journal of Advanced Manufacturing Technology 92 (2017) 4009–4016.

[48] S. Selvakumar, V. Sreebalaji, K. Ravikumar, Machinability analysis and optimization in micro turning on tool wear for titanium alloy, Materials and Manufacturing Processes 36 (2021) 792–802.

[49] M. Dogra, V. S. Sharma, A. Sachdeva, N. M. Suri, J. S. Dureja, Tool wear, chip formation and workpiece surface issues in cbn hard turning: A review, International Journal of Precision Engineering and Manufacturing 11 (2010) 341–358.

[50] T. Özel, Y. Karpat, A. Srivastava, Hard turning with variable micro-geometry pcbn tools, CIRP annals 57 (2008) 73–76.

[51] T. Özel, Computational modelling of 3d turning: Influence of edge micro-geometry on forces, stresses, friction and tool wear in pcbn tooling, Journal of Materials Processing Technology 209 (2009) 5167–5177.

[52] M. Kaymakci, Z. Kilic, Y. Altintas, Unified cutting force model for turning, boring, drilling and milling operations, International Journal of Machine Tools and Manufacture 54 (2012) 34–45.

[53] H. Liu, S. Wang, W. Zong, Tool rake angle selection in micro-machining of 45 vol.% sicp/2024al based on its brittle-plastic properties, Journal of Manufacturing Processes 37 (2019) 556–562.

[54] X. Wu, L. Li, N. He, C. Yao, M. Zhao, Influence of the cutting edge radius and the material grain size on the cutting force in micro cutting, Precision Engineering 45 (2016) 359–364.

[55] M. Shaw, Surface finish, 1984.

[56] K. Dhale, N. Banerjee, R. Singh, Investigation of a novel sub-surface work hardening phenomenon in micro-turning of zr-based bulk metallic glass, Intermetallics 150 (2022) 107690.

[57] R. Singh, S. N. Melkote, Characterization of a hybrid laser-assisted mechanical micromachining (lamm) process for a difficult-to-machine material, International Journal of Machine Tools and Manufacture 47 (2007) 1139–1150.

[58] K. K. Singh, V. Kartik, R. Singh, Modeling dynamic stability in high-speed micromilling of ti–6al–4v via velocity and chip load dependent cutting coefficients, International Journal of Machine Tools and Manufacture 96 (2015) 56–66.

[59] R. K. Mittal, R. K. Singh, S. S. Kulkarni, P. Kumar, H. Barshilia, Characterization of anti-abrasion and anti-friction coatings on micromachining response in high speed micromilling of ti-6al-4v, Journal of Manufacturing Processes 34 (2018) 303–312.

[60] G. Kiswanto, D. Zariatin, T. Ko, The effect of spindle speed, feed-rate and machining time to the surface roughness and burr formation of aluminum alloy 1100 in micro-milling operation, Journal of Manufacturing Processes 16 (2014) 435–450.

[61] V. Bajpai, A. K. Kushwaha, R. K. Singh, Burr formation and surface quality in high speed micromilling of titanium alloy (ti6al4v), in: International Manufacturing Science and Engineering Conference, volume 55461, American Society of Mechanical Engineers, p. V002T03A017.

[62] M. Kumar, V. Bajpai, Experimental investigation of top burr formation in high-speed micro-milling of ti6al4v alloy, Proceedings of the Institution of Mechanical Engineers, Part B: Journal of Engineering Manufacture 234 (2020) 730–738.

[63] S. Akıncıoğlu, H. Gökkaya, İ. Uygur, The effects of cryogenic-treated carbide tools on tool wear and surface roughness of turning of hastelloy c22 based on taguchi method, The International Journal of Advanced Manufacturing Technology 82 (2016) 303–314.

[64] O. S. O. S. T. METODO, Optimization of the turning parameters for the cutting forces in the hastelloy x superalloy based on the taguchi method, Materiali in tehnologije 48 (2014) 249–254.

[65] G. Zheng, R. Xu, X. Cheng, G. Zhao, L. Li, J. Zhao, Effect of cutting parameters on wear behavior of coated tool and surface roughness in high-speed turning of 300m, Measurement 125 (2018) 99–108.

[66] D.-W. Tan, W.-M. Guo, H.-J. Wang, H.-T. Lin, C.-Y. Wang, Cutting performance and wear mechanism of tib2-b4c ceramic cutting tools in high speed turning of ti6al4v alloy, Ceramics International 44 (2018) 15495–15502.

[67] J. Suh, D. G. Lee, R. Kegg, Composite machine tool structures for high speed milling machines, CIRP Ann 51 (2002) 285–288.

[68] J. B. Bryan, Design and construction of an ultraprecision 84 inch diamond turning machine, Precision Engineering 1 (1979) 13–17.

[69] M. P. Vogler, X. Liu, S. G. Kapoor, R. E. DeVor, K. F. Ehmann, Development of meso-scale machine tool (mmt) systems, TECHNICAL PAPERS-SOCIETY OF MANUFACTURING ENGINEERS-ALL SERIES- (2002).

[70] S. W. Lee, R. Mayor, J. Ni, Dynamic analysis of a mesoscale machine tool, Journal of Manufacturing Science and Engineering 128 (2006) 194–203.

[71] X. Luo, K. Cheng, D. Webb, F. Wardle, Design of ultraprecision machine tools with applications to manufacture of miniature and micro components, J Mater Process Technol 167 (2005) 515–528.

[72] Y.-b. Bang, K.-m. Lee, S. Oh, 5-axis micro milling machine for machining micro parts., International Journal of Advanced Manufacturing Technology 25 (2005).

[73] H. Li, X. Lai, C. Li, Z. Lin, J. Miao, J. Ni, Development of meso-scale milling machine tool and its performance analysis, Frontiers of Mechanical Engineering in China 3 (2008) 59–65.

[74] B. E. Clancy, Y. C. Shin, A comprehensive chatter prediction model for face turning operation including tool wear effect, Int J Mach Tools Manuf 42 (2002) 1035–1044.

[75] W. Chen, X. Luo, H. Su, F. Wardle, An integrated system for ultra-precision machine tool design in conceptual and fundamental design stage, Int J Adv Manuf Technol 84 (2016) 1177–1183.

[76] H. W. Park, Y. B. Park, S. Y. Liang, Multi-procedure design optimization and analysis of mesoscale machine tools, Int J Adv Manuf Technol 56 (2011) 1–12.

[77] Y. Liang, W. Chen, Q. Bai, Y. Sun, G. Chen, Q. Zhang, Y. Sun, Design and dynamic optimization of an ultraprecision diamond flycutting machine tool for large kdp crystal machining, Int J Adv Manuf Technol 69 (2013) 237–244.

[78] K. Venugopal, S. Paul, A. Chattopadhyay, Growth of tool wear in turning of ti-6al-4v alloy under cryogenic cooling, Wear 262 (2007) 1071–1078.

[79] B. Behera, S. Ghosh, P. Rao, et al., Wear behavior of pvd tin coated carbide inserts during machining of nimonic 90 and ti6al4v superalloys under dry and mql conditions, Ceramics International 42 (2016) 14873–14885.

[80] S. Ghosh, P. Rao, et al., Performance evaluation of deep cryogenic processed carbide inserts during dry turning of nimonic 90 aerospace grade alloy, Tribology international 115 (2017) 397–408.

[81] V. Parthiban, S. Vijayakumar, M. Sakthivel, Optimization of high-speed turning parameters for inconel 713c based on taguchi grey relational analysis, Transactions of the Canadian Society for Mechanical Engineering 43 (2019) 416–430.

[82] R. Viswanathan, S. Ramesh, V. Subburam, Measurement and optimization of performance characteristics in turning of mg alloy under dry and mql conditions, Measurement 120 (2018) 107–113.

[83] M. A. Sofuoğlu, F. H. Çakır, S. Gürgen, S. Orak, M. C. Kuşhan, Experimental investigation of machining characteristics and chatter stability for hastelloy-x with ultrasonic and hot turning, The International Journal of Advanced Manufacturing Technology 95 (2018) 83–97.

[84] X. Liu, J. Zhang, X. Hu, D. Wu, Influence of tool material and geometry on micro-textured surface in radial ultrasonic vibration-assisted turning, International Journal of Mechanical Sciences 152 (2019) 545–557.

[85] A. K. Srivastava, A. Nag, A. R. Dixit, J. Scucka, S. Hloch, D. Klichová, P. Hlaváček, S. Tiwari, Hardness measurement of surfaces on hybrid metal matrix composite created by turning using an abrasive water jet and wed, Measurement 131 (2019) 628–639.

[86] K. Y. Song, M. S. Park, C. N. Chu, et al., Edm turning using a strip electrode, Journal of Materials Processing Technology 213 (2013) 1495–1500.

[87] M. Kang, X. Fu, Y. Yang, Experimental study on numerical controlled electrochemical turning, in: Key Engineering Materials, volume 426, Trans Tech Publ, pp. 658–663.

[88] T. A. El-Taweel, S. Gouda, Performance analysis of wire electrochemical turning process—rsm approach, The International Journal of Advanced Manufacturing Technology 53 (2011) 181–190.

[89] M. Kunieda, K. Mizugai, S. Watanabe, N. Shibuya, N. Iwamoto, Electrochemical micromachining using flat electrolyte jet, CIRP annals 60 (2011) 251–254.

[90] M. Kunieda, Influence of micro indents formed by electro-chemical jet machining on rolling bearing fatigue life, ASM, PED, 1993 64 (1993) 693–699.

[91] D. Arulkirubakaran, V. Senthilkumar, V. Kumawat, Effect of micro-textured tools on machining of ti–6al–4v alloy: an experimental and numerical approach, International Journal of Refractory Metals and Hard Materials 54 (2016) 165–177.

[92] S. K. Rajbongshi, M. A. Singh, D. K. Sarma, A comparative study in machining of aisi d2 steel using textured and non-textured coated carbide tool at the flank face, Journal of Manufacturing Processes 36 (2018) 360–372.

[93] C. M. Rao, S. S. Rao, M. A. Herbert, Development of novel cutting tool with a micro-hole pattern on pcd insert in machining of titanium alloy, Journal of Manufacturing Processes 36 (2018) 93–103.

[94] N. T. Alagan, P. Zeman, P. Hoier, T. Beno, U. Klement, Investigation of micro-textured cutting tools used for face turning of alloy 718 with high-pressure cooling, Journal of Manufacturing Processes 37 (2019) 606–616.

[95] J. V. Elias, P. Venkatesh N, D. Lawrence K, J. Mathew, Tool texturing for micro-turning applications–an approach using mechanical micro indentation, Materials and Manufacturing Processes 36 (2021) 84–93.

[96] C. F. Cheung, W. B. Lee, Characterisation of nanosurface generation in single-point diamond turning, International Journal of Machine Tools and Manufacture 41 (2001) 851–875.

[97] K. C. Chan, C. F. Cheung, M. Ramesh, W. B. Lee, S. To, A theoretical and experimental investigation of surface generation in diamond turning of an al6061/sicp metal matrix composite, International journal of mechanical sciences 43 (2001) 2047–2068.

[98] X. Zhou, C. Zuo, Q. Liu, J. Lin, Surface generation of freeform surfaces in diamond turning by applying double-frequency elliptical vibration cutting, International Journal of Machine Tools and Manufacture 104 (2016) 45–57.

[99] M. Heidari, J. Yan, Fundamental characteristics of material removal and surface formation in diamond turning of porous carbon, International Journal of Additive and Subtractive Materials Manufacturing 1 (2017) 23–41.

[100] Y. Wang, W. Liao, K. Yang, X. Teng, W. Chen, Simulation and experimental investigation on the cutting mechanism and surface generation in machining sicp/al mmcs, The International Journal of Advanced Manufacturing Technology 100 (2019) 1393–1404.

[101] S. Zhang, Z. Li, Z. Xiong, S. To, Microwave formation mechanisms in surface generation of ultra-precision machining, The International Journal of Advanced Manufacturing Technology 104 (2019) 1239–1244.

[102] J. Xiong, H. Wang, G. Zhang, Y. Chen, J. Ma, R. Mo, Machinability and surface generation of pd40ni10cu30p20 bulk metallic glass in single-point diamond turning, Micromachines 11 (2019) 4.

[103] W. Huang, J. Yan, Surface formation mechanism in ultraprecision diamond turning of coarse-grained polycrystalline znse, International Journal of Machine Tools and Manufacture 153 (2020) 103554.

[104] S. To, W. B. Lee, C. Chan, Ultraprecision diamond turning of aluminium single crystals, Journal of materials processing technology 63 (1997) 157–162.

[105] X. Ding, A. Jarfors, G. Lim, K. Shaw, Y. Liu, L. Tang, A study of the cutting performance of poly-crystalline oxygen free copper with single crystalline diamond micro-tools, Precision engineering 36 (2012) 141–152.

[106] X. Ding, M. Rahman, A study of the performance of cutting polycrystalline al 6061 t6 with single crystalline diamond micro-tools, Precision Engineering 36 (2012) 593–603.

[107] K. Abou-El-Hossein, O. Olufayo, Z. Mkoko, Diamond tool wear during ultra-high precision machining of rapidly solidified aluminium rsa 905, Wear 302 (2013) 1105–1112.

[108] H. Wang, S. To, C. Chan, Investigation on the influence of tool-tip vibration on surface roughness and its representative measurement in ultra-precision diamond turning, International Journal of Machine Tools and Manufacture 69 (2013) 20–29.

[109] R. Horváth, Á. Czifra, Á. Drégelyi-Kiss, Effect of conventional and non-conventional tool geometries to skewness and kurtosis of surface roughness in case

of fine turning of aluminium alloys with diamond tools, The International Journal of Advanced Manufacturing Technology 78 (2015) 297–304.

[110] J. Guo, J. Zhang, H. Wang, K. Liu, A. S. Kumar, Surface quality characterisation of diamond cut v-groove structures made of rapidly solidified aluminium rsa-905, Precision Engineering 53 (2018) 120–133.

[111] L. Li, N. Yu, C. Chan, W. Lee, Al6061 surface roughness and optical reflectance when machined by single point diamond turning at a low feed rate, Plos one 13 (2018) e0195083.

[112] J. Oomen, J. Eisses, Wear of monocrystalline diamond tools during ultraprecision machining of nonferrous metals, Precision Engineering 14 (1992) 206–218.

[113] N. Furushiro, H. Tanaka, M. Higuchi, T. Yamaguchi, S. Shimada, Suppression mechanism of tool wear by phosphorous addition in diamond turning of electroless nickel deposits, CIRP annals 59 (2010) 105–108.

[114] A. Meier, Diamond turning of diffractive microstructures, Precision Engineering 42 (2015) 253–260.

[115] Y. Song, K. Nezu, C.-H. Park, T. Moriwaki, Tool wear control in single-crystal diamond cutting of steel by using the ultra-intermittent cutting method, International Journal of Machine Tools and Manufacture 49 (2009) 339–343.

[116] L. Zou, J. Yin, Y. Huang, M. Zhou, Essential causes for tool wear of single crystal diamond in ultra-precision cutting of ferrous metals, Diamond and Related Materials 86 (2018) 29–40.

[117] M. Zhou, G. Zhang, N. Chen, Effects of lubricant on cutting performance in single-point diamond turning of ferrous metal nak 80, The International Journal of Advanced Manufacturing Technology 109 (2020) 2549–2558.

[118] Z. Zhao, S. To, Z. Sun, R. Ji, K. M. Yu, Microstructural effects of ti6al4v alloys modified by electropulsing treatment on ultraprecision diamond turning, Journal of Manufacturing Processes 39 (2019) 58–68.

[119] P. Huang, H. Li, W.-L. Zhu, H. Wang, G. Zhang, X. Wu, S. To, Z. Zhu, Effects of eco-friendly cooling strategy on machining performance in micro-scale diamond turning of ti–6al–4v, Journal of Cleaner Production 243 (2020) 118526.

[120] W. Yip, S. To, Preliminary investigation on ultra-precision diamond turning of titanium alloys using thermoelectric cooler fixture, Journal of Manufacturing Processes 58 (2020) 187–192.

[121] M. S. Uddin, K. Seah, M. Rahman, X. Li, K. Liu, Performance of single crystal diamond tools in ductile mode cutting of silicon, Journal of Materials Processing Technology 185 (2007) 24–30.

[122] T. Leung, W. B. Lee, X. Lu, Diamond turning of silicon substrates in ductile-regime, Journal of materials processing technology 73 (1998) 42–48.

[123] M. Cai, X. Li, M. Rahman, Characteristics of "dynamic hard particles" in nanoscale ductile mode cutting of monocrystalline silicon with diamond tools in relation to tool groove wear, Wear 263 (2007) 1459–1466.

[124] S. Goel, X. Luo, R. L. Reuben, Wear mechanism of diamond tools against single crystal silicon in single point diamond turning process, Tribology International 57 (2013) 272–281.

[125] S. Goel, X. Luo, R. L. Reuben, H. Pen, Influence of temperature and crystal orientation on tool wear during single point diamond turning of silicon, Wear 284 (2012) 65–72.

[126] L. N. Abdulkadir, K. Abou-El-Hossein, A. I. Jumare, P. B. Odedeyi, M. M. Liman, T. A. Olaniyan, Ultra-precision diamond turning of optical silicon—a review, The International Journal of Advanced Manufacturing Technology 96 (2018) 173–208.

[127] S. Zhang, W. Zong, A novel surface roughness model for potassium dihydrogen phosphate (kdp) crystal in oblique diamond turning, International Journal of Mechanical Sciences 173 (2020) 105462.

[128] J. A. Patten, J. Jacob, Comparison between numerical simulations and experiments for single-point diamond turning of single-crystal silicon carbide, Journal of manufacturing processes 10 (2008) 28–33.

[129] J. Yan, Z. Zhang, T. Kuriyagawa, Mechanism for material removal in diamond turning of reaction-bonded silicon carbide, International Journal of Machine Tools and Manufacture 49 (2009) 366–374.

[130] B. Bulla, F. Klocke, O. Dambon, Analysis on ductile mode processing of binderless, nano crystalline tungsten carbide through ultra precision diamond turning, Journal of Materials Processing Technology 212 (2012) 1022–1029.

[131] W. Zong, Z. Cao, C. He, C. Xue, Theoretical modelling and fe simulation on the oblique diamond turning of zns crystal, International Journal of Machine Tools and Manufacture 100 (2016) 55–71.

[132] X. Yue, M. Xu, W. Du, C. Chu, Effect of cutting edge radius on surface roughness in diamond tool turning of transparent mgal2o4 spinel ceramic, Optical Materials 71 (2017) 129–135.

[133] L. Ma, C. Cai, Y. Tan, Y. Gong, L. Zhu, Theoretical model of transverse and longitudinal surface roughness and study on brittle-ductile transition mechanism for turning fluorophlogopite ceramic, International Journal of Mechanical Sciences 150 (2019) 715–726.

[134] K. Xiao, L. Zhang, The role of viscous deformation in the machining of polymers, International journal of mechanical sciences 44 (2002) 2317–2336.

[135] G. Gubbels, G. Van Der Beek, A. Hoep, F. Delbressine, H. Van Halewijn, Diamond tool wear when cutting amorphous polymers, CIRP Annals 53 (2004) 447–450.

[136] A. Mamalis, S. Lavrynenko, On the precision single-point diamond machining of polymeric materials, Journal of materials processing technology 181 (2007) 203–205.

[137] O. Olufayo, K. Abou-El-Hossein, M. Kadernani, Tribo-electric charging in the ultra-high precision machining of contact lens polymers, Procedia materials science 6 (2014) 194–201.

[138] B. Goel, S. Singh, R. G. V. Sarepaka, Precision deterministic machining of polymethyl methacrylate by single-point diamond turning, Materials and Manufacturing Processes 31 (2016) 1917–1926.

[139] M. M. Liman, K. Abou-El-Hossein, Modeling and multiresponse optimization of cutting parameters in spdt of a rigid contact lens polymer using rsm and desirability function, The International Journal of Advanced Manufacturing Technology 102 (2019) 1443–1465.

[140] N. Yu, F. Fang, B. Wu, L. Zeng, Y. Cheng, State of the art of intraocular lens manufacturing, The International Journal of Advanced Manufacturing Technology 98 (2018) 1103–1130.

[141] M. Ramesh, K. C. Chan, W. B. Lee, C. F. Cheung, Finite-element analysis of diamond turning of aluminium matrix composites, Composites science and technology 61 (2001) 1449–1456.

[142] S. S. Roy, Design of genetic-fuzzy expert system for predicting surface finish in ultra-precision diamond turning of metal matrix composite, Journal of Materials Processing Technology 173 (2006) 337–344.

[143] Z. Zhong, G. Lin, Ultrasonic assisted turning of an aluminium-based metal matrix composite reinforced with sic particles, The International Journal of Advanced Manufacturing Technology 27 (2006) 1077–1081.

[144] C. Fetecau, F. Stan, Study of cutting force and surface roughness in the turning of polytetrafluoroethylene composites with a polycrystalline diamond tool, Measurement 45 (2012) 1367–1379.

[145] T. Wang, X. Wu, G. Zhang, Y. Dai, B. Xu, S. Ruan, An experimental study on single-point diamond turning of a 55 vol% sicp/al composite below the ductile brittle transition depth of sic, The International Journal of Advanced Manufacturing Technology 108 (2020) 2255–2268.

[146] H. Shinno, H. Hashizume, Y. Ito, C. Sato, Structural configuration and performances of machining environment-controlled ultraprecision diamond turning machine 'capsule', CIRP annals 41 (1992) 425–428.

[147] P. Sriyotha, K. Nakamoto, M. Sugai, K. Yamazaki, Development of 5-axis linear motor driven super-precision machine, CIRP annals 55 (2006) 381–384.

[148] B. C. Ulmer Jr, T. R. Kurfess, Integration of an open architecture controller with a diamond turning machine, Mechatronics 9 (1999) 349–361.

[149] H. Yao, Z. Li, X. Zhao, T. Sun, G. Dobrovolskyi, G. Li, Modeling of kinematics errors and alignment method of a swing arm ultra-precision diamond turning machine, The International Journal of Advanced Manufacturing Technology 87 (2016) 165–176.

[150] X. Zou, X. Zhao, G. Li, Z. Li, T. Sun, Sensitivity analysis using a variance-based method for a three-axis diamond turning machine, The International Journal of Advanced Manufacturing Technology 92 (2017) 4429–4443.

[151] F. El-Dahabi, R. Dib, K. Abou-El-Hossein, S. Hatefi, A. Abbas, Z. Hweju, Effect of machine-tool rigidity on geometric error formation in turning operation, International Journal of Mechanical Engineering and Robotics Research 9 (2020).

[152] Y. Li, Y. Zhang, J. Lin, A. Yi, X. Zhou, Effects of machining errors on optical performance of optical aspheric components in ultra-precision diamond turning, Micromachines 11 (2020) 331.

[153] M. Buhmann, R. Roth, T. Liebrich, K. Frick, E. Carelli, M. Marxer, New positioning procedure for optical probes integrated on ultra-precision diamond turning machines, CIRP Annals 69 (2020) 473–476.

[154] C. F. Cheung, W. B. Lee, A theoretical and experimental investigation of surface roughness formation in ultra-precision diamond turning, International Journal of Machine Tools and Manufacture 40 (2000) 979–1002.

[155] D.-S. Kim, I.-C. Chang, S.-W. Kim, Microscopic topographical analysis of tool vibration effects on diamond turned optical surfaces, Precision Engineering 26 (2002) 168–174.

[156] H. Wang, S. To, C. Chan, C. F. Cheung, W. B. Lee, A theoretical and experimental investigation of the tool-tip vibration and its influence upon surface generation in single-point diamond turning, International Journal of Machine Tools and Manufacture 50 (2010) 241–252.

[157] H. Wang, S. To, C. Chan, C. F. Cheung, W. B. Lee, Dynamic modelling of shear band formation and tool-tip vibration in ultra-precision diamond turning, International Journal of Machine Tools and Manufacture 51 (2011) 512–519.

[158] S. Hatefi, K. Abou-El-Hossein, Review of single-point diamond turning process in terms of ultra-precision optical surface roughness, The International Journal of Advanced Manufacturing Technology 106 (2020) 2167–2187.

[159] W. S. Yip, S. To, Reduction of tool tip vibration in single-point diamond turning using an eddy current damping effect, The International Journal of Advanced Manufacturing Technology 103 (2019) 1799–1809.

[160] M. Tauhiduzzaman, A. Yip, S. Veldhuis, Form error in diamond turning, Precision Engineering 42 (2015) 22–36.

[161] P. Huang, W. B. Lee, C. Chan, Investigation on the position drift of the axis average line of the aerostatic bearing spindle in ultra-precision diamond turning, International Journal of Machine Tools and Manufacture 108 (2016) 44–51.

[162] S. Zhang, S. To, C. F. Cheung, H. Wang, Dynamic characteristics of an aerostatic bearing spindle and its influence on surface topography in ultra-precision diamond turning, International Journal of Machine Tools and Manufacture 62 (2012) 1–12.

[163] S. Zhang, J. Yu, S. To, Z. Xiong, A theoretical and experimental study of spindle imbalance induced forced vibration and its effect on surface generation in diamond turning, International Journal of Machine Tools and Manufacture 133 (2018) 61–71.

[164] S. Zhang, Z. Li, Z. Xiong, A theoretical and experimental study of forced spindle vibration under unbalanced magnetic forces in ultra-precision machining, The International Journal of Advanced Manufacturing Technology 103 (2019) 4689–4694.

[165] C. He, W. Zong, Influence of multifrequency vibration on the optical performance of diamond-turned optics and its elimination method, Applied Optics 58 (2019) 4241–4249.

[166] D. Fedorynenko, S. Sapon, S. Boyko, Accuracy of spindle units with hydrostatic bearings, acta mechanica et automatica 10 (2016) 117–124.

[167] X. Liu, R. DeVor, S. G. Kapoor, K. Ehmann, The mechanics of machining at the microscale: assessment of the current state of the science, J. Manuf. Sci. Eng. 126 (2004) 666–678.

[168] H. Hocheng, M. Hsieh, Signal analysis of surface roughness in diamond turning of lens molds, International Journal of Machine Tools and Manufacture 44 (2004) 1607–1618.

[169] M. Tauhiduzzaman, S. Veldhuis, Effect of material microstructure and tool geometry on surface generation in single point diamond turning, Precision Engineering 38 (2014) 481–491.

[170] W. Zong, Y. Huang, Y. Zhang, T. Sun, Conservation law of surface roughness in single point diamond turning, International Journal of Machine Tools and Manufacture 84 (2014) 58–63.

[171] D. P. Yu, Y. S. Wong, G. S. Hong, Optimal selection of machining parameters for fast tool servo diamond turning, The International Journal of Advanced Manufacturing Technology 57 (2011) 85–99.

[172] H. Wang, S. To, C. Chan, C. F. Cheung, W. B. Lee, A study of regularly spaced shear bands and morphology of serrated chip formation in microcutting process, Scripta Materialia 63 (2010) 227–230.

[173] Z. Wang, J. Zhang, J. Zhang, G. Li, H. Zhang, H. ul Hassan, A. Hartmaier, Y. Yan, T. Sun, Towards an understanding of grain boundary step in diamond cutting of polycrystalline copper, Journal of Materials Processing Technology 276 (2020) 116400.

[174] C. He, W. Zong, T. Sun, Origins for the size effect of surface roughness in diamond turning, International Journal of Machine Tools and Manufacture 106 (2016) 22–42.

[175] Y. Dai, G. Zhang, T. Luo, Q. Luo, Centre cone generation and its force performance in single-point diamond turning, International Journal of Mechanical Sciences 184 (2020) 105780.

[176] T. Moriwaki, E. Shamoto, Analysis of thermal deformation of an ultraprecision air spindle system, CIRP Annals 47 (1998) 315–319.

[177] J. Kumar, V. S. Negi, K. D. Chattopadhyay, R. V. Sarepaka, R. K. Sinha, Thermal effects in single point diamond turning: analysis, modeling and experimental study, Measurement 102 (2017) 96–105.

[178] W. Yip, S. To, Effects of magnetic field on microstructures and mechanical properties of titanium alloys in ultra-precision diamond turning, Materials Research Express 6 (2019) 056553.

[179] G. Jiang, Z. Jianguo, P. Yanan, K. Renke, N. Yoshiharu, S. Paul, Y. Xiaobin, W. Baorui, G. Dongming, A critical review on the chemical wear and wear suppression of diamond tools in diamond cutting of ferrous metals, International Journal of Extreme Manufacturing 2 (2020) 012001.

[180] L. Pei, H. Wu, Effect of ultrasonic vibration on ultra-precision diamond turning of ti6al4v, The International Journal of Advanced Manufacturing Technology 103 (2019) 433–440.

[181] L. C. Flórez García, H. A. González Rojas, A. J. Sánchez Egea, Estimation of specific cutting energy in an s235 alloy for multi-directional ultrasonic vibration-assisted machining using the finite element method, Materials 13 (2020) 567.

[182] S. To, C. F. Cheung, W. B. Lee, Influence of material swelling on surface roughness in diamond turning of single crystals, Materials science and technology 17 (2001) 102–108.

[183] M. Kong, W. B. Lee, C. F. Cheung, S. To, A study of materials swelling and recovery in single-point diamond turning of ductile materials, Journal of materials processing technology 180 (2006) 210–215.

[184] S. N. A. Kalkhoran, M. Vahdati, J. Yan, Effect of relative tool sharpness on subsurface damage and material recovery in nanometric cutting of mono-crystalline silicon: a molecular dynamics approach, Materials Science in Semiconductor Processing 108 (2020) 104868.

[185] W. Yip, S. To, Sustainable ultra-precision machining of titanium alloy using intermittent cutting, International Journal of Precision Engineering and Manufacturing-Green Technology 7 (2020) 361–373.

[186] I.-H. Choi, J.-D. Kim, Development of monitoring system on the diamond tool wear, International Journal of Machine Tools and Manufacture 39 (1999) 505–515.

[187] B. Lane, M. Shi, T. Dow, R. Scattergood, Diamond tool wear when machining al6061 and 1215 steel, Wear 268 (2010) 1434–1441.

[188] D. Wu, B. Wang, F. Fang, Effects of tool wear on surface micro-topography in ultra-precision turning, The International Journal of Advanced Manufacturing Technology 102 (2019) 4397–4407.

[189] A. Sharma, D. Datta, R. Balasubramaniam, A molecular dynamics simulation of wear mechanism of diamond tool in nanoscale cutting of copper beryllium, The International Journal of Advanced Manufacturing Technology 102 (2019) 731–745.

[190] M. H. Wang, S. Y. You, F. N. Wang, Q. Liu, Md simulation of tool wear behaviour based on changes of tool rake and flank angle caused by diamond tool position adjustment, Molecular Simulation 45 (2019) 509–517.

[191] Y. Wang, N. Suzuki, E. Shamoto, Q. Zhao, Investigation of tool wear suppression in ultraprecision diamond machining of die steel, Precision engineering 35 (2011) 677–685.

[192] S. To, W. B. Lee, Y. Zhu, Ultra-precision machining induced surface structural changes of zn–al alloy, Materials Science and Engineering: A 325 (2002) 497–502.

[193] W. B. Lee, S. To, Y. Sze, C. F. Cheung, Effect of material anisotropy on shear angle prediction in metal cutting—a mesoplasticity approach, International journal of mechanical sciences 45 (2003) 1739–1749.

[194] Y.-k. Sze, et al., The effect of preferred orientation in the single point diamond turning of polycrystalline materials (2006).

[195] S. S. To, H. Wang, W. B. Lee, et al., Materials characterisation and mechanism of micro-cutting in ultra-precision diamond turning, Springer, 2018.

[196] S. Zhang, P. Guo, Z. Xiong, S. To, Cyclic shear angle for lamellar chip formation in ultra-precision machining, Proceedings of the Institution of Mechanical Engineers, Part C: Journal of Mechanical Engineering Science 234 (2020) 2673–2680.

[197] C. Nobel, F. Klocke, D. Lung, S. Wolf, Machinability enhancement of lead-free brass alloys, Procedia CIRP 14 (2014) 95–100.

[198] J. Shimizu, L. Zhou, H. Eda, Simulation and experimental analysis of super high-speed grinding of ductile material, Journal of Materials Processing Technology 129 (2002) 19–24.

[199] D. Huo, K. Cheng, Micro cutting mechanics, Micro-Cutting: Fundamentals and Applications (2013) 19–44.

[200] A. Musfirah, J. Ghani, C. C. Haron, Tool wear and surface integrity of inconel 718 in dry and cryogenic coolant at high cutting speed, Wear 376 (2017) 125–133.

[201] B. Sen, M. Mia, G. Krolczyk, U. K. Mandal, S. P. Mondal, Eco-friendly cutting fluids in minimum quantity lubrication assisted machining: a review on the perception of sustainable manufacturing, International Journal of Precision Engineering and Manufacturing-Green Technology 8 (2021) 249–280.

[202] S. Filiz, C. M. Conley, M. B. Wasserman, O. B. Ozdoganlar, An experimental investigation of micro-machinability of copper 101 using tungsten carbide micro-endmills, Int J Mach Tools Manuf 47 (2007) 1088–1100.

[203] C. R. Friedrich, M. J. Vasile, Development of the micromilling process for high-aspect-ratio microstructures, J Microelectromech Syst 5 (1996) 33–38.

[204] Y. Wang, B. Zou, J. Wang, Y. Wu, C. Huang, Effect of the progressive tool wear on surface topography and chip formation in micro-milling of ti–6al–4v using ti (c7n3)-based cermet micro-mill, Tribol Int 141 (2020) 105900.

[205] Z. Z. Abidin, P. T. Mativenga, G. Harrison, Chilled air system and size effect in micro-milling of nickel- titanium shape memory alloys, Int J Precis Eng Manuf-Green Technol 7 (2020) 283–297.

[206] M. B. Jun, X. Liu, R. E. DeVor, S. G. Kapoor, Investigation of the dynamics of microend milling—part i: model development, J Manuf Sci Eng. Trans ASME 128 (2006) 893–900.

[207] M. Zaeh, D. Siedl, A new method for simulation of machining performance by integrating finite element and multi-body simulation for machine tools, CIRP Ann 56 (2007) 383–386.

[208] X. Yang, J. Zheng, J. Xu, W. Li, Y. Wang, M. Fan, Structural design and isolation characteristic analysis of new quasi-zero-stiffness, J Vib Eng Technol 8 (2020) 47–58.

[209] Z. Zhang, Y.-W. Zhang, H. Ding, Vibration control combining nonlinear isolation and nonlinear absorption, Nonlinear Dyn 100 (2020) 2121–2139.

[210] T. Semm, M. B. Nierlich, M. F. Zaeh, Substructure coupling of a machine tool in arbitrary axis positions considering local linear damping models, J Manuf Sci Eng. Trans ASME 141 (2019) 071014.

[211] X. Zhang, Z. Yin, J. Gao, J. Liu, R. X. Gao, H. Cao, X. Chen, Discrete time-delay optimal control method for experimental active chatter suppression and its closed-loop stability analysis, J Manuf Sci Eng. Trans ASME 141 (2019) 051003.

[212] K. Orra, S. K. Choudhury, Stability analysis in machining process by using adaptive closed-loop feedback control system in turning process, J Vib Control 0 (2020) 1–13.

[213] E. Yuksel, A. S. Erturk, E. Budak, A hybrid contact implementation framework for finite element analysis and topology optimization of machine tools, J Manuf Sci Eng. Trans ASME 142 (2020) 081001.

[214] Y. Mohammadi, K. Ahmadi, Single degree-of-freedom modeling of the nonlinear vibration response of a machining robot, J Manuf Sci Eng. Trans ASME 143 (2020) 051003.

[215] G. Raze, G. Kerschen, Multimodal vibration damping of nonlinear structures using multiple nonlinear absorbers, Int J Nonlin Mech 119 (2020) 103308.

[216] H. Saber, F. S. Samani, F. Pellicano, Nonlinear vibration absorbers applied on foot-bridges, Meccanica (2020) 1–18.

[217] J. Do Suh, et al., Design and manufacture of hybrid polymer concrete bed for high-speed cnc milling machine, Int J Mech Mater Des 4 (2008) 113–121.

[218] D. Huo, K. Cheng, A dynamics-driven approach to the design of precision machine tools for micro-manufacturing and its implementation perspectives, Proc Inst Mech Eng B J Eng Manuf 222 (2008) 1–13.

[219] S. Rao, Metal cutting machine tool design—a review, J Manuf Sci Eng. Trans ASME 119 (1997) 713–716.

[220] H.-C. Möhring, C. Brecher, E. Abele, J. Fleischer, F. Bleicher, Materials in machine tool structures, CIRP Ann 64 (2015) 725–748.

[221] T.-C. Chen, Y.-J. Chen, M.-H. Hung, J.-P. Hung, Design analysis of machine tool structure with artificial granite material, Adv Mech Eng 8 (2016) 1–14.

[222] H. Pérez, A. Vizán, J. Hernandez, M. Guzmán, Estimation of cutting forces in micromilling through the determination of specific cutting pressures, Journal of Materials Processing Technology 190 (2007) 18–22.

[223] K. Li, K. Zhu, T. Mei, A generic instantaneous undeformed chip thickness model for the cutting force modeling in micromilling, International Journal of Machine Tools and Manufacture 105 (2016) 23–31.

[224] A. Das, S. Shukla, M. Kumar, C. Singh, M. L. Chandravanshi, V. Bajpai, Development of a vibration free machine structure for high-speed micro-milling center, The International Journal of Advanced Manufacturing Technology 116 (2021) 3489–3506.

[225] A. I. Toulfatzis, G. A. Pantazopoulos, C. N. David, D. S. Sagris, A. S. Paipetis, Machinability of eco-friendly lead-free brass alloys: Cutting-force and surface-roughness optimization, Metals 8 (2018) 250.

[226] A. I. Toulfatzis, G. A. Pantazopoulos, G. J. Besseris, A. S. Paipetis, Machinability evaluation and screening of leaded and lead-free brasses using a non-linear robust multifactorial profiler, The International Journal of Advanced Manufacturing Technology 86 (2016) 3241–3254.

[227] F. Schultheiss, D. Johansson, V. Bushlya, J. Zhou, K. Nilsson, J.-E. Ståhl, Comparative study on the machinability of lead-free brass, Journal of Cleaner Production 149 (2017) 366–377.

[228] F. Schultheiss, C. Windmark, S. Sjöstrand, M. Rasmusson, J.-E. Ståhl, Machinability and manufacturing cost in low-lead brass, The International Journal of Advanced Manufacturing Technology 99 (2018) 2101–2110.

[229] H. Imai, Y. Kosaka, A. Kojima, S. Li, K. Kondoh, J. Umeda, H. Atsumi, Characteristics and machinability of lead-free p/m cu60–zn40 brass alloys dispersed with graphite, Powder Technology 198 (2010) 417–421.

[230] A. I. Toulfatzis, G. A. Pantazopoulos, C. N. David, D. S. Sagris, A. S. Paipetis, Final heat treatment as a possible solution for the improvement of machinability of pb-free brass alloys, Metals 8 (2018) 575.

[231] L. Amaral, R. Quinta, T. E. Silva, R. M. Soares, S. D. Castellanos, A. M. de Jesus, Effect of lead on the machinability of brass alloys using polycrystalline diamond cutting tools, The Journal of Strain Analysis for Engineering Design 53 (2018) 602–615.

[232] Z. Rajabi, H. Doostmohammadi, Effect of addition of tin on the microstructure and machinability of α-brass, Materials Science and Technology 34 (2018) 1218–1227.

[233] W. Grzesik, Prediction of surface topography in precision hard machining based on modelling of the generation mechanisms resulting from a variable feed rate, The International Journal of Advanced Manufacturing Technology 94 (2018) 4115–4123.

[234] M. Malekian, M. Mostofa, S. Park, M. Jun, Modeling of minimum uncut chip thickness in micro machining of aluminum, Journal of Materials Processing Technology 212 (2012) 553–559.

[235] S. S. Warsi, S. H. I. Jaffery, R. Ahmad, M. Khan, L. Ali, M. H. Agha, S. Akram, Development of energy consumption map for orthogonal machining of al 6061-t6 alloy, Proceedings of the Institution of Mechanical Engineers, Part B: Journal of Engineering Manufacture 232 (2018) 2510–2522.

[236] T. Terabayashi, J. Yan, Surface formation behaviors in wavy microgroove cutting on various workpiece materials, International Journal of Automation Technology 14 (2020) 245–252.

[237] X. Pang, Y. Zeng, J. Zhang, W. Deng, Analytical model and experimental verification of poisson burr formation in ductile metal machining, Journal of Materials Processing Technology 290 (2021) 116966.

[238] G. Struzikiewicz, W. Zębala, B. Słodki, Cutting parameters selection for sintered alloy alsi10mg longitudinal turning, Measurement 138 (2019) 39–53.

[239] S. V. Laakso, M. Hokka, E. Niemi, V.-T. Kuokkala, Investigation of the effect of different cutting parameters on chip formation of low-lead brass with experiments and simulations, Proceedings of the Institution of Mechanical Engineers, Part B: Journal of Engineering Manufacture 227 (2013) 1620–1634.

[240] B. Wang, Z. Liu, Serrated chip formation mechanism based on mixed mode of ductile fracture and adiabatic shear, Proceedings of the Institution of Mechanical Engineers, Part B: Journal of Engineering Manufacture 228 (2014) 181–190.

[241] V. Bushlya, D. Johansson, F. Lenrick, J.-E. Ståhl, F. Schultheiss, Wear mechanisms of uncoated and coated cemented carbide tools in machining lead-free silicon brass, Wear 376 (2017) 143–151.

[242] Ç. V. Yıldırım, Experimental comparison of the performance of nanofluids, cryogenic and hybrid cooling in turning of inconel 625, Tribology International 137 (2019) 366–378.

[243] J. Airao, N. Khanna, C. K. Nirala, Tool wear reduction in machining inconel 718 by using novel sustainable cryo-lubrication techniques, Tribology International (2022) 107813.

[244] P. Kalita, A. P. Malshe, S. A. Kumar, V. Yoganath, T. Gurumurthy, Study of specific energy and friction coefficient in minimum quantity lubrication grinding using oil-based nanolubricants, Journal of Manufacturing Processes 14 (2012) 160–166.

[245] D. Umbrello, F. Micari, I. Jawahir, The effects of cryogenic cooling on surface integrity in hard machining: A comparison with dry machining, CIRP annals 61 (2012) 103–106.

[246] Y. Yildiz, M. Nalbant, A review of cryogenic cooling in machining processes, International Journal of Machine Tools and Manufacture 48 (2008) 947–964.

[247] C. Arcona, T. A. Dow, An empirical tool force model for precision machining, J. Manuf. Sci. Eng., Transaction of the ASME (1998).

[248] M. Jiang, L. Dai, Formation mechanism of lamellar chips during machining of bulk metallic glass, Acta Materialia 57 (2009) 2730–2738.

[249] S. Zhang, S. To, S. Wang, Z. Zhu, A review of surface roughness generation in ultra-precision machining, International Journal of Machine Tools and Manufacture 91 (2015) 76–95.

[250] F. Wardle, Ultra-precision bearings, Elsevier, 2015.

[251] Z. Ke, G. Liuwang, W. Zhan, Y. Haipeng, W. Zinan, Z. Liqi, Nonlinear dynamic analysis of ceramic motorized spindle considering bearing preload and span, Proceedings of the Institution of Mechanical Engineers, Part C: Journal of Mechanical Engineering Science (2022) 09544062221132190.

[252] Z. Ke, Z. Liqi, W. Zhan, G. Liuwang, Nonlinear dynamic characteristics of full-ceramic motorized spindle considering axial transfer of unbalanced magnetic pull,

Proceedings of the Institution of Mechanical Engineers, Part C: Journal of Mechanical Engineering Science (2022) 09544062221122078.

[253] K. Zhang, Z. Wang, X. Bai, H. Shi, Q. Wang, Effect of preload on the dynamic characteristics of ceramic bearings based on a dynamic thermal coupling model, Advances in Mechanical Engineering 12 (2020) 1687814020903851.

[254] Z. Xia, Y. Wu, T. Ma, Z. Bao, J. Tian, L. Gao, J. Sun, S. Li, Experimental study on adaptability of full ceramic ball bearings under extreme conditions of cryogenics and heavy loads, Tribology International 175 (2022) 107849.

[255] J. Ni, Dynamic stability and debugging of aerostatic-pressurized bearings in magnetic disk comprehensive instrumentation, J Huazhong Univ Sci Technolog Med Sci 13 (1985) 69–74.

[256] S. Ma, G. Zhang, J. Wang, Y. Wen, J. Han, H. Wang, An on-line identification method of tool-below-center error in single-point diamond turning, Journal of Manufacturing Processes 79 (2022) 154–165.

[257] E. Brinksmeier, W. Preuss, O. Riemer, R. Rentsch, Cutting forces, tool wear and surface finish in high speed diamond machining, Precision Engineering 49 (2017) 293–304.

[258] X. Zhang, R. Huang, K. Liu, A. S. Kumar, X. Shan, Rotating-tool diamond turning of fresnel lenses on a roller mold for manufacturing of functional optical film, Precision Engineering 51 (2018) 445–457.

[259] D. Kramar, D. Cica, Modeling and optimization of finish diamond turning of spherical surfaces based on response surface methodology and cuckoo search algorithm, Advances in Production Engineering & Management 16 (2021) 326–334.

[260] H. Narita, N. Desmira, H. Fujimoto, Environmental burden analysis for machining operation using lca method, in: Manufacturing systems and technologies for the new frontier, Springer, 2008, pp. 65–68.

[261] D. M. Kim, H. I. Kim, H. W. Park, Tool wear, economic costs, and co2 emissions analysis in cryogenic assisted hard-turning process of aisi 52100 steel, Sustainable Materials and Technologies 30 (2021) e00349.

List of Publications and Presentations

Published articles

1. **Arnab Das**, Vivek Bajpai, “Machinability analysis of lead free brass in high speed micro turning using minimum quantity lubrication”, CIRP Journal of Manufacturing Science and Technology (2023) 41: 180-195 (Q2) Impact factor: 3.56.

2. **Arnab Das**, Abisoor Rishi Sharan Mundu, Vivek Bajpai, "Enhancing tribological performance of lead free brass in high speed micro turning via hybrid cryogenic cooling technique", Tribology International (2022) 179 : 108090 (Q1) Impact factor: 5.62.

3. **Arnab Das**, Shashank Shukla, Mohan Kumar, Chitransh Singh, M.L. Chandravanshi, Vivek Bajpai, “Development of vibration free machine structure for high-speed micromilling center”, International Journal of Advanced Manufacturing Technology (2021) 116 : 3489–3506 (Q2) Impact factor: 3.563.

4. **Arnab Das**, Vivek Bajpai, “Turning insert with lubricating passage along the normal plane for minimization of friction, cutting force and tool wear”, Journal of Manufacturing Processes (2023) 101 : 141–155 (Q2) Impact factor: 5.684.

Communicated articles

1. **Arnab Das**, Chitransh Singh, Vivek Bajpai, Madan Lal Chandravanshi, “Feasibility of cost-effective ultra-precision diamond turning using ceramic bearing spindle”, International Journal of Advanced Manufacturing Technology (2022) (Q2) Impact factor: 3.563.

Patents

1. Vivek Bajpai, **Arnab Das**, Shashank Shukla, Chitransh Singh, Mohan Kumar and Madan Lal Chandravanshi, "A machine structure to reduce vibration of micro-milling machine". (Published) Application no.201931049978 A, Patent office journal no. 30/2020 Dated 24/07/2020.

2. Vivek Bajpai, **Arnab Das**, "Turning insert with lubricating passage along the normal plane for minimization of friction and cutting force". (Published) Application no. 202231032536 A, Patent office journal no. 27/2022 Dated 08/07/2022.

International Conferences

1. **Arnab Das**, Vivek Bajpai, “Improvement in tool wear behavior and tool life in high-speed micro turning using hybrid cryogenic cooling technique”, International Conference on Frontiers in Materials Engineering (ICFME-2022), IIT Indore, India.

2. **Arnab Das**, Vivek Bajpai, “Development of an Ultra-High Speed Micro-Milling Center: An FEM Approach”, 2nd International Conference on Industry 4.0 and Advanced Manufacturing (I-4AM 2022), IISc Bangalore, India. (Achieved "One of The Distinguished Paper Award")

3. **Arnab Das**, Vivek Bajpai, “Analysis and prediction of surface roughness on lead free brass in high speed micro turning”, World Congress on Micro & Nano Manufacturing 2021 (WCMNM 2021), IIT Bombay, India.

4. **Arnab Das**, Deepak Kumar, Mohan Kumar, Vivek Bajpai, “Experimental investigation of electrochemical micro turning of Ti6Al4V with NaOH solution”, ASME 2020 15th International Manufacturing Science and Engineering Conference (MSEC2020), Cincinnati, OH, USA.

5. **Arnab Das**, Vivek Bajpai, “Fabrication of super-finished surfaces in high-speed turning and micro turning: A review”, International Conference on Precision, Meso, Micro and Nano Engineering (COPEN 2019), IIT Indore, India.